Adam Mickiewicz University, Poznań
Faculty of Physics and Astronomy
Astronomical Observatory Institute

SIZES AND THERMAL PROPERTIES OF ASTEROIDS

Antoine Choukroun

PhD Thesis

supervisor: prof. UAM dr hab. Anna Marciniak

2025

Acknowledgments

I wish to express my deepest gratitude to my supervisor, Prof. AMU Anna Marciniak, for her unwavering support throughout this thesis, as well as for her patience, guidance, and valuable advice. Her attentiveness and rigor have helped me avoid many obstacles along the way.

I would also like to thank the other members of the team, Julia Perła and Bartosz Ziółkowski, for their invaluable help, both with the work on this thesis and in using and improving the various tools presented in this manuscript.

Finally, I would like to thank the members of my family who, even from afar, have greatly supported me. I would also like to dedicate this thesis to my grandfather, in his memory, who sadly passed away one month before its completion.

The author obtained funding for a research project, PRELUDIUM-BIS no. 2020/39/O/ST9/00713, from the National Science Centre, Poland. He also obtained funding for the foreign internship from the National Agency for Academic Exchange, Poland, stipend no. BPN/PRE/2022/U/0001.

Summary

Asteroids are fundamental tracers of Solar System history, yet their physical properties remain poorly constrained for many objects. Accurate size determination is particularly critical for deriving bulk densities and interpreting internal structures, but published estimates often differ by more than 30%, leading to density uncertainties exceeding 90%. This thesis addresses these challenges through the combined use of photometry, thermophysical modelling, and stellar occultations, applied within the framework of two long-standing international observing campaigns.

The core result comes from the analysis of 15 main-belt asteroids using the Convex Inversion Thermophysical Model (CITPM) and multichord stellar occultations. Reconstructed 3D shapes, unique spin axis solutions, and reliable diameters were obtained. Sizes determined independently with the two methods show excellent agreement, typically within 5%, with no systematic bias, thereby validating CITPM as a robust technique when applied to high-quality data. Thermal inertia values were also derived, ranging from a few up to more than 200 $\mathrm{Jm^2s^{-1/2}K^-1}$, revealing a diversity of surface properties consistent with both fine and coarse regolith. The majority of the above-mentioned work was done by the author of this thesis.

In parallel, the author of this thesis contributed to the long-term programme on slow rotators by processing essential photometric data for spin and shape models for 16 asteroids with periods up to 60 h. Scaling them with stellar occultations not only resolved long-standing inconsistencies in their size estimates but also broke mirror-pole ambiguities, substantially enriching the population of unique asteroid models of slowly rotating asteroids.

This thesis also presents the thermophysical characterization of the unusual main-belt asteroid (269) Justitia, which spectroscopic and polarimetric properties suggest an origin in the trans-Neptunian region. Using CITPM, its size was constrained to a narrow range of 55–60 km, a fourfold improvement over previous estimates, together with the first determinations of its thermal inertia and surface roughness. Here, the contribution ot the thesis author was in the photometric data processing but also in validating the obtained model. These results aided the telescope deployment for a special occultation campaign in the US and provided essential input for the upcoming Emirates MBR Explorer mission, which has Justitia as a prime target.

To support these studies, the author developed two main open source tools written in Python: STEROID, the pipeline for automated asteroid photometry and the occultation fitting code. With the former the author processed over a hundred lightcurves of asteroids studied here. This suite of methods ensures reproducible and scalable analyses of asteroid properties.

Overall, this work delivers the most precise physical characterisation to date for a representative set of poorly studied asteroids, confirms the reliability of CITPM against direct occultation scaling, and provides unique insights into the diversity of asteroid surface properties, with applications ranging from density determinations to space mission design.

Key words: asteroids - minor planets of the Solar System - photometry - thermophysical model - stellar occultations - asteroid diameters

Streszczenie

Planetoidy zawierają w sobie unikalny zapis historii Układu Słonecznego, a mimo to na temat własności fizycznych wielu z nich wiadomo bardzo mało. Dokładne wyznaczanie ich rozmiarów jest szczególnie istotne dla wyliczania gęstości w kontekście ich budowy wewnętrznej, tymczasem publikowane wartości średnic nierzadko różnią się o ponad 30%, co powoduje, że wyznaczona gęstość obarczona jest niepewnością rzędu 90%. Niniejsza praca podejmuje się rozwiązania tego problemu poprzez synergiczne użycie fotometrii, modelowania termofizycznego oraz zakryć gwiazdowych, opierając się na dwóch wieloletnich kampaniach obserwacyjnych.

Główny wynik tej pracy pochodzi z analizy piętnastu planetoid Głównego Pasa przy użyciu modelu termofizycznego z inwersją wypukłą (z ang. CITPM) oraz bogato pokrytych zjawisk zakryć gwiazd przez planetoidy. Odtworzono tu ich trójwymiarowe kształty, uzyskano jednoznaczne rozwiązania na parametry rotacji oraz miarodajne wartości średnic. Te ostatnie, wyznaczone niezależnie z użyciem obu wspomnianych metod wykazują doskonałą zgodność, zwykle w granicach 5%, bez żadnych systematycznych odchyłek. Tym samym potwierdzono wiarygodność metody CITPM zastosowanej na wysokiej jakości danych. Wyznaczono również bezwładność cieplną badanych obiektów, uzyskując wartości w szerokim zakresie of kilku do ponad dwustu $\mathrm{Jm^2s^{-1/2}K^-1}$, co ukazuje różnorodność własności ich powierzchni, pokrytych drobno- oraz gruboziarnistym regolitem. Większość wspomnianych wyżej zadań została wykonana przez autora niniejszej rozprawy.

Dodatkowo autor brał udział w wieloletnim projekcie badania planetoid o wolnej rotacji, przeprowadzając obróbkę danych fotometrycznych niezbędnych do uzyskania modeli kształtu i rotacji szesnastu planetoid o okresach sięgających 60 godzin. Wyskalowanie tych modeli za pomocą zakryć gwiazdowych nie tylko rozwiązało długotrwałe niezgodności w ich wyznaczanych rozmiarach, ale także problem niejednoznaczności położenia osi rotacji, znacząco wzbogacając zbiór wolno rotujących planetoid o wyznaczonych modelach.

Rozprawa zawiera także charakterystykę termofizyczną nietypowej planetoidy głównego pasa, (269) Justitia, której spektralne i polarymetryczne własności powierzchni sugerują pochodzenie tego ciała z rejonu obiektów transneptunowych. Dzięki użyciu metody CITPM, czterokrotnie zawężono możliwy zakres jej rozmiarów, ograniczając go do wartości 55-60 km. Po raz pierwszy wyznaczono też jej bezwładności cieplną i chropowatość powierzchni. Wkład autora rozprawy polegał tu na obróbce danych fotometrycznych, ale też na weryfikacji otrzymanego modelu. Otrzymane wyniki wspomogły rozmieszczenie stacji obserwacyjnych podczas szeroko zakrojonej kampanii zakryciowej w Stanach Zjednoczonych. Uzyskane tu wyniki stanową też istotne informacje dla planowanej misji agencji kosmicznej Emiratów Arabskich MBR Explorer, której głównym celem jest Justitia.

Dla wsparcia tych badań autor rozprawy stworzył dwa główne narzędzia napisane w języku Python i udostępnione na licencji open source: kod STEROID, automatyzujący fotometrię planetoid oraz narzędzie occultationFit, służące do dopasowywania modeli planetoid do obserwacji zakryciowych. Dodatkowo, za pomocą pierwszego z nich autor uzyskał ponad sto krzywych blasku badanych tu planetoid. Z połączenia tych narzędzi powstał zestaw metod gwarantujących powtarzalną i skalowalną analizę własności planetoid.

Podsumowując, niniejsza praca zawiera najdokładniejszą jak dotąd charakterystykę reprezentatywnej próbki słabo uprzednio zbadanych planetoid, potwierdza wiarygodność metody CITPM weryfikując jej wyniki za pomocą bezpośredniego skalowania modeli planetoid do obserwacji zakryciowych oraz daje wyjątkowy wgląd w różnorodność cech powierzchni planetoid. Jej dalsze zastosowania sięgają od wyznaczeń gęstości planetoid po planowanie misji kosmicznej.

Słowa kluczowe: planetoidy - małe ciała Układu Słonecznego - fotometria - model termofizyczny - zakrycia gwiazdowe - średnice planetoid

Contents

Chapter 1

Introduction

1.1 Historic context and current state of the art

Although asteroids are among the celestial objects closest to Earth, their small size makes them a challenging subject of study. Indeed, since ancient times, the view of stars has been within our ancestors' sight – and, under a pristine night sky, even nebulae and galaxies could be seen. However, the first asteroid was not discovered until the night of January 1, 1801. When the Italian astronomer Giuseppe Piazzi was compiling a new star catalogue, he spotted an object that did not appear in any earlier records: Ceres. In the years that followed, several other similar objects were brought to light in that same region of the solar system. As early as 1802, the astronomer Heinrich Olbers discovered (2) Pallas, then (3) Juno was found in 1804 by Karl Harding, and (4) Vesta in 1807 (again by Olbers). The existence of this quartet of "small planets" between Mars and Jupiter gave rise to the hypothesis that they might be fragments of a once-complete planet shattered by collision. In 1802, William Herschel even coined the term "asteroid" to distinguish these star-like points from the true planets. Despite numerous new finds that came afterwards, asteroids long remained mysterious in their physical properties. Their point-like appearance in telescopes prevented any direct measurement of their size or shape. Early diameter estimates for Ceres, for example, proved wildly imprecise: Herschel himself judged it to be only about 260 km across, based on its brightness relative to reference stars, whereas in 1811 Johann Schröter guessed a diameter of some 2600 km, an order of magnitude larger. A turning point occurred at the very end of the nineteenth century with the introduction of photography to astronomy. In 1891, the astronomer Max Wolf used photographic plates for the first time to ease the detection of asteroids: in a long-exposure image, these objects show up as short streaks among the stars. This technological breakthrough triggered a leap in discoveries: whereas only a few hundred asteroids were known around 1890, their number quickly exceeded the thousand mark by the early twentieth century.

In 1906, Henry Norris Russell's paper "On the Light-Variations of Asteroids and Satellites" (Russell, 1906) laid the groundwork for asteroid studies. Russell showed that one can determine an asteroid spin axis position from the shape of its lightcurves, yet he concluded that its exact three-dimensional form could not be recovered from lightcurves alone. As a result, asteroids have been modelled as simple ellipsoids for many decades. Mikko Kaasalainen eventually overturned this impasse in the 1990s with his now-classic convex inversion method, proving that a unique

convex shape can indeed be extracted. One cannot fault Russell, since the first commercial computers (UNIVAC I) only appeared in the 1950s, and the first digital imaging systems for astronomy appeared in the 1970s. By enabling rapid image acquisition and producing vast amounts of data, they revolutionised the field. It was precisely the explosion of asteroid lightcurve observations under diverse viewing geometries, combined with the advent of iterative nonlinear optimisation techniques, unimaginable during Russell's time, that made Kaasalainen's breakthrough possible. Other observational methods have similarly taken advantage of computational and technical advances: radar imaging, spectroscopy and thermal-infrared measurements, just to name a few. For instance, the advent of modern high-speed cameras coupled with GPS-synchronised timing has enabled the democratisation and worldwide observations of stellar occultations, which form the basis of the work presented in this thesis. As technology advanced, the human mind evolved alongside it, adapting to new possibilities. Thus, new modelling techniques have emerged today, utilising various types of data or even combining multiple sources to unlock deeper insights. The work presented in this thesis reflects both aspects, demonstrating technical advancements as well as enhancing our understanding of asteroid properties. The next parts will be dedicated to introducing some of these techniques and their impact on the field of asteroid studies.

1.2 Asteroid observing techniques and their significance

1.2.1 Scientific relevance of asteroids

Asteroids hold a uniquely important place in planetary science as primitive remnants of the early Solar System. In our current understanding, asteroids, large ones in particular, are direct survivors of the original planetesimals that coalesced into planets, and as such they retain a relatively pristine record of the Solar System initial conditions from ∼4.6 billion years ago (Bottke et al., 2002). Their physical and orbital diversity today, spanning a range of compositions from primitive carbonaceous bodies to molten or aqueously processed fragments, provides powerful constraints on models of large planets formation and migration. For instance, the unexpected mixing of asteroid types across the main belt (e.g. inner-belt asteroids with compositions of colder outer regions and vice versa) or across much larger distances, like in the case of asteroid Justitia (Hasegawa et al., 2021), is best explained by early planetary migration events (such as inward-then-outward wandering of Jupiter) that redistributed small bodies throughout the protoplanetary disk (Walsh et al., 2011, DeMeo & Carry 2013). In this way, the asteroid belt serves as a "living fossil" of Solar System evolution, preserving evidence of the accretion, collision and dynamical processes that shaped the planets. Studying asteroids thus offers a window into the conditions of planet formation that would otherwise be inaccessible by examining the evolved planets alone.

Asteroids are also fundamentally linked to the meteorites studied in laboratories, allowing us to bridge astronomical observations with touchable samples. Orbital analyses of meteorite falls have confirmed that the vast majority of meteorites are fragments of asteroids (Borovička et al., 2015). These rocks, serendipitously

delivered to Earth, serve as chemical and isotopic archives of asteroidal material, recording primordial Solar System matter that can be probed in detail in the lab. Indeed, meteorites (especially the carbonaceous chondrites) contain presolar grains and organic compounds that shed light on the inventory of water-bearing minerals and organic molecules available during planet formation (Shober et al., 2025). One limitation, however, is that meteorites are often altered by their transit through Earth atmosphere and residence on our planet. To overcome this, recent sample-return missions, e.g. JAXA's Hayabusa2 to Ryugu (Tsuda et al., 2019) and NASA's OSIRIS-REx to Bennu (Lauretta et al., 2019) have collected pristine asteroid material that has never been contaminated by Earth environment and would not even survive the atmospheric entry. Analysis of these returned samples, in parallel with meteorite studies, provides rich information on composition of asteroids and their formation histories, and calibrates the laboratory findings with respect to known parent bodies.

One of the most important asteroid parameters is their bulk density. That parameter is essential for studies of their internal structure and mineralogical composition to find the link between meteorites and their parent bodies. Asteroids with diameters greater than 100 km are regarded as primitive and mostly unaltered since their formation (Morbidelli et al., 2009). In contrast, smaller asteroids are thought to be fragments resulting from collisions and subsequent reaccumulations, often exhibiting significant macroporosity, complicating mineralogical studies based on their density.

Beyond their historical record, asteroids have taken on practical significance through the field of planetary defence. It is now well recognised that asteroid impacts have played a major role in shaping Earth geological and biological history – a notable example being the $\sim$10 km asteroid impact at the end of the Cretaceous period, which is linked to a global mass extinction event. Asteroids continue to pose a non-negligible impact hazard, motivating international efforts to catalogue Near-Earth Objects (NEOs) and model impact scenarios. This has culminated in the first experimental test of asteroid deflection: NASA's Double Asteroid Redirection Test (DART) mission in 2022 (Cheng et al., 2023) successfully demonstrated that a kinetic impact can measurably alter an asteroid orbit, validating the kinetic impactor technique as a feasible method of impact hazard mitigation. The success of DART represents a milestone in translating our scientific understanding of asteroids into a strategy to protect Earth, and ongoing research on asteroid orbits, compositions, and internal strength directly informs future defence capabilities.

Recent spacecraft missions have revealed that small asteroids such as Dimorphos possess extremely loose, rubble-pile structures that undergo surface reshaping under even modest perturbations. For instance, DART observations indicate that the kinetic impact triggered not only a deflection but also significant surface restructuring and particle ejection, suggesting low material strength and mechanical cohesion (Cheng et al., 2023). These bodies provide rare natural conditions to study how granular materials behave under minimal gravitational and cohesive forces – conditions impossible to reproduce on Earth, as suggested by the observed boulder fracturing and regolith mobility on Dimorphos (Raducan et al., 2024). Asteroids studied in situ inadvertently offer valuable insights into surface mechanics, regolith evolution, and impact dynamics at a range of scales.

Finally, asteroids are increasingly recognised as potential resources for future space exploration and industry. Many carbonaceous asteroids (C-types), especially those coming from the outer main belt, contain water-rich minerals and volatiles that

could be exploited for in-situ resource utilisation (ISRU). Studies have shown that phyllosilicates and hydrated minerals are widespread in these bodies, as revealed by both spectroscopic surveys (Rivkin et al., 2002; Milliken & Rivkin, 2009) and direct observations from missions such as Hayabusa2 and OSIRIS-REx (Watanabe et al., 2017, Lauretta et al., 2017). Water extracted from such materials could enable life support systems, or could be electrolysed into hydrogen and oxygen for propulsion, dramatically reducing the need to launch fuel from Earth.

In addition, metal-rich asteroids (M-type) are thought to contain high concentrations of platinum-group elements (PGEs), nickel, cobalt, and iron, making them attractive targets for future space mining (Sonter, 1997, Elvis, 2014). While current economic models remain speculative, the strategic importance of rare Earth elements and PGEs, coupled with their limited availability in terrestrial mines, has motivated both governmental and private initiatives to investigate asteroid mining (Hein et al., 2020). Some estimates suggest that a single metallic asteroid of $\sim$1 km diameter could contain more platinum than has ever been mined on Earth (Kargel, 1994). Although major engineering challenges remain, the concept of harvesting resources from asteroids is now being actively evaluated in mission concepts and international roadmaps. As such, asteroids are not only archives of the Solar System past, but also candidates to support future sustainment and expansion of humanity.

1.2.2 Photometry: brightness variations and rotational clues

Photometry is the measurement of the variations in brightness of celestial objects over time. By recording and plotting the flux received from a target as a function of time, astronomers construct lightcurves, fundamental tools for inferring key physical properties.

The application of photometry to asteroid studies began in the early 20th century. In 1901, Austrian astronomer Edmund von Oppolzer identified periodic variations in the brightness of asteroid (433) Eros, producing the first recorded asteroid lightcurve and providing direct evidence of rotational modulation caused by an elongated, irregular shape (von Oppolzer, 1901). Throughout the 20th century, coordinated observations by professional and amateur astronomers yielded lightcurves for hundreds of asteroids. These data revealed the diversity of asteroid spin states and shapes, suggesting that many objects were non-spherical and displaying complex rotational behaviour (Pravec et al., 2002).

In modern asteroid science, photometry plays a central role in characterising physical properties such as rotation, shape, and light scattering by their surfaces. Observations can be classified by two main features: temporal sampling and photometric calibration. From a temporal perspective, dense photometry refers to high-cadence observations, typically continuous or regularly spaced measurements over several hours or nights. These are crucial for deriving rotation periods, resolving short-term brightness modulations, and constraining detailed shape models, when lightcurves from multiple apparitions are gathered. In contrast, sparse photometry consists of isolated brightness measurements acquired over extended time intervals. Although each observation is temporally disconnected, the cumulative dataset, especially from large-scale surveys or space missions, offers broad coverage of viewing geometries and phase angles, enabling statistical modelling and spin-state determination. Apart from cadence, photometric data may be either relative or absolute. Relative photometry

measures changes in brightness with respect to comparison stars within the same field, making it particularly effective for rotational lightcurves. Absolute photometry, on the other hand, requires calibration against standard stars with known fluxes to determine the intrinsic brightness of the object, and is essential for constructing phase curves and interpreting surface reflectivity. A key example of sparse, absolute photometry is provided by ESA's Gaia mission. With its BP/RP photometric instruments (Gaia Collaboration, Prusti et al., 2016), Gaia has collected precise brightness measurements for over 150,000 asteroids across a wide range of solar phase angles (Tanga et al., 2023). Though temporally sparse, the data are highly complementary to dense, ground-based relative lightcurves. The synergy of both datasets allows for robust reconstruction of rotation periods, spin axes, 3D shape models, and calibrated phase curves (Ďurech et al., 2019; Wilawer et al., 2022).

Photometry is arguably the most widely applicable method in the characterisation of small bodies. It extends from fast-rotating Near-Earth Asteroids (NEAs), where high-cadence data can probe their internal structure and reveal binary systems, to faint Trans-Neptunian Objects (TNOs), for which sparse surveys remain the most viable tool. For Main Belt Asteroids (MBAs), long-term monitoring across multiple apparitions has to date yielded detailed spin and shape models for thousands of bodies collected in the DAMIT database[1] (Database for Asteroid Models from Inversion Techniques, Ďurech et al. (2010)). From Hipparchus's magnitude ranks to today's digital sky surveys, photometry has evolved from a qualitative observational practice into a quantitative basis of planetary science. Lightcurves now serve as precise diagnostic tools, unveiling the dynamical and structural complexity of small Solar System bodies beyond the reach of direct imaging.

1.2.3 Infrared observations: thermal emission and size determination

While visible-light photometry provided the first hints of asteroid shapes, infrared observations provided the first accurate measure of their sizes. At the end of the XVIII century, Pierre Prévost was the first one to mention that all bodies radiate heat, no matter how hot or cold they are. This statement was important because it pointed out the interaction between the light and the temperature. In other terms, a hot body emits "light", but received light warms up a body too. Therefore, using works done on black body, it is possible to build simple thermal models based on radiative transfer:

$$(1 - A)S = 4\epsilon\sigma T^4 \tag{1.1}$$

with A being the bolometric Bond albedo, S the solar constant at the orbit of the asteroid, σ the Stefan-Boltzman constant, ϵ the emissivity and T the asteroid surface temperature. In simple terms, this equation describes the equilibrium between the energy received by an asteroid, considering that the only source of heating is the Sun (left side of 1.1) and the energy emitted by the asteroid by radiative emission (right side of 1.1). This model is very simple and assumes a spherical asteroid with a homogeneous temperature distribution. We will go into details of more complex models in the section 3.2. Initially, the true challenge was to measure asteroid

[1] https://damit.cuni.cz/

thermal flux. Early attempts to detect asteroid thermal emission in the 1970s, using ground-based infrared radiometers, were challenging and limited to the largest, closest asteroids. The breakthrough came in 1983 with the launch of the Infrared Astronomical Satellite (IRAS), the first all-sky infrared survey (Neugebauer et al., 1984). IRAS scanned the sky at thermal wavelengths and detected the heat signatures of hundreds of asteroids. For the first time, diameters and albedos (reflectivities) could be determined systematically: the infrared flux from an asteroid, combined with its reflected visible light, yielded a radiometric size estimate via a simple thermal model. By the end of its mission, IRAS had measured diameters and albedos for 1,884 asteroids using standard at the time thermal modelling approach (Walker, 2003). This Standard Thermal Model (STM) by Lebofsky et al. (1986a), though simple, was an innovative first step. One can imagine the excitement in the 1980s as IRAS data revealed that Ceres was about 950 km across, Pallas ∼550 km, etc., finally putting real numbers to objects that for nearly two centuries had been merely "points of light".

Infrared asteroid astronomy has since blossomed, especially from space-based platforms. NASA's Wide-field Infrared Survey Explorer (WISE, Wright et al., 2010), launched in 2009, performed an even more sensitive all-sky survey. In its NEOWISE mission phase (Mainzer et al., 2011), WISE specifically focused on small bodies. The results have been spectacular: until 2024, the NEOWISE survey alone had made over 1.5 million infrared measurements of 43,926 different solar system objects, including more than 1,500 NEOs (Near Earth Objects)[2]. From these data, diameters and albedos are being derived using improved thermal models (e.g. the Near-Earth Asteroid Thermal Model by Harris, 1998, which accounts for slow rotation and which uses a fitted beaming parameter to approximate the combined effects of surface roughness and finite thermal inertia). NEOWISE provided size estimates for over 1,850 NEAs in particular, greatly improving our knowledge of the size distribution within the near-Earth population. Main Belt and even Trojan asteroids of Jupiter have infrared (IR) measurements from WISE and the earlier Japanese Akari space telescope (Usui et al., 2011). For TNOs, infrared observation is more challenging (their black-body temperatures are very low); still, the largest TNOs like Pluto, Eris, or Sedna were detected in far-IR mainly by the Herschel mission in the 2010s, which helped constrain their sizes (Müller et al., 2020).

The constant increase of the amount of thermal data, coupled with projects like "TNOs are cool" (Lellouch et al., 2013) or SBNAF ("Small Bodies: Near and Far", Mueller et al., 2016) led to the creation of a public database of expert-reduced thermal IR observations from all major missions (Szakáts et al., 2020)[3], supporting the usage of more advanced techniques of modelling named thermophysical models (TPMs). TPMs are a big improvement over STM (Delbo et al., 2015). Indeed, TPM no longer considers the shape of asteroids to be spherical and does not assume zero thermal inertia as STM did. This improvement allowed more accurate size determinations but also investigation on very subtle physical processes like the Yarkovsky effect (a force caused by anisotropic thermal re-radiation, Vokrouhlický et al., 2015).

[2]WISE/NEOWISE: https://science.nasa.gov/mission/neowise/ (accessed 24 April 2025).
[3]SBNAF IR database: `https://ird.konkoly.hu/`

1.2.4 Astrometry: pinpointing positions and orbits

Astrometry – the measurements of celestial body positions – is the oldest of all asteroid observing techniques, dating right back to the discovery of Ceres in 1801. In fact, it was through painstaking astrometric tracking that Gauss was able to calculate Ceres orbit from just a few observations, inaugurating the era of minor planet dynamical studies. For much of the 19th and 20th centuries, astrometry was the only asteroid science: observers would record the coordinates of asteroids against background stars night after night, enabling the determination of orbits. Historically, the accuracy of asteroid astrometry improved from perhaps one-arcminute uncertainty in the 1800s (via filar micrometres and later photographic plates) to the sub-arcsecond level by the late 20th century with CCDs. The Minor Planet Center (MPC) was established by the International Astronomical Union as the clearinghouse for all these observations. Thanks to multiple surveys such as Pan-STARRS (Chambers et al., 2016), Catalina Sky Survey (Drake et al., 2009) or ATLAS (Tonry et al., 2018) and thanks to extremely accurate space missions like Gaia (Gaia Collaboration, Prusti et al., 2016), the amount of accurate positional data never stops growing. The recently started Rubin/LSST survey will also greatly contribute to that (Ivezić et al., 2019). These data allow not only precise orbit determination but also the detection of subtle forces acting on asteroids. For example, the cumulative astrometric data of a small NEA over years can reveal the slight orbital drift caused by the Yarkovsky effect (Dziadura et al., 2023). Today, more than 340 positive detections have been made (Fenucci et al., 2024).

Gaia space telescope has further revolutionised asteroid astrometry. Although designed for mapping stars, Gaia also observed solar system objects. Its Data Release 2 (Gaia Collaboration, Brown et al., 2018) included ∼14,000 asteroids with superb positional accuracy, and Data Release 3 (Gaia Collaboration, Vallenari et al., 2023) expanded that to ∼158,000 asteroids spanning many families and even some TNOs. Gaia's astrometry is so precise (on the order of milliarcseconds) that it can detect minute anomalies in asteroid motion. For instance, by comparing predicted vs. Gaia-measured positions, one can sometimes infer the presence of a moon of an asteroid or detect the slight wobble due to an irregular shape (Liberato et al., 2024). In essence, astrometry today not only secures orbits but also opens a door to asteroid mass and density estimates (via gravitational perturbations) and even tests of physics (such as confirming general relativity in the solar system or constraining planetary ephemerides, Shahid-Saless & Yeomans, 1994).

The importance of precise astrometry depends on the asteroid population. For NEAs, astrometry supports planetary defence. Every potential Earth-impacting asteroid is closely tracked astrometrically; the precision of these measurements determines how far into the future we can predict close approaches or impacts (see e.g. Reddy et al., 2022). Astrometry also allows detection of tiny orbital changes, so for NEAs it is the primary way to measure Yarkovsky acceleration that can shift an asteroid from a harmless orbit into a hazardous one (or vice versa, Vokrouhlický et al., 2015). For MBAs, astrometry helps to identify asteroid families or to determine perturbations that can reveal mass of an asteroid. For example, when two asteroids pass relatively close to each other, the slight deviation in their paths – observable in high-precision astrometry – can be used to estimate their masses (Fienga et al., 2020). This has been done for the largest asteroids, contributing to our knowledge of bulk density and composition (Carry, 2012; Kretlow, 2022). For distant objects,

astrometry is often the only way to study these remote bodies. With few observations, a TNO orbit remains very uncertain. But with sustained astrometry over years, even Pluto-distance objects have well-determined orbits. This is crucial for solar system dynamic studies, for planning spacecraft missions or predicting stellar occultations by these bodies.

1.2.5 Radar: probing shape, spin and surface from afar

The idea behind radar observation is to bounce radio waves off an asteroid and catch the returning echo. This technique is highly challenging but remains rewarding. The first experiment took place in June 1968, when asteroid (1566) Icarus made a close approach to Earth. Eager to test the power of the newly developed radar astronomy, scientists at MIT's Haystack Observatory and NASA's Goldstone antenna pointed their dishes at that asteroid. The successful detection of Icarus by radar (Goldstein, 1968) marked the starting point of radar astronomy for asteroids. Over the next few decades, as larger radars came online (most notably the 305-m Arecibo Observatory in Puerto Rico), the technique grew from simple detections to high-resolution imaging. In the 1970s, only a few asteroids (mostly NEAs) were detected as faint echoes. By the late 1980s and 1990s, however, pioneers like Steven Ostro had developed delay-Doppler imaging, wherein the radar echoes are analysed for time delay and frequency shift, yielding pixelated representations of the asteroid (Ostro, 1993). The first such radar "pictures" – for instance, of asteroid 4769 Castalia in 1989 – surprised the community, revealing a contact-binary shape that no telescope on Earth could have resolved (Hudson & Ostro, 1994). For the first time, humanity had almost direct images (albeit made by radio waves) of asteroids that were just dots in the optical light.

The strength of radar lies in the rich information its echoes carry. By timing the echo return, one gets a distance (range) accurate to tens of meters; by measuring frequency broadening, one obtains the asteroid rotation speed (Doppler shifts from the rotating surfaces). Through sophisticated processing, radar can even produce images with resolution as fine as a few meters in the best cases – Lance Benner says, some radar images of asteroids "rival the resolutions of spacecraft flyby missions" [4]. These capacities also allow determination of precise size, shape and spin state of asteroids (e.g. Hudson & Ostro, 1995, Cannon et al., 2025). One can also imagine that using radar to get precise measurements can help to reduce degrees of freedom of thermophysical models (explained in the section 1.2.3) and help to precisely determine physical properties such as surface roughness and thermal inertia. The practical importance of radar is most pronounced for NEAs, especially those that come nearest to Earth. From a planetary defence perspective, radar provides unparalleled orbital precision. When radar ranging is available, the along-track position of an asteroid can be pinned down so accurately that we can confidently predict its trajectory for decades. A great example is 99942 Apophis: optical observations left a lingering uncertainty that it might impact Earth in 2068, but radar measurements in 2013 and 2021 refined its orbit and helped to eliminate any possibility of it impacting Earth (Vinogradova et al., 2008, Pérez-Hernández & Benet, 2022) For MBAs, radar is generally out of reach – they are too far for the radar signal to return detectably in most cases (though a few, like Ceres and Vesta, have been attempted). However,

[4] www.space.com (accessed 30 April 2025).

radar did play a role in imaging Mars-crossers during favourable oppositions (Ostro et al., 2001), and could do so for other large MBAs if transmitters improve.

1.2.6 Spectroscopic analysis: unveiling composition through light

While photometry and astrometry tell us about the motion and the shape of an asteroid, reflectance spectroscopy reveals what it is made of. The technique involves dispersing the light reflected from an asteroid into a spectrum and studying its slope and absorption characteristics, which are wide dips at specific wavelengths where certain minerals and molecules absorb light. Asteroid spectroscopy has a rich historical record. In the 1970s, astronomers achieved the first reliable spectral measurements of asteroids across visible and near-infrared wavelengths. A landmark event was in 1970 when McCord and colleagues obtained a high-quality reflectance spectrum of Vesta (McCord & Chapman, 1975a,b). They found that its spectrum has a strong absorption band near $0.9\,\mu$m (and a weaker one around $0.5\,\mu$m), indicative of pyroxene, a mineral found in basalt. This was the first definitive link found between an asteroid and a meteorite type: basaltic surface composition of Vesta tied it to the HED meteorites (howardite-eucrite-diogenite class, De Sanctis et al., 2013). Building on early work by Clark Chapman and colleagues, who identified a broad bimodal distribution of asteroid colours corresponding to carbonaceous (C-type) and silicate (S-type) surfaces (Chapman et al., 1975), the Eight-Color Asteroid Survey (ECAS) (Zellner et al., 1985) in the late 1970s provided broadband colours of hundreds of asteroids. Using this dataset, David J. Tholen developed the first comprehensive asteroid taxonomy in his 1984 PhD thesis, classifying asteroids into types (C, S, M, D, etc.) based on spectral shape and albedo (Tholen, 1984, Barucci et al., 1987). Spectroscopy had matured enough that asteroids were no longer seen as homogeneous; instead, they fell into categories like dark, carbon-rich C-types, stony S-types, metallic M-types and others, reflecting different compositions and histories.

Today's spectroscopic techniques are far more advanced and cover a wide wavelength range from the ultraviolet to near- and mid-infrared. Large telescopes equipped with spectrographs (on 8-10 m class telescopes like Keck (Wizinowich et al., 2006), VLT (Moorwood, 2008), or Subaru (Iye, 2021) can obtain high-resolution spectra of asteroids, albeit mostly for brighter (larger or nearer) targets. Even smaller telescopes can contribute via low-resolution prism or grating spectra. In addition, earth-bound telescopes and space missions have joined the effort: for example, the Infrared Telescope Facility (IRTF) in Hawaii routinely measures asteroid spectra in the 0.8-2.5 μm range (Pajuelo et al., 2018), and missions like OSIRIS-REx (Lauretta et al., 2017) or Hayabusa2 (Watanabe et al., 2017) carried onboard spectrometers to map asteroid mineralogy up close.

A major recent contribution has again come from ESA's Gaia mission, which in its 2022 data release included average reflectance spectra for over 60,000 asteroids (Tanga et al., 2023). While these Gaia spectra are low-resolution (mostly capturing broad colour trends), such a huge and homogeneous dataset is unprecedented; essentially, we have "spectral fingerprints" for tens of thousands of MBAs now. The current practice combines visible spectra (which probe electronic transitions in some minerals, revealing silicates, oxides and organics) and infrared spectra (which probe vibrational modes, crucial for detecting ices and hydrated minerals). For instance, in TNOs

and Centaurs, infrared spectroscopy has detected signatures of water ice, methane, methanol, and complex organics on their surfaces, hinting at primitive outer solar system chemistry (Pinilla-Alonso et al., 2020). In addition, recent JWST (James Webb Space Telescope) observations show that reflectance spectra of TNOs cluster into distinct compositional families; most objects fall into two macro-groups, 'Cliff' and 'Double-Dip' (Brunetto et al., 2025). Within the Cliff family, however, the spectra split further into two subgroups (Cliff1 and Cliff2; with Cliff2 encompassing both Cold Classicals and more eccentric objects), so depending on the granularity one can speak of two families (Cliff vs. Double-Dip) or three subgroups (Cliff1, Cliff2, Double-Dip) (Brunetto et al., 2025).

In the main belt, spectroscopy is the key to linking asteroids with meteorites: e.g., S-type asteroids show the 1 μm olivine/pyroxene band just like ordinary chondrite meteorites do, whereas C-types have a very flat, featureless spectrum consistent with carbonaceous chondrites. NEAs are often observed spectroscopically to assess their composition (particularly if one might be headed our way and we wish to know if it is metallic or carbonaceous before any deflection mission). Notably, some NEAs exhibit weathered surfaces with muted spectral features; a discovery by early 2000s spectroscopists that indicated space weathering alters asteroid surfaces over time (Nesvorný et al., 2005).

1.2.7 Stellar occultations: silhouettes in the starlight

The technique that truly brings out the citizen-science spirit is the observing of stellar occultations by asteroids. An occultation occurs when an asteroid passes in front of a distant star, momentarily blocking its light for observers along a narrow path on Earth. For a few seconds (often even less), the star disappears, hidden by the asteroid, and from the duration of this blink we can deduce the asteroid size (given the relative speed of this body). Stellar occultation timing is an old trick in astronomy, historically used to measure planetary diameters (Rubashevskii, 1966) or even to discover the rings of Uranus (Elliot et al., 1977). However, applying this technique to asteroids was long thought impractical due to their small sizes and the narrowness of the shadow paths. It was already 1961 when the first predicted asteroidal occultation was successfully observed[5]. But it was not until 1990s, when occultation attempts became more common, aided by better asteroid orbit calculations and more observers ready to watch. Early successes were few (the events are brief and at the time required multiple observers spread across the path for one of them to successfully observe it), but each provided something invaluable: a lower bond on an asteroid diameter, independent of assumptions. In fact, before spacecraft visits, the most accurate sizes of asteroids like Vesta or a TNO Arrokoth, came from occultation chords traced by teams of observers Povenmire (2001); Buie et al. (2020).

Today, asteroid occultation observations have become highly organised and yield astonishing precision. Networks such as the International Occultation Timing Association (IOTA)[6] and other regional groups coordinate predictions (using up-to-date orbits from the JPL Horizons and star positions from Gaia DR3), observations, and reporting. Thanks to inexpensive CCD cameras and specialised high-frame-rate video cameras coupled with GPS, observers can record occultations with accurate

[5] `https://iota-es.de/JOA/JOA2014_4.pdf`

[6] IOTA : `https://www.iota-es.de/`

time-stamps (down to milliseconds), which remain the principal source of uncertainties. Each observation leads to either a positive chord or a negative observation, depending on the observers' positions along the true shadow path. Both positive and negative observations are valuable. Positive chords allow for the reconstruction of the asteroid silhouette, enabling precise diameter determinations and improving prediction accuracy for future events. Negative observations, on the other hand, provide constraints that also contribute to refining predictions and size determinations if coupled with positive ones.

With current level of precision, it is even possible to detect non-convex shape irregularities (Buie et al., 2020). In favourable cases, features like large mountains or binary companions are revealed (Rommel et al., 2023; Gault et al., 2022). The practical role of occultations complements other techniques. For main belt asteroids, occultations have been especially valuable for large and medium-sized MBAs, where they provide diameter and albedo constraints that calibrate other methods (e.g. if an occultation finds an asteroid diameter is 100±5 km, it can validate or refute an infrared-derived diameter that assumed a certain albedo). Occultations also sometimes reveal extreme shapes – for example, the asteroid (216) Kleopatra was found to have a dog-bone shape from occultation chords long before radar imaging confirmed its two-lobed nature (Dunham et al., 1991; Ostro et al., 2000). In the case of TNOs and other distant objects occultations are often the only way to get a precise size (since direct imaging is impossible and thermal flux is very weak). A dramatic example was the dwarf planet Eris: an occultation in 2010 allowed astronomers to pin down Eris diameter (∼2326 km) with a few-kilometer uncertainty, showing it is slightly smaller in size from Pluto. Occultations have also been used to detect and study tenuous atmospheres (as in the case of Pluto – a 1988 occultation was when Pluto thin atmosphere was discovered, Elliot et al., 1989), and even rings around small bodies: the rings of Chariklo (Braga-Ribas et al., 2014), Haumea (Ortiz et al., 2017) and Quaoar (Morgado et al., 2023) were discovered via occultation dips in the star lightcurve before and/or after the main event. For Near-Earth Asteroids, occultation observations have been successfully conducted, albeit less frequently due to their smaller sizes and rapid apparent motions. Notably, a multi-chord observation of a NEA approximately 5–6 km in diameter provided unprecedented details for as small object as Phaeton (Yoshida et al., 2023). Additionally, the ACROSS project (Asteroid Collaborative Research via Occultation Systematic Survey)[7] has demonstrated that combining observations from multiple sites can yield high-resolution information on the shape and size of NEAs below 1 km in diameter (Souami et al., 2023).

In the context of asteroid modelling, occultation data can be combined with lightcurve models to produce 3D shape models with accurate absolute scaling. For instance, a shape model from lightcurve inversion gives the relative shape, but combining it with an occultation silhouette (which provides an absolute size in one instance) can scale the entire model to the correct dimensions and refine it. Occultation timings can also improve asteroid orbital elements, if a predicted shadow path is off by a certain amount, that indicates the asteroid's ephemeris (orbit) needs to be corrected, which in turn sharpens future predictions for both occultations and close approaches to Earth.

[7] `https://www.oca.eu/fr/home-across`

1.3 Thesis objectives and methodology

In the previous section, we reviewed several observational techniques, some of which are interdependent, by tracing their development from their origins to modern-day applications and their impact on different areas of asteroid studies. However, despite significant progress in the field, much work remains to be done. The number of known asteroids continues to grow, and so does the need for high-quality data to obtain precise physical parameters.

In this study, we focus on a selection of main-belt asteroids (MBAs) that have, until recently, received relatively little attention due to their long periods of rotation and small amplitudes of their lightcurves (Marciniak et al., 2015). Yet, avoiding slow rotators distorts our view of the asteroid population as a whole, influencing theories of the solar system evolution. Our primary objective is to determine their sizes with high precision and to compare two of the most accurate size determination methods. This parameter is crucial for many other scientific purposes, for example, the determination of bulk density. The problem is that for certain asteroids, the size estimates are poorly constrained, with values in the literature differing by more than 30% (see Table 2 in Marciniak et al., 2023 and Table 1 in Choukroun et al., 2025), leading to uncertainties in density determination exceeding 90% (Carry, 2012). To address this challenge, we chose to employ two independent techniques, both relying exclusively on high-quality data, to derive reliable asteroid sizes.

The first method is based on advanced thermophysical modelling, and it is known as Convex Inversion Thermophysical Model (CITPM, Ďurech et al., 2017). This technique, which we describe in chapter 3.2, enables the precise determination of multiple parameters such as size, surface roughness, and thermal inertia, in addition to refined spin and shape.

The second approach is purely observational and is based on stellar occultations, a method renowned for its exceptional accuracy. In both cases, a prerequisite is the availability of a shape model and a solution for the asteroid's spin axis position. Consequently, the first step in our work involves constructing shape models for our targets from lightcurves and determining their spin states using a technique called lightcurve inversion (Kaasalainen & Torppa, 2001, Kaasalainen et al., 2001), which is discussed in detail inchapters 2.3 and 2.4.

The advantage of applying both methods to determine asteroid sizes is twofold: not only can we compare the results to verify their consistency, but we can also assess the potential added value of the CITPM approach, opening new possibilities for future work. Furthermore, beyond the determination of size, this study yields highly accurate values for the sidereal rotation period, unique spin axis position, shape models, thermal inertia, surface roughness, and albedo for 15 asteroids. For 17 others (including, a future space mission target) also the spin and shape models were delivered, while their size was determined with one method only (Marciniak et al., 2023, Marciniak et al., 2025). Our investigation begins with telescopic observations and culminates in the precise determination of their key physical properties. A substantial part of this work has involved data collection, processing, standardisation, and exploitation. To facilitate this, we developed a suite of dedicated tools, which will also be presented in the following chapters.

Chapter 2

Asteroid spin and shape models

2.1 Photometric campaign

The modelling techniques employed in this work, both lightcurve inversion and the Convex Inversion Thermophysical Model (CITPM), are highly data-intensive, particularly in terms of photometric data input. One of the major challenges arises from the need to sample the target asteroid under a wide diversity of observing geometries. This diversity cannot be brought about directly; instead, it requires waiting for the asteroid to naturally evolve along its orbit, making the data collection process inherently time-consuming. In this study, we aimed at deriving the most precise possible size determinations, which first required the use of high-quality dense photometric datasets for shape reconstruction. Indeed, the photometric accuracy of sparse data from ground-based surveys is often insufficient, with typical scatter reaching up to $\sim$0.1 mag (Hanuš et al., 2011). Consequently, a large-scale collaborative effort was necessary to acquire the dense lightcurves required for our modeling. This international photometric campaign, originally introduced in Marciniak et al. (2015) and further described in Section 2 of Marciniak et al. (2021), involved over 20 observing stations operating telescopes with apertures up to 1 meter. Among them, the TRAPPIST telescopes (Gillon et al., 2011) played a significant role. To complement ground-based observations, we also included high-precision photometric data from the Kepler Space Telescope (Borucki et al., 2010) in its extended K2 mission, and from TESS (Transiting Exoplanet Survey Satellite, Ricker et al., 2015). For the 15 main-belt asteroids studied in Choukroun et al. (2025), a total of 1151 lightcurves were collected including literature data. Substantial part of this dataset was in the form of raw FITS images from our campaign, and they required data reductions and photometric processing. Next, all the lightcurves had to be cleaned and standarized. This process included the identification and removal of defective measurements, such as stellar passages, instrumental outliers, or inconsistencies caused by atmospheric effects. The resulting dataset, unprecedented in its density and quality for this class of objects, enabled robust spin and shape modeling through the combined inversion of optical and infrared data as described in chapter 3.2.

2.2 STEROID pipeline

In this work, precise and efficient processing of photometric data was a crucial step. To derive reliable shape and spin models for asteroids, we needed high-quality lightcurves built from a large number of observations, often taken over many nights, with varying geometries and observing conditions. This resulted in a significant volume of data to process, and the reliability of each individual lightcurve was essential: even minor centroiding errors or undetected contaminations could propagate into the lightcurve inversion results. To meet this challenge, the author of this thesis developed the STEROID library[1] (Choukroun et al., submitted (Paper 1)), a modular Python package designed to handle the full photometric processing of astronomical targets, both fixed and moving, with a strong focus on adaptability and automation. Unlike most of software pipelines, STEROID is not a rigid tool. It provides a set of independent, well-documented modules that users can combine or repurpose to build custom processing chains adapted to their needs. This makes it especially suited for research contexts requiring flexibility, for example, when switching between stars and asteroids, or between different telescope setups.

For our specific application, which is differential photometry of main-belt asteroids, we built a custom pipeline using the tools included in STEROID. This pipeline is encapsulated in the Photometry class, which combines the successive steps of frame correction, object detection and tracking, aperture photometry, and lightcurve construction. We used the following core modules from STEROID:

- `Corrector`: to measure and correct for image drift and rotation without interpolating the pixels
- `Detector`: to identify objects in the field (stars or slowly moving targets)
- `Fit`: to manage images (read images, handle FITS headers, compute histograms, etc.).
- `Apertures`: to manage aperture placement and perform photometry.

One of the most critical contributions of STEROID lies in its ability to precisely register image sequences without relying on classical plate solving. Traditional tools often use blind plate solving which is a method that matches star positions to a sky catalogue to estimate the field orientation. While robust, this technique:

- requires precise WCS (World Coordinate System) headers or reliable pointing,
- is computationally expensive,
- can miss subtle distortions (e.g. differential atmospheric refraction, instrumental optical distortions),
- typically requires a sky catalogue, limiting the tool flexibility in case of uncatalogued, moving or transient objects.

[1]STEROID GitHub : `https://github.com/antoinech13/Steroid`

By contrast, STEROID `Corrector` module performs image registration directly from the pixel data, using an approach based on pattern recognition. It builds local configurations of stars (e.g., groups of 5 stars forming triangles), and compares these geometric patterns between frames. If a match is found, the relative translation and rotation are inferred from the matched triangles, using vector algebra and median filtering across all patterns. This approach has three major advantages:

- No need for any stellar catalogue access or for WCS headers, making it suitable for raw or experimental data.
- No pixel interpolation, which avoids introducing errors into the flux measurements (especially critical in high-precision photometry).
- Higher adaptability, especially when objects are not listed in standard star catalogues or when dealing with faint or blended images.

In terms of photometric accuracy, STEROID also avoids reprojecting the image after rotation, which would degrade SNR through resampling. Instead, it tracks objects and adjusts aperture positions analytically, ensuring consistent measurements. Main processes designed for our STEROID pipeline can be find in the Figure 2.1.

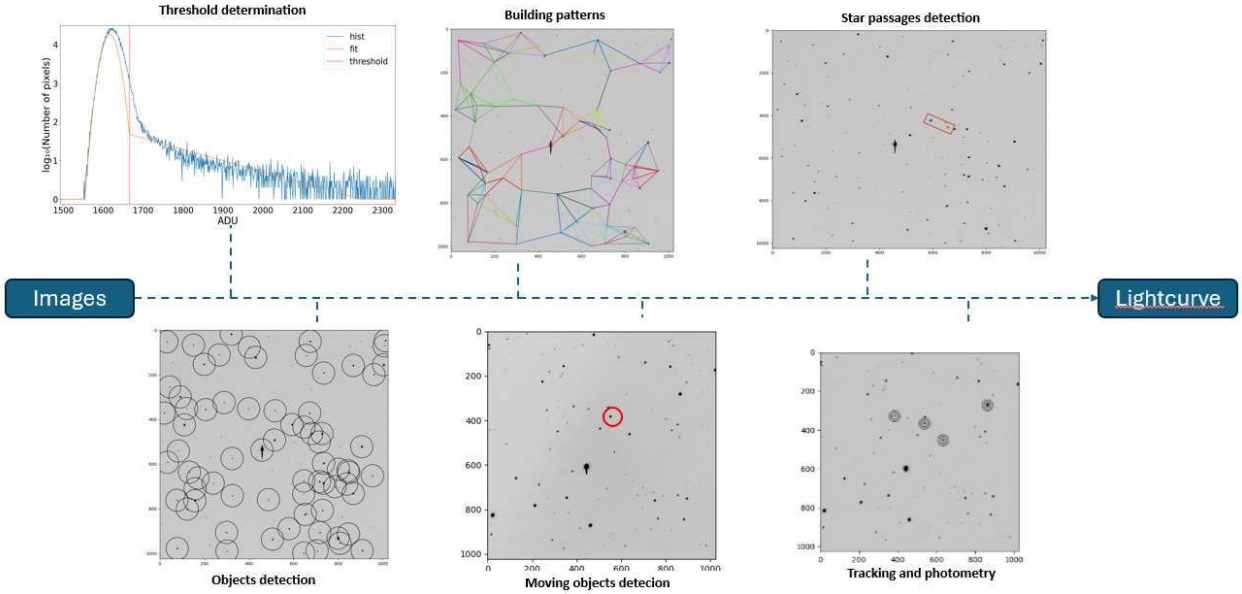

Figure 2.1: Main processes applied in STEROID to extract lightcurves from image sequences (see Choukroun et al., submitted (Paper 1))

Naturally, STEROID also handles image calibration for bias, dark, and flat frames. The reduction formula used is as follows:

$$\mathrm{src}_{\mathrm{red}} = \frac{(\mathrm{src} - \mathrm{bias} - (\mathrm{dark} - \mathrm{bias}) \cdot s) \cdot \overline{(\mathrm{flat} - \mathrm{bias})}}{\mathrm{flat} - \mathrm{bias}}, \tag{2.1}$$

where s corresponds to a scale factor applied to dark frames in case when they are provided with a different exposure time than the science image. Using STEROID, around a hundred of lightcurves were obtained by the author of this thesis and used in all the publications presented in this manuscript.

2.3 Lightcurve inversion

The challenge of reconstructing the shape of a rotating celestial body from its variations in brightness is almost as old as asteroid photometry itself. In 1906, Henry Norris Russell articulated what would become a foundational barrier to the problem: that it is, in general, impossible to determine the shape of a minor body from its light variations alone (Russell, 1906). Russell's insight was based on geometrical reasoning: two very different bodies, one spherical but with large spots of different albedo, the other elongated and irregular, can exhibit similar or even indistinguishable lightcurves under certain viewing conditions. In other words, the problem is non-injective: the mapping from shape to lightcurve is many-to-one. Small changes in the observed flux can correspond to vastly different surface topographies. This non-uniqueness, coupled with observational noise and limited viewing geometries, led Russell to conclude that shape inversion from brightness alone was fundamentally underdetermined. For nearly a century, this pessimistic verdict held sway. Attempts at lightcurve inversion either required strong priors (e.g. assuming ellipsoidal bodies), or were unable to yield more than qualitative estimates of elongation and sideral spin period. The absence of a general, rigorous method meant that asteroid shape models derived from photometry remained speculative.

This deadlock was broken at the verge of 1990s and 2000s by the works of Mikko Kaasalainen and colleagues (Kaasalainen et al., 1992, Kaasalainen & Torppa, 2001, Kaasalainen et al., 2001) who reframed the problem in a fundamentally new way. By restricting the class of permitted shapes to strictly convex bodies, and reformulating the geometry in terms of a Gaussian surface density defined on the unit sphere, Kaasalainen was able to demonstrate that the lightcurve inversion problem could, under reasonable conditions, become well-posed, solvable, and even unique. Moreover, Russell limited himself to a narrow class of observing geometries, primarily those near opposition, that is, configurations where the Sun, the observer, and the object are nearly aligned. In such cases, the illumination and viewing directions are almost identical, leading to highly degenerate lightcurves that reveal only limited information about the shape of an object.

Kaasalainen's approach fundamentally differs from Russell's in several key aspects:

- It relies on **multiple and diverse observing geometries**, including different phase angles (sun - target - observer angle) and aspect angles (angle between northern part of spin axis and viewing direction), which help to break the symmetries and degeneracies present in single-geometry observations.
- It introduces a **convexity constraint** and reformulates the problem in terms of a Gaussian density function on the unit sphere, allowing for a mathematically well-posed and physically meaningful inversion.
- It employs **advanced mathematical and numerical techniques**, including spherical harmonics expansion, regularization theory, and nonlinear optimization, made tractable by modern computational resources.

2.3.1 Theory

The problem of reconstructing the shape of an asteroid from its photometric lightcurve is generally ill-posed: many different shapes can produce nearly indistinguishable

brightness variations when observed under limited geometries. To address this, Mikko Kaasalainen developed a formulation that transforms the problem into a mathematically tractable one by assuming strict convexity and describing the body through its Gaussian image, the distribution of surface area on the unit sphere as a function of orientation. The brightness observed from a given geometry, defined by the observer direction E and the illumination direction E_0, is given by the surface integral:

$$L(E, E_0) = \int_{A^+} S(\mu, \mu_0, \alpha) G(\theta, \phi) d\sigma \tag{2.2}$$

where A^+ defines the integration domain which includes only surface elements for which $\mu, \mu_0 \geq 0$, that is those which are simultaneously visible and illuminated, $\mu = \mathbf{n} \cdot E$ and $\mu_0 = \mathbf{n} \cdot E_0$ are the cosines of the angles between the surface normal $\mathbf{n}(\theta, \phi)$ and the observer/Sun directions, $S(\mu, \mu_0, \alpha)$ is the bidirectional reflectance function (typically a combination of Lommel-Seeliger, Lommel (1889), and Lambertian terms, Lambert (1892)), $G(\theta, \phi)$ is the Gaussian surface density, describing how the surface area of the body is distributed over directions (θ, ϕ) on the unit sphere and $d\sigma$ is the surface element.

The use of the Gaussian surface density function $G(\theta, \phi)$ implicitly assumes convexity of the body. This assumption is essential to ensure the uniqueness of the solution: under convexity, each surface normal corresponds to a unique point on the object, making the inverse problem mathematically well-posed. This idea is illustrated in Figure 2.2, which shows how the mapping from a 1D surface to its Gaussian representation behaves differently in the convex and non-convex cases.

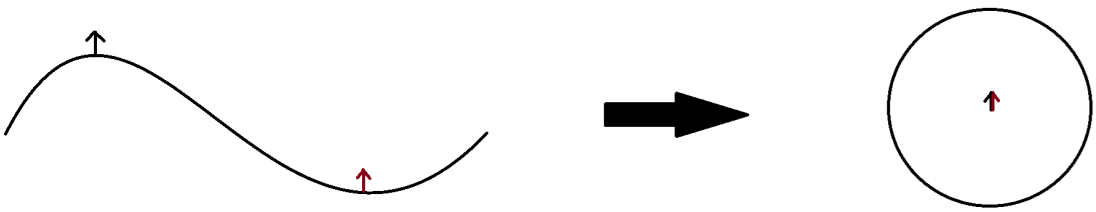

a) Mapping from a non-convex 1D surface to a 1D Gaussian surface density.

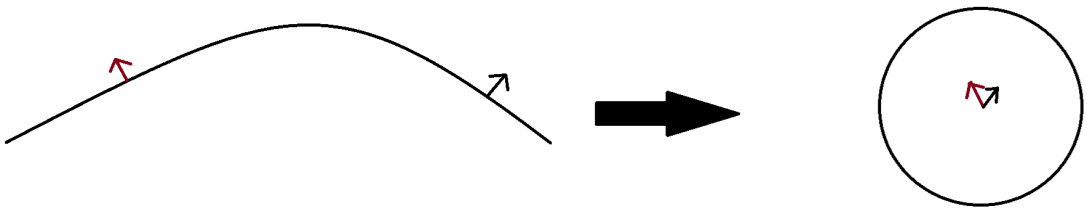

b) Mapping from a convex 1D surface to a 1D Gaussian surface density.

Figure 2.2: Comparison between the Gaussian surface density derived from (a) a non-convex and (b) a convex 1D surface. In the non-convex case, multiple points on the surface may share the same normal direction, leading to ambiguity in the Gaussian representation. This non-uniqueness violates the assumptions required for the shape reconstruction. In contrast, the convex case guarantees a one-to-one correspondence between surface normals and surface elements, yielding an unambiguous Gaussian density.

To ensure that G > 0 (a physical requirement for convex shapes), it is parametrized using an exponent of a spherical harmonic expansion:

$$\mathrm{G}(\theta,\phi) = \exp(\sum_{l=0}^{L}\sum_{m=-l}^{l} a_{lm}\mathrm{Y}_l^m(\theta,\phi)) \tag{2.3}$$

This guarantees positivity by construction, while still allowing the function G to be expressed compactly and smoothly. The coefficients a_{lm} become the parameters of the optimization problem, and the monotonic nature of the exponent ensures the existence of a single global minimum under standard regularization. Once $G(\theta,\phi)$ is known, the original 3D shape of the body can be reconstructed using results from convex geometry, particularly the Minkowski minimisation (Minkowski, 1903). The link between G and the geometry of the body is encoded in the support function $p(\theta,\phi)$, defined as the scalar product of the position vector $\mathbf{r}$ and the surface normal $\mathbf{n}$. The unique convex shape corresponding to a given G can be obtained by minimizing the mixed volume function:

$$V = \frac{1}{3}\int_{S^2} \mathrm{p}(\theta,\phi)\mathrm{G}(\theta,\phi)d\sigma \tag{2.4}$$

subject to a fixed volume constraint. This can be solved either continuously (via harmonic expansions of p) or discretely using the polyhedral method described in the Appendix C of Kaasalainen & Torppa (2001) paper.
To determine G, a Levenberg–Marquardt (Levenberg, 1944, Marquardt, 1963) algorithm is used to optimise:

$$\chi^2 = \sum_i (\frac{\mathbf{L}^{(i)} - A^{(i)}\mathbf{g}}{\bar{L}^{(i)}})^2 \tag{2.5}$$

where $\mathbf{L}$ the vector of the observed brightnesses, $\mathbf{g}$ is the vector that contains the parameters to be solved and A is the matrix defined by:

$$A_{ij} = S_j(\mu^{(ij)}, \mu_o^{(ij)})\varpi_j \tag{2.6}$$

where S_j and ϖ_j are the scattering law and the albedo at the facet (discrete surface element) j. The index i stands for the observation number. This last equation illustrates the inherent ambiguity between an asteroid shape and its surface albedo. Such ambiguity is generally unsolvable using photometric data alone. As a result, within the framework of convex inversion, the albedo is assumed to be constant and uniform across the entire surface of the asteroid. Another important point to address here, as it will appear in our results, is that convex inversion requires substantial diversity in the observing geometries (so it takes many years, at least 6, to gather necessary data). In the case of main-belt asteroids, which are our targets, their orbits lie close to the ecliptic plane. This restricted geometry causes a lack of latitudinal information and leads to the so-called mirror pole ambiguity (Kaasalainen & Lamberg, 2006). As a result, each inversion model typically yields two possible pole solutions, differing by approximately 180° in longitude. Determining which of these two solutions reflects real asteroid spin generally requires complementary observations beyond photometry alone. For this reason, pole solutions are usually reported in pairs, referred to as solution 1 and solution 2.

2.4 Sample results

This section presents the data and the model for one of our targets as an example, including some of the lightcurves obtained using STEROID, and it shows the sample results of the convex inversion. In short, this section summarizes the methods described so far in this Chapter.

Target: asteroid (931) Whittemora

Information on asteroid (931) Whittemora, like for the majority of the targets studied, was scarce prior to this work. No shape model was available in the DAMIT[2] database, and also no spin solution was present in the LCDB[3] database. The results presented here are therefore not an improvement upon existing data, but new and previously unavailable parameters and model for this asteroid. For (931) Whittemora, a total of sixty dense lightcurves had to be standarised and cleaned, part of which (6 lightcurves) were obtained from raw FITS frames using STEROID. Figure 2.3 shows an example of a lightcurve produced with STEROID, based on observations from 22 June 2023, with the 0.6 m telescope of the Mt. Suhora Astronomical Observatory in Poland. Panels (a) and (b) show the lightcurve with binning values of 1 and 3, respectively. Binning is needed for slow rotators to avoid oversampling the full lightcurve of an asteroid. The red points in panel (a) highlight STEROID ability to automatically detect and remove outliers.

[2] `https://damit.cuni.cz/`, accessed 15 December 2023.

[3] The Asteroid Lightcurve Database (Warner et al., 2009), updated 1 October 2023. `https://minplanobs.org/mpinfo/php/lcdb.php`

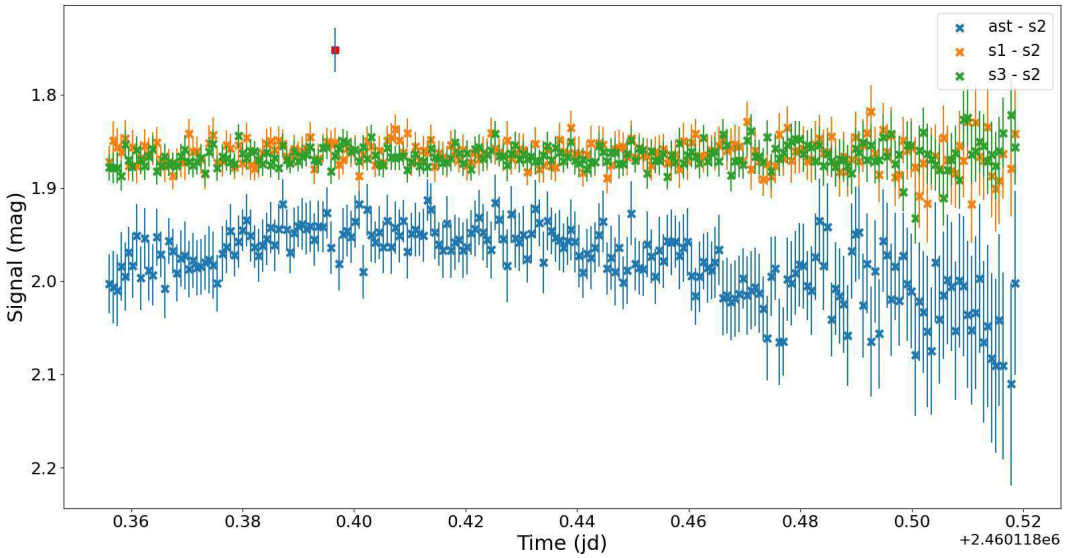

(a)

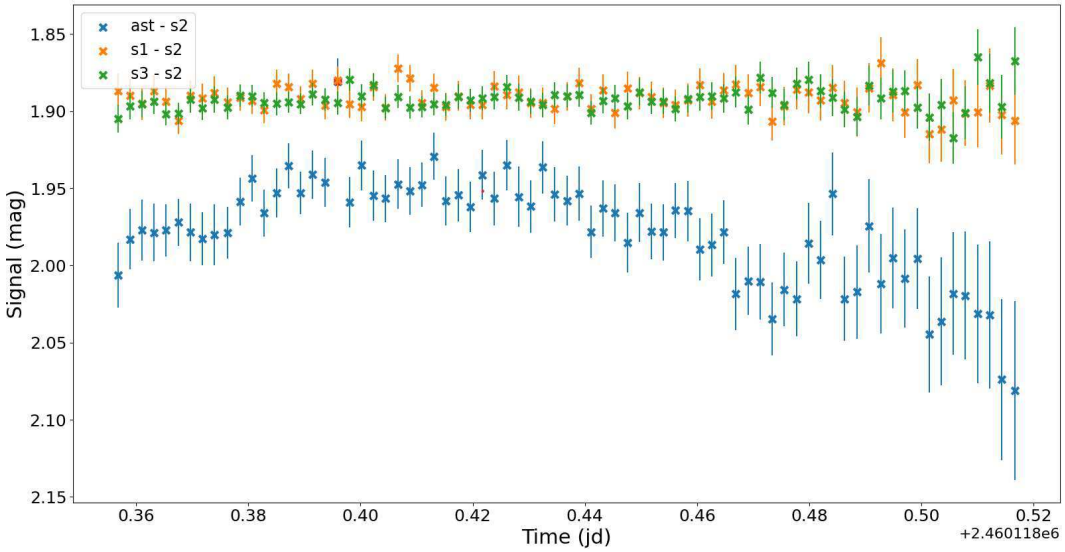

(b)

Figure 2.3: Lightcurve of asteroid (931) Whittmora produced with observations done on 22 Jun 2023 with the 0.6m telescope of Mt. Suhora Astronomical Observatory. Panel a) shows each point of the lightcurve, while b) shows the lightcurve automatically binned by STEROID pipeline with a binning value equal to 3, to avoid oversampling. The red point on a) corresponds to an outlier detected and removed by STEROID.

After producing the individual lightcurves, we can combine them to generate composite lightcurves. This process involves phasing the individual lightcurves to obtain fuller and more representative curve. Composite lightcurves represent a complete coverage of the rotation phase, enable control of the correctness of the detected synodic rotation period, and provide strong constraints for the sideral period search in the convex inversion (see section 2.4.1). For (931) Whittemora, the large number of dense lightcurves available enabled production of clean composite lightcurves.

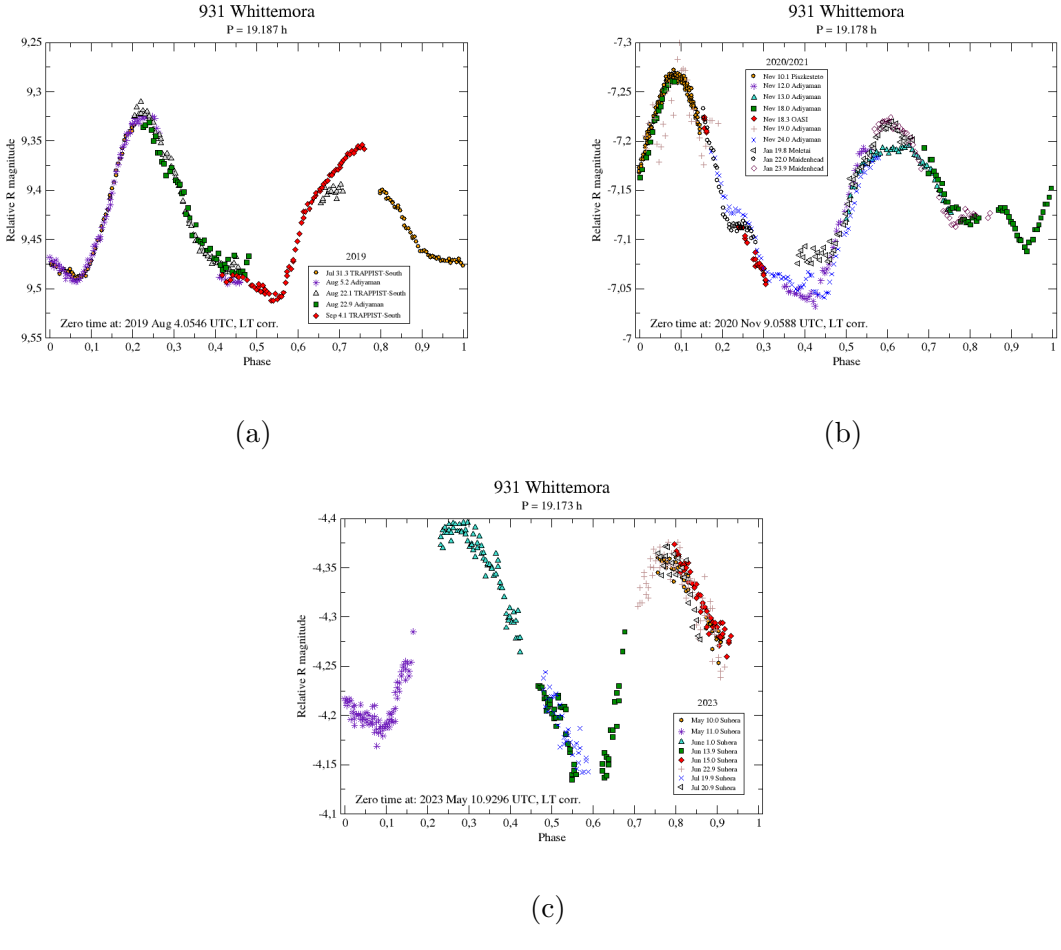

Figure 2.4: Composite lightcurves of (931) Whittemora from three apparitions in the years: a) 2019, b) 2020-2021 and c) 2023.

An example of some composites can be found in the Figure 2.4 where panel a) is the composite produced with lightcurves obtained during the apparition in the year 2019, b) on the verge of 2020-2021 and c) in 2023. In the last apparition brightness of this asteroid was below 15 magnitude, unlike in the remaining ones, when it was around 13.5 mag, so that this composite lightcurve is slightly noisier. An interesting effect is visible in panel b. Some lightcurve segments slightly misfit each other, however these are not artifacts, but real phase angle effects. They are connected to various shadowing on the surface at various dates. Lightcurves exhibiting such effects are especially valuable for the asteroid shape reconstruction.

The next step is to use a modified version of the full convex inversion method to accurately determine the sidereal rotation period of an asteroid. To do so, we can

use the synodic periods derived during the construction of the composite lightcurves to narrow the search range. Indeed, scanning the full range of possible periods is a time-consuming process, and applying such constraints allows for a more efficient work. Figure 2.5 shows the result of the period scan for (931) Whittemora. The y-axis corresponds to rms deviations value ($\sqrt{\chi^2}/N$, N being the number of data points) and the x-axis corresponds to the sample period. As we can see, a clear minimum value is reached (for a period of 19.17592 hours).

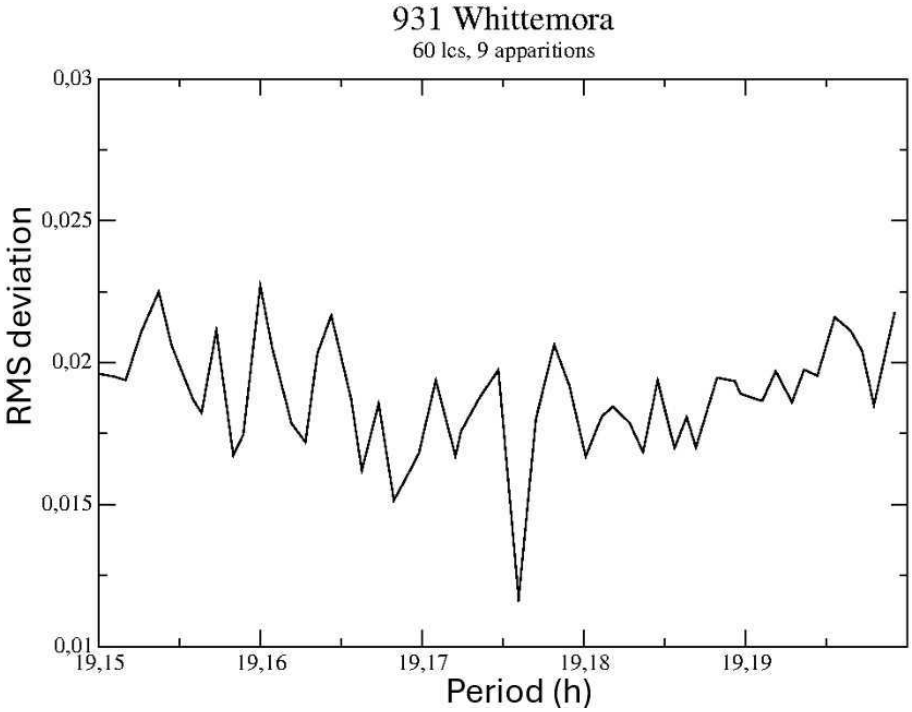

Figure 2.5: Scan of the sidereal periods of (931) Whittemora. The y-axis is the sum of the rms deviations of simplified model lightcurves vs observed lightcurves, and the x-axis is the rotation period in hours.

This period can now be used as the starting point for the final step, namely the modeling of the shape and the determination of the spin-axis position in space. To achieve this, the standard procedure consists of scanning the parameter space defined by ecliptic λ and β and identifying the minimum. Initially, this step was performed manually. In the context of this thesis, the author developed a script to automate and improve this process, interpolating the response of the system within the parameter space to identify the optimal solutions. Figure 2.6 shows the result of this script for the case of (931) Whittemora. The green contour marks the region where the solutions are considered acceptable. This contour is usually set at 10% higher than the deviations value of the best fit solution.

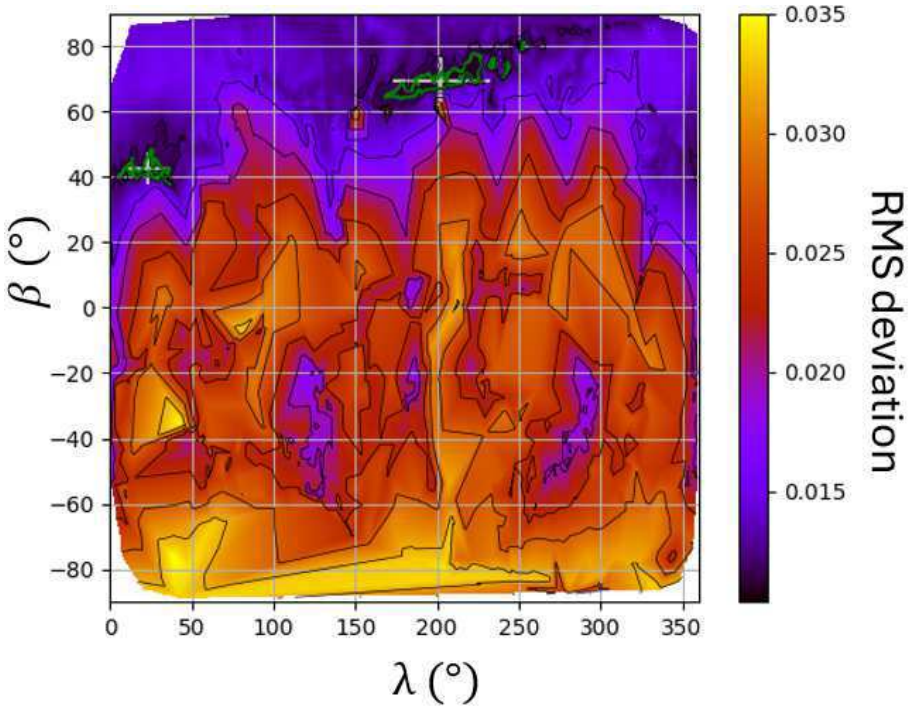

Figure 2.6: Map of the rms deviation values as a function of the ecliptic coordinates λ (x-axis) and β (y-axis) of sample spin axis position. The green contour shows the region where the solutions are considered acceptable.

Best pole solutions are as follows:

- Solution 1 : $\lambda = 33 \pm 14$ (°), $\beta = 52 \pm 5$ (°) and $P = 19.17589 \pm 0.00006$ (hours)
- Solution 2 : $\lambda = 213 \pm 30$ (°), $\beta = 79 \pm 7$ (°), $P = 19.17590 \pm 0.00005$ (hours)

The corresponding shape model is shown in Figure 2.7, illustrating the two mirror pole solutions. Each panel displays three orthogonal projections of the convex shape model, in the z–y, x–z, and x–y planes, providing complementary views of the asteroid overall geometry. To assess whether the shape model is physically plausible, several criteria can be applied, for example, ensuring the model is not unrealistically flat or excessively angular. The most important check though is to verify that the model rotates stably around the axis corresponding to the maximum moment of inertia. To do this, the model is re-projected along its principal inertia axes to confirm that the rotation axis remains well aligned with the z-axis.

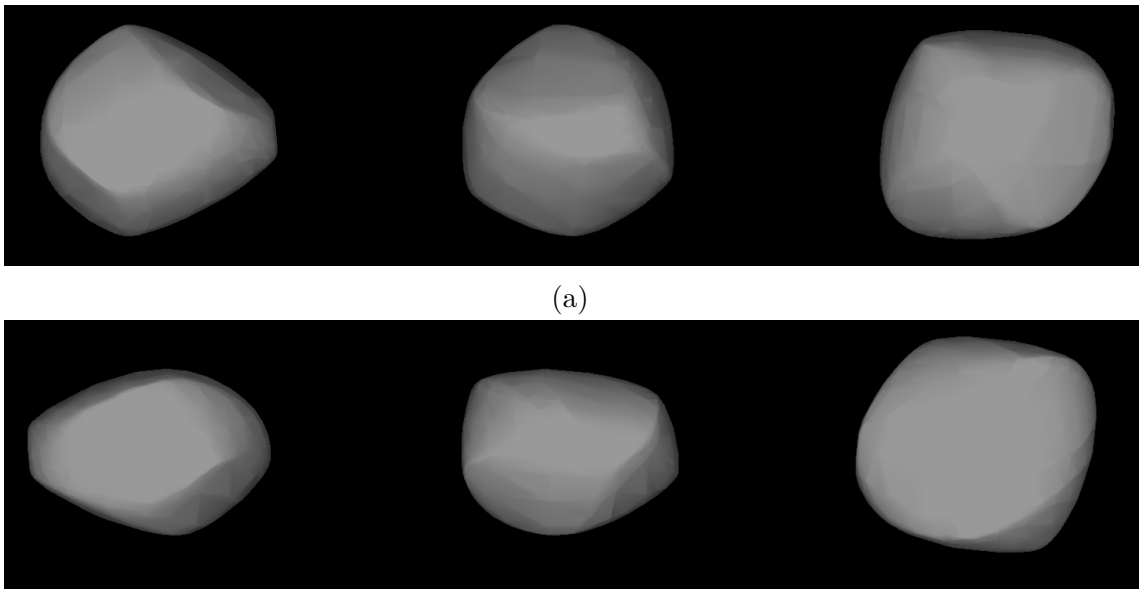

(a)

(b)

Figure 2.7: Shape model of asteroid (931) Whittemora. Panel (a) corresponds to solution 1 and panel (b) to solution 2. Each panel is composed of three views, from left to right: the projections in the z–y, x–z, and x–y planes.

It can be noted that the two shape solutions are not exact mirror reflections of each other, especially in the stretch along the z-axis. Minor misfits reflect the shape model uncertainty, and poorly constained stretch along the z-axis reveals the main weakness of the inversion method models. It was overcome in this thesis, in two ways: by testing ten versions of each shape model in occultation fitting (see chapter chapter 3.1) and by adding calibrated photometric data in CITPM (see chapter 3.2).

2.4.1 Synodic period versus sidereal period

The rotation period of an asteroid can be expressed in two different but related ways: the sidereal period and the synodic period. Although they are often close in value, they represent distinct physical quantities and must be carefully distinguished in data analysis.

The sidereal period corresponds to the true physical rotation of the asteroid with respect to an inertial reference frame, typically the stars. In other words, it is the time that the asteroid takes to complete one full rotation around its spin axis relative to distant celestial objects. This value is intrinsic to the asteroid and does not depend on the position of the observer. Figure 2.8 illustrates this concept: the asteroid rotates once with respect to the fixed background of stars.

The synodic period, on the other hand, is the apparent rotation period as measured by an observer from Earth. Because both the asteroid and the Earth are moving around the Sun, the relative geometry between the observer, the asteroid, and the Sun continuously changes. As a result, the asteroid lightcurve obtained from Earth does not reflect the pure sidereal rotation but instead an apparent rotation rate influenced by the orbital motion of the Earth. This effect can cause the observed period to be slightly longer or shorter than the true sidereal period, depending on the relative direction of orbital motion. Figure 2.9 shows how the synodic period

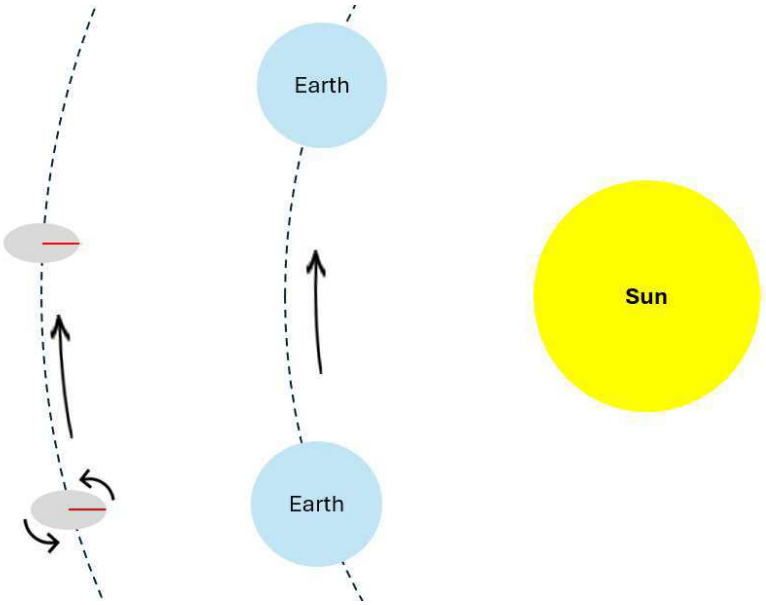

Figure 2.8: Illustration of the sidereal rotation period of an asteroid. After completing one rotation around its spin axis while orbiting the Sun, the asteroid returns to its initial orientation with respect to the stars.

arises from the combined motions.

The relation between both quantities can be expressed as:

$$\frac{1}{P_{\text{syn}}} = \frac{1}{P_{\text{sid}}} - \frac{d\lambda}{dt}, \tag{2.7}$$

where P_{syn} is the synodic period, P_{sid} the sidereal period, and $\frac{d\lambda}{dt}$ the apparent angular motion of the asteroid as seen from Earth (relative to the stars). In practice, the difference between synodic and sidereal periods is usually small, but it becomes significant for accurate modeling of lightcurves and shape inversion techniques. It also explains why the value for P_{syn} is slightly different in the composite lightcurves from various apparitions (Fig. 2.4).

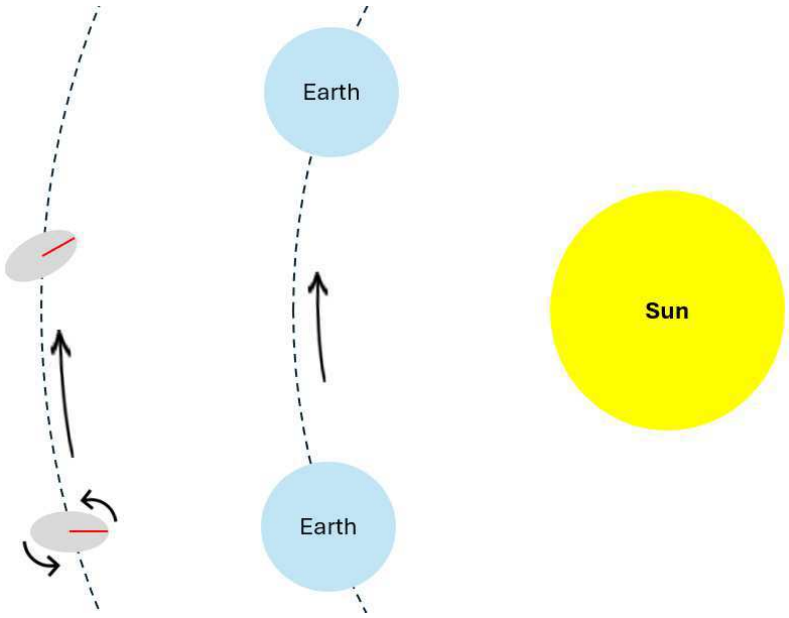

Figure 2.9: Illustration of the synodic rotation period of an asteroid observed from Earth. After the combined motion of the Earth and the asteroid along their respective orbits, together with the asteroid own rotation, the asteroid returns to the same apparent orientation as seen by an observer on Earth.

Chapter 3

Diameter determination

3.1 Stellar occultations by asteroids

Stellar occultations are increasingly used to calibrate scale-free shape models obtained from photometry. For example, in Marciniak et al. (2023) (Paper 4) we scaled 16 slow rotators using multi-chord occultations, achieving size accuracies of a few percent. Although such studies do not provide surface thermophysical parameters, they remain essential for reliable size determination when infrared datasets are insufficient.

3.1.1 Method

The fundamental idea behind the stellar occultation method is straightforward. Just like the Moon can produce an eclipse when it passes in front of the Sun, an asteroid may block the light of a distant star when it crosses the line of sight between the Earth and that star. In such cases, the asteroid shadow travels across the surface of the Earth. An observer located within this shadow path will perceive the star suddenly disappearing, only to reappear a short time later. The duration of this disappearance depends on several factors: the observer's position relative to the shadow track, the asteroid size and shape (plus its aspect angle and rotation phase), and the relative velocity vector between the asteroid and the Earth. It follows that, if the disappearance and reappearance times are measured accurately, and the relative motion is known, the asteroid size can be derived with remarkable precision. This inverse problem is clearly formalized in the work of Ďurech et al. (2011). The first step consists in defining a common coordinate system in which observations from multiple geographically distributed observers can be consistently projected. Following Ďurech et al. (2011), we introduce a reference plane, called the fundamental plane, which passes through the center of the Earth and has a normal vector aligned with the line of sight from the Earth center to the occulted star. To define this plane and the coordinates on it, we use the following orthonormal basis vectors:

$$\begin{aligned} \hat{\vec{s}}_\xi &= (-\sin\delta\cos\alpha,\ -\sin\delta\sin\alpha,\ \cos\delta), \\ \hat{\vec{s}}_\eta &= (\sin\alpha,\ -\cos\alpha,\ 0), \end{aligned} \tag{3.1}$$

where $\hat{\vec{s}}\xi$ and $\hat{\vec{s}}\eta$ are unit vectors lying in the fundamental plane, and where α and δ represent the right ascension and declination of the occulted star. With this coordinate system in place, the geocentric coordinates of each observer can be projected onto the fundamental plane using the expression:

$$\begin{pmatrix} \xi \\ \eta \end{pmatrix} = \begin{bmatrix} \hat{\vec{s}}_\xi \cdot \left(\vec{x} + \Delta\vec{v}\Delta t + \frac{1}{2}\Delta\dot{\vec{v}}(\Delta t)^2 \right) \\ \hat{\vec{s}}_\eta \cdot \left(\vec{x} + \Delta\vec{v}\Delta t + \frac{1}{2}\Delta\dot{\vec{v}}(\Delta t)^2 \right) \end{bmatrix}. \tag{3.2}$$

Here, ξ and η are the coordinates of the observer projected onto the fundamental plane, $\vec{x}$ is the observer's geocentric position in the sidereal equatorial frame, $\Delta\vec{v}$ is the relative velocity between the Earth and the asteroid, and Δt is the time interval between the disappearance or reappearance of the star and a reference epoch. The sidereal equatorial frame is chosen for two main reasons. First, the geographic coordinate system (longitude, latitude) does not contain the Earth orientation at the time of observation. Second, the sidereal equatorial frame is naturally aligned with the equatorial coordinate system used to describe the star position: its z-axis points toward the celestial north pole, x-axis toward the vernal equinox, and y-axis completes a right-handed orthonormal basis. This consistency avoids any need for basis transformations and simplifies the overall computations.

3.1.2 Occultation campaign

Occultation observations are significantly more complex than photometric ones for rotational lightcurves. In addition to requiring specific equipment (notably cameras equipped with a GPS module to ensure accurate time-stamping), the observation of a single event typically yields only one chord. In the context of our work, at least two chords from two different observing sites are required. Consequently, beyond the limitation imposed by whether or not an occultation occurs for a given target and the geographic constraint of where the event takes place, there is also a major limitation in terms of human resources. In other words, when an event occurs, a sufficient number of observers must be located near the shadow path and be ready to observe it simultaneously. Due to this, in the past many of our targets were not observed via occultations, or only one chord was available, insufficient for our purposes. In 2020, an observation campaign was therefore initiated, and this campaign was even assigned a specific tag on the Occult Watcher Cloud platform. In this thesis the results of this campaign were combined with archival data from the Planetary Data System (PDS) archive (Herald et al., 2024), as well as from the Occult programme archive, and the International Occultation Timing Association (IOTA) regional coordinators.

3.1.3 Occultation fitting tool

During this work, scaling our 3D convex shape models using stellar occultation data required the assistance of a non-open-source tool developed by a team at Charles University in Prague (Ďurech et al., 2011). We used to send them both our convex shape models and the corresponding occultation observations; they would then handle the fitting process. This approach had the clear advantage of delegating the responsibility of a successful fit to an experienced team using a well-established and validated tool used in the papers by Marciniak et al. (2023) and Choukroun et al. (2025). However, it also presented several limitations. One of the issues was our dependency: relying on an external, closed-source pipeline reduced our operational independence and our capacity to upgrade tools according to our own needs. To overcome this limitation, the author of this thesis developed a custom Python tool

consisting of over 4000 lines of modular code named occultationFit[1], structured into several core components (classes). Below is a brief description of the most important ones:

`Event:` This class is a parser for XML files storing occultation observations. Such files are downloaded from Occult programme archive. In principle, a user can implement their own parser, provided that it outputs three specific dictionaries:

- `star`: must include keys such as `"catName"` (star catalogue name, e.g., Tycho2), `"catNum"` (catalog number of an occulted star), `"gaia_id"` (Gaia identifier), and the star celestial coordinates `"ra"` and `"dec"` in degrees.
- `ast`: must contain `"id"` (asteroid number) and `"name"` (asteroid name).
- `observer`: uses the observer ID (as an integer) as the key and stores sub-dictionaries with:
  - `"name1"`: main observer's name
  - `"name2"`: second observer(s), if any
  - `"long"` and `"lat"`: geographic coordinates in degrees
  - `"alt"`: altitude of the observing site
  - `"isPositif"`: boolean for positive detection (to be replaced by `"status"`)
  - `"d"`, `"d_err"`: disappearance time and timing uncertainty
  - `"r"`, `"r_err"`: reappearance time and timing uncertainty
  - `"status"`: observation status (0 = positive, 1 = negative, 2 = partial chord, when only "d" or "r" was observed).

Additionally, `Event` class can fetch updated star data from external catalogs, useful for resolving inconsistencies in the XML metadata.

`ModelParser:` This class parses shape model `.tri` files and provides several tools for model visualisation and analysis:

- `plot3_vertices(...)`: displays interactive views in x-y, y-z, and x-z planes.
- `plot_vertices(...)`: displays a 3D view.

It also calculates volume- and surface-equivalent radii of the complex shape models.

`Occultation:` This class wraps an `Event` parser (or every type of parser with the good dictionaries) and provides:

- `plot(...)`: occultation chord visualization on the fundamental plane
- `plot3dChart(...)`: plots the Earth and observer positions for parser validation

`OcFitInputParser:` A simple parser to load user-defined configuration parameters for the fitting procedure.

[1]occultationFit GitHub repository : `https://github.com/antoinech13/occultationFit`

`OccultationFit:` The core class performing the fit between occultation data and the 3D model. It computes the silhouette of the asteroid as seen from Earth at a given epoch and projects it onto the fundamental plane to compare it with the observed chords.

OccultationFit: how it works

Compared to the original Prague code, `OccultationFit` offers several major advantages:

- It supports both simultaneous and independent optimisation of the model size for multiple events.
- It allows the optimisation of the silhouette centroid, and size scale but also slight improvement of the spin axis orientation (λ, β), and rotation period.
- Constraints on uncertainty margins can be enforced to avoid overfitting beyond physically plausible limits.
- It supports several optimisation algorithms, including a custom-built one, and allows chaining or hybridising them to improve the final result.

The computation of an error between chords and silhouette is also more sophisticated than the linear method used in Ďurech et al. (2011). When all positive chords intersect the silhouette and no negative chords do, the error metrics for each individual chord is:

$$\chi^2 = \left(\frac{d_1^2}{\sigma_1^2} + \frac{d_2^2}{\sigma_2^2} \right) \cdot w \tag{3.3}$$

where:

- d_1, d_2 are the distances between the silhouette and the chord endpoints,
- σ_1, σ_2 are their respective uncertainties coming from timing uncertainties (both can be set to 1 by the user),
- w is a weight factor (by default = 1), modifiable by the user to emphasize specific chords.

If a negative chord crosses the silhouette or a positive chord fails to intersect it, a large artificial penalty is added to the χ^2 to push the optimizer away from invalid solutions.

Sample results

In this section, we show sample results obtained with our algorithm. For comparison, these are same targets to those presented in Choukroun et al. (2025), where they were processed using the non-open-source code developed by the Prague team. The color scheme is consistent between the two codes: blue represents the first pole solution, and magenta represents the second one. In the lower-left corner of each plot, a circle with either a dot or a cross indicates the orientation of the spin axis

(aspect angle). A dot means that the spin axis vector is pointing towards the reader, while a cross indicates it is pointing away. This is a common convention for representing 3D vectors in 2D diagrams. However, unlike the standard notation, where the dot or cross is placed at the center of the circle, here their position within the circle conveys additional information about spin axis orientation. A mark at the center means the spin axis is aligned with the observer's line of sight; a mark on the circumference implies an angle of approximately 90° between the spin axis and the observer. Figures 3.1 and 3.2 show the stellar occultation fits obtained with OccultationFit for asteroids (279) Thule and (395) Delia, respectively. The corresponding figures in Choukroun et al. (2025) are Fig. E.2 and Fig. E.5. Each figure is composed of three panels, corresponding to the three occultation events observed for each object. The diameters derived with OccultationFit are directly indicated on the plots. In all panels, the same diameter value is presented, as the software was configured to perform a joint fit of multiple events, thereby providing a single, more robust diameter determination for both mirror-pole solution. Although OccultationFit also allows each event to be fitted independently, this option was not employed here. For (279) Thule, the resulting diameters for the two mirror-pole solutions are $d_1 = 117 \pm 3$ km and $d_2 = 122 \pm 9$ km. For (395) Delia, we obtained $d_1 = 56^{+2}{-1}$ km and $d_2 = 53^{+3}{-1}$ km. These values are in excellent agreement with those reported by Choukroun et al. (2025) (Table 5), namely $d_{1c} = 115 \pm 12$ km and $d_{2c} = 119 \pm 13$ km for (279) Thule, and $d_{1c} = 56 \pm 3$ km and $d_{2c} = 55 \pm 3$ km for (395) Delia. The close correspondence between the diameters derived in this work and those from Choukroun et al. (2025) demonstrates the reliability and robustness of the new OccultationFit tool for multi-event scaling of spin and shape models.

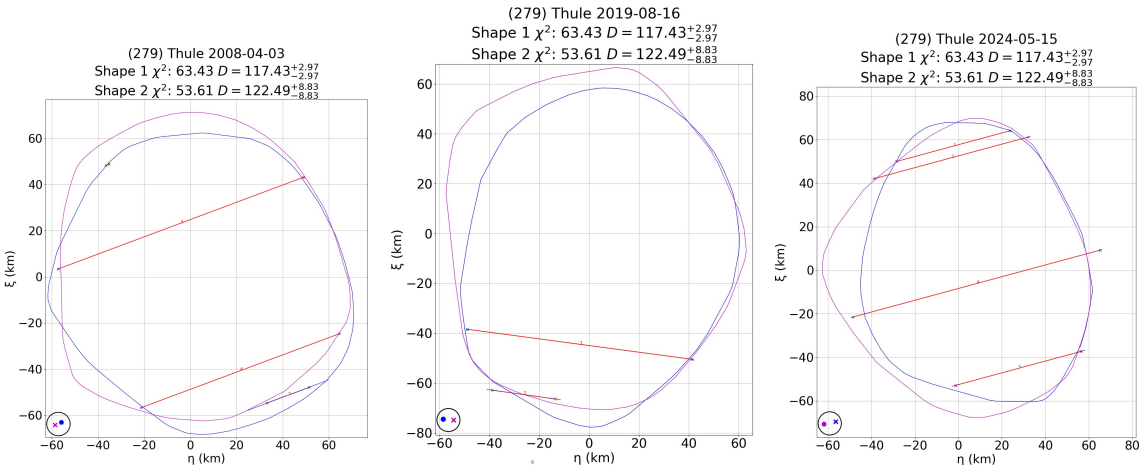

Figure 3.1: Occultation fits for asteroid (279) Thule (cf. Fig. E.2 in the paper Choukroun et al., 2025)

3.2 Convex Inversion Thermophysical Model

3.2.1 Method

CITPM is an advanced thermophysical modeling technique developed by Ďurech et al. (2017). Standard TPMs, even the most modern ones, typically take as input a predefined shape model, usually non-spherical if available, and optimize modelled

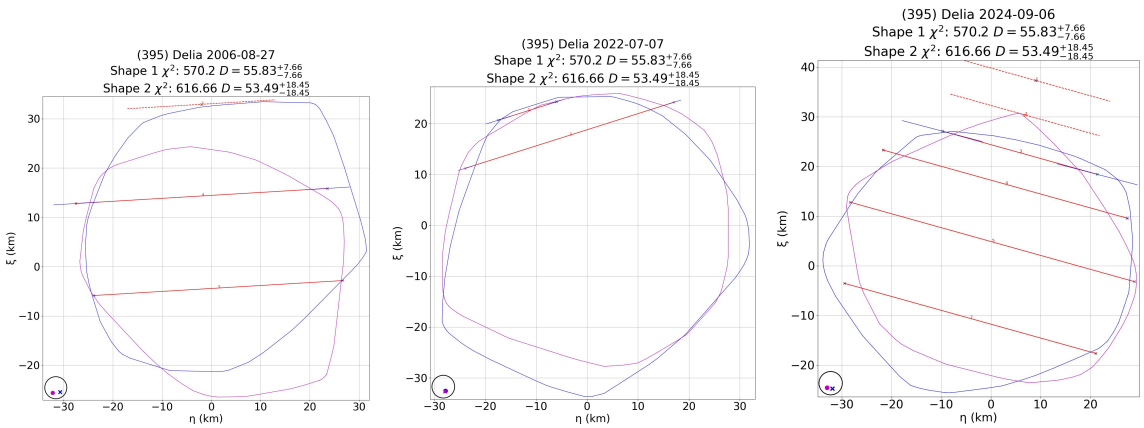

Figure 3.2: Occultation fits for asteroid (395) Delia (cf. Fig. E.5 in the paper Choukroun et al., 2025)

thermal flux based on that fixed geometry. However, if the shape model is not sufficiently accurate, its structural errors can propagate during the thermophysical optimization, potentially leading to large uncertainties or, in the worst cases, incorrect results (Hanuš et al., 2015). CITPM addresses this limitation by incorporating also the photometric data in the visible range that were used to construct the shape model. These optical data are used simultaneously with the thermal data, meaning that the photometric shape model itself is adjusted basing on thermal observations too. To achieve this, CITPM combines two methods: convex inversion (as described in Section 2.3) and a thermophysical model following the approach of Lagerros (Lagerros, 1996a, 1996b, 1997 and 1998). In this section, we therefore outline the main components that make up CITPM, before describing the functioning of the method in more detail.

Thermophysical model of Lagerros

The thermophysical model developed by Johan Lagerros in the 1990s significantly improved the modeling of asteroid thermal emission. Prior to its introduction, classical thermal models assumed highly idealized shapes, typically a sphere (as in the Standard Thermal Model, STM, by Lebofsky et al., 1986b, or in the Near-Earth Asteroids Thermal Model, NEATM, by Harris, 1998) and occasionally an ellipsoid, and added surface roughness effects empirically. These simplifications limited the accuracy of size and surface temperature estimates, especially for irregularly shaped asteroids. Lagerros extended these models by proposing a more general framework capable of handling arbitrary shapes and explicitly incorporating several key physical effects. His thermophysical model, detailed in a series of articles (Lagerros 1996a, 1996b, 1997 and 1998), allows simulations of elongated or rugged asteroids while maintaining computational efficiency. Several key assumptions underlie the Lagerros model. First, the asteroid surface is represented as a mesh of polygonal facets describing a complex (potentially non-convex) shape. On each facet, subsurface heat conduction is modeled by solving the one-dimensional heat diffusion equation perpendicular to the surface:

$$\rho c \frac{\partial T}{\partial t} = \kappa \frac{\partial^2 T}{\partial z^2}, \tag{3.4}$$

where κ is the thermal conductivity, ρ is the density, c is the heat capacity of the regolith, and $T(z,t)$ is the temperature profile evolving with sub-surface depth and the time. This local conduction allows part of the daytime heat to penetrate below the surface and re-emerge later, a necessary mechanism to reproduce the observed phase shift and nighttime cooling. A boundary condition imposes radiative equilibrium at the surface: the solar flux absorbed by each facet (proportional to $(1-A)S\cos i$, with S being the solar irradiance, A the local albedo and i the angle between the facet normal and the Sun–facet vector) must balance the sum of the emitted thermal flux ($\epsilon\sigma T^4$, via Stefan–Boltzmann, law where ϵ is the emissivity and corresponds to how much a surface is close to the emissivity of a black body) and the conductive flux into the subsurface. This energy balance, solved at each time step, determines the temperature of each facet throughout the rotation cycle.

Second, the model incorporates surface roughness at two scales. Large-scale roughness is directly accounted for through the detailed geometry of the shape, which may include craters or depressions if resolved in the mesh. For small-scale roughness (below the facet resolution), Lagerros adopts a statistical approach: each facet may be partially covered by hemispherical micro-craters, characterized by a coverage fraction ρ_c and an average opening angle γ_c (see Fig. 3.3). This crater model induces a thermal beaming effect, that is, a tendency for the rough surface to emit more heat in the direction of the Sun and observer, due to inclined slopes that "focus" the thermal emission. By tuning the roughness parameters, the model can reproduce the increased infrared flux often observed, unlike smooth surfaces can.

Finally, the Lagerros model includes multiple scattering and mutual radiative heating between facets. Specifically, when a facet faces another within a concave area, some reflected solar radiation and re-emitted infrared energy can reach the opposite facet and increase its temperature. This self-illumination and self-heating effects are modeled by computing view factors between adjacent surfaces. While these are second-order effects (studies by Lagerros have shown that global self-illumination is weak for most observed asteroids), they become significant for highly rugged surfaces or deep micro-craters, further contributing to thermal beaming. Altogether, these refinements, irregular shape, heat conduction with thermal inertia, multiscale roughness, and internal radiative exchange, give the Lagerros thermophysical model strong predictive capabilities. It can generate synthetic infrared lightcurves consistent with observations, and provide more reliable determinations of asteroid diameter, albedo, temperature, and thermal inertia. This model serves as the physical basis of the CITPM, allowing realistic interpretation of thermal data. It is also important to note that, as the CITPM works with convex shapes, the mutual illumination or radiative heating between facets do not impact the result.

Photometric model of Hapke

In parallel with thermophysical calculations, a photometric model is required to describe the directional reflectance of the asteroid surface. The most commonly used model in this context is that of Bruce Hapke (Hapke, 1981, 1981, 1984 and 1986) originally developed for planetary surfaces and airless regoliths (Moon, asteroids, etc.). Hapke's model provides a semi-analytical formulation of the bidirectional reflectance factor $r(i,e,\alpha)$, i.e. the fraction of incident sunlight reflected toward the observer, as a function of the incidence angle i, emergence angle e, and phase angle α. Hapke captures the physics of reflectance using five main parameters:

(1) the single scattering albedo w (the fraction of light that a surface particle scatters rather than absorbs in a single interaction), which defines the intrinsic brightness of the material;

(2) the asymmetry parameter g of the particle phase function, describing the probability of light being scattered forward or backward (with $g < 0$ indicating predominantly backward scattering, typical of surfaces reflecting toward the source);

(3) and (4) the opposition effect parameters B_0 (amplitude) and h (angular width), modeling the brightness surge observed as $\alpha \to 0°$ due to shadow hiding and coherent backscattering within the regolith;

(5) the roughness angle $\bar{\theta}$, quantifying the average slope of microscopic surface facets (macroscopic roughness). This last parameter simulates mutual shadowing between grains at local scale, a surface with high $\bar{\theta}$ appears darker at non-zero phase angles, as more facets are partially shadowed.

Together, these parameters allow accurate reproduction of photometric phase curve of the body, that is, the variation of its brightness with Sun-object-observer angle. Without entering into full mathematical details, we note that Hapke's formulation combines a single scattering component and a multiple scattering component. The single scattering is modulated by a phase function $P(\alpha)$ (often approximated using a Henyey-Greenstein type function with parameter g) and weighted by w. Multiple scattering is treated approximately using Chandrasekhar's $H(x)$ functions, which account for the role of multiple light interactions within the granular medium. The opposition effect $B(\alpha)$ only modulates the single scattering term, i.e., $(1+B(\alpha))P(\alpha)$, and not the multiple scattering contribution $H(\mu_0)H(\mu)$. The model also includes a geometric projection factor $\frac{\mu_0}{\mu_0+\mu}$ (with $\mu_0 = \cos i$ and $\mu = \cos e$), ensuring proper flux normalization. Overall, we obtain an expression of the form:

$$r(i, e, \alpha) \approx \frac{\omega}{4\pi} \cdot \frac{\mu_0}{\mu_0 + \mu} \left[(1 + B(\alpha))P(\alpha) + H(\mu_0)H(\mu) - 1\right] \cdot \Pi(\bar{\theta}, i, e), \tag{3.5}$$

where $\Pi(\bar{\theta}, i, e)$ is the correction term due to macroscopic roughness (function of $\bar{\theta}$ and the observation geometry). Although mathematically complex, this expression allows us to compute, for each surface facet, the portion of light reflected toward a given observer, considering the facet orientation and solar illumination. Summing the contributions of all visible facets yields the modeled brightness of the asteroid in the visible range, which can be compared to photometric observations. The use of Hapke parameters in a thermophysical model is not just aesthetic, it is essential to correctly link the absorbed solar energy to the re-emitted thermal flux. For each facet, the absorbed flux depends on its directional albedo. Hapke's model allows us to compute the effective absorption rate via the hemispherical albedo A_h, which represents the fraction of incident light scattered into the upper hemisphere (reflected back to space). This A_h depends on the incidence angle and on the optical parameters (w, g, B_0, h, $\bar{\theta}$ via the equation 3.5) and can be written as :

$$A_h(i) = \frac{1}{\mu_0} \int_\Omega r(i, e, \alpha)\, \mu \, d\Omega. \tag{3.6}$$

The integration is performed over the upper hemisphere Ω. This quantity, averaged over the solar spectrum, determines the energy balance used in the heat conduction equation. Once $A_\mathrm{h}(i)$ is known, we deduce the absorbed portion $(1 - A_\mathrm{h})$, which

serves as the heat input in the thermal equation. Thus, integrating Hapke into the TPM ensures a locally accurate energy balance, rather than relying on a Lambertian or arbitrarily fixed albedo. Furthermore, Hapke model provides a unified framework linking the classical albedo definitions of an object, for instance, the geometric albedo p_V (brightness at $\alpha = 0$) or the Bond albedo (total reflected energy fraction) can both be computed from the model parameters by integrating reflectance over angular space. This is particularly useful in the CITPM framework, where the goal is to avoid definition ambiguities tied to non-spherical shapes. In practice, when absolute photometric calibration data are available (e.g., magnitude H or calibrated observations over a phase angle range), the Hapke parameters can be adjusted to fit the observed phase curve. This enables simultaneous determination of both albedo and asteroid size: to match a given observed brightness, a brighter model must correspond to a smaller size, and vice versa. Introducing the Hapke model into the TPM thus guarantees a physically consistent link between optical and thermal data, each facet receives and reflects the appropriate amount of energy, and the modeled visible flux matches observations. This approach enhances the physical fidelity of the global model, especially when compared to simplified methods using a mean albedo without angular variation.

CITPM

The Convex Inversion Thermophysical Model (CITPM) is an innovative method that directly combines the two previously described components, lightcurve inversion and thermophysical modeling, within a joint optimization. Introduced by Ďurech et al. (2017), this unified approach relies on the robustness of Kaasalainen's convex inversion for shape and rotation on one hand, and on the predictive power of Lagerros' thermophysical model on the other. In practice, the CITPM simultaneously takes as input the optical observations (visual lightcurves, with the addition of sparse data points calibrated in intensity) and the thermal observations (infrared fluxes at different wavelengths), for example from IRAS (Neugebauer et al., 1984), Akari (Usui et al., 2011), and WISE satellites (Wright et al., 2010). The model assumes an initial convex shape (often described by spherical harmonics or a polyhedron with several hundred facets) and associates it with a set of physical parameters to be optimized. An important feature of this method is the use of the bolometric hemispherical albedo, computed from the Hapke photometric parameters (see equation 3.6). This albedo represents the total fraction of incident energy reflected by the surface, integrated over all directions and all wavelengths. For each facet, the hemispherical albedo depends on the incidence angle i.

The parameters optimized simultaneously include: the 3D shape of the asteroid (coefficients describing the convex shape model), its rotation state (sideral period, spin-axis orientation, initial phase), the absolute size (scale factor of the shape model), the photometric surface parameters (Hapke model), as well as thermal parameters such as the thermal inertia Γ. The macroscopic roughness parameters, the fraction of surface covered by craters ρ_c, the opening angle γ_c from Hapke model, are not directly optimized. Instead, they are fixed at different values and explored on a grid to identify the combination providing the best overall fit. $\bar{\theta}$ is determined based on the formula from Hapke (1984):

$$\tan(\bar{\theta}) = \frac{2}{\pi}\int_0^{\frac{\pi}{2}} \tan(\theta)a(\theta)d\theta, \tag{3.7}$$

where $a(\theta)$ is a function that describes the distribution of tilt angles θ within a crater and in the flat surface element to which that crater belongs, weighted by the proportion of the surface area occupied by the craters relative to that of the flat area. With the assumption of spherical craters, it is possible to give an analytic expression of the equation 3.7 depending of ρ_c and γ_c.

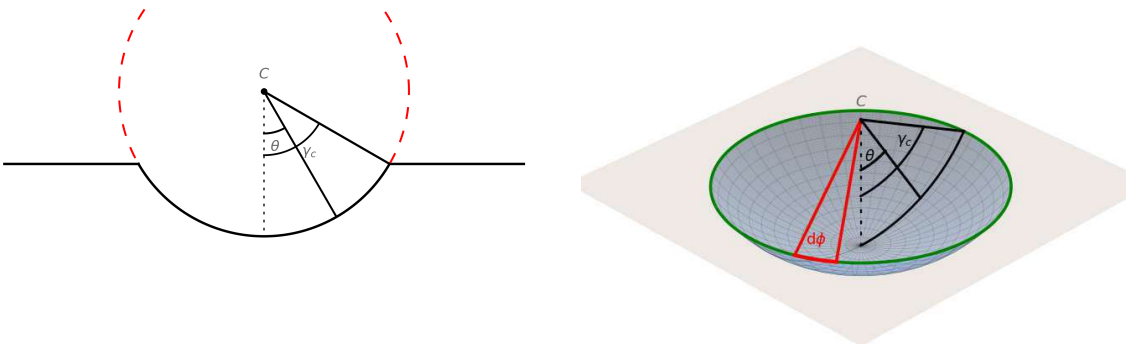

(a) (b)

Figure 3.3: Scheme of a spherical crater in 2D (a) and 3D (b)

Indeed, for spherical craters we can note:

$$dA = R^2 \sin(\theta)d\theta d\phi, \tag{3.8}$$

where dA is an element of surface of the crater, and $R^2\sin(\theta)$ corresponds to the determinant of the Jacobian in spherical coordinates (r, θ, ϕ). The integration of the equation 3.8 give the area of the crater :

$$A_{cap} = 2\pi R^2(1 - \cos(\gamma_c)). \tag{3.9}$$

It is now possible to give an expression for $a(\theta)$:

$$a(\theta) = \frac{\sin(\theta)}{1 - \cos(\gamma_c)}. \tag{3.10}$$

Therefore, placing the equation 3.10 in 3.7 it is easy to show that:

$$\tan(\bar{\theta}) = \frac{2}{\pi(1 - \cos(\gamma_c))}[\int_0^{\gamma_c} \frac{1}{\cos(\theta)}d\theta - \int_0^{\gamma_c} \cos(\theta)d\theta]. \tag{3.11}$$

Remembering $1/\cos(\theta) = \sec(\theta)$ and $\int \sec(\theta)d\theta = \ln|\sec(\theta) + \tan(\theta)| + C$:

$$\tan(\bar{\theta}) = \frac{2\rho_c}{\pi(1 - \cos(\gamma_c))}[\ln|\sec(\gamma_c) + \tan(\gamma_c)| - \sin(\gamma_c)]. \tag{3.12}$$

The equation 3.12 is equivalent to the equation at page 5 in Lagerros (1996a). The thermal emission of each facet is computed at each iteration by solving the 1D heat conduction equation, while the brightness in the visible domain is calculated using the Hapke model. Model deviations from visible lightcurves and thermal data are combined in a merit function defined as:

$$\chi^2_{\text{total}} = \chi^2_{\text{VIS}} + \omega_{\text{IR}}\,\chi^2_{\text{IR}}, \tag{3.13}$$

where ω_{IR} is a weighting factor determined according to the maximum compatibility estimate method (Kaasalainen, 2011) to balance the fit quality of the two datasets. The optimization is performed using the Levenberg-Marquardt algorithm (Levenberg, 1944, Marquardt, 1963) which minimizes χ^2_{total} while accounting for parameter correlations. A crucial point is that the photometric data must include at least one absolute calibration data point to resolve the size - albedo degeneracy. In practice, calibrated V-band magnitude measurements over a range of phase angles are incorporated, which sets the scale of the Hapke model and thus the physical size of the shape model. By directly optimizing the shape with the infrared data, the CITPM ensures that the adopted solution reproduces both the variation in visible brightness and the measured thermal fluxes as accurately as possible. This approach yields consistent physical parameters with better-quantified uncertainties, typically obtaining diameters within $\pm 5\,\%$ and constrained thermal inertia. Tests on well-characterized targets (by stellar occultations and spacecraft-derived shapes) confirm the reliability and robustness of this integrated method.

3.2.2 Procedures, scripts and improvements

At the beginning of this thesis, many procedures were manual or semi-automated, from data preparation to the final execution of the CITPM itself, so producing a single asteroid model could sometimes take up to one month. In Choukroun et al. (2025) we present the results for 15 models, which would therefore have represented more than 15 months of work on their own. In addition, the other tasks carried out (familiarization with the research field, mastering the various modeling techniques, test runs with a mobile occultation observing station, data processing, creating STEROID pipeline, developing the code to fit occultations, a required 3-month internship abroad, etc.) could have made it difficult to complete this thesis within the imposed deadlines. A substantial effort was therefore made by the author of this thesis to automate and standardize the procedures in order to save time, so that a model can now be produced in roughly one week. In this section, we will focus on a particular case study in order to explain the applied procedure and highlight the developments that were made.

Target: asteroid (279) Thule

Creating an asteroid model with the use of the CITPM can be divided into four main steps: preparation of input data, determination of hyperparameters, search for minima and estimation of uncertainties, and finally, production of the final solution.

Input files for CITPM

As mentioned in Section 3.2, despite the fact that the CITPM needs the results of the convex inversion as initial data, it simultaneously optimizes an asteroid spin and shape model to fit both thermal data and data in the visible range. Consequently, three types of input files are required.

The first file stores lightcurves in the visible. Its structure is identical to the one used by the convex inversion (see Section 2.3), with one important difference:

this file must contain at least one set of *calibrated* brightness measurements. Unlike relative lightcurves, a calibrated dataset with good coverage near opposition (i.e., when the asteroid is located opposite to the Sun as seen from Earth) is necessary to constrain the Hapke parameters, which are used internally by the CITPM. We downloaded the calibrated data from USNO (US Naval Obervatory) archive[2].

The second input file contains thermal infrared observations. These data are retrieved as CSV files from the IR database[3] (Szakáts et al., 2020). However, the raw CSV files cannot be read directly by CITPM, since their structure differs from the expected input format. In the CSV, each row corresponds to a single measurement. By contrast, the CITPM input file is organized into blocks, each defined by an observation epoch (Julian date). An example block is shown below:

```
 2445419.0305959997   3
 0.507262 4.267926 0.028804
-0.486850 4.188458 0.028795
 12.   1.7480 0.3530 -1
 25.   2.7620 0.6270 -1
 60.   1.8030 0.4560 -1
```

The first line indicates the observation time (Julian Date) and the number of measurements performed at that epoch. The next two lines contain the position vectors: first one of the Sun as seen from the asteroid, and then the one of the Earth as seen from the asteroid. The following lines provide, for each measurement, the observing wavelength [μm], flux [Jy], associated flux uncertainty [Jy], and a flag which indicates if the measurement is color corrected or not. In earlier implementations, this file had to be produced manually from the CSV tables, which was time-consuming and prone to human error. Today, our csv2Err.py script automatically generates the input file with infrared data.

The third input file contains the asteroid ephemeris. Each line stores the asteroid heliocentric position vector at a given epoch. A subtle but important detail is that the first epoch of this file does not coincide with the first thermal data block. Instead, it must begin at least ten asteroid rotations earlier. For example, if the sidereal rotation period is 24 hours, the ephemeris file should start at least 10 days before the first thermal data epoch. This procedure ensures that the asteroid reaches thermal equilibrium before the optimization step. As with the thermal data, this file was previously generated manually, but it is now produced automatically by another script. The script requires as input the thermal data file and the sidereal rotation period, the latter determined beforehand through convex inversion (see Section 2.3).

Determination of hyperparameters

A hyperparameter is a parameter that is not directly optimized by the model and therefore remains fixed throughout the optimization. In CITPM, several hyperparameters exist, and in some cases, parameters can also be fixed, which effectively turns them into hyperparameters. In this section we focus on the hyperparameter

[2]downloaded from AstDys database `https://newton.spacedys.com/astdys2/index.php?pc=3.0`

[3]`https://ird.konkoly.hu/`

ω_{IR} from the equation 3.13. This variable controls the relative weight between the optical and thermal datasets. As explained in Ďurech et al. (2017), the objective is to determine the value of the weight of infrared data that minimizes χ^2_{total}. In the former procedure, the first step was to determine good initial Hapke parameters by running the code with $\omega_{\mathrm{IR}} = 0$, using the spin axis solutions and the rotation period obtained from convex inversion. In some cases, the CITPM diverged numerically, producing errors. When this happened, the code had to be restarted with different initial Hapke parameters until a stable solution was found. Once this was successful, the resulting Hapke parameters could be used as the new initial values for future steps. The next step was to run the code multiple times with different values of ω_{IR} and to apply the method described in chapter 2 in Choukroun et al. (2025). Each of these steps had to be carried out manually, which was problematic in several ways. First, CITPM procedures are relatively slow, so performing many runs manually was extremely time-consuming. Moreover, the determination of suitable Hapke starting parameters could be difficult, as most random combinations led to convergence errors. Finally, as noted in Choukroun et al. (2025), this procedure was originally performed for only a single combination of crater parameters approximating surface roughness, which may not be representative and can complicate the determination of the optimal ω_{IR}. To improve this process, a dedicated script was developed to automate the procedure. Both the determination of the initial Hapke parameters and the successive runs with different ω_{IR} values are now performed automatically. In addition, the scan is carried out for three different surface crater combinations, which provides a more representative sampling and makes it possible to determine the optimal ω_{IR} more reliably. An example corresponding to asteroid (279) Thule is shown in Figure 3.4. Panels a), b), and c) display the same diagnostic plot but for different surface roughnesses. It can be seen in particular that for surface crater parameters $\gamma_c = 20°$ and $\rho = 0.2$ (panel a), the shape of the plot is less well defined than for higher roughness levels. This provides a preliminary indication that Thule may have a relatively high surface roughness. This hypothesis is later confirmed when the final solution is produced, since (279) Thule turns out to be the asteroid with the highest value of $\bar{\theta}$ in our sample (see Table 4 in Choukroun et al., 2025). For this object, the adopted value of ω_{IR} is 0.008, as this choice best represents the three scans performed at different roughness levels.

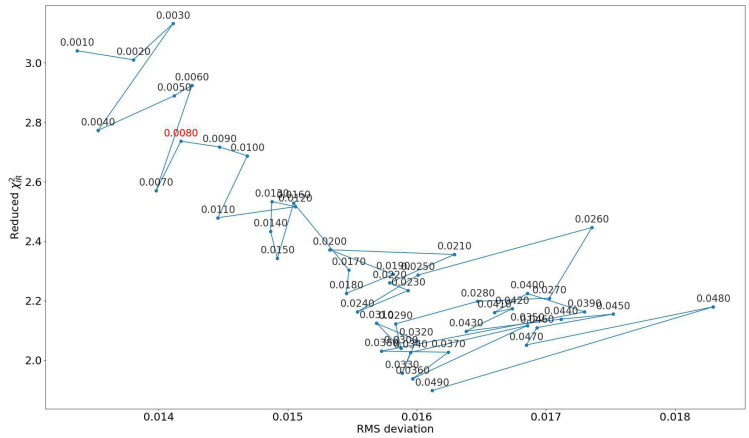

(a)

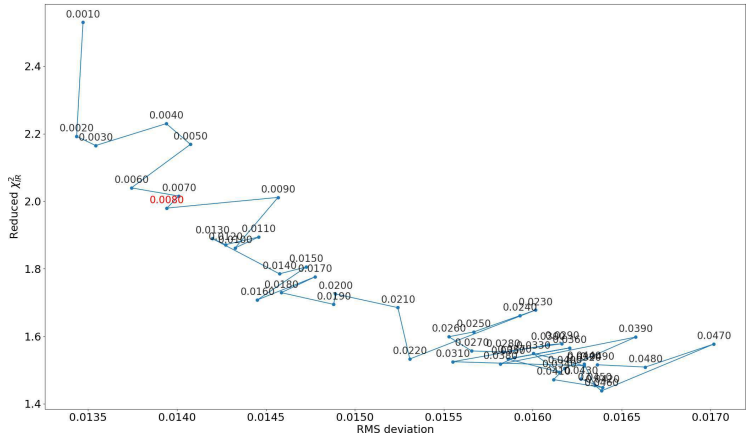

(b)

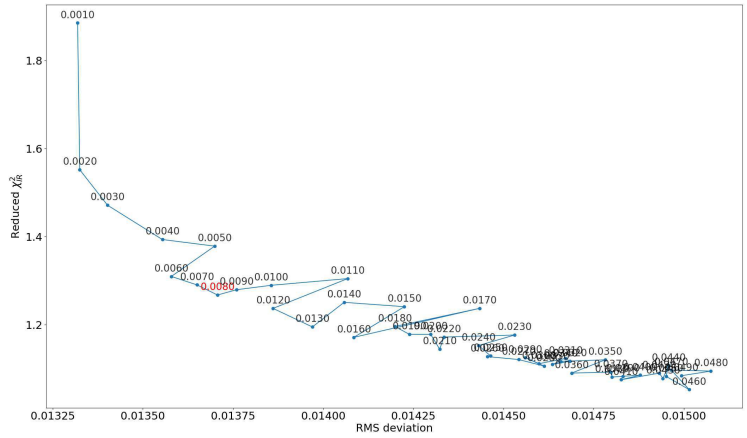

(c)

Figure 3.4: RMS deviations of data in the visible vs. reduced χ^2_{IR} for asteroid (279) Thule. The values next to the points indicate the corresponding ω_{IR} value. Panel a shows the results of the ω_{IR} scan for $\rho_c = 0.2$ and $\gamma_c = 20$; panel b for $\rho_c = 0.5$ and $\gamma_c = 50$; and panel c for $\rho_c = 0.8$ and $\gamma_c = 80$.

Looping through the parameter space

CITPM is a high-dimensional multivariable model with a complex structure that can produce a large number of local minima. The response of the model as a function of parameter space is therefore much less stable than in the case of convex inversion,

illustrated in Figure 2.6. For this reason, it is not possible to leave all the parameters free, since we would risk that the process never converges towards the best solution. Instead, the surface roughness parameters (crater aperture and crater coverage) are kept fixed and thus treated as hyperparameters. In order to find the best result, we do not scan the parameter space for value of spin axis orientation (λ, β) as in convex inversion (since these values are already well constrained by that method). Instead, the code is run multiple times for numerous combinations of the surface roughness parameters (kept fixed during each run) together with the fixed thermal inertia. We have at our disposal a version of the code specially developed to perform, for a given thermal inertia value, several CITPM runs with different values of crater aperture (ranging from 10° to 90° in steps of 10°) and crater coverage (ranging from 0.0 to 1.0 in steps of 0.1). At the end of a full loop over roughness parameters, the code stores the results file for each combination of surface crater parameters. This procedure is repeated for multiple values of thermal inertia, namely 1, 3, 6, 10, 20, 30, 40, 50, 60, 70, 80, 90, 100, 120, 150, 200, 250, and 300 $\mathrm{J\,m^{-2}\,s^{-1/2}\,K^{-1}}$. Since a single run for one thermal inertia value typically takes about 6 hours, this step is by far the most time-consuming. It was therefore important to automate the procedure as much as possible. In future work, the CITPM code could be rewritten and optimized to enhance performance and generality, allowing the combination of more than two techniques within the same framework. Once all runs are completed, the next step is to identify the best solution as well as all solutions that can be considered acceptable. Three criteria are applied for this purpose.

Threshold condition

A solution is considered acceptable if both χ^2_{vis} and χ^2_{IR} remain below given thresholds:

$$\begin{cases} \chi^2_{\mathrm{vis}} < \min(\chi^2_{\mathrm{vis}}) \cdot 1.1 \\ \chi^2_{\mathrm{IR}} < 1 + \sqrt{\frac{2}{\nu}}, \end{cases} \tag{3.14}$$

where ν is the number of thermal measurements minus the number of degrees of freedom. For asteroid (279) Thule, these thresholds are illustrated in Figure 3.5. The left panel corresponds to the criterion on χ^2_{IR}, while the right panel corresponds to the criterion on the RMS deviation between observed and modelled lightcurves in the visible. The blue line shown in both panels represents the threshold defined by Eq. (3.14). The points correspond to the model solutions obtained from the loop. Every point lying below both blue lines is considered an acceptable solution.

Physical feasibility

The 3D shape model must also be physically plausible. One important check is to project the model along the principal axes of the inertia tensor. Since each vertex of the model is expressed in the asteroid co-rotating reference frame, the model is expected to rotate around its z-axis. Therefore, if after projection onto the principal axes of the inertia tensor the model still rotates around the z-axis, it can be considered acceptable.

Consistency between thermal inertia and roughness parameters

A final procedure introduced in this work is to plot all acceptable solutions in a three-dimensional diagram (thermal inertia vs crater aperture vs crater coverage).

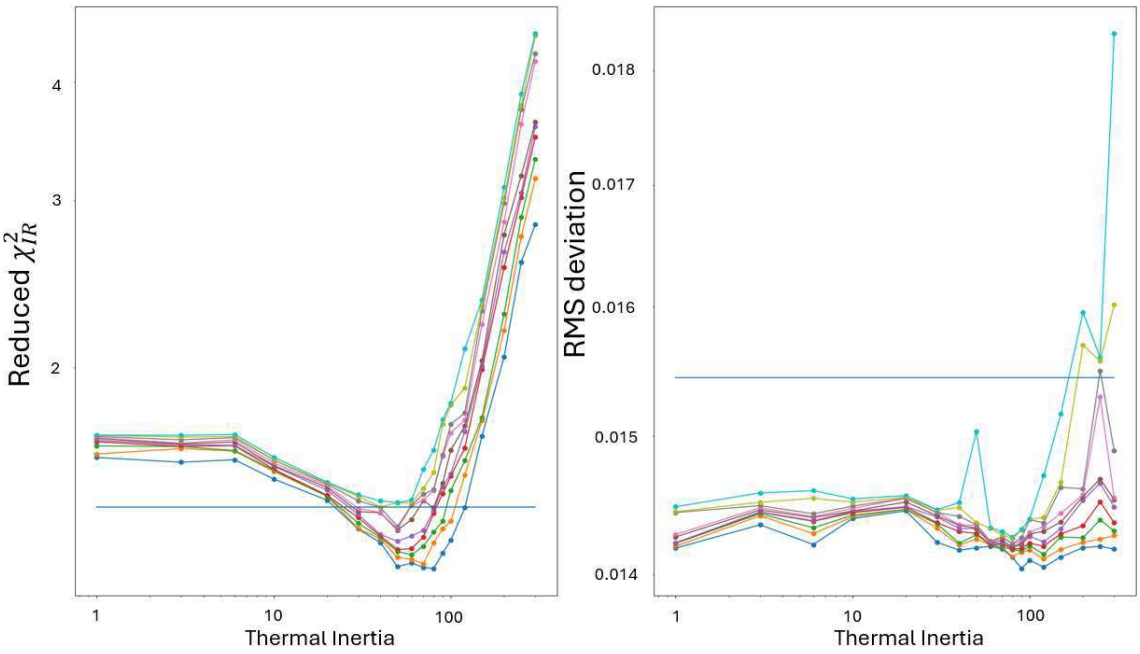

Figure 3.5: Left panel: reduced $\chi^2_{\rm IR}$ as a function of thermal inertia for the models produced by the loop over surface roughness; right panel: RMS deviation (visible data) as a function of thermal inertia. The blue line in each panel corresponds to the threshold value defined by Eq. (3.14).

This check, illustrated in Fig. 2 of Choukroun et al. (2025), allows us to verify the absence of outliers and to ensure consistency between the solutions.

If a solution from a given run satisfies all three criteria, it is considered acceptable. The best solution is then used as the initial parameter set for the final model, while the ensemble of acceptable solutions serves to estimate its uncertainties. As for the other steps, those that were not originally introduced in this work were previously carried out manually. A substantial effort of automation and standardization has therefore been implemented, which greatly improved both the efficiency and the reproducibility of the procedure.

Final solution

The final model solution is obtained from the results of the previously described roughness loop. Once the final solution is produced, we verify that all output parameters remain consistent with the uncertainties estimated from the acceptable solutions of the loop. If this condition is satisfied, the last elements can then be generated, namely the 3D shape model (via Minkowski minimisation, see chapter 2.3.1), the lightcurve fits, and the thermal data fits (see the figures C.1 to C.10 and D.1 to D.21 in Choukroun et al., 2025).

Target: asteroid (269) Justitia, an extremely red main-belt asteroid

(269) Justitia stands apart from the main sample analyzed in this thesis. Unlike the other targets, for which both stellar occultations and thermophysical modelling

were combined, Justitia was investigated independently using the Convex Inversion Thermophysical Model (CITPM) only. This main belt asteroid was selected for a dedicated study because of its extremely red reflectance, redder than typical D-types and more similar to some Centaur and trans-Neptunian object (TNO) surfaces enriched in complex organics. Such a spectral behavior strongly suggests an origin in the outer solar system, followed by implantation into the main belt. Owing to these unique characteristics and its potential primitive composition, Justitia has been chosen as the primary target of the upcoming MBR Explorer space mission. The CITPM solution presented here was developed as a pre-mission study, aiming to provide robust size, albedo, spin, and surface-property constraints prior to the spacecraft arrival. In parallel, a separate team conducted a multi-chord stellar occultation campaign in August 2023 to derive an independent absolute scaling (Buie et al., 2023). Our work therefore complements these efforts by offering a consistent thermophysical interpretation and by establishing a reference model for mission planning and surface environment predictions.

Data and method.

Before the August 2023 multi-chord occultation campaign, we built spin and shape solutions and a thermophysical solution by combining (i) dense lightcurves processed in our program on slow rotators (multi-site, 30–60 cm class telescopes), (ii) calibrated photometry from ATLAS (Tonry et al., 2018) to constrain the axial ratios, and (iii) thermal fluxes from IRAS (Neugebauer et al., 1984), AKARI (Usui et al., 2011) and WISE (Wright et al., 2010). As described in this chapter, convex lightcurve inversion provided period and pole candidates, which we then fed to the CITPM. This method solved facet-wise 1D heat conduction and jointly fitted the visible and infrared domains according to equation 3.13, adjusting thermal inertia Γ, macroscopic roughness (crater opening angle and areal fraction), and Hapke photometric parameters (Marciniak et al., 2025).

Main results.

The two mirror-pole solutions converge to virtually identical physical properties. The effective diameter is tightly constrained to $\sim$55–60 km, with a nominal value of 58 ± 2 km for pole 1, and the geometric albedo to $p_V = 0.058 \pm 0.006$. The spin is retrograde, with the pole far from the ecliptic plane; the mirror ambiguity was expected given the low orbital inclination. The best-fitting thermal models favor low-to-moderate thermal inertia, $\Gamma \approx 41^{+110}_{-40}\,\mathrm{J\,m^{-2}\,s^{-1/2}\,K^{-1}}$ (SI units) at the observing heliocentric distance (scaling to $\sim$87 SIu at 1 au), together with high macroscopic roughness; this combination is consistent with a fine regolith and an optically red, organics-rich surface. The model reproduces both data domains with low residuals (reduced χ^2 in the IR $\sim$0.3 and visible rms $\sim$0.013 mag), indicating a stable joint solution (Marciniak et al., 2025).

Scientific and operational relevance.

Produced prior to the August 2023 occultation, this CITPM solution provided the absolute scale needed to optimize observer placement and served as a pre-mission reference for MBR Explorer (thermal environment, diurnal temperatures,

and surface texture expectations). More broadly, Justitia exemplifies the value of the joint approach used throughout this work: combining processed dense lightcurves, calibrated sparse photometry, and multi-mission infrared fluxes within CITPM yields mutually consistent size/albedo and surface-property constraints, which are key to testing the asteroid implantation scenarios and planning spacecraft observations.

3.3 Diameter comparison results

For the 15 asteroids included in the study led by the author of this thesis, we were able to determine diameters using two independent approaches: stellar occultations and thermophysical modeling. Comparing these two methods is particularly valuable, since cross-validation is often essential in science to confirm the reliability of derived results. Most previous works aiming to estimate asteroid diameters relying on a single technique, which may partly explain the large dispersion of values reported in the literature (see Table 1 in Choukroun et al. 2025). In our case, the application of both methods represents a major strength. As shown in Figure 3 of Choukroun et al. (2025) or in Figure 3.6 here, the diameters obtained from the two techniques are generally in excellent agreement. In the few cases where a discrepancy is observed (e.g., asteroid (215) Oenone), the cause is usually easy to identify. For this object, only one occultation event with two positive chords was available, the minimum number required according to our criteria. For a moderately elongated body, a single silhouette is insufficient to constrain the diameter robustly, despite the intrinsic accuracy of occultation timings. In such cases, the diameter determined by CITPM is likely to be more realistic. We also compared our results with the values from the literature (see Fig. 5 in Choukroun et al. 2025 and Fig. 3.7 here). When previous works reported a single best-fit value, we used it; when they gave averages or multiple diameters (e.g., mirror-pole solutions), we used the average—and did the same for our own unresolved pole cases. The comparison shows our values agree with previous works, and the residuals are, on average, smaller than those based solely on literature values. The complementarity of these two approaches is evident. Occultations offer unrivalled precision on individual diameters but are difficult to obtain, requiring coordinated efforts from several observers for each event. Thermophysical models of asteroids, on the other hand, have become increasingly feasible thanks to the growing availability of thermal data from dedicated surveys and archives (Hung et al., 2022). While they remain limited by the number of asteroids observed in the thermal infrared, they provide a practical and powerful alternative.

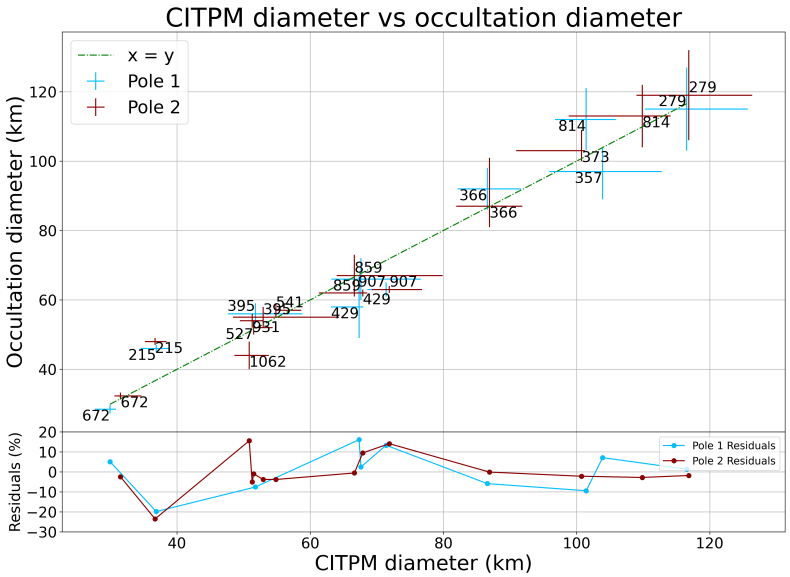

Figure 3.6: Comparison of asteroid diameters derived from CITPM and from stellar occultations obtained in Choukroun et al. (2025). The x-axis shows the CITPM-derived size and the y-axis the occultation-derived size; the dashed green line indicates $y = x$. Blue symbols correspond to pole 1 solutions and brown symbols to pole 2 solutions. Relative residuals are defined as $100 \times (D_{\mathrm{CITPM}} - D_{\mathrm{occ}})/D_{\mathrm{occ}}$.

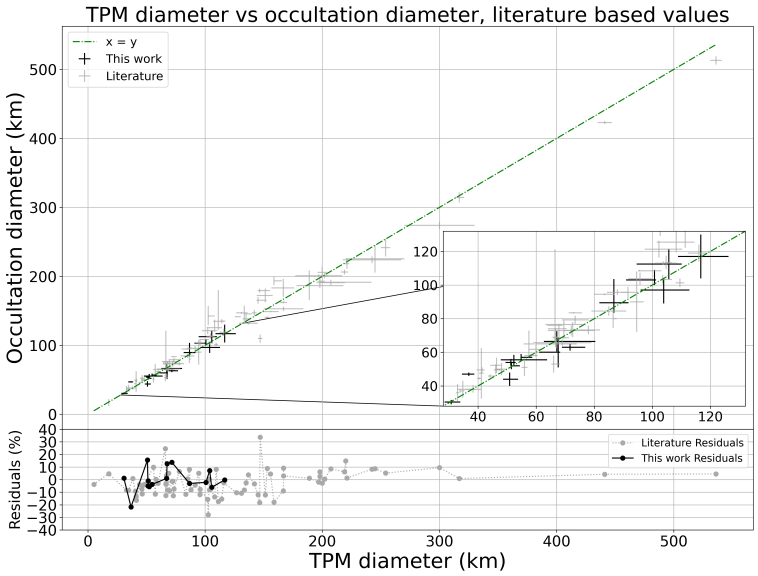

Figure 3.7: Comparison of asteroid sizes inferred from thermophysical modeling and from stellar occultations reported in the literature. The abscissa gives the TPM-derived size and the ordinate the occultation-derived size; the dashed green line indicates the $y = x$ identity. Gray symbols plot literature measurements, whereas black symbols show this work values averaged over mirror-pole solutions. Relative differences are defined as $100 \times \left(D_{\mathrm{TPM}} - D_{\mathrm{occ}}\right)/D_{\mathrm{occ}}$.

Chapter 4

Conclusions and future prospects

In conclusion, comparison between diameters from occultations and thermophysical modeling has never been performed before on such a scale (see also Table A.1 and Figure 5 in Choukroun et al., 2025). While Herald et al. (2020) determined occultation diameters from complex shape fitting, they compared them to the averaged values for diameters from simplified thermal models, which assume spherical asteroid shapes. For most of the asteroids in our sample, spin and shape models were obtained here for the first time, and none had previously determined thermal inertia values. By combining these two methods, we were able to resolve inconsistencies in diameter and albedo estimates, reducing the discrepancies from several tens of percent down to only a few percent (Choukroun et al., 2025). This not only strengthens the robustness of our results but also demonstrates the power of using complementary approaches in asteroid characterization. From a methodological standpoint, the CITPM approach jointly fits visible light curves and thermal infrared data through the cost function given in Eq. 3.13. This unified optimization makes it possible to optimise and scale shape models while simultaneously constraining thermal inertia and surface roughness, rather than relying on fixed shape solutions. Internal comparisons show that, when data quality is sufficient, CITPM diameters are consistent with those derived from multichord occultations, and that remaining discrepancies can mostly be explained by chord coverage and geometry.

The processing pipeline STEROID (Choukroun et al., submitted (Paper 1)) played a crucial role in efficiently handling large sets of images and extracting accurate photometry for moving targets. Its automation and robustness significantly improved the homogeneity and quality of the lightcurves used as input to asteroid shape modeling and thermophysical analysis.

Scientifically, the combined approach has proven its operational value beyond the main sample. The case of (269) Justitia illustrates how a spin and shape model scaled with CITPM can narrow down the size ($\approx 58 \pm 2$ km) and albedo ($\approx 0.058 \pm 0.006$), while also providing useful constraints on surface roughness and thermal inertia, particularly in the context of planned dedicated space mission (Marciniak et al., 2025).

In addition, part of this work contributed to the large-scale effort of scaling slowly rotating asteroids through stellar occultations only (Marciniak et al., 2023). In that study, 16 main-belt slow rotators were modeled using dense light curves and precisely scaled by fitting multichord occultation events. This approach not only resolved long-standing inconsistencies in size determinations but also helped to

break mirror-pole ambiguities inherent to light-curve inversion, leading to the first reliable spin and shape models for many of these bodies. The resulting well-scaled models provide a robust foundation for accurate density estimates when combined with future mass determinations.

This work also sets the stage for further developments. Because CITPM is a high-dimensional multivariable model with a complex response surface containing many local minima, extensive scans over thermal inertia and surface roughness are required. Automating these procedures has greatly improved both efficiency and reproducibility. Moreover, the additive form of the cost function (Eq. 3.13) can naturally be extended to include additional datasets by adding weighted terms. Rewriting and optimizing the CITPM code to generalize this scheme and reduce computational time will be a key step for future work. Combined with continued photometric monitoring and well-coordinated occultation campaigns, these improvements will enable an increasing number of asteroids to be characterized with percent-level diameters and well-constrained thermophysical properties.

Moreover, systematic and significant discrepancies between occultation diameters (with good chord coverage) and CITPM solutions can flag excess thermal flux not accounted for by a single body (Brown & Butler, 2018). Such an excess can be consistent with an unresolved companion (a binary), making this joint analysis a powerful pre-screening tool for binary asteroid candidates to be confirmed by other techniques.

List of publications

1. Choukroun, A., Kamiński, K. & Marciniak, A. (2025) *STEROID: A Python package to automate asteroid and star photometry*, submitted to Acta Astronomica.

   This article describes in detail the Python package STEROID, introduced in Section 2.2. The package was fully developed and documented by the author of this thesis. Over the course of its use, which made it possible to reduce and process data from more than a hundred nights, the package was improved and corrected for potential bugs that can exist in a young project, making it today a reliable and efficient tool, tested by different users in multiple environments. The article has already obtained a positive review.

2. Choukroun, A., Marciniak, A., Ďurech, J., Perła, J., Ogłoza. et al. (2025) *Asteroid sizes determined with thermophysical model and stellar occultations*, Astronomy & Astrophysics, 698, A298
   `https://doi.org/10.1051/0004-6361/202554476`

   This article presents the main results of this thesis. The work reported includes all CITPM models, the procedures used to build and validate these models, and part of the data processing performed by an author with STEROID (around 50 lightcurves). The author of this thesis carried out the thermophysical modeling of all the targets, the analysis of the results, and their comparison with occultation-derived diameters. He also proposed the interpretation of discrepancies between the two methods and the discussion of their respective uncertainties. The author also performed a thorough literature review for asteroid diameters based on stellar occultations and thermophysical modelling. The article text was written by the author of this thesis, with the exception of subsections 4.2 and 4.3.

3. Marciniak, A., Choukroun, A., Perła, J., Ogłoza, W., Szakáts, R. et al. (2025) *Thermophysical model of (269) Justitia – Main Belt Asteroid Possibly Implanted from Trans-Neptunian Region.*, The Planetary Science Journal, 6, 60
   `https://doi.org/10.3847/PSJ/adb28b`

   This article is a case study of asteroid (269) Justitia modeled with the CITPM. The significance of these results is twofold. First, this main-belt asteroid exhibits several properties that are usually associated with trans-Neptunian objects. Second, it is the primary target of the upcoming MBR Explorer space mission, which gives this study a high value as a preliminary investigation. At the time of this work, the author of this thesis was learning to use the CITPM, and therefore produced a model in parallel with that of the lead author of this article in order to validate the results. The author of this thesis also

contributed to the generation of the shape model plots and with lightcurves reductions (2 nights).

4. Marciniak, A., Ďurech, J., Choukroun, A., Hanuš, J., Ogłoza, W. et al (2023) *Scaling slowly rotating asteroids with stellar occultations.* Astronomy & Astrophysics, 679, A60
https://doi.org/10.1051/0004-6361/202346191

   This study focused on scaling 16 shape models of slow rotators, obtained through convex inversion, by using stellar occultations. In addition to deriving accurate diameter values and spin and shape models, the method also allowed us, in some cases, to resolve pole ambiguities. For this work, the author of this thesis contributed by reducing some lightcurves (few tens), generating the 3D shape model plots with axis representations, and by producing the table summarizing the details of all photometric observations.

Bibliography

Barucci, M. A., Capria, M. T., Coradini, A., & Fulchignoni, M. 1987, Icarus, 72, 304, doi: 10.1016/0019-1035(87)90177-1

Borovička, J., Spurný, P., & Brown, P. 2015, in Asteroids IV, ed. P. Michel, F. E. DeMeo, & W. F. Bottke, 257–280, doi: 10.2458/azu_uapress_9780816532131-ch014

Borucki, W. J., Koch, D., Basri, G., et al. 2010, Science, 327, 977, doi: 10.1126/science.1185402

Bottke, Jr., W. F., Cellino, A., Paolicchi, P., & Binzel, R. P. 2002, in Asteroids III, ed. W. F. Bottke, Jr., A. Cellino, P. Paolicchi, & R. P. Binzel, 3–15

Braga-Ribas, F., Sicardy, B., Ortiz, J. L., et al. 2014, Nature, 508, 72, doi: 10.1038/nature13155

Brown, M. E., & Butler, B. J. 2018, AJ, 156, 164, doi: 10.3847/1538-3881/aad9f2

Brunetto, R., Hénault, E., Cryan, S., et al. 2025, ApJ, 982, L8, doi: 10.3847/2041-8213/adb977

Buie, M. W., Hayne, P. O., AlMazmi, H. A., Landis, M. E., & Bottke, W. F. 2023, in AGU Fall Meeting Abstracts, Vol. 2023, AGU Fall Meeting Abstracts, P33E–3192

Buie, M. W., Porter, S. B., Tamblyn, P., et al. 2020, AJ, 159, 130, doi: 10.3847/1538-3881/ab6ced

Cannon, R. E., Rożek, A., Brozović, M., et al. 2025, MNRAS, 538, 2311, doi: 10.1093/mnras/staf371

Carry, B. 2012, Planet. Space Sci., 73, 98, doi: 10.1016/j.pss.2012.03.009

Chambers, K. C., Magnier, E. A., Metcalfe, N., et al. 2016, arXiv e-prints, arXiv:1612.05560, doi: 10.48550/arXiv.1612.05560

Chapman, C. R., Morrison, D., & Zellner, B. 1975, Icarus, 25, 104, doi: 10.1016/0019-1035(75)90191-8

Cheng, A. F., Agrusa, H. F., Barbee, B. W., et al. 2023, Nature, 616, 457, doi: 10.1038/s41586-023-05878-z

Choukroun, A., Marciniak, A., Ďurech, J., et al. 2025, A&A, 698, A298, doi: 10.1051/0004-6361/202554476

De Sanctis, M. C., Ammannito, E., Capria, M. T., et al. 2013, Meteorit. Planet. Sci., 48, 2166, doi: 10.1111/maps.12138

Delbo, M., Mueller, M., Emery, J. P., Rozitis, B., & Capria, M. T. 2015, in Asteroids IV, ed. P. Michel, F. E. DeMeo, & W. F. Bottke, 107–128, doi: 10.2458/azu_uapress_9780816532131-ch006

DeMeo, F. E., & Carry, B. 2013, Icarus, 226, 723, doi: 10.1016/j.icarus.2013.06.027

Drake, A. J., Djorgovski, S. G., Mahabal, A., et al. 2009, ApJ, 696, 870, doi: 10.1088/0004-637X/696/1/870

Dunham, D. W., Osborn, W., Williams, G., et al. 1991, in LPI Contributions, Vol. 765, Asteroids, Comets, Meteors 1991, ed. LPI Editorial Board, 54

Ďurech, J., Delbo', M., Carry, B., Hanuš, J., & Alí-Lagoa, V. 2017, A&A, 604, A27, doi: 10.1051/0004-6361/201730868

Ďurech, J., Hanuš, J., & Vančo, R. 2019, A&A, 631, A2, doi: 10.1051/0004-6361/201936341

Ďurech, J., Sidorin, V., & Kaasalainen, M. 2010, A&A, 513, A46, doi: 10.1051/0004-6361/200912693

Ďurech, J., Kaasalainen, M., Herald, D., et al. 2011, Icarus, 214, 652, doi: 10.1016/j.icarus.2011.03.016

Dziadura, K., Oszkiewicz, D., Spoto, F., et al. 2023, A&A, 680, A77, doi: 10.1051/0004-6361/202347342

Elliot, J. L., Dunham, E., & Mink, D. 1977, Nature, 267, 328, doi: 10.1038/267328a0

Elliot, J. L., Dunham, E. W., Bosh, A. S., et al. 1989, Icarus, 77, 148, doi: 10.1016/0019-1035(89)90014-6

Elvis, M. 2014, Planet. Space Sci., 91, 20, doi: 10.1016/j.pss.2013.11.008

Fenucci, M., Micheli, M., Gianotto, F., et al. 2024, A&A, 682, A29, doi: 10.1051/0004-6361/202347820

Fienga, A., Avdellidou, C., & Hanuš, J. 2020, MNRAS, 492, 589, doi: 10.1093/mnras/stz3407

Gaia Collaboration, Brown, A. G. A., Vallenari, A., Prusti, T., et al. 2018, A&A, 616, A1, doi: 10.1051/0004-6361/201833051

Gaia Collaboration, Prusti, T., de Bruijne, J. H. J., Brown, A. G. A., et al. 2016, A&A, 595, A1, doi: 10.1051/0004-6361/201629272

Gaia Collaboration, Vallenari, A., Brown, A. G. A., Prusti, T., et al. 2023, A&A, 674, A1, doi: 10.1051/0004-6361/202243940

Gault, D., Nosworthy, P., Nolthenius, R., Bender, K., & Herald, D. 2022, Minor Planet Bulletin, 49, 3

Gillon, M., Jehin, E., Magain, P., et al. 2011, in European Physical Journal Web of Conferences, Vol. 11, European Physical Journal Web of Conferences, 06002, doi: 10.1051/epjconf/20101106002

Goldstein, R. M. 1968, Science, 162, 903, doi: 10.1126/science.162.3856.903

Hanuš, J., Delbo', M., Ďurech, J., & Alí-Lagoa, V. 2015, Icarus, 256, 101, doi: 10.1016/j.icarus.2015.04.014

Hanuš, J., Ďurech, J., Brož, M., et al. 2011, A&A, 530, A134, doi: 10.1051/0004-6361/201116738

Hapke, B. 1981, J. Geophys. Res., 86, 3039, doi: 10.1029/JB086iB04p03039

—. 1984, Icarus, 59, 41, doi: 10.1016/0019-1035(84)90054-X

—. 1986, Icarus, 67, 264, doi: 10.1016/0019-1035(86)90108-9

Hapke, B., & Wells, E. 1981, J. Geophys. Res., 86, 3055, doi: 10.1029/JB086iB04p03055

Harris, A. W. 1998, Icarus, 131, 291, doi: 10.1006/icar.1997.5865

Hasegawa, S., Marsset, M., DeMeo, F. E., et al. 2021, ApJ, 916, L6, doi: 10.3847/2041-8213/ac0f05

Hein, A. M., Matheson, R., & Fries, D. 2020, Acta Astronautica, 168, 104, doi: 10.1016/j.actaastro.2019.05.009

Herald, D., Gault, D., Anderson, R., et al. 2020, MNRAS, 499, 4570, doi: 10.1093/mnras/staa3077

Herald, D., Gault, D., Carlson, N., et al. 2024, Small Bodies Occultations Bundle V4.0, NASA Planetary Data System, urn:nasa:pds:smallbodiesoccultations::4.0, doi: 10.26033/ehqs-jp27

Hudson, R. S., & Ostro, S. J. 1994, Science, 263, 940, doi: 10.1126/science.263.5149.940

—. 1995, Science, 270, 84, doi: 10.1126/science.270.5233.84

Hung, D., Hanuš, J., Masiero, J. R., & Tholen, D. J. 2022, PSJ, 3, 56, doi: 10.3847/PSJ/ac4d1f

Ivezić, Ž., Kahn, S. M., Tyson, J. A., et al. 2019, ApJ, 873, 111, doi: 10.3847/1538-4357/ab042c

Iye, M. 2021, Proceedings of the Japan Academy, Series B, 97, 337, doi: 10.2183/pjab.97.019

Kaasalainen, M. 2011, Inverse Problems and Imaging, 5, 37, doi: 10.3934/ipi.2011.5.37

Kaasalainen, M., & Lamberg, L. 2006, Inverse Problems, 22, 749, doi: 10.1088/0266-5611/22/3/002

Kaasalainen, M., Lamberg, L., Lumme, K., & Bowell, E. 1992, A&A, 259, 318

Kaasalainen, M., & Torppa, J. 2001, Icarus, 153, 24, doi: 10.1006/icar.2001.6673

Kaasalainen, M., Torppa, J., & Muinonen, K. 2001, Icarus, 153, 37, doi: 10.1006/icar.2001.6674

Kargel, J. S. 1994, J. Geophys. Res., 99, 21129, doi: 10.1029/94JE02141

Kretlow, M. 2022, A&A, 668, A141, doi: 10.1051/0004-6361/202243968

Lagerros, J. S. V. 1996a, A&A, 310, 1011

—. 1996b, A&A, 315, 625

Lagerros, J. S. V. 1997, in AAS/Division for Planetary Sciences Meeting Abstracts, Vol. 29, AAS/Division for Planetary Sciences Meeting Abstracts #29, 07.23

Lagerros, J. S. V. 1998, A&A, 332, 1123

Lambert, J. H. 1892, Photometria, sive De mensura et gradibus luminus, colorum et umbrae (Leipzig: W. Engelmann)

Lauretta, D. S., Balram-Knutson, S. S., Beshore, E., et al. 2017, Space Sci. Rev., 212, 925, doi: 10.1007/s11214-017-0405-1

Lauretta, D. S., DellaGiustina, D. N., Bennett, C. A., et al. 2019, Nature, 568, 55, doi: 10.1038/s41586-019-1033-6

Lebofsky, L. A., Sykes, M. V., Tedesco, E. F., et al. 1986a, Icarus, 68, 239, doi: 10.1016/0019-1035(86)90021-7

—. 1986b, Icarus, 68, 239, doi: 10.1016/0019-1035(86)90021-7

Lellouch, E., Santos-Sanz, P., Lacerda, P., et al. 2013, A&A, 557, A60, doi: 10.1051/0004-6361/201322047

Levenberg, K. 1944, Quarterly of Applied Mathematics, 2, 164, doi: 10.1090/qam/10666

Liberato, L., Tanga, P., Mary, D., et al. 2024, A&A, 688, A50, doi: 10.1051/0004-6361/202349122

Lommel, E. 1889, Annalen der Physik, 272, 473, doi: 10.1002/andp.18892720211

Mainzer, A., Bauer, J., Grav, T., et al. 2011, ApJ, 731, 53, doi: 10.1088/0004-637X/731/1/53

Marciniak, A., Pilcher, F., Oszkiewicz, D., et al. 2015, Planet. Space Sci., 118, 256, doi: 10.1016/j.pss.2015.06.002

Marciniak, A., Ďurech, J., Alí-Lagoa, V., et al. 2021, A&A, 654, A87, doi: 10.1051/0004-6361/202140991

Marciniak, A., Ďurech, J., Choukroun, A., et al. 2023, A&A, 679, A60, doi: 10.1051/0004-6361/202346191

Marciniak, A., Choukroun, A., Perła, J., et al. 2025, PSJ, 6, 60, doi: 10.3847/PSJ/adb28b

Marquardt, D. W. 1963, Journal of the Society for Industrial and Applied Mathematics, 11, 431, doi: 10.1137/0111030

McCord, T. B., & Chapman, C. R. 1975a, ApJ, 195, 553, doi: 10.1086/153355

—. 1975b, ApJ, 197, 781, doi: 10.1086/153565

Milliken, R. E., & Rivkin, A. S. 2009, Nature Geoscience, 2, 258, doi: 10.1038/ngeo478

Minkowski, H. 1903, Mathematische Annalen, 57, 447, doi: 10.1007/BF01445180

Moorwood, A. F. M. 2008, in Society of Photo-Optical Instrumentation Engineers (SPIE) Conference Series, Vol. 7014, Ground-based and Airborne Instrumentation for Astronomy II, ed. I. S. McLean & M. M. Casali, 701403, doi: 10.1117/12.786545

Morbidelli, A., Bottke, W. F., Nesvorný, D., & Levison, H. F. 2009, Icarus, 204, 558, doi: 10.1016/j.icarus.2009.07.011

Morgado, B. E., Sicardy, B., Braga-Ribas, F., et al. 2023, Nature, 614, 239, doi: 10.1038/s41586-022-05629-6

Mueller, T., Marciniak, A., Bartczak, P., et al. 2016, in 41st COSPAR Scientific Assembly, Vol. 41, B0.4–72–16

Müller, T., Lellouch, E., & Fornasier, S. 2020, in The Trans-Neptunian Solar System, ed. D. Prialnik, M. A. Barucci, & L. Young, 153–181, doi: 10.1016/B978-0-12-816490-7.00007-2

Nesvorný, D., Jedicke, R., Whiteley, R. J., & Ivezić, Ž. 2005, Icarus, 173, 132, doi: 10.1016/j.icarus.2004.07.026

Neugebauer, G., Habing, H. J., van Duinen, R., et al. 1984, ApJ, 278, L1, doi: 10.1086/184209

Ortiz, J. L., Santos-Sanz, P., Sicardy, B., et al. 2017, Nature, 550, 219, doi: 10.1038/nature24051

Ostro, S. J. 1993, Reviews of Modern Physics, 65, 1235, doi: 10.1103/RevModPhys.65.1235

Ostro, S. J., Hudson, R. S., Benner, L. A. M., et al. 2001, Meteorit. Planet. Sci., 36, 1225, doi: 10.1111/j.1945-5100.2001.tb01956.x

Ostro, S. J., Hudson, R. S., Nolan, M. C., et al. 2000, Science, 288, 836, doi: 10.1126/science.288.5467.836

Pajuelo, M., Birlan, M., Carry, B., et al. 2018, MNRAS, 477, 5590, doi: 10.1093/mnras/sty1013

Pinilla-Alonso, N., Stansberry, J. A., & Holler, B. J. 2020, in The Trans-Neptunian Solar System, ed. D. Prialnik, M. A. Barucci, & L. Young, 395–412, doi: 10.1016/B978-0-12-816490-7.00018-7

Povenmire, H. 2001, Meteoritics and Planetary Science Supplement, 36, A165

Pravec, P., Harris, A. W., & Michalowski, T. 2002, in Asteroids III, ed. W. F. Bottke, Jr., A. Cellino, P. Paolicchi, & R. P. Binzel, 113–122

Pérez-Hernández, J. A., & Benet, L. 2022, Communications Earth & Environment, 3, 10, doi: 10.1038/s43247-021-00337-x

Raducan, S. D., Jutzi, M., Cheng, A. F., et al. 2024, Nature Astronomy, 8, 445, doi: 10.1038/s41550-024-02200-3

Reddy, V., Kelley, M. S., Dotson, J., et al. 2022, PSJ, 3, 123, doi: 10.3847/PSJ/ac66eb

Ricker, G. R., Winn, J. N., Vanderspek, R., et al. 2015, Journal of Astronomical Telescopes, Instruments, and Systems, 1, 014003, doi: 10.1117/1.JATIS.1.1.014003

Rivkin, A. S., Howell, E. S., Vilas, F., & Lebofsky, L. A. 2002, in Asteroids III, ed. W. F. Bottke, Jr., A. Cellino, P. Paolicchi, & R. P. Binzel, 235–253

Rommel, F. L., Braga-Ribas, F., Ortiz, J. L., et al. 2023, A&A, 678, A167, doi: 10.1051/0004-6361/202346892

Rubashevskii, A. A. 1966, Soviet Ast., 10, 124

Russell, H. N. 1906, ApJ, 24, 1, doi: 10.1086/141361

Shahid-Saless, B., & Yeomans, D. K. 1994, AJ, 107, 1885, doi: 10.1086/116999

Shober, P. M., Devillepoix, H. A. R., Vaubaillon, J., et al. 2025, Nature Astronomy, 9, 799, doi: 10.1038/s41550-025-02526-6

Sonter, M. J. 1997, Acta Astronautica, 41, 637, doi: 10.1016/S0094-5765(98)00087-3

Souami, D., Desmars, J., Tanga, P., et al. 2023, in LPI Contributions, Vol. 2851, Asteroids, Comets, Meteors Conference, 2099

Szakáts, R., Müller, T., Alí-Lagoa, V., et al. 2020, A&A, 635, A54, doi: 10.1051/0004-6361/201936142

Tanga, P., Pauwels, T., Mignard, F., et al. 2023, A&A, 674, A12, doi: 10.1051/0004-6361/202243796

Tholen, D. J. 1984, PhD thesis, University of Arizona

Tonry, J. L., Denneau, L., Heinze, A. N., et al. 2018, PASP, 130, 064505, doi: 10.1088/1538-3873/aabadf

Tsuda, Y., Yoshikawa, M., Saiki, T., Nakazawa, S., & Watanabe, S.-i. 2019, Acta Astronautica, 156, 387, doi: 10.1016/j.actaastro.2018.01.030

Usui, F., Kuroda, D., Müller, T. G., et al. 2011, PASJ, 63, 1117, doi: 10.1093/pasj/63.5.1117

Vinogradova, T. A., Kochetova, O. M., Chernetenko, Y. A., Shor, V. A., & Yagudina, E. I. 2008, Solar System Research, 42, 271, doi: 10.1134/S0038094608040011

Vokrouhlický, D., Bottke, W. F., Chesley, S. R., Scheeres, D. J., & Statler, T. S. 2015, in Asteroids IV, ed. P. Michel, F. E. DeMeo, & W. F. Bottke, 509–531, doi: 10.2458/azu_uapress_9780816532131-ch027

von Oppolzer, E. 1901, Astronomische Nachrichten, 154, 309, doi: 10.1002/asna.19001541604

Walker, R. G. 2003, in AAS/Division for Planetary Sciences Meeting Abstracts, Vol. 35, AAS/Division for Planetary Sciences Meeting Abstracts #35, 34.19

Walsh, K. J., Morbidelli, A., Raymond, S. N., O'Brien, D. P., & Mandell, A. M. 2011, Nature, 475, 206, doi: 10.1038/nature10201

Warner, B. D., Harris, A. W., & Pravec, P. 2009, Icarus, 202, 134, doi: 10.1016/j.icarus.2009.02.003

Watanabe, S.-i., Tsuda, Y., Yoshikawa, M., et al. 2017, Space Sci. Rev., 208, 3, doi: 10.1007/s11214-017-0377-1

Wilawer, E., Oszkiewicz, D., Kryszczyńska, A., et al. 2022, MNRAS, 513, 3242, doi: 10.1093/mnras/stac1008

Wizinowich, P. L., Le Mignant, D., Bouchez, A. H., et al. 2006, PASP, 118, 297, doi: 10.1086/499290

Wright, E. L., Eisenhardt, P. R. M., Mainzer, A. K., et al. 2010, AJ, 140, 1868, doi: 10.1088/0004-6256/140/6/1868

Yoshida, F., Hayamizu, T., Miyashita, K., et al. 2023, PASJ, 75, 153, doi: 10.1093/pasj/psac096

Zellner, B., Tholen, D. J., & Tedesco, E. F. 1985, Icarus, 61, 355, doi: 10.1016/0019-1035(85)90133-2

ACTA ASTRONOMICA
Vol. **0** (0) pp. 0–0

STEROID: A python package to automatise asteroid and star photometry

A. Choukroun , K. Kamiński and A. Marciniak

Astronomical Observatory Institute, Faculty of Physics and Astronomy, Adam Mickiewicz University, Słoneczna 36, 60-286 Poznań, Poland.
e-mail:antoine.choukroun@amu.edu.pl

Received Month Day, Year

ABSTRACT

Multiple areas involving photometric studies experience a flood of raw telescopic data, that need to be processed automatically. Although many software solutions exist, few of them are capable of making automated detection and precise measurements of moving targets.

In this study we developed a modular package to automate photometric procedures in Python. Our package can reduce image frames, estimate drift and rotation between the frames, and/or perform aperture photometry for accurate lightcurves. We also integrated tools for detecting and tracking moving objects, particularly asteroids. Utilizing this package, we processed a large volume of data, extracting over a hundred asteroid lightcurves, validating its robustness.

Key words: *Photometry — Package — Python — Asteroids*

1. Introduction

The advent of large, telescopic surveys, but also automatisation of ground-based telescopes result in unprecedentedly large amounts of imaging data. Such raw data need to be corrected (reduced) for instrumental effects, and measured for a photometric measurement. Automated aperture photometry, although simple in principle (Howell 1989), often requires overcoming many adversities, like field drift and rotation during the observing sequence. The issue becomes even more complex if moving objects, like asteroids, are studied. Their movement against the star background challenges their measurements, because apertures need to be shifted accordingly, also their brightness can get distorted when when passing close to background stars.

In response to these challenges, we developed a photometric analysis package named STEROID. It aims to be modular, easily adaptable, efficient to run, able to deal with substantial image drifts and rotations, independent on plate solving, automatically detects slowly moving objects (asteroids) which are present in most

of the analyzed images, automatically deal with potential target and star field image blending and freely available to the community.

Certain tools already exist (see for example Photometry Pipeline: Mommert (2017), a pipeline by Ofek et al. (2023), TSD-YOLOv4 coupled with TSCNet classifier: Shi et al. (2022) or PRAIA by Assafin (2023)), but we found them missing in certain of important areas depending to the tool. Some algorithms are unable to detect moving objects, while others can only identify those previously cataloged in a database. Furthermore, the detection sensitivity may be insufficient for faint targets. Moreover, these tools are often highly specialized within their respective domains, which limits their adaptability and prevents other fields of research from benefiting from their advancements.

It is noteworthy that many of existing photometric tools rely on plate solving for positioning photometric apertures. While this approach has its advantages, it is not flawless. Blind plate solving requires significant processing power, often disregards some subtle effects such as differential atmospheric refraction, higher order optical distortions or differential atmospheric dispersion. Many of them also require an a priori knowledge of accurate targets coordinates, which limits the analysis to well known objects.

In this work we provide a detailed description of our algorithm and example lightcurves processed exclusively with our package, from raw images to final curves. The Discussion section addresses strengths, weaknesses, and potential improvements, concluding with a summary of STEROID's capabilities in the Conclusions section. Because of its open nature we anticipate future improvements, as elaborated further in the Discussion section. We will maintain an updated description of the current design and provide documentation on the GitHub page: `https://github.com/antoinech13/Steroid` (antoinech13 (2022)).

2. SPECIFICATIONS AND STRUCTURE

STEROID is written in Python using the following external libraries: numpy, matplotlib, scipy, tensorflow, pandas, opencv, astropy and photutils. The general structure with the software is presented in Fig. 1 or in the GitHub repository.

One of the main ideas of STEROID is to be modular. Main modules have clearly defined inputs, outputs and configuration, and can be used independently of others. Therefore, each block of code can be imported into independent projects according to user needs, allowing them to build their own pipeline. In our work we were focused on asteroids, therefore we used STEROID's blocks to build our pipeline, which is also available in STEROID and which can be use as an example and starting point for other projects. This pipeline is stored in *photometry.py* file. Our pipeline requires a series of images in FITS format containing at least several common stars in all images. Bias, dark and flat images can also be provided, but already reduced FITS images can also be used. For the photometry, we used photutil

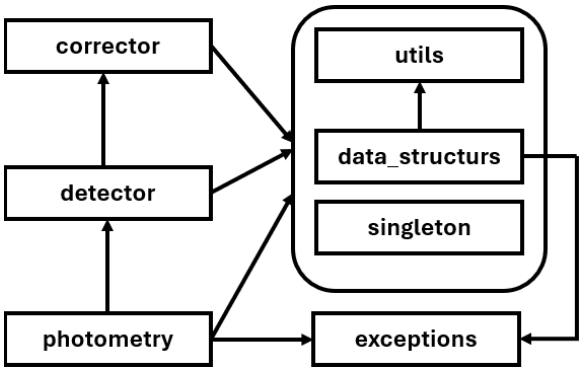

Figure 1: Main components of STEROID package (blocks) and typical photometric data processing flow (arrows).

however other photometric libraries can also be easily integrated.

STEROID provides multiple classes. A description of them as well as their methods can be find on the GitHub page. However the most important ones are the following classes: - The class *Corrector* to correct images from image drifts and rotations - The class *Detector* to detect moving objects - The class *Fit* which manage individual images - The static class *Utils* which provide multiple usefull methods. The principles of algorithms behind these methods are described in the section 4.

3. IMAGE INTERPOLATION

Telescope tracking is seldom perfect, resulting in misalignment or "drift" between consecutive images of the same field. There may also be a rotational misalignment between images, especially for horizontal mounts. Therefore, it is crucial for the code to estimate both the drift and rotation angle for each image regardless of its source. Common image processing software addresses this issue with data interpolation algorithms (see Danielsson & Hammerin (1992)). Each interpolation introduces errors as is demonstrated in Table. 1. A test image was rotated by several interpolation methods: nearest-neighborhood, bilinear, bicubic and adaptive and each time aperture photometry with identical apertures was obtained.

It is clearly visible that pixel interpolation can influence the quality of photometry at the level of about 0.1 mag for the simplest interpolation and about 0.01 mag for the most sophisticated interpolation method tested. Therefore our algorithm deals with image shifts and rotation without any pixel manipulation, only by carefully calculating aperture positions.

T a b l e 1

Errors in aperture photometry from bright stars in images obtained by different interpolation methods.

	average difference [mag]	RMS [mag]
Original (reference)	0	0
nearest-neighborhood	-0.0175	0.099
bilinear	-0.01	0.015
bicubic	-0.005	0.018
biquadratic	-0.005	0.018
adaptative	-0.0125	0.013

4. ALGORITMS

4.1. Detection

The detection process can be cut in two steps: the first one to binarise images in order to detect objects and to isolate them from the background (cf. Garg & Garg (2013)). During that process each pixel above a selected threshold is assigned a value of 1 while other pixels are set to 0. The second step is to determine the centers of all objects detected during the binarisation step.

4.1..1 Binarisation

The general idea of binarisation algorithm can be found in the literature (see Bertin & Arnouts (1996), or Bradley et al. (2023)). The main difference in our approach comes from our way to automatically estimate a signal threshold value.

Following our empirical investigations, the decision was made to establish the threshold value based on the inflection point present on the logarithmically transformed histogram (cf. Figure 2). This approach improves object detection accuracy, basing on the inherent characteristics of the signal distribution.

To determine the position of the deflection point in the image intensity histogram we model it as a superposition h(ADU) = o(ADU) + n(ADU) of density function characterizing signal from objects o(ADU) and density function associated with noise inherent to the frame n(ADU). To model the histogram, we combine the logarithm of a Gaussian (for the noise part of the histogram) plus a linear equation (for the signal part of the histogram). Fig. 2 presents and example fit of h(ADU) function to a histogram of a star field image. Such a simple approach is sufficient to estimate the ADU value of the histogram deflection point and determine binarisation threshold with high accuracy. If non-gaussian noise is dominant or signal distribution is atypical other functions can be used instead. Fig. 3 shows a comparison of binarisation using common threshold of median + standard deviation and our histogram modeling method. It is clearly visible that our approach

results in detection of more stars.

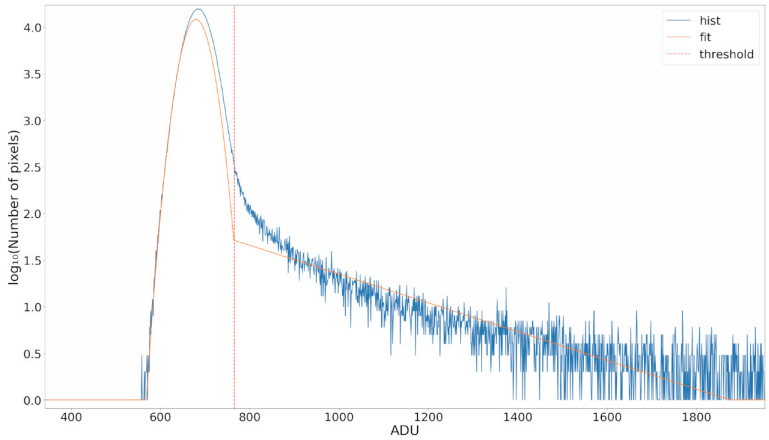

Figure 2: Blue curve: logarithmic histogram of an image signal. Orange curve: fit to the blue curve. As can be seen, the model is able to find the point where the slope is changing (visible on the orange curve as the fast oscillation intersecting the data on the red point).

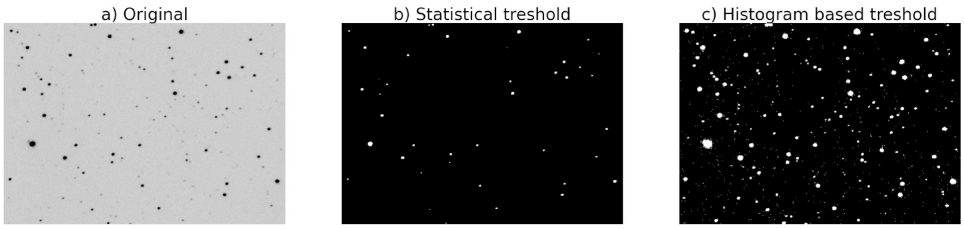

Figure 3: a):A zoom in an original image of a random star field. b) and c): Binarised image a) using two different techniques for threshold signal (standard statistics and slope break technique, respectively).

4.1..2 Determination of objects position

STEROID uses a method close to Modified Moments, suggested in Stone (1989). Modified Moments technique uses a threshold level to determine which pixels should be included or excluded from the computation by applying value 0 to all pixels below that threshold. This approach helps to mitigate the influence of background noise and ensures more accurate moment calculations. STEROID applies a modification to Stone's approach by using only pixels from a contour of a particular object of the binarised image. Our approach have two major advantages which improve performances: The first advantage is using a contour detection algorithm

on binarised images will, by nature, isolate each objects to each other. The second advantage is that, as each contour is closed and $\mathcal{C}^1$ by parts, it is possible, via Green's theorem (Green 2008, Yang & Albregtsen 1996), to change double integral (double sum) at the surface of the image for each objects into one integral along contours. The importance of determining the threshold, as explained in Section 4.1..1, becomes clear here: the more accurately the threshold is estimated, the more objects will be detected. Another significant advantage of using contours instead of directly calculating image moments is evident in cases where the object's signal is asymmetric and the highest ADU pixel is not centrally located. In such situations, the computed centroid may also be off-center, leading to suboptimal aperture placement. By using contours defined by a threshold, the centroid is calculated within an iso-intensity boundary, which helps ensure it is centered on the actual signal distribution, thereby maximizing the signal-to-noise ratio (SNR) when used to determine aperture positions.

Currently, our algorithm does not use any deblending of merged images. This is done for two reasons. For star background matching blended images are as good as deblended images, for targets we decided to disregard such photometry because of its lower quality.

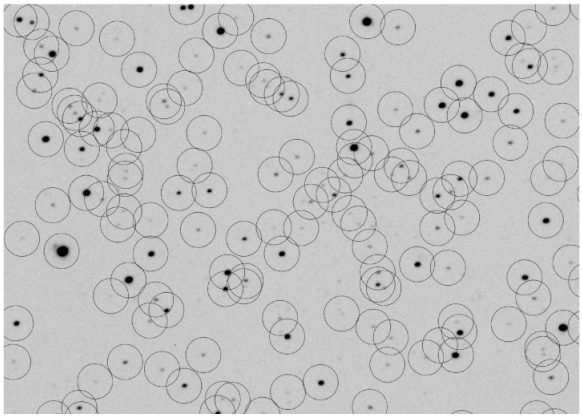

Figure 4: Detected object centers (cirlces) overploted on original image.

4.2. Frame correction: pattern recognition

We assume that most objects (stars) in the field of view have undetectable low proper motion and that at least a fraction of them is recorded in a sequence of images which are being analyzed. Our algorithm is looking for repeatable star patterns and uses them to determine relative image shifts and rotation.

4.2..1 Building Patterns

The following procedure is used for building patterns composed of groups of 5 close stars.

- Select the first star of the initial frame: determine centroids of all objects in the first frame using procedure described in section 4.1. and store them in an array. The first one is used as a starting point for pattern creation.
- Determine four nearest stars: Locate four stars closest to the selected star. This step defines the group of stars included in the initial pattern.
- Construct triangles using these five stars: Utilize these five stars to form five distinct triangles, then store them in a dedicated object called "pattern".
- Repeat the process for each detected star on the first frame: Iterate this process for every star detected in the image, creating a list of patterns for the image.
- Iterate this process for each frame in the sequence: Apply this process to each frame in the sequence, generating a series of patterns for each image.

The decision to construct patterns using five stars stems from the fact that smaller number of stars significantly increases the probability of false positive identification of such pattern. This is partly due to the fact that we intentionally select nearby stars to increase the probability of finding the same pattern even when large drift is observed. Therefore relative position errors are larger than for patterns composed from more distant stars. It also decreases the influence of false positive detection of stars to the pattern recognition process. Illustration of pattern creation is presented in Fig. 5.

4.2..2 Evaluation of the field position correction

Once the algorithm completes the pattern construction process for each frame, the subsequent step involves comparing these patterns to those from the initial frame of the sequence. Identifying identical stars between the first and the ith frame, where $i \in N$ and N represents the total number of frames in the sequence, relies on the assumption that stars in a pattern are stored in the same order as in the first image. Identifying identical patterns between images comes down to comparison of pixel

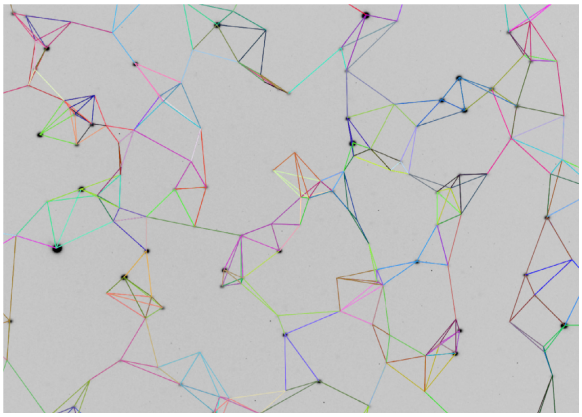

Figure 5: Same image as in Figure 3, and in Figure 4, with all the patterns built by the algorithm. Colour code is used to distinguish patterns. Patterns on borders are cut because this image is a zoom of a bigger image

distances between the different sides of the triangles that form the pattern. If they are all identical within a margin of ε (which have a default value set to 2 pixels in STEROID), then the two patterns are considered identical.

To calculate the angle of rotation between two images all cross-idetified star pairs are used to construct vectors. A median angle and direction between all corresponding vectors, which are composed of the same stars, are calculated using inner and cross products.

Subsequently, after correcting for image rotation, the median value of pixel position differences Δx and Δy drifts are evaluated between the corresponding stars in the first image and the ith image.

4.3. Moving objects detection

The method used in STEROID involves selecting one frame from the beginning and another from the end of the sequence, and comparing the positions of objects (after correction for frame rotation and drift) in both images. Any object present at position P_i in the initial frame, but absent in the second one, can be classified as a potential moving object (PMO). Subsequently, we employed additional algorithms, such as a convolutional neural network (CNN), to identify false detections and find moving objects (MO).

Procedure

The MO detection algorithm works as follows:

- Find two similar images: one at the beginning and one at the end of the sequence (the definition of "similar images" will be described later).
- Compare pixel positions of all objects in the second frame with those in the

first frame. If an object from the first frame is not found at the same position in the second frame, classify it as a potential moving object (PMO).

- To classify PMOs as either moving objects (MOs) or false positives, extract a crop from the first frame, spanning approximately 10 to 20 pixels around each PMO. Repeat the process at the same position in the second frame. The rationale behind this approach is that after correction for rotation and drift, stars should consistently occupy the same position in all the frames. Therefore, if a star was detected as a PMO due to not behing detected on one images (see Figure 6), the crops made at the same position on both frames should have this star in both of them.

- For all crops, pass the crop from the first frame through a simple convolutional neural network (CNN) for binary classification (identifying whether there are any objects). Repeat the process for the corresponding crop from the second frame. If an object is detected in the crop from the first image, but not the second, the PMO can be classified as a MO. If an object is present in both crops, the PMO can be classified as a false positive (e.g hot pixel).

Using the first and the last image of a long series is not always optimal for target detection. Due to multiple causes (twilight, cloud passages, seeing changes...), the SNR (signal to noise ratio) can change substantially during the series. The consequences of this is, first: the number of objects detected on these two frames will not be representative of the average number of detected objects on each frame of the sequence, and second: the number of objects detected on the first frame can be substantially different from that on the last one. So, we make sure to select two frames which have high and similar number of detected objects (see Figure 6). By doing that we reduce the number of PMOs and, at the same time, reduce the computational time and potential false detections.

4.3..1 Classification of PMOs

We developed and trained a simple CNN based on the AlexNet architecture (Krizhevsky et al. 2012) to facilitate the classification of frames based on the presence or absence of objects. If the object is absent in the second frame, it is classified as a MO; if it remains in the same position, it is considered a static object.

To train the network, we manually cropped 8588 objects and background from various images. This approach allows the CNN to learn to classify presence or lack of objects in the cropped images. Consequently, the CNN is trained not only to recognize objects but also to find object-free regions. 80% of this dataset was utilized as the training set, while the remaining 20% was allocated to a validation set. The datasets were randomly partitioned to mitigate the risk of overfitting. Additionally, 85 more crops with labels were included as a test set. Following the training process, the algorithm achieved a good F1 score of 99% (see Table 2).

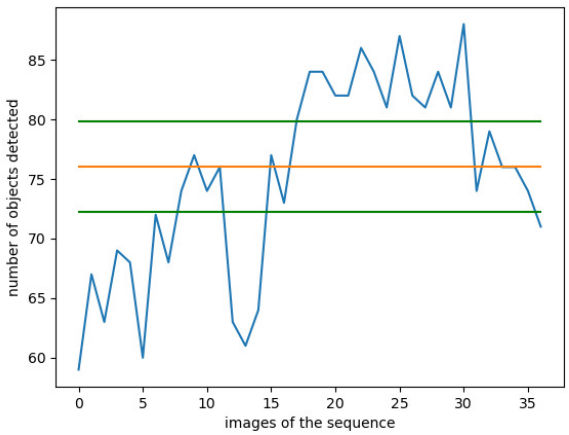

Figure 6: Changes in number of detected objects along a sequence of example images. The orange line corresponds to the median. Green lines correspond to median $\pm$ 5%. The first frame selected for defining the field shift is frame number 8 and the second one is number 35.

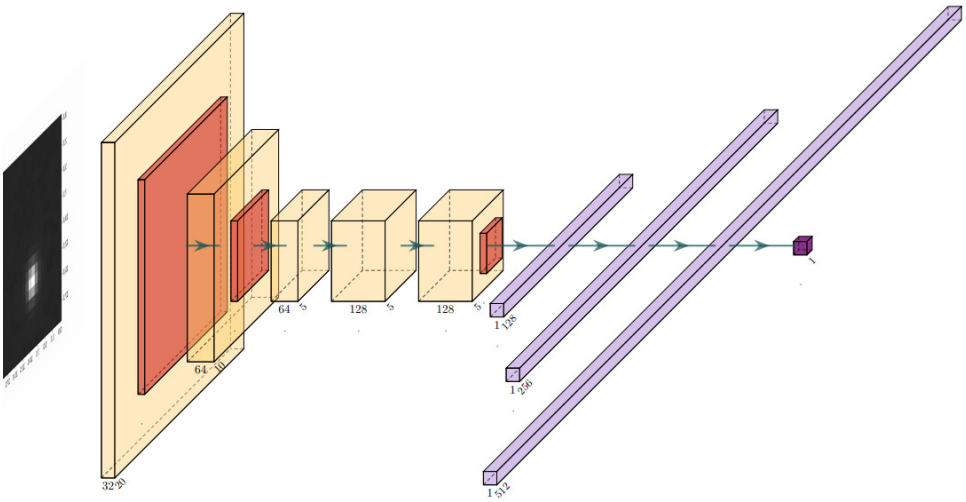

Figure 7: CNN based on the AlexNet Architecture. Input image should be a crop of a maximum of 20x20 pixels. The output is simply a boolean. If an object is present on input image (as here), the output will be true. If no object is present, the output should be false. Orange boxes are convolutional layers and red ones represent max pooling. Violet colour denotes dense, fully connected layers and the last box represents the output classification layer. Numbers under the corner of boxes represent the width and height of the layer. Numbers under the boxes represent the channel (example: the first layer is (20 x 20 x 32)).

T a b l e 2

Results of neural network training. "Crop empty" line presents classification result of background crops (without any objects). "Object present" line is the same for crops with objects.

	precision	**recall**	**F1-score**
Crop empty	1	0.98	0.99
Object present	0.98	1	0.99

Despite the good results of the CNN, it does not score perfectly. It is for this reason that all previous steps are important. Reducing the number of PMOs also reduces the number of errors (1% of 100 PMO is still higher than 1% of 10).

4.4. Full width at half maximum (FWHM) estimation

The algorithm for automatic determination of FWHM works as follows: This algorithm, is needed for automatic determination of the aperture size. It works as follows: for each star of interest, locate the pixel $\{P(i_0, j_0) \mid i_0 \in X \wedge j_0 \in Y\}$ with the maximum value MAX, then scan along the x and y axes around it to identify pixels such as

$$\begin{cases} \{P(i, j_0) \mid P(i, j_0) \geq \frac{MAX}{2} \wedge P(i \pm 1, j_0\} < \frac{MAX}{2}\} \\ \{P(i_0, j) \mid P(i_0, j) \geq \frac{MAX}{2} \wedge P(i_0, j \pm 1\} < \frac{MAX}{2}\}, \end{cases} \tag{1}$$

In the Discussion section, we describe potential enhancements to make this algorithm more accurate.

4.5. Star passages

When working with Moving Objects (MOs), it is quite likely that along the on-sky path of the target, there may appear static objects, primarily stars, which can temporarily interfere with the photometric measurements. STEROID automatically detects such situations to avoid performing photometry on such frames to prevent introducing errors into the lightcurves. For each MO it first filters the detected stars to those close to the object's path. This is done by identifying stars that lie within a box surrounding the MO's trajectory. It then compares the positions of these stars with the position of the object in each frame. The advantage of this approach is that, instead of comparing the MO's position with all detected stars in each frame—which has a computational complexity of $N_s \times N_o \times N_i$, where N_s is the number of detected stars, N_o the number of MOs and N_i is the number of images—the code only compares MO positions with stars within the defined box. This reduces the complexity to $N_{sb} \times N_o \times N_i$, where N_{sb} is the number of stars inside the box. Since $N_{sb} \ll N_s$ ((typically fewer than 3, whereas N_s can reach several hundreds), the performance is significantly improved.

Constructing the box is a key step in the algorithm. It must be placed around the MO's path and oriented in the same direction. In the code, the box is built analytically by solving the following system:

$$\begin{cases} A_y = -\frac{A_x}{a} + b \\ (P_x - A_x)^2 + (P_y - A_y)^2 = c \times FWHM, \end{cases} \tag{2}$$

The meaning of the variables P and A is illustrated in Figure 8. The parameter c is adjustable (default value: 3), and a and b are the parameters of the red line shown in the same figure. The first equation corresponds to the blue line in Figure 8, while the second equation represents the green circle.

The analytical solutions of the system described by Equation 2 are as follows:

$$P^1_{xy} = \begin{cases} P^1_x = A_x + 2\sqrt{c \times FWHM \times \frac{a^2}{a^2+1}} \\ P^1_y = A_y - \frac{2}{a}\sqrt{c \times FWHM \times \frac{a^2}{a^2+1}} \end{cases} \tag{3}$$

$$P^2_{xy} = \begin{cases} P^2_x = A_x - 2\sqrt{c \times FWHM \times \frac{a^2}{a^2+1}} \\ P^2_y = A_y + \frac{2}{a}\sqrt{c \times FWHM \times \frac{a^2}{a^2+1}}, \end{cases} \tag{4}$$

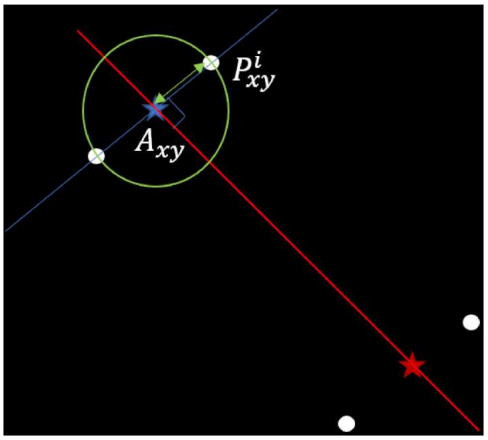

Figure 8: Explanatory diagram of the box construction process. A_{xy} represents the position of the MO, while P^i_{xy} denotes the position of corner i of the box. The blue star indicates the initial MO position, and the red star indicates the final MO position.

4.6. Photometry

STEROID uses circular apertures to perform automatic, relative (uncalibrated) photometry. Target aperture is placed at centroid position and by default has r_{target}

= 2*FWHM radius. Sky annulus has default radius of 1.5*r_{target} and 2*r_{target}. The photometry is managed by the photutils librairy. Input images are assumed to be in ADU. Uncertainties are evaluated following (Merline & Howell 1995):

$$N = \sqrt{N_{source} + n_{pix}(1 + \frac{n_{pix}}{n_B})(N_S + N_D + N_R^2 + G^2\sigma_f^2)}, \tag{5}$$

where N_{source} is the signal from the source, n_{pix} is the number of pixels in the photometric aperture, n_B is the number of pixels in the background annulus, N_S is the sky background signal, N_D is the dark current, $N_R^2 = (G\sigma_R)^2$ is the variance of the read noise, $G^2\sigma_f^2$ is the variance of the flat-field noise and G is the gain. The determination of the gain and σ_R is based on a linear regression approach of the methode described in (Howell 2006):

$$\sigma^2 = \frac{1}{G}\mu + \sigma_R^2, \tag{6}$$

We define $\sigma^2 = \frac{\text{Var}(F_1 - F_2)}{2}$, where F_1 and F_2 are two flat images. Similarly, we define $\mu = \frac{\langle F_1\rangle + \langle F_2\rangle}{2}$, where $\langle F_1\rangle$ and $\langle F_2\rangle$ are the mean values of the two flat images. The read noise variance is given by $\sigma_R^2 = \frac{\text{Var}(B_1 - B_2)}{2}$, where B_1 and B_2 are two bias images. This procedure is applied in four different scenarios depending on the data provided by the user.

Case 1:

Both flat and bias images are provided. In this case, we directly compute σ_R^2 from the bias images, and use linear regression to determine the gain.

Case 2:

Only flat images are provided. In this case, we cannot directly compute σ_R^2, but we can still calculate σ^2 and μ from the flat images. Then, using linear regression, we can estimate both the gain G and an effective value of σ_R^2. It is important to note that in this case, σ_R^2 does not solely represent the read noise, but also includes other noise sources, leading to lower accuracy.

Case 3:

Only bias images are provided. In this case, we can accurately determine σ_R^2, but not σ^2 or μ, as flat images are unavailable. However, we can still perform a linear regression using equation 6, replacing flat images with source images.

Case 4:

Neither bias nor flat images are provided. In this case, we follow the same approach as in Case 2, but replace flat images with source images.

In the case of differential photometry, the differential light curve is given by $lc_\Delta = lc_{\text{target}} - lc_{\text{ref}}$. The associated uncertainty is given by:

$$N_{\Delta} = \sqrt{N_{\text{target}}^2 + N_{\text{ref}}^2} \tag{7}$$

where lc_{target} and N_{target} are the light curve and the uncertainty of the target, and lc_{ref} and N_{ref} are the light curve and the uncertainty of the reference object.

Optionally user can filter deviating points from a resulting lightcurve and bin the results. Filtering is done by used defined polynomial fit and threshold. Binning is used with user defined time step. Moving average is not used because of the risk of combining distant point in case of large gaps in the lightcurve.

5. RESULTS

In this section, we show an example lightcurve created with our pipeline tailored to asteroids, which is available as the Photometry class for differential photometry.

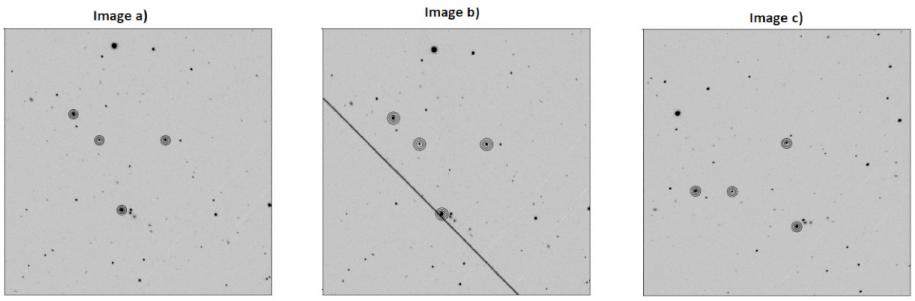

Figure 9: Images taken at different moments of another observing sequence. Image a) shows an asteroid surrounded by three stars chosen as potential reference stars. Image b): another frame from the same sequence, where an artificial satellite crossed the field, passing through the aperture of a reference star. Despite this minor disturbance, the aperture remains centered on the star and does not lose tracking. Image c): similar field as in a) and b), but after rotation and automatic aperture re-centering.

Figure 9 shows three images from a sequence of 34 frames each exposed 300s of the asteroid (901) Brunsia, taken on May 20, 2022 by the 0.7m Roman Baranowski Telescope (RBT) of Astronomical Observatory of Adam Mickiewicz University located in Arizona, USA. As can be seen in the figure, several disturbances occurred during the observation. In image b) a satellite traversed the field through one of apertures. In image c) the field underwent a rotation caused by the filed rotation of alt-az telescope when tracking close to zenith. Despite these a big shift between images and this two events, which could challenge more traditional photometric softwares, the apertures remained well-centered on their targets and were

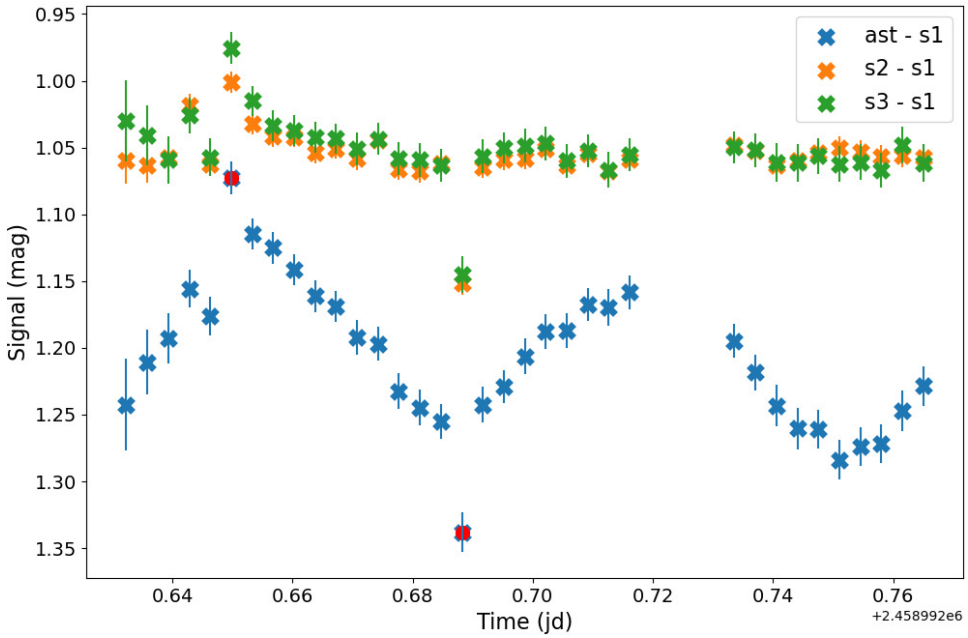

Figure 10: Light curve of asteroid (901) Brunsia produced by our pipeline using STEROID. Blue symbols represent the brightness of the asteroid relative to the main reference star (s1). The other two symbols represent the relative brightness of additional reference stars compared to s1. Red points correspond to data rejected by the outlier removal algorithm. The aperture labeled s1 corresponds to the one affected by a satellite passage, visible in panel b) of Figure 9. $\sigma_{s2-s1} = 0.012$

not disturbed. The satellite passage in image b) create an extreme point in the final lightcurve, but this is effectively handled by the algorithm dedicated to outliers removal as shown on Figure 10. A gap in the lightcurve is also visible around JD 2458992.72. This gap is not caused by the pipeline, it corresponds to the time required for the alt-az telescope had to stop tracking close to zenith. Another example of light curves produced by STEROID can be found in Figures 11 and 12.

Figure 11 shows three images from a sequence of 225 90s frames frames of the asteroid (657) Gunlöd, taken on October 22, 2020. The sequence was acquired by the 0.6m telescope of Mt. Suhora Astronomical Observatory in Poland. This figure is similar to Figure 9. However, in image b), the aperture around the asteroid appears red. This is due to the star passage detection algorithm. This behavior is also visible in Figure 12, which shows the light curve of asteroid (657) Gunlöd. The gap in the light curve is caused by the algorithm flagging and removing data affected by a star passage. Without this correction, the light curve in that region would increase by up to 0.5 magnitudes. Another noteworthy aspect is that, since the asteroid tracking does not rely on aperture centering, it remains unaffected by the brighter star.

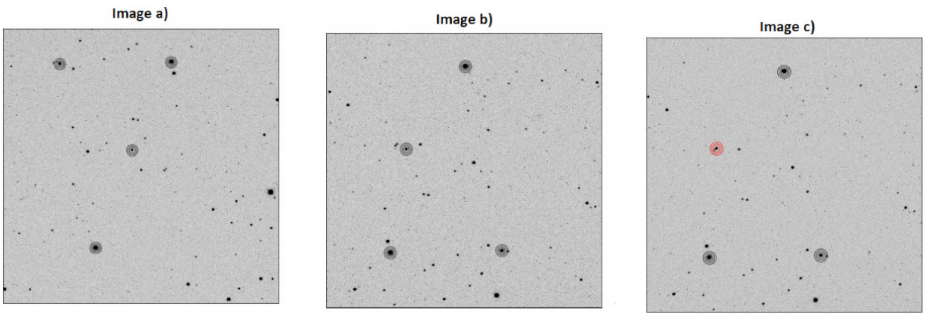

Figure 11: Three different images taken at different moments of the series. a): Image taken at the beginning of the sequence. The topmost aperture marks an asteroid. Three other apertures in the bottom mark reference stars automatically selected by the code. b): Same field after when the asteroid has already moved. The aperture is now red, because the pipeline has detected a star passage. c): Image taken at the end of the sequence.

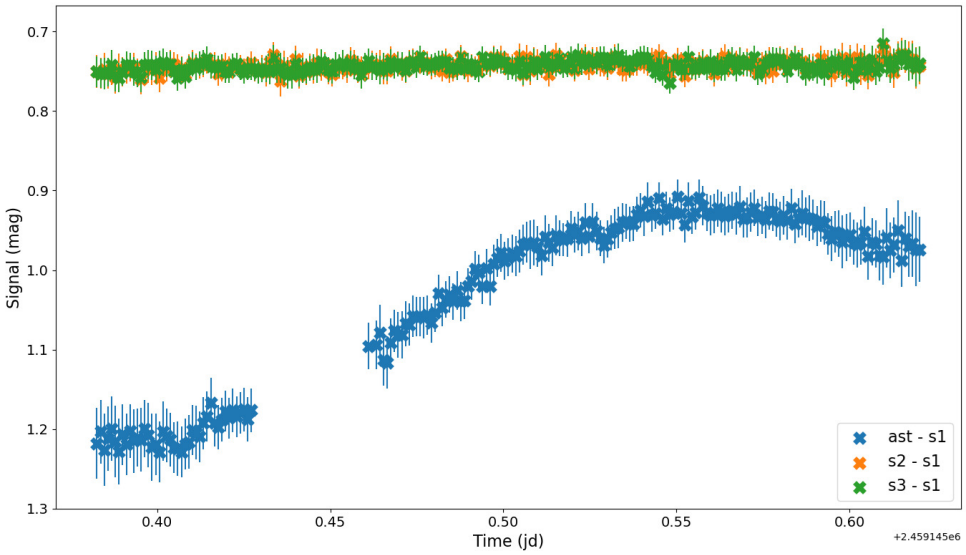

Figure 12: Light curve of asteroid (657) Gunlöd created with our pipeline. Blue symbols represent brightness of asteroid versus main reference star (s1). Two other symbols represent relative brightness of other stars versus main star (based on data published in (Marciniak et al. 2023)). $\sigma_{s2-s1} = 0.004$

The STEROID package demonstrates its ability to produce clean and accurate lightcurves and can properly track reference stars, asteroids, flag star passages, and reject transient disturbances such as Earth satellite trails.

6. DISCUSSION

STEROID was tested on dataset composed of over 110 nights which contained more than 20 000 frames, without counting reduction frames. It worked reliable for images with relatively flat sky background, but exhibited problems in detecting objects in images with severe background variations. This is due to difficulty in estimation of a single threshold for the whole image.

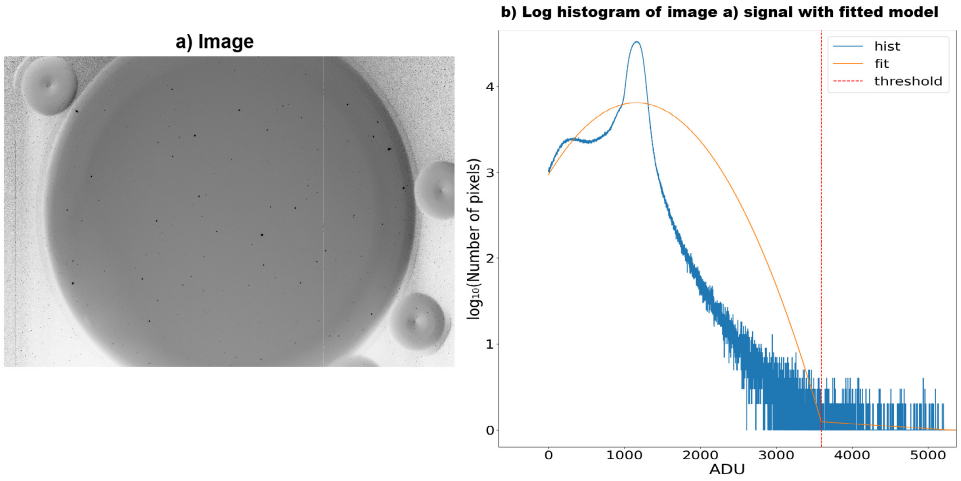

Figure 13: a): An image with faults. These faults might be due to technical problems or numerical failures if the reduction for flat-fields was done with another code that failed, or had poorly adapted parameters. Image b) presents, in blue, the histogram of image a) and, in orange, the model

Figure 13 shows a case that can be problematic for STEROID. Due to multiple flaws of different origins, the histogram significantly deviates from the typical logarithmic shape, as illustrated in Figure 2. In such cases, the threshold determined by STEROID tends to be high in order to avoid detecting noise. However, the user has the option to add an offset to the threshold value and manually adjust the detection level. This feature can be useful if the targets of interest are sufficiently bright. On the other hand, for faint targets, setting the threshold too low may result in the detection of artifacts, which can interfere with proper image correction. For this reason, the offset value can be adjusted dynamically. It can be set higher during the star detection stage in the image correction process, and lowered during the moving object (MO) detection phase. Because of this flexibility in threshold adjustment, evaluating STEROID's performance remains complex. Moreover each computer, each systems and each environment are different which directly impact performances of python. Nevertheless, with a smart strategy—using a high offset for frame correction and a low offset for MO detection–the algorithm is able to process 600 frames of 1528×1528 pixels in around 5 minutes. Considering that

STEROID is written in Python, its performance remains impressive. Moreover, the modularity between image correction, moving object detection, and photometry offers a significant advantage: if users need to adjust parameters during any of these steps (e.g., during the photometric process), they do not need to repeat the previous ones, saving valuable time. From an algorithmic point of view, STEROID provides multiple solutions to various problems. However, not all of these solutions are optimal. For example, the FWHM determination (see Section 4.4.) is performed separately along the x and y axes of the image. Yet, astronomical objects are not always perfectly circular, nor aligned with the image axes-they may be oriented along rotated axes $X(x,y)$ and $Y(x,y)$. In such cases, the algorithm could be improved by using higher-order moments. The detection of moving objects could also be improved. In particular, STEROID can sometimes overdetect objects and, in images with a high object density, may struggle to accurately identify the direction of motion. Using a deep learning model that retains temporal dependencies-unlike CNNs, which only preserve spatial ones-could be a promising approach. Despite these limitations, STEROID's flexibility allows users to overcome most potential issues with ease. Another point worth improving is that STEROID performs photometry on ADU images. If the input images are in electrons, STEROID can still perform photometry, but the uncertainties will be incorrect. Finally, it is worth noting that by the time readers consult this article, some or all of these points may already have been addressed. To stay updated on the latest developments, please visit the GitHub project page : `https://github.com/antoinech13/Steroid`.

7. CONCLUSIONS

The STEROID package has demonstrated very good performance in automatic reduction and photometric analysis of asteroid imaging observations, particularly in the realm of frame positional correction. Although certain improvements are planned for specific aspects of the tool, we have already established robust solutions for most of its functionalities. Given our focus on asteroid photometry, it is possible that some tools might be lacking for other specific research areas, but the modular structure of the package allows for easy adaptation and integration with other tools. Since the primary objective of this library is to empower users to comfortably develop their own procedures without undue time consumption, we want to emphasize that the STEROID code is open source. Anyone interested in contributing or offering insights on algorithms, with potential to enrich those currently present in STEROID, is more than welcome to join our collaborative effort.

REFERENCES

Assafin, M. (2023), *Planetary and Space Science* **239**, 105816
Bertin, E., Arnouts, S. (1996), *A&Aps* **117**, 393-404
Bradley, Larry, Sipőcz, Brigitta, Robitaille, Thomas, *et al.* (2023), *Zenodo* **v1.8.0**,
Danielsson, Per-Erik, Hammerin, Magnus (1992), *CVGIP: Graphical Models and Image Processing* **54**, 340-344
Garg, Naresh, Garg, N (2013), *International Journal of Computer Applications* **71**, 8–11
Green, George (2008), *arXiv e-prints* , arXiv:0807.0088
Howell, Steve B. (1989), *Publications of the Astronomical Society of the Pacific* **101**, 616
Howell, Steve Bruce (2006), *Cambridge University Press* **5**,
Krizhevsky, Alex, Sutskever, Ilya, Hinton, Geoffrey E (2012), *Advances in Neural Information Processing Systems* **25**,
Marciniak, A., Ďurech, J., Choukroun, A., *et al.* (2023), *A&Ap* **679**, A60
Merline, W. J., Howell, Steve B. (1995), *Experimental Astronomy* **6**, 163-210
Mommert, M. (2017), *Astronomy and Computing* **18**, 47–53
Ofek, E. O., Ben-Ami, S., Polishook, D., *et al.* (2023), *Publications of the Astronomical Society of the Pacific* **135**, 065001
Shi, Jing-Hang, Qiu, Bo, Luo, A-Li, *et al.* (2022), *Monthly Notices of the Royal Astronomical Society* **516**, 264–278
Stone, Ronald C. (1989), *AJ* **97**, 1227
Yang, Luren, Albregtsen, Fritz (1996), *Pattern Recognition* **29**, 1061-1073

A&A, 698, A298 (2025)
https://doi.org/10.1051/0004-6361/202554476

Astronomy & Astrophysics

Asteroid sizes determined with thermophysical model and stellar occultations

A. Choukroun[1,⋆], A. Marciniak[1], J. Ďurech[2], J. Perła[1], W. Ogłoza[3], R. Szakáts[4,5], L. Molnár[4,5,6,7], A. Pál[4,5,8], F. Monteiro[9,10], I. Mieczkowska[1], W. Beisker[11], D. Agnetti[11], C. Anderson[12], S. Andersson[11], D. Antuszewicz[11], P. Arcoverde[9], R.-L. Aubry[13], P. Bacci[11], R. Bacci[11], P. Baruffetti[11], L. Benedyktowicz[11], M. Bertini[11], D. Błażewicz[11], R. Boninsegna[11], Zs. Bora[4], M. Borkowski[11], E. Bredner[12], J. Broughton[12], M. Butkiewicz-Bąk[1], N. Carlson[12], G. Casalnuovo[11], F. Casarramona[11], Y.-J. Choi[14], S. Cikota[15], M. Collins[12], B. Cseh[4,6,16], G. Csörnyei[4], H. De Groot[11], P. Delincak[11], P. Denyer[12], R. Dequinze[12], M. Dogramatzidis[11], M. Dróżdż[3], R. Duffard[17], D. Eisfeldt[12], M. Eleftheriou[11], C. Ellington[18], S. Fauvaud[13,19], M. Fauvaud[13,19], M. Ferrais[20], M. Filipek[11], P. Fini[11], M. Frits[4], B. Gährken[11], G. Galli[11], D. Gault[21], S. Geier[22,23], B. Gimple[12], J. Golonka[24], L. Grazzini[11], J. Grice[25], K. Guhl[11], W. Hanna[21], M. Harman[11], W. Hasubick[11], T. Haymes[11], D. Herald[21], D. Higgins[26], R. Hirsch[1], J. Horbowicz[1], Á. Horti-Dávid[4], B. Ignácz[4,5], E. Jehin[27], A. Jones[28], R. Jones[12], D. Dunham[12], Cs. Kalup[4], K. Kamiński[1], M. K. Kamińska[1], P. Kankiewicz[29], M. Kaplan[30], A. Karagiannidis[11], B. Kattentidt[11], S. Kidd[11], B. Kirpluk[24], D.-H. Kim[14,31], M.-J. Kim[14], I. Konstanciak[1], G. Krannich[11], M. Kretlow[17], J. Kubánek[11,32,33], V. Kudak[34], P. Kulczak[1], M. Lecossois[35], R. Leiva[17], M. Libert[11], J. Licandro[22,36], P. Lindner[11], R. Liu[12], Y. Liu[12], G. Lyzenga[12], M. Maestripieri[11], C. Malagon[11], P. Maley[12,37], A. Manna[11], S. Messner[12], O. Michniewicz[38], M. A. Miftah[27], M. Mizutani[39], N. Morales[17], M. Murawiecka[1], J. Nadolny[1,22,36], T. Nemoto[39], J. Newman[21], V. Nikitin[12], P. Nosal[11], P. Nosworthy[21], M. O'Connell[11], J. Oey[41], A. M. Ortiz-Ochoa[40], A. Ossola[11], D. Oszkiewicz[1], E. Pakštienė[42], M. Pawłowski[1], V. Perig[34], E. Petrescu[27], F. Pilcher[43], E. Podlewska-Gaca[1], M. Poláček[11], J. Polák[11], T. Polakis[44], M. Polińska[1], A. Popowicz[45], V. Reddy[46], J.-J. Rives[13], M. Rottenborn[33], N. Ruocco[11,47], A. Rutkowski[3], K. Saci[11], T. Santana-Ros[48,49], K. Sárneczky[4], O. Schreurs[11,35], V. Sempronio[12], B. Skiff[50], J. Skrzypek[1], D. Smith[11], K. Sobkowiak[1], E. Sonbas[51,52], S. Sposetti[11], C. Stewart[12], W. Stewart[11], T. Swift[12], M. Szkudlarek[38], K. Szyszka[24], N. Takács[4], Ł. Tychoniec[53], M. Uno[39,†], S. Urakawa[54], K. Vida[4], C. Weber[11], N. Wünsche[11], H. Yamamura[39], H. Yoshihara[39], M. Zawilski[11], P. Zelený[55,11], S. Zoła[56], M. Żejmo[38], and K. Żukowski[1]

(Affiliations can be found after the references)

Received 11 March 2025 / Accepted 17 April 2025

ABSTRACT

Context. The sizes of many asteroids, especially slowly rotating, low-amplitude targets, remain poorly constrained due to selection effects. These biases limit the availability of high-quality data, leaving size estimates reliant on spherical shape assumptions. Such approximations introduce significant uncertainties propagating, for example, into density determinations or thermophysical and compositional studies, affecting our understanding of asteroid properties.

Aims. This work targets poorly studied main-belt asteroids, for most of which no shape models were previously available. Using only high-quality, dense light curves, thermal infrared observations (systematically including WISE data), and stellar occultations, we aimed to produce reliable shape models and scale them using two independent techniques, allowing for size comparison at the end. We conducted two observing campaigns to achieve this: one to obtain dense photometric light curves and another to acquire multi-chord stellar occultations by these objects.

Methods. Shape and spin models were reconstructed using light curve inversion techniques. Sizes were determined via two methods: (1) advanced thermophysical modelling using the convex inversion thermophysical model (CITPM), which optimises spin and shape models to light curve data in the visible range together with infrared data, and (2) scaling the shape models with stellar occultations.

Results. We obtained precise sizes and shape models for 15 asteroids. CITPM and occultation-derived sizes agree within 5% for most cases, demonstrating the reliability of the modelling approach. Larger discrepancies are usually linked to incomplete occultation chord coverage. The study also provides insights into surface properties, including albedo, surface roughness and thermal inertia.

Conclusions. The use of high-quality data, coupled with an advanced TPM that uses both thermal and visible data while allowing the shape model to be adjusted according to both types of data, enabled us to determine sizes with precision comparable to those derived from multichord stellar occultations. We resolved substantial inconsistencies in previous size determinations for target asteroids, providing good input for future studies on asteroid densities and surface properties.

Key words. radiation mechanisms: thermal – techniques: photometric – minor planets, asteroids: general

⋆ Corresponding author: antoine.choukroun@amu.edu.pl
† Deceased.

1. Introduction

Asteroids, large ones in particular, as remnants of the early Solar System, play a crucial role in our understanding of its formation processes (Morbidelli et al. 2009). Consequently, determining their physical parameters such as size, density, or thermal inertia is in high demand. Many areas of study are directly dependent on these parameters. For example, asteroid surface properties are linked to how the Sun heats them. This heating is correlated with the orientation of the asteroid spin axis and the rotation period. An asteroid with a very slow rotation or a low pole inclination has part of its surface exposed for long durations (Delbo' et al. 2015; Čapek & Vokrouhlický 2010). These differences in exposure times directly influence how the surface evolves. Thermal inertia also plays a crucial role and can provide insights into the past of asteroids. Young asteroid surfaces tend to be composed mainly of coarse regolith grains, which have higher thermal inertia, while older surfaces consist of finer regolith, resulting in lower thermal inertia (Delbo' & Tanga 2009). However, recent studies (Cambioni et al. 2021) have shown that some young, rocky surfaces with high porosity may also exhibit low thermal inertia despite having minimal regolith coverage. So the presence or lack of surface regolith inferred from thermal inertia is not always a good indicator of age.

The size of an asteroid is a parameter that remains difficult to determine without thermophysical modelling, stellar occultations, radar observations, or adaptive optics. Since all these techniques have their own limitations, for most asteroids this parameter is poorly constrained. In many cases, the size is estimated with an assumed geometric albedo (Harris & Harris 1997) leading to errors and inconsistencies on size estimation reaching sometimes 30% or more (Tanga et al. 2013, see also Table 1), which can propagate to uncertainties on density estimation of more than 90%. The reasons for such large errors can vary, but they are often linked to the quality of the data used as well as the methods employed. Without advanced observing techniques like radar or adaptive optics, extracting precise diameter (and other physical parameters) often relies on thermophysical modelling (TPM, see Delbo' et al. 2015 for the review). Such modelling techniques require an input shape model, while the majority of asteroids lack such models. Consequently, to extract these parameters, the use of ellipsoidal shape models (Lu et al. 2013) or spherical shape assumption becomes an undesirable necessity, as in the most commonly used technique called near-earth thermal model (NEATM, Harris 1998).

To obtain a representative shape model of an asteroid, several methods exist. One can consider the relatively recent SAGE (shaping asteroid using genetic evolution) modelling approach by Bartczak & Dudziński (2017), for example. However, the most widely used technique is the light curve inversion technique producing convex shape representations (Kaasalainen & Torppa 2001, Kaasalainen et al. 2001). Asteroid models generated from this technique are stored in the DAMIT database (database of asteroid models from inversion techniques, Ďurech et al. 2010)[1]. Although these models are mostly scale-free due to unknown albedo (Kaasalainen & Ďurech 2020), they are still representative of the general shape of asteroids, making them necessary inputs for thermophysical modelling (Delbo' et al. 2015).

However, certain problems remain affecting the accuracy and completeness of available models. It has been shown that there are a few selection biases favouring targets with high light curve amplitudes and fast rotators (Marciniak et al. 2015). With the increasing number of surveys, space missions, and ground-based light curve observations, these biases are gradually diminishing. Nevertheless, the available spin and shape models are often based on sparse data (Ďurech et al. 2009), good for spin state determination, but resulting in limited applicability of shape models (Hanuš et al. 2013). Moreover, popular thermophysical modelling techniques (see ATPM from Rozitis & Green 2011 or TPM from Lagerros 1996a,b, 1997, 1998) use the input shape model as it is, without modification, merely optimising model thermal flux. As a result, shape model errors propagate into the final thermophysical parameters (MacLennan & Emery 2019). Even when a shape model is available, it is possible to end up with relatively large uncertainties in size as well as in thermal inertia (Hanuš et al. 2015). The solution to this problem is a simultaneous shape optimisation to fit both visible light curves and thermal data as proposed by the convex inversion thermophysical model (CITPM, Ďurech et al. 2017), the method used here.

In parallel to that area of asteroid studies, advances in technology and observing techniques now allow us to observe stellar occultations by asteroids with high precision (Rommel et al. 2020, Ferreira et al. 2022). With the developments in techniques capable of annotating precise times obtained via GPS to the images, it has become possible to obtain practically direct measurements of asteroid sizes with great accuracy (Herald et al. 2020), sometimes even sufficient to extract topological information when shape features are large enough compared to measurement uncertainties (see e.g. Dias-Oliveira et al. 2017, Leiva et al. 2017, or Rommel et al. 2023). Although this type of observation is much more feasible than radar or adaptive optics observations, since it can be done with amateur equipment, obtaining multiple chords (segments on asteroid projection defined by star reappearance and disappearance) remains a complex task. Indeed, there are three constraints for this type of observation:

- Temporal constraint: although occultations are relatively frequent events, those involving a particular target and a sufficiently bright star, within the reach of most observers' equipment, occur rarely.
- Geographical constraint: just like a solar eclipse is not observable everywhere on the Earth's surface, asteroid stellar occultation shadow paths are very narrow, as the shadow path width is comparable to the size of the object.
- Human resource constraint: to overcome the previous geographical constraint and to obtain usable observations, multiple observers are needed. Occultations resulting in only one or two positive chords provide limited constraints on size. Multichord (with at least three chords) stellar occultation observations are therefore usually only the result of coordinated observing campaigns.

Due to these constraints, the number of asteroids with available multichord occultations remains relatively limited. However, it is important to note that, thanks to significant collaborative efforts and the participation of amateur astronomers, more and more asteroids are being observed in occultations with such results (Herald et al. 2020).

In this work, we use a methodology to consecutively combine two modelling techniques (the light curve inversion, followed by the CITPM) to obtain precise shape models and spin parameters, with the main aim of determining the asteroid sizes. In parallel, we also organised occultation observing campaigns to determine target asteroid sizes through an independent method. In total, we modelled and precisely scaled 15 main-belt asteroids. The targets we chose were relatively understudied until now, being slow

[1] https://astro.troja.mff.cuni.cz/projects/damit/

Table 1. Target asteroid diameters from the literature.

Asteroid	D_{min} (km)	D_{min} reference	D_{max} (km)	D_{max} reference	$\overline{D}$ (km)
(215) Oenone	35.21 ± 0.4	[1]	43.69 ± 4.370	[2]	41.82 ± 0.10
(279) Thule	113.04 ± 3.11	[3]	136.78 ± 7.105	[4]	122.62 ± 2.05
(357) Ninina	92.54 ± 3.015	[4]	124.11 ± 0.86	[5]	113.77 ± 0.61
(366) Vincentina	83.84 ± 8.38	[2]	98.25 ± 4.638	[4]	86.65 ± 0.30
(373) Melusina	84.55 ± 8.45	[2]	107.74 ± 5.815	[4]	95.94 ± 0.61
(395) Delia	44.19 ± 0.45	[5]	61.49 ± 0.7	[5]	50.16 ± 0.34
(429) Lotis	54.2 ± 4.56	[6]	89.69 ± 38.25	[5]	69.79 ± 0.68
(527) Euryanthe	48.55 ± 13.62	[7]	58.56 ± 0.62	[5]	53.99 ± 0.27
(541) Deborah	49.04 ± 17.985	[8]	65.60 ± 3.801	[4]	55.42 ± 0.31
(672) Astarte	27.49 ± 2.75	[2]	35.58 ± 0.495	[9]	33.37 ± 0.33
(814) Tauris	98.77 ± 33.9	[6]	122.26 ± 1.819	[4]	111.9 ± 0.97
(859) Bouzareah	65.21 ± 2.758	[4]	86.02 ± 1	[5]	70.28 ± 0.39
(907) Rhoda	62.73 ± 1.7	[10]	98.01 ± 32.58	[11]	80.91 ± 0.30
(931) Whittemora	40.62 ± 2.02	[5]	63.51 ± 11.434	[4]	50.1 ± 0.42
(1062) Ljuba	51.02 ± 0.887	[9]	63.16 ± 12.63	[2]	54.91 ± 0.52

Notes. Data extracted from the MP3C database (https://mp3c.oca.eu/). D_{min} and D_{max} are the minimum and the maximum published value, respectively, and $\overline{D}$ is the error-weighted mean diameter from all the literature values computed as follows: $\overline{D} = \sum(\frac{D_i}{\sigma_i^2}) / \sum(\frac{1}{\sigma_i^2})$. The uncertainties were evaluated with: $\sigma_{\overline{D}} = \sqrt{1/\sum(\frac{1}{\sigma_i^2})}$. References: [1] Masiero et al. (2014), [2] Alí-Lagoa et al. (2018), [3] Usui et al. (2011), [4] Ryan & Woodward (2010), [5] Masiero et al. (2012), [6] Nugent et al. (2016), [7] Masiero et al. (2020), [8] Masiero et al. (2017), [9] Masiero et al. (2011), [10] Tedesco et al. (2002), [11] Masiero et al. (2021).

rotators with small light curve amplitudes (Marciniak et al. 2015). This procedure allowed us first to provide precise spin parameters and detailed shapes for the target asteroids, and second, to demonstrate that using only flux measurement techniques, it is possible to obtain highly precise size values (by 'size' we mean the diameter of the equivalent volume sphere, see Section 2). In the end, we compare diameters for the same targets obtained with both methods to check their agreement and identify trends and biases. The current paper is the continuation of our work presented in Marciniak et al. (2021) and Marciniak et al. (2023), now combining the two approaches from these works. Section 2 is dedicated to explaining the methodology we employed and detailing the used techniques. Section 3 presents the asteroids we selected and the current state of knowledge existing on them. Results are presented in Section 4, with comparisons to a broad picture based on data from the literature. Section 5 contains conclusions and prospects for future work.

2. Methodology

Modern methods of thermophysical modelling take an asteroid shape model as an input and optimise physical parameters to best fit thermal data. The results are therefore very dependent on input shape models, and it is not uncommon to obtain the results with a high value of reduced χ^2_{IR} indicating an imperfect fit between the physical model and the data (Hanuš et al. 2015, Hung et al. 2022). In this paper, we use a methodology to obtain precise physical parameters of asteroids (such as spin axis orientation, 3D shape approximation, size, albedo, and thermal inertia) based on high-quality data in both the visible and infrared ranges. We applied this methodology to characterise around a dozen main-belt asteroids.

– First, we apply the convex inversion method which allows us to construct three-dimensional shape models from photometric light curves, as long as data from five independent apparitions were gathered in the form of dense light curves. The resulting asteroid models describe the shape and rotational state of our targets. Since the studied asteroids are located in the main belt, this technique often results in two possible solutions for the spin axis orientation due to the mirror pole ambiguity (Kaasalainen & Lamberg 2006). However, these shape models are scale-free, preventing the direct determination of object physical dimensions. Complementary techniques are therefore required to precisely derive asteroid sizes.

– The second step involves utilising these spin solutions as a necessary input to the CITPM. This method combines convex inversion with the thermophysical model ('model' refers here the modelling method) in the approach of Lagerros, following the equation:

$$\chi^2 = \chi^2_{vis} + \omega_{IR} \times \chi^2_{IR}, \quad (1)$$

where ω_{IR} is a parameter dedicated to weighing infrared data (Kaasalainen 2011), χ^2_{vis} evaluates how well the model from the CITPM method ('model' here and throughout the rest of this text meaning the shape representation with accompanying set of physical parameters) fits the visible data, and χ^2_{IR} evaluates the model fit to the thermal data. An important step to ensure good results is to well estimate ω_{IR}. A weight value that is too small will result in models that overfit visible data, yielding a low χ^2_{vis} but a high χ^2_{IR}. On the other hand, a weight value that is too high will cause models to overfit thermal data. Determining analytically the best ω_{IR} remains challenging due to the highly non-linear nature of the CITPM. We investigated the influence of ω_{IR} on the diameter and found it to be non-trivial. Models react differently, with the diameter varying by a few percent when starting near a good solution—and more so when starting from a poor one. The main effect of ω_{IR} is on convergence. Moreover focusing solely on diameter changes does not fully assess model quality. Since CITPM also refines the shape, ω_{IR}

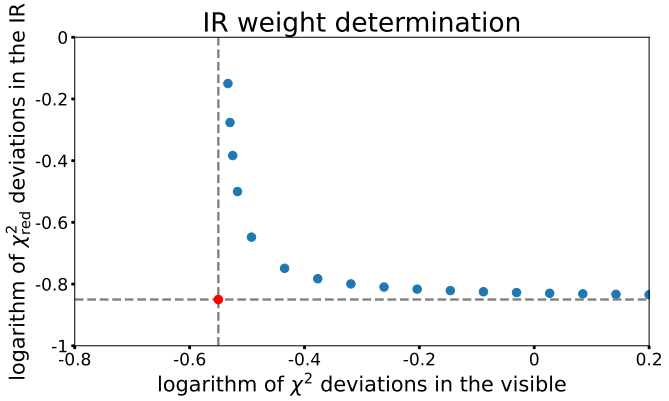

Fig. 1. Ideal evolution of $\chi^2_{\rm vis}$ and reduced $\chi^2_{\rm IR}$ as a function of $\omega_{\rm IR}$. Each blue point corresponds to a different IR weight. This plot is constrained by two asymptotes along the x-axis and the y-axis. These two asymptotes are used to determine a new origin (red point). The best $\omega_{\rm IR}$ value corresponds to the point closest to the new origin.

influences also shape and spin axis orientation, of the order of several percent too. However, a good $\omega_{\rm IR}$ can be obtained by following the procedure described by Kaasalainen & Viikinkoski (2012) and shown in Figure 1. The idea is to run the CITPM multiple times with different values of $\omega_{\rm IR} \in [0.001, 0.05]$ (blue points) and to determine a vertical and a horizontal asymptote defined by the logarithm of the minimum $\chi^2_{\rm vis}$ and the logarithm of the minimum $\chi^2_{\rm IR}$ obtained. The intersection between these two asymptotes defines a new origin. The best $\omega_{\rm IR}$ value is the one which minimises the distance between this new origin and the points $P_{\omega_{\rm IR}}(\log(\chi^2_{\rm vis}), \log(\chi^2_{\rm IR}))$. However, plotting the logarithm of $\chi^2_{\rm IR}$ vs the logarithm of $\chi^2_{\rm vis}$ does not always produce results as clean as the one shown in Figure 1. Some noise or instabilities may be present. For this reason, the obtained $\omega_{\rm IR}$ is not perfect but remains close. We also examined how the amount of visible and infrared data affect ω_{IR}, but found no clear trend. Data quality remains the primary source of ω_{IR} variability, assuming their sufficient amount and diversity. This combined approach adjusts the shape model to both types of data, providing significant advantages. Traditional TPM methods treat the input shape model as absolute truth, which can pose problems when the shape model is of poor resolution or, in extreme cases, when no shape model exists and a simple spherical model is used as input. However, the CITPM allows us to improve the spin and shape models, scale them in size, and determine other thermophysical parameters such as thermal inertia, hemispherical albedo – derived using Hapke parameters, which differs from the geometric albedo that assumes a spherical shape for asteroids – and an estimate of surface roughness. A few studies using the TPM also took into account the uncertainties introduced by the input shape (see e.g. Hanuš et al. 2015), but they did not optimise the shape model to both data types at the same time. The CITPM optimise Hapke parameters (Hapke 1981, 1984, 1986) to derive the hemispherical albedo of the model, providing a more accurate approach, and simultaneously optimises parameters for the facets (surface elements), allowing a precise determination of global model parameters like the asteroid size, thermal inertia Γ and the surface roughness.

– Finally, the third step involves using stellar occultations to scale the initial shape models obtained with convex inversion, independently from the second step. To perform this, the occultation chords are projected onto the fundamental plane (plane perpendicular to the star-asteroid direction and goes through the Earth) following the procedure described in Ďurech et al. (2011), using the equations:

$$\begin{aligned} \hat{\boldsymbol{s}}_\xi &= (-\sin\delta\cos\alpha,\ -\sin\delta\sin\alpha,\ \cos\delta), \\ \hat{\boldsymbol{s}}_\eta &= (\sin\alpha,\ -\cos\alpha,\ 0), \end{aligned} \tag{2}$$

and

$$\begin{pmatrix} \xi \\ \eta \end{pmatrix} = \begin{bmatrix} \hat{\boldsymbol{s}}_\xi \cdot \left(\boldsymbol{x} + \Delta\boldsymbol{v}\Delta t + \frac{1}{2}\Delta\dot{\boldsymbol{v}}(\Delta t)^2\right) \\ \hat{\boldsymbol{s}}_\eta \cdot \left(\boldsymbol{x} + \Delta\boldsymbol{v}\Delta t + \frac{1}{2}\Delta\dot{\boldsymbol{v}}(\Delta t)^2\right) \end{bmatrix}, \tag{3}$$

where $\hat{\boldsymbol{s}}_\xi$ and $\hat{\boldsymbol{s}}_\eta$ correspond to unit vectors on the fundamental plane, and α and δ are the right ascension and declination of the occulted star. Next, ξ and η correspond to the geocentric co-ordinates of an observer's position projected on the fundamental plane, $\boldsymbol{x}$ is the observer's position on the Earth in the sidereal equatorial frame, $\Delta\boldsymbol{v}$ is the relative velocity of the Earth and the asteroid, and $\Delta\boldsymbol{t}$ corresponds to the time between the star disappearance or reappearance and an arbitrary epoch. The sidereal equatorial frame is used here for two main reasons. The first is that the geographic co-ordinate system (longitude, latitude) does not account for the Earth's orientation at the moment of observation. The second is connected to the sidereal equatorial system definition: the z axis points towards the celestial pole, the x axis points towards the vernal equinox, and the y axis is chosen such that it forms a right-handed orthonormal reference frame. This co-ordinate system is expressed on the same basis as the equatorial system, used for the co-ordinates of the occulted star. This significantly simplifies calculations, as transitioning between the two systems does not require a change of basis. The corresponding silhouettes of the shape model (for both pole solutions) constructed during the first step are also projected onto the fundamental plane. The centroid position and the size of the asteroid silhouette are then optimised using both positive and negative chords. At this stage, shape models are scaled based on occultation observations, and the final size corresponds to the diameter of a sphere with the same volume as the scaled shape model. It is often possible to verify the obtained dimensions and resolve ambiguities in pole solutions (see e.g. Marciniak et al. 2023).

After this stage we compare the results for diameters from the second and third steps, providing cross-validation between the two approaches. The diameters from thermophysical modelling are defined for a sphere of the same surface area as our shape model, so we recalculate them for a sphere of the same volume as our model, and then thermally derived diameters can be directly compared to diameters from occultation fitting. If the sizes obtained by thermophysical modelling and by occultation fitting are in agreement, we could reasonably assume that for any target modelled following CITPM methodology, obtained size values are accurate without requiring a double-check through occultations.

3. Targets and data

The targets we selected are main-belt asteroids that have been poorly studied before. The reason for this was the fact that these targets are challenging to observe. They are all slow rotators (P > 12 h) with low maximum light curve amplitude (below 0.3 mag). Available photometric data on these targets were mostly sparse data from sky surveys, and not many dense light curves that we needed were available. Even in cases where the Nyquist-Shannon theorem was satisfied (Shannon 1949),

there were often too few data points to cover a complete light curve. Furthermore, the photometric quality of sparse data from ground-based surveys is not always sufficient, with photometric scatter being of an order of 0.1 mag at best (Hanuš et al. 2011). On the other hand, the low-scatter data from the Gaia mission is not abundant enough to enable unique spin and shape models of our targets.

Also, to obtain the size values as precisely as possible, our input data must be abundant and of high quality. To achieve these objectives, we used only dense light curves with low photometric scatter from a large photometric campaign described in Marciniak et al. (2015). Thanks to the wide collaboration and a long-time campaign, we managed to cover enough apparitions for all our targets to obtain unique spin and shape models using the convex inversion method. Also, for each light curve, we carefully eliminated any problematic data points (e.g., star passages, outlying points, too noisy fragments, etc.).

Regarding infrared data, it is important to note that the transition between reflected light and thermal emission is continuous, and the transition phase where the flux is a mix of both, for main-belt asteroids, is usually located around 3–5 μm (Harris & Lagerros 2002). Therefore, our thermal dataset does not include any points observed at wavelengths shorter than 9 μm. Moreover, intending to obtain the most accurate parameters possible, we focused on targets that were observed by WISE spacecraft in W3 (11.1 μm) and W4 (22.64 μm) bands (Wright et al. 2010, Mainzer et al. 2011), taking care of rejecting all of the partially saturated points. We also included thermal data from IRAS (Neugebauer et al. 1984) and AKARI missions (Usui et al. 2011), provided that WISE data were available. All thermal data have been downloaded from the infrared database (IRDB, Szakáts et al. 2020)[2]. According to IRDB documentation, for most instruments and filters, the colour correction was derived from the relative response profiles of the specific filters while assuming an estimated effective temperature for the target, calculated as described in Lang (1999). The number of visible light curves and IR data points is presented in Table 2. Since the determination of Hapke model parameters in CITPM requires calibrated data in the visible range, we added the V-band data from USNO (US naval observatory) archive[3] in this step.

For occultation observations, in October 2020 we initiated another observing campaign as outlined in Marciniak et al. (2023). Information regarding both the photometric and occultation observing campaigns can be found here. The ultimate goal was to achieve sufficiently well-covered occultation events to accurately determine the sizes of our targets using an independent approach. For earlier events, we utilised archival data from the asteroid occultations v4.0 archive of the NASA planetary data system (Herald et al. 2024), and from the software 'Occult v4.2024'[4].

Since our research focused on poorly studied targets, for the majority of them, neither spin solutions nor shape models existed. Only for five of them, spin and shape models derived from sparse data were available in the DAMIT database. In addition, for (279) Thule, a spin solution was listed in the LCDB[5] (Pilcher 2014), although no shape model was provided. The spin axis solutions for (279) Thule were determined there using an approximative method based on the amplitudes of light curves. Information on all prior spin/shape models is gathered in Table 3.

[2] https://ird.konkoly.hu/
[3] https://newton.spacedys.com/astdys2/index.php?pc=3.0
[4] http://lunar-occultations.com/iota/occult4.htm
[5] Light curve database (Warner et al. 2009), https://minplanobs.org/mpinfo/php/lcdb.php

Table 2. Data summary.

Target	Taxon.	N_{lc}	N_{app}	N_{IR}	N_{WISE}	N_{occ} (N_{pos})
(215) Oenone	S	78	8	53	22	1(2)
(279) Thule	X	107	13	33	15	3(5, 2, 4)
(357) Ninina	CX	89	7	38	10	4(7, 2, 4, 7)
(366) Vincentina	Ch	69	9	67	21	3(6, 6, 2)
(373) Melusina	C	31	6	40	11	1(2)
(395) Delia	Ch	68	7	20	11	3(3, 2, 2)
(429) Lotis	C	79	8	41	11	1(2)
(527) Euryanthe	Cb	90	6	35	19	2(6, 5)
(541) Deborah	B	44	6	48	30	3(2, 4, 6)
(672) Astarte	S	62	8	24	16	1(4)
(814) Tauris	C	101	11	19	8	1(5)
(859) Bouzareah	X	49	7	39	12	3(2, 3, 4)
(907) Rhoda	Xk	92	9	46	22	1(2)
(931) Whittemora	M	60	9	49	24	3(3, 2, 2)
(1062) Ljuba	C	132	9	27	14	2(2, 2)

Notes. 'Taxon.' refers to the taxonomic type. N_{lc} is the number of dense light curves for each target registered at N_{app} apparitions, N_{IR} is the number of all infrared data points, and N_{WISE} is the number of data points obtained by WISE spacecraft. N_{occ} represents the number of stellar occultation events, with the number of positive chords for each event shown in parentheses. Taxonomic types come from Tholen (1984), Bus & Binzel (2002) and from Vereš et al. (2015).

Table 3. Prior spin/shape solutions available for our targets.

Target	λ (°)	β (°)	Period (hours)	Reference
(215) Oenone	227 ± 4	66 ± 5	27.9081	[1]
(279) Thule	70 ± 8	0	15.94	[2]
	250 ± 8	0	15.94	[2]
(357) Ninina	49 ± 10	0 ± 10	35.984	[3]
	230 ± 10	36 ± 10	35.984	[3]
(373) Melusina	19 ± 5	−48 ± 5	12.98629	[4]
	147 ± 5	−61 ± 5	12.98632	[4]
(395) Delia	15 ± 3	−50 ± 4	19.6802	[1]
	196 ± 4	−53 ± 4	19.6803	[1]
(672) Astarte	–	59 ± 18	22.5799	[1]

Notes. Ecliptic J2000 co-ordinates λ and β correspond to the spin axis orientation in space. References: [1] Ďurech et al. (2020), [2] Pilcher (2014), [3] Franco et al. (2024), [4] Ďurech et al. (2018).

4. Results

4.1. Finding the best model in CITPM

As described in Section 2, the first step involves obtaining the shape models and spin solutions of each of our targets. This step is crucial for accurately determining the solutions for the spin axis and the sideral rotation period, where a sub-second precision is required to achieve reliable results with the CITPM. Also, a good shape model is important to determine the size via stellar occultation fitting (see Sections 4.2, 4.3, and Table 5).

To constrain the thermophysical parameters of the models derived in the first step, it is essential to determine the weight of the infrared data in the first place. Following the procedure described in Section 2 and illustrated in Figure 1, our approach involves running CITPM multiple times for one of the two spin

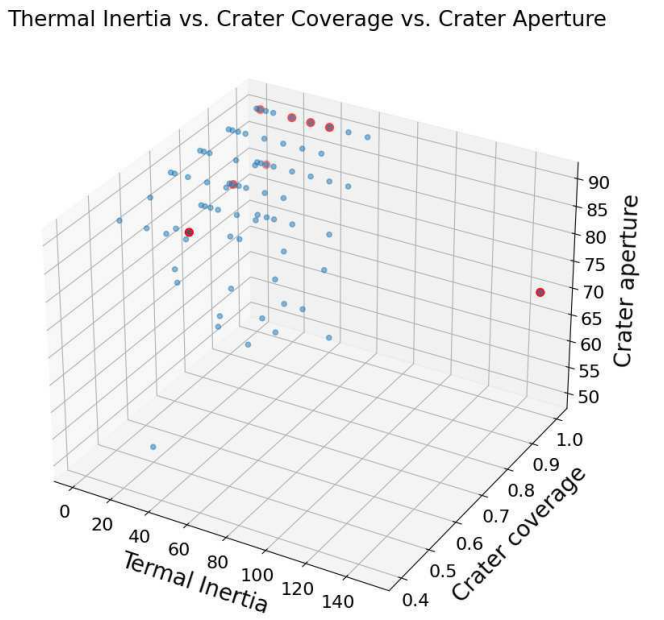

Fig. 2. Crater coverage ρ_c against crater aperture γ_c against thermal inertia Γ in $\mathrm{J\,m^{-2}\,s^{-\frac{1}{2}}\,K^{-1}}$ of the best solutions for asteroid (814) Tauris. All blue points correspond to acceptable solutions according to Equation (4). The red points represent the 10 best solutions among all acceptable ones. All points are grouped, except for the red point with $\Gamma > 140$, which is isolated. This point was not used to determine final parameter uncertainties.

solutions while certain parameters remain unchanged, such as thermal inertia and surface roughness. The only parameter that varies between each run is the infrared data weight. These successive runs allow us to plot the curve like the one shown in Figure 1, thereby identifying the weight that provides the best balance between thermal and visible data.

The next step involves running the code multiple times (in a loop as an iterative way) for a given thermal inertia value while varying the surface roughness parameters: the crater aperture that is changed from 10(°) to 90(°) with a step of 10(°), and crater coverage, changed from 0.1 to 1 with a step of 0.1. These parameters correspond to the hemispherical crater opening angle and the extent to which the surface of the target is covered by craters, and they are not optimised during the run and remain fixed. This process is repeated for a range of thermal inertia values. Although this step is computationally intensive, it is critical because it ensures a good representation of the model within the parameter space. A solution is considered acceptable if:

$$\begin{cases} \chi^2_{\mathrm{vis}} < \min(\chi^2_{\mathrm{vis}}) \cdot 1.1 \\ \chi^2_{\mathrm{IR}} < 1 + \sqrt{\frac{2}{\nu}}, \end{cases} \tag{4}$$

where ν is the number of thermal measurements minus the number of degrees of freedom. The number of degrees of freedom is set to four (size, thermal inertia and two parameters for surface roughness). The parameters of the best of all acceptable solutions from the loop over surface roughness are used as input for a final CITPM run. The other acceptable solutions are used to determine uncertainty ranges. To not overestimate uncertainties, we also produce a 3D plot of crater coverage vs crater apertures vs thermal inertia of all acceptable solutions. If an isolated point is found out of the general cluster, this solution is not taken into account to calculate uncertainties (see Figure 2).

All the results obtained with this procedure are presented in Table 4, where each target entry is split into two lines corresponding to the solutions for each pole. Columns 2 to 5 describe the spin axis parameters, as these are also optimised by the CITPM. The last four columns provide the diameter of the sphere with equivalent volume, geometric albedo derived from Hapke parameters following equation 65 of Hapke (1984), thermal inertia in SI units ($\mathrm{J\,m^{-2}\,s^{-\frac{1}{2}}\,K^{-1}}$), and the mean surface slope according to Hapke (1984), Lagerros (1996a). To achieve these results, we automatised a large part of the procedure. As shown in Table 4, some parameters are well constrained, such as spin parameters, diameter, and albedo. However, surface roughness and thermal inertia are not always well constrained because of the entanglement existing between them (see Figures B.1 to B.15). Although, for some of our targets, everything proceeded smoothly without setbacks, for others, direct decisions had to be made to ensure that the obtained results were robust. The reasons for this can be multiple and varied: insufficient data, insufficient diversity in the observation geometry, convex assumption of the model, inadequate spectral diversity in the thermal data, etc. The CITPM remains a multivariable optimisation model that is highly sensitive to the input data. The number of local minima can, therefore be large.

Model fits to data in the visible range are shown in Figures C.1–C.10. We present only a small part of the whole light curve dataset here, and only for targets where data from Kepler or TESS spacecraft were available. The fit to all of the light curve data can be found in the DAMIT database. Only the uninterrupted observations from space show substantial coverage of rotation phases for our slow rotators. Model fits to thermal data, on the other hand, are shown in Figures D.1 to D.21. These plots present fits to data from WISE spacecraft because only these observations were rich enough to reveal thermal light curves. Both kinds of fit are presented for the pole solution preferred by occultations, or pole 1 in case of no preference.

With thermophysical modelling, the most common issue we encountered was the difficulty in determining a suitable value for ω_{IR}. Sometimes, the procedure described in Section 2 did not yield a plot as clear as the one shown in Figure 1; instead, some plots of both χ^2 values tended to be chaotic, showing no discernible trend. In such cases, our approach was to produce two additional plots. As previously explained, these plots were generated by running the CITPM code multiple times, with the only difference between runs being the ω_{IR} weight value. This means that other parameters remained the same for each run of a given target. We also used the same parameters across different targets (except for λ, β, and the period, which are specific to each target), to facilitate direct comparability of the results. Originally, we used crater opening angle γ_c of 50° and crater coverage ρ_c of 0.5, as the parameters of the surface roughness. However, due to the difficulties we faced, we modified the procedure to produce three plots for different surface crater combinations: $\gamma_c = 20, \rho_c = 0.2$; $\gamma_c = 50, \rho_c = 0.5$; and $\gamma_c = 80, \rho_c = 0.8$. This updated method had two advantages. First, comparing each of these plots helped us identify a ω_{IR} weight value that better reflected the surface roughness. Second, in situations where the plots appeared chaotic, it was often the case that at least one of them contained a less chaotic region that allowed us to estimate ω_{IR}. Although we could not be certain this value was optimal, it provided a sufficiently reliable approximation for ω_{IR}. The targets affected by this issue were: (373) Melusina, (814) Tauris, (859) Bouzareah, and (1062) Ljuba.

Table 4. Results obtained through modelling with the Convex Inversion Thermophysical Model.

Target name	Pole	λ (°)	β (°)	Period (h)	D (km)	p_V	Γ (J m^{-2} s$^{-\frac{1}{2}}$ K^{-1})	$\bar{\theta}$ (°)
(215) Oenone	1	45^{+13}_{-7}	85^{+5}_{-5}	27.90773 ± 0.00005	37^{+2}_{-2}	$0.227^{+0.006}_{-0.038}$	63^{+86}_{-62}	68
	2	233^{+14}_{-6}	85^{+5}_{-9}	27.90774 ± 0.00006	37^{+2}_{-2}	$0.22^{+0.01}_{-0.03}$	62^{+88}_{-61}	42
(279) Thule	1	58^{+24}_{-4}	2^{+9}_{-7}	23.8964 ± 0.0003	116^{+9}_{-6}	$0.039^{+0.005}_{-0.005}$	76^{+44}_{-75}	68
	2	236^{+28}_{-1}	3^{+5}_{-8}	23.8963 ± 0.0004	117^{+10}_{-8}	$0.038^{+0.007}_{-0.005}$	69^{+81}_{-68}	68
(357) Ninina	**1**	$\mathbf{41^{+2}_{-16}}$	$\mathbf{7^{+25}_{-4}}$	**35.9845 ± 0.0005**	$\mathbf{104^{+9}_{-8}}$	$\mathbf{0.08^{+0.03}_{-0.02}}$	$\mathbf{40^{+208}_{-39}}$	**59**
	2	224^{+7}_{-21}	42^{+13}_{-6}	35.9845 ± 0.0004	101^{+12}_{-2}	$0.08^{+0.01}_{-0.03}$	6^{+194}_{-5}	34
(366) Vincentina	1	51^{+2}_{-1}	19^{+9}_{-1}	17.3484 ± 0.0002	87^{+5}_{-4}	$0.081^{+0.037}_{-0.009}$	48^{+151}_{-47}	25
	2	234^{+2}_{-1}	-0^{+5}_{-2}	17.3484 ± 0.0003	87^{+5}_{-5}	$0.080^{+0.043}_{-0.009}$	41^{+109}_{-40}	24
(373) Melusina	1	20^{+24}_{-1}	-68^{+1}_{-2}	12.986274 ± 0.00003	99^{+13}_{-4}	$0.040^{+0.006}_{-0.007}$	13^{+87}_{-12}	19
	2	$\mathbf{132^{+14}_{-1}}$	$\mathbf{-54^{+4}_{-4}}$	**12.986283 ± 0.00002**	$\mathbf{101^{+1}_{-10}}$	$\mathbf{0.038^{+0.009}_{-0.002}}$	$\mathbf{5^{+95}_{-4}}$	**13**
(395) Delia	1	5^{+24}_{-2}	-49^{+5}_{-15}	19.68097 ± 0.00005	52^{+7}_{-4}	$0.039^{+0.007}_{-0.007}$	26^{+94}_{-25}	45
	2	207^{+14}_{-23}	-56^{+5}_{-20}	19.68103 ± 0.00008	53^{+11}_{-5}	$0.038^{+0.008}_{-0.01}$	39^{+61}_{-38}	59
(429) Lotis	1	133^{+3}_{-6}	-16^{+5}_{-10}	13.58081 ± 0.00002	67^{+1}_{-4}	$0.036^{+0.06}_{-0.001}$	183^{+317}_{-182}	21
	2	312^{+4}_{-4}	5^{+5}_{-6}	13.58081 ± 0.00003	68^{+1}_{-7}	$0.036^{+0.059}_{-0.001}$	128^{+372}_{-127}	21
(527) Euryanthe	1	147^{+7}_{-6}	-59^{+11}_{-4}	42.8379 ± 0.0004	53^{+1}_{-2}	$0.039^{+0.005}_{-0.003}$	31^{+68}_{-30}	3
	2	$\mathbf{284^{+9}_{-6}}$	$\mathbf{-58^{+9}_{-6}}$	**42.8378 ± 0.0002**	$\mathbf{51^{+3}_{-1}}$	$\mathbf{0.039^{+0.005}_{-0.003}}$	$\mathbf{31^{+68}_{-30}}$	**28**
(541) Deborah	1	155^{+11}_{-18}	63^{+9}_{-20}	29.4223 ± 0.0001	57^{+1}_{-4}	$0.0488^{+0.0001}_{-0.009}$	2^{+60}_{-1}	38
	2	$\mathbf{310^{+19}_{-2}}$	$\mathbf{63^{+16}_{-5}}$	**29.422425 ± 0.0002**	$\mathbf{54^{+4}_{-1}}$	$\mathbf{0.043^{+0.003}_{-0.002}}$	$\mathbf{2^{+28}_{-1}}$	**17**
(672) Astarte	1	184^{+6}_{-6}	65^{+1}_{-26}	22.57993 ± 0.00004	30^{+1}_{-2}	$0.047^{0.01}_{-0.004}$	4^{+446}_{-3}	55
	2	307^{+9}_{-8}	65^{+3}_{-11}	22.57990 ± 0.00005	31^{+3}_{-1}	$0.048^{+0.003}_{-0.008}$	37^{+263}_{-36}	59
(814) Tauris	1	169^{+2}_{-2}	-43^{+10}_{-7}	36.0581 ± 0.0001	101^{+4}_{-5}	$0.043^{+0.011}_{-0.003}$	4^{+75}_{-3}	38
	2	298^{+26}_{-11}	-84^{+6}_{-1}	36.05858 ± 0.0002	110^{+4}_{-11}	$0.040^{+0.015}_{-0.004}$	2^{+148}_{-1}	10
(859) Bouzareah	1	29^{+24}_{-12}	-45^{+20}_{-17}	24.9287 ± 0.0003	68^{+9}_{-4}	$0.041^{+0.009}_{-0.006}$	6^{+198}_{-5}	38
	2	200^{+24}_{-21}	-32^{+4}_{-30}	24.9286 ± 0.0002	67^{+13}_{-3}	$0.041^{+0.017}_{-0.006}$	6^{+198}_{-5}	32
(907) Rhoda	1	94^{+1}_{-11}	30^{+14}_{-4}	22.4511 ± 0.0001	71^{+5}_{-3}	$0.045^{+0.009}_{-0.016}$	8^{+242}_{-7}	16
	2	279^{+2}_{-2}	-7^{+14}_{-2}	22.45117 ± 0.00007	72^{+5}_{-3}	$0.038^{+0.012}_{-0.008}$	4^{+146}_{-3}	13
(931) Whittemora	1	32^{+6}_{-14}	46^{+12}_{-9}	19.17588 ± 0.00006	50^{+4}_{-2}	$0.13^{+0.01}_{-0.02}$	86^{+114}_{-85}	45
	2	$\mathbf{220^{+11}_{-23}}$	$\mathbf{70^{+5}_{-8}}$	**19.17589 ± 0.00006**	$\mathbf{51^{+2}_{-2}}$	$\mathbf{0.12^{+0.02}_{-0.01}}$	$\mathbf{40^{+160}_{-39}}$	**21**
(1062) Ljuba	1	122^{+1}_{-4}	-13^{+7}_{-4}	33.7907 ± 0.0006	50^{+4}_{-2}	$0.077^{+0.005}_{-0.023}$	29^{+220}_{-28}	42
	2	$\mathbf{305^{+3}_{-3}}$	$\mathbf{-20^{+4}_{-8}}$	**33.7909 ± 0.0005**	$\mathbf{51^{+3}_{-2}}$	$\mathbf{0.063^{+0.015}_{-0.009}}$	$\mathbf{29^{+220}_{-28}}$	**55**

Notes. The columns present parameters derived from the CITPM for the pole 1 and pole 2 solutions of each target: J2000 ecliptic pole longitude (λ) and latitude (β), sidereal rotation period, diameter (D), geometric albedo p_V, thermal inertia (Γ), and Hapke's mean surface slope ($\bar{\theta}$). The diameter corresponds to the diameter of a sphere with a volume equivalent to that of the model. Pole solutions preferred by occultations are marked with boldface.

4.2. Size determination via occultation fitting

CITPM is one way to determine asteroid sizes. In parallel to this, we also determined their sizes using stellar occultations. Table 5 presents the results of scaling the models from light curve inversion with the chords from stellar occultations. The asteroid models we used here were based on dense light curves in the visible range only (first step, see Section 2). As such, their shapes are less smooth (we found that adding thermal data tends to smooth the shape models out), however, they had poorly constrained stretch along the spin axis in some cases. The 'D RMS' in Table 5 are formal diameter uncertainties from the occultation fitting. On the other hand, the '+/-' diameter uncertainties in the preceding column also take model uncertainties into account if these were larger than the formal uncertainties. To determine the influence of the shape model uncertainty on diameter, we created ten versions of each shape model using various levels of shape regularisation. Such a procedure, described in more detail in Marciniak et al. (2023), resulted in spin and shape models similarly well-fitting light curves but with different

Table 5. Occultation derived diameters.

Target	Spin solution	D (km)	D RMS (km)
(215) Oenone	1	46 ± 1	1
	2	48 ± 1	1
(279) Thule	1	115 ± 12	12
	2	119 ± 13	13
(357) Ninina	**1**	$\mathbf{97^{+7}_{-8}}$	**6**
	2	113 ± 11	11
(366) Vincentina	1	92 ± 6	5
	2	87^{+14}_{-6}	6
(373) Melusina	1	99 ± 8	8
	2	$\mathbf{103^{+6}_{-3}}$	**3**
(395) Delia	1	56 ± 3	3
	2	55 ± 3	3
(429) Lotis	1	58 ± 9	9
	2	62 ± 1	1
(527) Euryanthe	1	53 ± 6	6
	2	**52 ± 2**	**2**
(541) Deborah	1	60 ± 5	5
	2	**57 ± 2**	**2**
(672) Astarte	1	28.5 ± 1.3	1.3
	2	32.3 ± 1.0	0.9
(814) Tauris	1	112 ± 9	9
	2	113 ± 9	9
(859) Bouzareah	1	66 ± 6	6
	2	67 ± 6	6
(907) Rhoda	1	63 ± 2	2
	2	63 ± 1	1
(931) Whittemora	1	49 ± 5	5
	2	**54 ± 2**	**2**
(1062) Ljuba	1	41 ± 4	4
	2	**44 ± 4**	**4**

Notes. For each target and pole solution presented in Table 4, the diameter of the equivalent volume sphere is given, together with its best estimate of uncertainty, influenced by the uncertainty of both occultation timings and the shape model itself. The last column contains the formal RMS uncertainty of the occultation fit only (see text in Section 4.2 for details). Solutions preferred by occultations are marked with boldface.

levels of stretch along the rotation axis ('flatter' and 'rounder' shapes), since that shape dimension is usually worse determined by light curve inversion. Each version of the shape was then fitted to all available occultations with at least two well-spaced chords, resulting in a range of plausible diameters. Some variations in the shape misfitted the occultations by more than three sigma, and in such a case, their diameters were not taken into account to assess the diameter range. On the other hand, some regularised shapes provided a better fit than the original shape model did, and then they replaced it. Figures E.1 to E.13 present the best-fitting shapes in this respect, and Table 5 contains diameters for such improved models.

The plots shown in Figures E.1 to E.13 present the instantaneous silhouettes of the light curve inversion models on the fundamental plane, with the scale expressed in kilometres. Blue and magenta contours pertain to mirror solutions for pole 1 and pole 2, respectively, unless stated otherwise, see Table 4 for the spin axis parameters. To be more precise, the original λ and β from pure light curve inversion (our step one) were a few degrees different than those from CITPM presented in Table 4 (our step two), as the other method optimises the spin axis orientation as well. However, the values for the pole solution from both methods were close enough to each other (within the error bars) that we decided not to present those from step one here to avoid confusion. Both versions of the shape models with their spin parameters are available in the DAMIT database. When occultation fits do not show a clear preference for one model versus the other, both models are shown as solid contours. Otherwise, the preferred model is shown with a solid contour, while the less preferred one is shown with a dashed contour.

4.3. Detailed description of specific targets

Below, we describe the results for a few particular targets in more detail.

4.3.1. (279) Thule

None of the two solutions for spin and shape fit the occultations perfectly, particularly the event from 2008/04/03 (see Fig. E.2). There were five chords in this event, but one of them could have been registered with a gross timing error, so we decided to exclude it. Satō et al. (2015) interpreted that chord as produced by a nearby, large satellite, but we did not find any other signatures from additional large objects around Thule, neither in other occultation events nor in thermophysical analysis. Thermal flux from two bodies would lead to overestimated size when treated as a single object, inconsistent with a single body of the size determined by occultations. On the contrary, we find a good agreement of sizes determined with both methods (see the values for D in Table 4 and Table 5), thus excluding the large satellite hypothesis. The two shortest chords from that occultation outline the very edges of the real body, but such small details of real shapes are problematic to be reproduced by light curve inversion or sometimes tend to be shifted over the surface of the shape model. Taking this into account, the first pole (blue contour) is slightly preferred.

4.3.2. (366) Vincentina

Solution for pole 2 seems slightly preferred by occultations, and as such is marked in blue in Fig. E.4. Although two multichord events are available, they do not constrain the size for model 1 well. Due to the lack of chords in the northernmost part of that model silhouette, longer shapes, up to 100 km are almost equally possible as the best fitting one, with its 87 km.

4.3.3. (373) Melusina

In spite of only two-chord event available for this asteroid, the lengths and positions of these chords relative to each other enabled us to identify a preferred solution (pole 2, marked with the solid contour in Fig. E.6). Here, only the procedure of testing shapes with various regularisations enabled us to find a good-fitting shape. On the other hand, each version of the shape for pole 1 fitted worse than the one shown with the dashed contour.

4.3.4. (395) Delia

Here, similarly to the case of 279 Thule, we had to exclude one occultation observation (from the event on 2006/08/27), to be able to fit any shape model to it. Interestingly, this time that observation was negative. That negative chord was placed 8 km south of the southernmost positive chord, 50.5 km long, shown in the first panel of Fig. E.5. It was too close not to be intersected by each of the tested model contours. We investigated that observation closely and found that it was a visual observation of an event with a very bright, 6-magnitude star, where another observer reported ingress and egress of a certain duration. These

facts probably point to effects complicating the observations, like for instance non-negligible angular extent of an occulted star.

4.3.5. (429) Lotis

Although for Lotis, there was only a two-chord event available, the size is quite secure: it cannot be much larger or smaller than 60 km due to the long chord and its placement against the short chord (see Fig. E.6). The shape solution connected to pole 2 (marked here in blue) is slightly preferred, but still, it probably has an underestimated uncertainty (Table 5).

4.3.6. 814 Tauris

The only multichord occultation for Tauris has been registered in our 'SlowRotators' campaign and both shape solutions fit it well (Fig. E.11). Interestingly, a few years earlier, there was another event with Tauris (George et al. 2019), where a single station registered a double dip in brightness, which might have been caused by distinct topographic features on the surface of an asteroid. A chord from this event, treated as a single-dip one, would fit the edge of our shape model 1 of Tauris, confirming this hypothesis. However, the light curve inversion method used here for shape reconstruction produces only convex shape models, so we cannot confirm this nonconvex topography. The contact binary or double asteroid hypotheses also made by George et al. (2019) are rather improbable, because our shape model of Tauris would have a brick-like or a cone-like appearance if that was the case (see the DAMIT database for a full view of the model).

4.3.7. (907) Rhoda

The fit to the two-chord event does not give reliable size determination in this case. Both chords could as well intersect the northern hemisphere, leading to a larger size determination (see Fig. E.11). That probably explains the inconsistency between the occultation (63 ± 2 km) and the CITPM (74^{+5}_{-3} km) diameters that we obtained. Values from the latter method are more robust in this case.

4.3.8. (1062) Ljuba

The size and RMS from occultation fitting are not robust here (see Fig. E.13). Shape model uncertainties are larger than the timing uncertainties, and the fit is accidentally forced to chords with perfect timings, but the size can also be 10% larger than the adopted 44 km. Here too the size from CITPM (51^{+4}_{-2} km) is more reliable. Curiously, despite such a relatively poorly constrained size, a preferred pole solution (pole 2) is found: only this shape shows the abrupt narrowing in the southern part, necessary to explain the observed occultation durations (though imperfectly).

Models for the remaining asteroids (357) Ninina, (527) Euryanthe, (541) Deborah and (931) Whittemora provided very good fit to occultations and showed a clear preference for one of two mirror pole solutions (see the Figures: E.3, E.7, E.8 and E.12). On the other hand, both mirror-pole models for (215) Oenone (Fig. E.1), (672) Astarte (Fig. E.9) and (859) Bouzareah (Fig. E.10) fitted similarly.

4.4. Size comparison

When comparing the size values determined through modelling with the CITPM method and those determined through detailed shape model fitting to occultations (see Figure 3), we observe

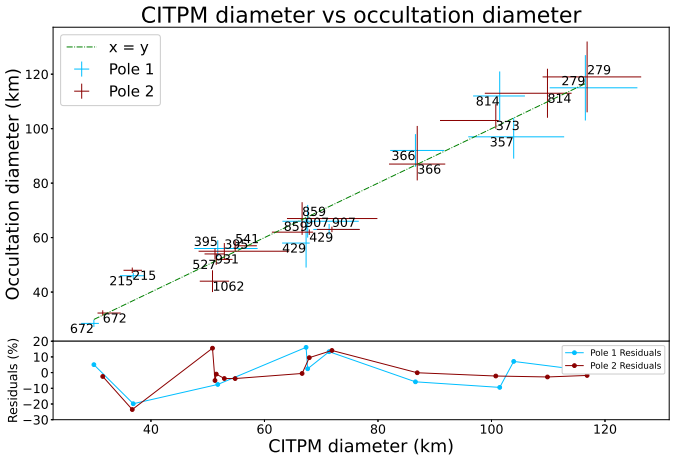

Fig. 3. Comparison between thermally derived asteroid diameters and occultation-based diameters, both determined in this work (Tables 4 and 5). The horizontal axis corresponds to the CITPM-derived size, while the vertical axis is the occultation-derived size. The dashed green line is for y = x. Blue points are for the pole 1 solution, while brown points are for the pole 2 solution. Relative residuals are computed as follows: $100 \times (D_{\mathrm{CITPM}} - D_{\mathrm{occ}})/D_{\mathrm{occ}}$.

that the two methods yield consistent results. This demonstrates that, although CITPM determines size through thermophysical modelling and occultations do so through direct observation if the input data are of high quality, the CITPM provides as accurate results as multichord occultations. Targets which lay a little bit farther from the agreement line in Figure 3 can find an explanation in insufficient chord number or their poor placement, leading to the conclusion that CITPM size should be considered as more reliable in these cases (see Section 4.3).

In this work, we also compiled results for asteroid sizes from the literature, and present them in Table A.1. We focused on size values determined either through thermophysical modelling or via occultations. In some cases, particularly for occultations, a single value was reported in the literature, corresponding to the best-fit solution. These values are directly included in Table A.1. In other cases, both for occultations and for size values derived from TPM, the authors provided averaged size estimates. These values are also included as they were in Table A.1. For cases where the authors presented multiple values for diameters (often corresponding to mirror pole solutions), we averaged the results to ensure consistency with the rest of the dataset and to avoid having multiple entries for a single target. When occultation data did not allow us to resolve the mirror pole ambiguity, we also averaged our results between pole 1 and pole 2 to facilitate comparison with the values reported in the literature. The results are shown in Figure 5. The black points represent the values obtained in this work, while the grey points correspond to values from the literature. This plot demonstrates that our values are consistent with those published by other teams. Furthermore, when examining the residuals plot, it can be seen that our residuals are, on average, smaller than those based on the literature values.

Figure 4 shows MP3C error-weighted average values for diameters (available in Table 1) compared to CITPM values. CITPM values are also error-weighted averages between pole 1 and pole 2 in cases where no pole solution is preferred. Values in the last column of Table 1 correspond to the error-weighted mean diameters obtained by averaging results from multiple techniques listed in the MP3C database, whereas CITPM values are

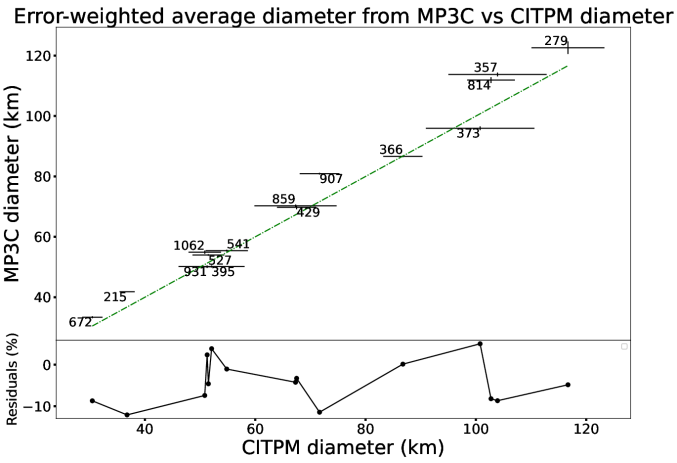

Fig. 4. Comparison between the error-weighted average of thermally derived asteroid diameters from the MP3C database and CITPM diameters derived in this work (Tables 1 and 4). The horizontal axis corresponds to the CITPM-derived size, while the vertical axis represents the average diameter from values listed in MP3C database. The dashed green line indicates y = x. If a certain pole solution is preferred, this solution is directly used for the CITPM value. If no solution is preferred, we apply the same error-weighted average that we applied to MP3C values (see Table 1).

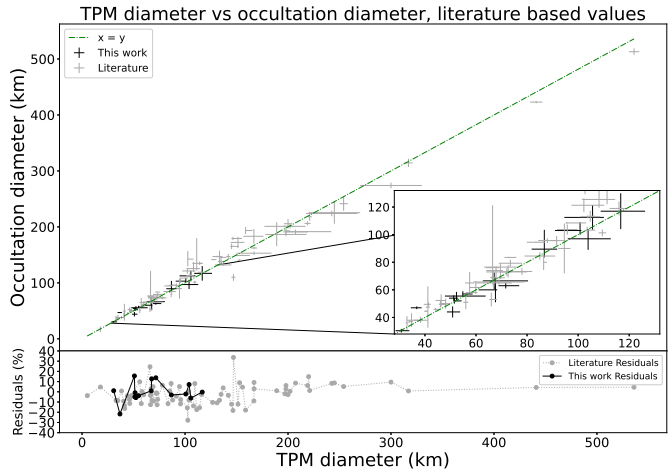

Fig. 5. Comparison between thermally derived diameters and occultation-based diameters from the literature (Table A.1). The horizontal axis corresponds to TPM size while the vertical axis is the occultation size. The dashed green line is for y = x. Grey points correspond to values from the literature, while black points correspond to pole-averaged values from this work. Relative residuals are computed as follows: $100 \times (D_{\mathrm{TPM}} - D_{\mathrm{occ}})/D_{\mathrm{occ}}$.

derived using a single, consistent modelling approach. Interestingly, when comparing the values from Table 1 and Table 4 with those in Table 5, CITPM estimates are generally slightly closer to those derived from occultations and provide a more accurate estimation of the associated uncertainties, despite relying on a single methodology.

4.5. Thermal inertia versus period

In this work, we primarily focused on the precise determination of asteroid sizes. However, since thermal inertia and rotation period are two other parameters simultaneously optimised in the CITPM, our results provide a good opportunity to compare these

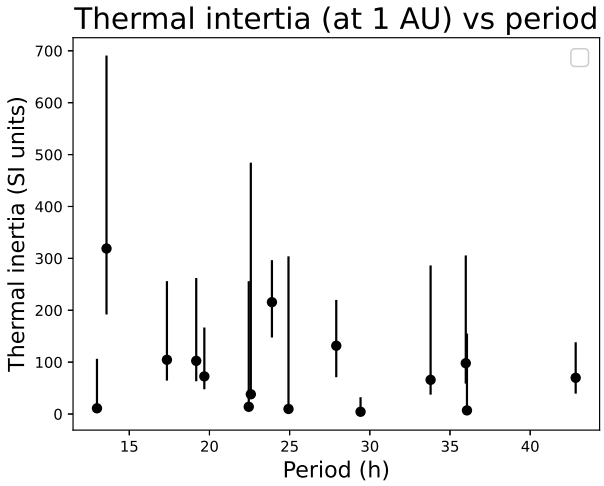

Fig. 6. Thermal inertia normalised to 1 AU (in $\mathrm{J\,m^{-2}\,s^{-\frac{1}{2}}\,K^{-1}}$, vertical axis) vs. rotation period (in hours, horizontal axis). Values for the mirror pole solutions have been averaged. No trend can be seen.

two parameters and assess a potential correlation, as suggested by Harris & Drube (2016). The result can be seen in Figure 6, where the x axis is the rotation period and the y axis represents the thermal inertia normalised to 1 AU following this equation (Mueller et al. 2010):

$$\Gamma_{\mathrm{norm}} = \Gamma * \left(\frac{R_{\mathrm{norm}}}{R_{\mathrm{target}}}\right)^{-\frac{3}{4}}, \tag{5}$$

where Γ and Γ_{norm} are, respectively, the thermal inertia and the normalised thermal inertia, R_{norm} and R_{target} being, respectively, the distance from the Sun at which the thermal inertia is normalised and an average distance between the target and the Sun during infrared observations.

In Figure 5 of Harris & Drube (2016), an increasing trend of greater thermal inertia for longer rotation periods is seen for periods above 10 hours. Our results cover a range of periods between 10 and 40 hours, which should be sufficient to observe this correlation. However, Figure 6 shows no such correlation, aligning with the conclusions drawn by other studies (Marciniak et al. 2019, 2021 and Hanuš et al. 2018).

5. Conclusions and future work

In this study, we combined two modelling techniques to determine the shapes and sizes of 15 main-belt asteroids: the light curve Inversion followed by CITPM. In parallel, we scaled their shape models using stellar occultation observations. Through two extensive observing campaigns, requiring significant human and observational resources, we obtained a substantial amount of dense light curves and occultation data (see the information in Zenodo repository described in Section 6). Using thermal data, systematically including observations from WISE spacecraft, coupled with an innovative thermophysical modelling approach (CITPM), allowed us to accurately determine asteroid sizes. Furthermore, the results show a good agreement with those obtained from stellar occultation fitting, confirming the robustness of the methodology. Discrepancies were generally around 5%, and in cases of greater differences, they were often due to the insufficient number of positive occultations or poor distribution of chords, making the CITPM model-derived values more reliable. Despite these significant advances, some challenges remain. For

example the dependence on convex approximation for the shape models may affect the ability to decouple thermal inertia from surface roughness (Delbo' et al. 2015, Ďurech et al. 2017).

Albedo values found here lay within a range for the target taxonomic types defined in the literature. However, contrary to studies suggesting a correlation between rotation period and thermal inertia (Harris & Drube 2016), our results did not find any significant trend, aligning with conclusions from other recent investigations.

The results of this study resolve substantial inconsistencies in size determinations for some large and medium-sized asteroids. These are essential for refining models of the evolution of the solar system, particularly concerning asteroid internal structure, composition and collisional processes, which require precise knowledge of the density, so a well-determined mass and even better-determined diameter (Carry 2012, Hanuš et al. 2017). Future advancements, including thermal data from space missions such as JWST or NEO Surveyor, could enable the determination of more precise thermophysical parameters for a larger number of asteroids. Finally, strengthening multi-chord observation campaigns for stellar occultations, supported by international collaborations, remains a primary objective to improve asteroid size determinations. In future work, reliable sizes from multichord stellar occultations could be used as a fixed parameter in (CI)TPM, better constraining the thermal inertia and surface roughness (Müller et al. 2018).

Data availability

Details of the observing campaigns: https://zenodo.org/records/15274451

Acknowledgements. This work was supported by the National Science Centre, Poland, through grant no. 2020/39/O/ST9/00713, and by the Polish National Agency for Academic Exchange through stipend agreement no. BPN/PRE/2022/U/0001. This project has been supported by the Lendület grant LP2012-31 of the Hungarian Academy of Sciences and by the KKP-137523 grant of the Hungarian National Research, Development and Innovation Office (NKFIH). This work was partially supported by a program of the Polish Ministry of Science under the title 'Regional Excellence Initiative', project no. RID/SP/0050/2024/1. This work was partly supported by the grant K-138962 of the National Research, Development and Innovation Office (NKFIH, Hungary). F.M. thanks the fellowship granted by FAPESP (2024/16260-6) and the IMPACTON team for the technical support at OASI. This work uses data obtained from the Asteroid Light-Curve Data Exchange Format (ALCDEF) database, which is supported by funding from NASA grant 80NSSC18K0851. This work is based on data provided by the Minor Planet Physical Properties Catalogue (MP3C) of the Observatoire de la Côte d'Azur. Observations at the Molėtai Observatory has been partially funded by Europlanet 2024. Europlanet 2024 RI has received funding from the European Union's Horizon 2020 research and innovation programme under grant agreement No 871149. The Joan Oró Telescope (TJO) of the Montsec Astronomical Observatory (OAdM) is owned by the Catalan Government and operated by the Institute for Space Studies of Catalonia (IEEC). This article is based on observations made in the Observatorios de Canarias del IAC with the 0.82m IAC80 telescope operated on the island of Tenerife by the Instituto de Astrofísica de Canarias (IAC) in the Observatorio del Teide. This article is based on observations made with the SARA telescopes (Southeastern Association for Research in Astronomy), whose nodes are located at the Observatorios de Canarias del IAC on the island of La Palma in the Observatorio del Roque de los Muchachos; Kitt Peak, AZ under the auspices of the National Optical Astronomy Observatory (NOAO); and Cerro Tololo Inter-American Observatory (CTIO) in La Serena, Chile. This project uses data from the SuperWASP archive. The WASP project is currently funded and operated by Warwick University and Keele University, and was originally set up by Queen's University Belfast, the Universities of Keele, St. Andrews, and Leicester, the Open University, the Isaac Newton Group, the Instituto de Astrofisica de Canarias, the South African Astronomical Observatory, and by STFC. TRAPPIST-South is a project funded by the Belgian Fonds (National) de la Recherche Scientifique (F.R.S.-FNRS) under grant PDR T.0120.21. TRAPPIST-North is a project funded by the University of Liège, in collaboration with the Cadi Ayyad University of Marrakech (Morocco). Funding for the Kepler and K2 missions are provided by the NASA Science Mission Directorate. The data presented in this paper were obtained from the Mikulski Archive for Space Telescopes (MAST). STScI is operated by the Association of Universities for Research in Astronomy, Inc., under NASA contract NAS5-26555. Support for MAST for non-HST data is provided by the NASA Office of Space Science via grant NNX09AF08G and by other grants and contracts. Data from Pic du Midi Observatory have been obtained with the 0.6-m telescope, a facility operated by Observatoíre Midi Pyrénées and Association T60, an amateur association. This research is partly based on observations obtained with the 60-cm Cassegrain telescope (TC60) and 90-cm Schmidt-Cassegrain telescope (TSC90) of the Institute of Astronomy of the Nicolaus Copernicus University in Toruń. This publication makes use of data products from the Wide-field Infrared Survey Explorer, which is a joint project of the University of California, Los Angeles, and the Jet Propulsion Laboratory/California Institute of Technology, funded by the National Aeronautics and Space Administration. We acknowledge the contributions of the occultation observers who have provided the observations in the dataset. Most of those observers are affiliated with one or more of: European Asteroidal Occultation Network (EAON), International Occultation Timing Association (IOTA), IOTA European Section (IOTA/ES), and IOTA East Asia Section (IOTA/EA), Japanese Occultation Information Network (JOIN), and Trans Tasman Occultation Alliance (TTOA).

References

Alí-Lagoa, V., Müller, T. G., Usui, F., & Hasegawa, S. 2018, A&A, 612, A85
Alí-Lagoa, V., Müller, T. G., Kiss, C., et al. 2020, A&A, 638, A84
Bartczak, P., & Dudziński, G. 2017, MNRAS, 473, 5050
Bus, S. J., & Binzel, R. P. 2002, Icarus, 158, 146
Cambioni, S., Delbo, M., Poggiali, G., et al. 2021, Nature, 598, 49
Čapek, D., & Vokrouhlický, D. 2010, A&A, 519, A75
Carry, B. 2012, Planet. Space Sci., 73, 98
Carry, B., Vachier, F., Berthier, J., et al. 2019, A&A, 623, A132
Carry, B., Vernazza, P., Vachier, F., et al. 2021, A&A, 650, A129
Delbo', M., & Tanga, P. 2009, Planet. Space Sci., 57, 259
Delbo', M., Mueller, M., Emery, J. P., Rozitis, B., & Capria, M. T. 2015, in Asteroids IV, eds. P. Michel, F. E. DeMeo, & W. F. Bottke, 107
Dias-Oliveira, A., Sicardy, B., Ortiz, J. L., et al. 2017, AJ, 154, 22
Ďurech, J., Kaasalainen, M., Warner, B. D., et al. 2009, A&A, 493, 291
Ďurech, J., Sidorin, V., & Kaasalainen, M. 2010, A&A, 513, A46
Ďurech, J., Kaasalainen, M., Herald, D., et al. 2011, Icarus, 214, 652
Ďurech, J., Delbo', M., Carry, B., Hanuš, J., & Alí-Lagoa, V. 2017, A&A, 604, A27
Ďurech, J., Hanuš, J., & Alí-Lagoa, V. 2018, A&A, 617, A57
Ďurech, J., Tonry, J., Erasmus, N., et al. 2020, A&A, 643, A59
Ferrais, M., Vernazza, P., Jorda, L., et al. 2020, A&A, 638, L15
Ferrais, M., Jorda, L., Vernazza, P., et al. 2022, A&A, 662, A71
Ferreira, J. F., Tanga, P., Spoto, F., Machado, P., & Herald, D. 2022, A&A, 658, A73
Franco, L., Pilcher, F., Oey, J., et al. 2024, Minor Planet Bull., 51, 100
Fuksa, M., Brož, M., Hanuš, J., et al. 2023, A&A, 677, A189
George, T., Garlitz, J., & Morton, A. 2019, J. Occult. Astron., 9, 3
Hanuš, J., Ďurech, J., Brož, M., et al. 2011, A&A, 530, A134
Hanuš, J., Ďurech, J., Brož, M., et al. 2013, A&A, 551, A67
Hanuš, J., Delbo', M., Ďurech, J., & Alí-Lagoa, V. 2015, Icarus, 256, 101
Hanuš, J., Delbo', M., Vokrouhlický, D., et al. 2016, A&A, 592, A34
Hanuš, J., Viikinkoski, M., Marchis, F., et al. 2017, A&A, 601, A114
Hanuš, J., Delbo', M., Ďurech, J., & Alí-Lagoa, V. 2018, Icarus, 309, 297
Hapke, B. 1981, J. Geophys. Res., 86, 3039
Hapke, B. 1984, Icarus, 59, 41
Hapke, B. 1986, Icarus, 67, 264
Harris, A. W. 1998, Icarus, 131, 291
Harris, A. W., & Drube, L. 2016, ApJ, 832, 127
Harris, A. W., & Harris, A. W. 1997, Icarus, 126, 450
Harris, A. W., & Lagerros, J. S. V. 2002, in Asteroids III, eds. W. F. Bottke, Jr., A. Cellino, P. Paolicchi, & R. P. Binzel, 205
Herald, D., Gault, D., Anderson, R., et al. 2020, MNRAS, 499, 4570
Herald, D., Gault, D., Carlson, N., et al. 2024, Small Bodies Occultations Bundle V4.0, NASA Planetary Data System, urn:nasa:pds:smallbodiesoccultations::4.0
Hung, D., Hanuš, J., Masiero, J. R., & Tholen, D. J. 2022, Planet. Sci. J., 3, 56
Jiang, H., Ji, J., & Yu, L. 2020, AJ, 159, 264
Kaasalainen, M. 2011, Inverse Problems and Imaging, 5, 37

Kaasalainen, M., & Ďurech, J. 2020, arXiv e-prints [arXiv:2005.09947]
Kaasalainen, M., & Lamberg, L. 2006, Inverse Probl., 22, 749
Kaasalainen, M., & Torppa, J. 2001, Icarus, 153, 24
Kaasalainen, M., & Viikinkoski, M. 2012, A&A, 543, A97
Kaasalainen, M., Torppa, J., & Muinonen, K. 2001, Icarus, 153, 37
Lagerros, J. S. V. 1996a, A&A, 310, 1011
Lagerros, J. S. V. 1996b, A&A, 315, 625
Lagerros, J. S. V. 1997, in AAS/Division for Planetary Sciences Meeting Abstracts, 29, 07.23
Lagerros, J. S. V. 1998, A&A, 332, 1123
Lang, K. R. 1999, Astrophysical formulae (New York: Springer)
Leiva, R., Sicardy, B., Camargo, J. I. B., et al. 2017, AJ, 154, 159
Lu, X.-P., Zhao, H.-B., & You, Z. 2013, Res. Astron. Astrophys., 13, 471
MacLennan, E. M., & Emery, J. P. 2019, AJ, 157, 2
MacLennan, E. M., & Emery, J. P. 2021, Planet. Sci. J., 2, 161
Mainzer, A., Bauer, J., Grav, T., et al. 2011, ApJ, 731, 53
Marciniak, A., Pilcher, F., Oszkiewicz, D., et al. 2015, Planet. Space Sci., 118, 256
Marciniak, A., Bartczak, P., Müller, T., et al. 2018, A&A, 610, A7
Marciniak, A., Alí-Lagoa, V., Müller, T. G., et al. 2019, A&A, 625, A139
Marciniak, A., Ďurech, J., Alí-Lagoa, V., et al. 2021, A&A, 654, A87
Marciniak, A., Ďurech, J., Choukroun, A., et al. 2023, A&A, 679, A60
Marsset, M., Carry, B., Dumas, C., et al. 2017, A&A, 604, A64
Marsset, M., Brož, M., Vernazza, P., et al. 2020, Nat. Astron., 4, 569
Masiero, J. R., Mainzer, A. K., Grav, T., et al. 2011, ApJ, 741, 68
Masiero, J. R., Mainzer, A. K., Grav, T., et al. 2012, ApJ, 759, L8
Masiero, J. R., Grav, T., Mainzer, A. K., et al. 2014, ApJ, 791, 121
Masiero, J. R., Nugent, C., Mainzer, A. K., et al. 2017, AJ, 154, 168
Masiero, J. R., Mainzer, A. K., Bauer, J. M., et al. 2020, Planet. Sci. J., 1, 5
Masiero, J. R., Mainzer, A. K., Bauer, J. M., et al. 2021, Planet. Sci. J., 2, 162
Matter, A., Delbo, M., Carry, B., & Ligori, S. 2013, Icarus, 226, 419
Morbidelli, A., Bottke, W. F., Nesvorný, D., & Levison, H. F. 2009, Icarus, 204, 558
Mueller, M., Marchis, F., Emery, J. P., et al. 2010, Icarus, 205, 505
Müller, T., Marciniak, A., Kiss, C., et al. 2018, Adv. Space Res., 62, 2326
Neugebauer, G., Habing, H. J., van Duinen, R., et al. 1984, ApJ, 278, L1
Nugent, C. R., Mainzer, A., Bauer, J., et al. 2016, AJ, 152, 63
Pilcher, F. 2014, Minor Planet Bull., 41, 73
Podlewska-Gaca, E., Marciniak, A., Alí-Lagoa, V., et al. 2020, A&A, 638, A11
Rommel, F. L., Braga-Ribas, F., Desmars, J., et al. 2020, A&A, 644, A40
Rommel, F. L., Braga-Ribas, F., Ortiz, J. L., et al. 2023, A&A, 678, A167
Rozitis, B., & Green, S. F. 2011, MNRAS, 415, 2042
Ryan, E. L., & Woodward, C. E. 2010, AJ, 140, 933
Satō, I., Hamanowa, H., Tomioka, H., & Uehara, S. 2015, Int. J. Astron. Astrophys., 5, 193
Shannon, C. 1949, Proc. IRE, 37, 10
Szakáts, R., Müller, T., Alí-Lagoa, V., et al. 2020, A&A, 635, A54
Tanga, P., Delbo', M., & Gerakis, J. 2013, in AAS/Division for Planetary Sciences Meeting Abstracts, 45, 208.29
Tanga, P., Carry, B., Colas, F., et al. 2015, MNRAS, 448, 3382
Tedesco, E. F., Noah, P. V., Noah, M., & Price, S. D. 2002, AJ, 123, 1056
Tholen, D. J. 1984, PhD thesis, University of Arizona, USA
Usui, F., Kuroda, D., Müller, T. G., et al. 2011, PASJ, 63, 1117
Vereš, P., Jedicke, R., Fitzsimmons, A., et al. 2015, Icarus, 261, 34
Warner, B. D., Harris, A. W., & Pravec, P. 2009, Icarus, 202, 134
Wright, E. L., Eisenhardt, P. R. M., Mainzer, A. K., et al. 2010, AJ, 140, 1868
Yu, L. L., Yang, B., Ji, J., & Ip, W.-H. 2017, MNRAS, 472, 2388

[1] Astronomical Observatory Institute, Faculty of Physics and Astronomy, Adam Mickiewicz University, Słoneczna 36, 60-286 Poznań, Poland
[2] Astronomical Institute, Faculty of Mathematics and Physics, Charles University, V Holešovičkách 2, 80 00 Prague 8, Czech Republic
[3] Mt. Suhora Observatory, University of the National Education Commission, Podchorążych 2, 30-084 Cracow, Poland
[4] Konkoly Observatory, HUN-REN Research Centre for Astronomy and Earth Sciences, Konkoly Thege Miklós út 15–17, 1121 Budapest, Hungary
[5] CSFK, MTA Centre of Excellence, Budapest, Konkoly Thege Miklós út 15–17, 1121 Hungary
[6] MTA CSFK Lendület Near-Field Cosmology Research Group, Hungary
[7] ELTE Eötvös Loránd University, Institute of Physics and Astronomy, 1117, Pázmány Péter sétány 1/A, Budapest, Hungary
[8] Astronomy Department, Eötvös Loránd University, Pázmány P. s. 1/A, 1171 Budapest, Hungary
[9] Observatório Nacional, R. Gen. José Cristino 77, São Cristóvão, 20921-400 Rio de Janeiro, RJ, Brazil
[10] Grupo de Dinâmica Orbital e Planetologia, São Paulo State University, UNESP, Guaratinguetá, CEP 12516-410, São Paulo, Brazil
[11] International Occultation Timing Association/European Section e.V. (IOTA/ES), Am Brombeerhag 13, 30459 Hannover, Germany
[12] International Occultation Timing Association (IOTA) PO Box 20313 Fountain Hills, AZ 85269-0313, USA
[13] Association T60, Observatoire Midi-Pyrénées, 14, avenue Edouard Belin, 31400 Toulouse, France
[14] Korea Astronomy and Space Science Institute, 776 Daedeok-daero, Yuseong-gu, Daejeon 34055, Korea
[15] Centro Astronómico Hispano en Andalucía, Observatorio de Calar Alto, Sierra de los Filabres, 04550 Gérgal, Spain
[16] MTA-ELTE Lendület "Momentum" Milky Way Research Group, Hungary
[17] Instituto de Astrofísica de Andalucía (CSIC), Glorieta de la Astronomía s/n, 18008 Granada, Spain
[18] Maastricht University, Maastricht Science Programme, Maastricht, The Netherlands
[19] Observatoire du Bois de Bardon, 16110 Taponnat, France
[20] Florida Space Institute, University of Central Florida, Orlando, FL, USA
[21] Trans-Tasman Occultation Alliance (TTOA), Wellington, PO Box 3181, New Zealand
[22] Instituto de Astrofísica de Canarias, C/ Vía Lactea, s/n, 38205 La Laguna, Tenerife, Spain
[23] Gran Telescopio Canarias (GRANTECAN), Cuesta de San José s/n, 38712, Breña Baja, La Palma, Spain
[24] Institute of Astronomy, Faculty of Physics, Astronomy and Informatics, Nicolaus Copernicus University in Toruń, ul. Grudziądzka 5, 87-100 Toruń, Poland
[25] Open University, School of Physical Sciences, The Open University, MK7 6AA, UK
[26] Hunters Hill Observatory, 7 Mawalan Street, Ngunnawal, ACT 2913, Australia
[27] Space sciences, Technologies and Astrophysics Research Institute, Université de Liège, Allée du 6 Août 17, 4000 Liège, Belgium
[28] British Astronomical Association, PO Box 702, Tonbridge TN9 9TX, UK
[29] Institute of Physics, Jan Kochanowski University, ul. Uniwersytecka 7, 25-406 Kielce, Poland
[30] Akdeniz University, Department of Space Sciences and Technologies, Antalya, Türkiye
[31] Chungbuk National University, 1, Chungdae-ro, Seowon-gu, Cheongju-si, Chungcheongbuk-do, Republic of Korea
[32] Czech Astronomical Society, Fričova 298, 251 65 Ondřejov, Czech Republic
[33] Observatory in Rokycany and Pilsen, p.o., Voldušská 721, 337 01 Rokycany, Czech Republic
[34] Laboratory of Space Researches, Uzhhorod National University, Daleka st. 2a, 88000 Uzhhorod, Ukraine
[35] Observatoire de Nandrin, Société Astronomique de Liège, 17 Avenue des Platanes, 4000 Liège, Belgium
[36] Departamento de Astrofísica, Universidad de La Laguna – ULL, 38205 Tenerife, Spain
[37] NASA Johnson Space Center Astronomical Society, Houston, TX, USA
[38] Janusz Gil Institute of Astronomy, University of Zielona Góra, Szafrana 2, 65-516 Zielona Góra, Poland
[39] Japan Occultation Information Network (JOIN), Japan
[40] B-PHOT, Building F, Pleinlaan 2, 1050 Elsene, Brussels, Belgium
[41] Blue Mountains Observatory, 94 Rawson Parade, Leura, NSW 2780, Australia

[42] Institute of Theoretical Physics and Astronomy, Vilnius University, Saulėtekio al. 3, 10257 Vilnius, Lithuania
[43] Organ Mesa Observatory, 4438 Organ Mesa Loop, Las Cruces, NM 88011, USA
[44] Command Module Observatory, 121 W. Alameda Dr., Tempe, AZ 85282, USA
[45] Silesian University of Technology, Department of Electronics, Electrical Engineering and Microelectronics, Akademicka 16, 44-100 Gliwice, Poland
[46] Lunar and Planetary Laboratory, University of Arizona, Tucson, AZ 85721, USA
[47] Osservatorio Astronomico Via Nastro Verde 50, 80067, Sorrento (Na), Italy
[48] Departamento de Física, Ingeniería de Sistemas y Teoría de la Señal, Universidad de Alicante, Carr. de San Vicente del Raspeig, s/n, 03690 San Vicente del Raspeig, Alicante, Spain
[49] Institut de Ciències del Cosmos (ICCUB), Universitat de Barcelona (IEEC-UB), Carrer de Martí i Franquès, 1, 08028 Barcelona, Spain
[50] Lowell Observatory, 1400 West Mars Hill Road, Flagstaff, AZ, 86001 USA
[51] Department of Physics, Adiyaman University, 02040 Adiyaman, Türkiye
[52] Astrophysics Application and Research Center, Adıyaman University, Adiyaman 02040, Türkiye
[53] European Southern Observatory, Karl-Schwarzschild-Strasse 2, 85748 Garching bei München, Germany
[54] Japan Spaceguard Association, Bisei Spaceguard Center, 1716-3, Okura, Bisei, Ibara, Okayama 714-1411 Japan
[55] Observatory, Vsetínská 78, Valašské Meziříčí, Czech Republic
[56] Astronomical Observatory, Jagiellonian University, ul. Orla 171, 30-244 Cracow, Poland

Appendix A: Published TPM and Occultation values

Table A.1: Diameters from the literature obtained through TPM and those determined with the use of stellar occultations.

Target	D_{tpm}	$references_{TPM}$	D_{occ}	$references_{occ}$
(2) Pallas	536.0 ± 5.0	Alí-Lagoa et al. (2020)	513.0 ± 6.0	Marsset et al. (2020)
(3) Juno	254.0 ± 4.0	Alí-Lagoa et al. (2020)	241.5 ± 12.7	Herald et al. (2020)
(5) Astraea	$103.8^{+4.8}_{-2.9}$	Hung et al. (2022)	113.0 ± 1.0	Herald et al. (2020)
(6) Hebe	$198.0^{+4.0}_{-2.0}$	Marsset et al. (2017)	193.0 ± 6.0	Marsset et al. (2017)
(8) Flora	142.0 ± 2.0	Alí-Lagoa et al. (2020)	147.0 ± 4.7	Herald et al. (2020)
(10) Hygeia	441.0 ± 6.0	Alí-Lagoa et al. (2020)	423.0 ± 2.0	Herald et al. (2020)
(14) Irene	$133.45^{+6.6}_{-0.0}$	Hung et al. (2022)	145.5 ± 12.0	Podlewska-Gaca et al. (2020)
(16) Psyche	242.5 ± 25.0	Matter et al. (2013)	224.0 ± 5.0	Ferrais et al. (2020)
(17) Thetis	$72.6^{+1.6}_{-0.0}$	Hung et al. (2022)	73.5 ± 4.5	Herald et al. (2020)
(18) Melpomene	135.0 ± 3.0	Alí-Lagoa et al. (2020)	138.4 ± 6.3	Herald et al. (2020)
(19) Fortuna	219.0 ± 3.0	Alí-Lagoa et al. (2020)	206.3 ± 3.6	Herald et al. (2020)
(20) Massalia	147.0 ± 2.0	Alí-Lagoa et al. (2020)	$110.0^{+5.5}_{-6.35}$	Podlewska-Gaca et al. (2020)
(21) Lutetia	95.76 ± 4.0	Alí-Lagoa et al. (2020)	103.7 ± 3.7	Herald et al. (2020)
(22) Kalliope	167.0 ± 17.0	Delbo' et al. (2015)	153.0 ± 3.0	Ferrais et al. (2022)
(27) Euterpe	$95.6^{+7.5}_{-0.5}$	Hung et al. (2022)	108.5 ± 0.5	Herald et al. (2020)
(29) Amphitrite	202.0 ± 3.0	Alí-Lagoa et al. (2020)	201.0 ± 3.8	Herald et al. (2020)
(41) Daphne	189.0 ± 1.0	Delbo' et al. (2015)	187.0 ± 21.5	Carry et al. (2019)
(43) Ariadne	$59.9^{+2.0}_{-2.6}$	Hung et al. (2022)	61.7 ± 4.4	Herald et al. (2020)
(45) Eugenia	198.0 ± 20.0	Delbo' et al. (2015)	186.5 ± 3.2	Herald et al. (2020)
(52) Europa	317.0 ± 4.0	Alí-Lagoa et al. (2020)	314.4 ± 7.5	Herald et al. (2020)
(54) Alexandra	153.0 ± 2.0	Alí-Lagoa et al. (2020)	140.5 ± 1.5	Herald et al. (2020)
(56) Melete	$104.75^{+1.8}_{-0.3}$	Hung et al. (2022)	113.4 ± 4.0	Herald et al. (2020)
(63) Ausonia	94.6 ± 2.4	Jiang et al. (2020)	90.0 ± 18.0	Ďurech et al. (2011)
(64) Angelina	$46.05^{+2.1}_{-0.1}$	Hung et al. (2022)	$49.8^{+2.95}_{-2.65}$	Podlewska-Gaca et al. (2020)
(68) Leto	$102.7^{+5.6}_{-0.3}$	Hung et al. (2022)	$142.4^{+14.6}_{-13.15}$	Podlewska-Gaca et al. (2020)
(71) Niobe	$72.9^{+2.9}_{-1.7}$	Hung et al. (2022)	83.5 ± 0.5	Herald et al. (2020)
(76) Freia	$151.4^{+6.3}_{-7.3}$	Hung et al. (2022)	172.3 ± 10.1	Herald et al. (2020)
(80) Sappho	$66.7^{+4.6}_{-0.8}$	Hung et al. (2022)	68.7 ± 5.7	Herald et al. (2020)
(85) Io	$145.2^{+7.2}_{-1.3}$	Hung et al. (2022)	165.2 ± 4.8	Herald et al. (2020)
(87) Sylvia	300.0 ± 30.0	Delbo' et al. (2015)	274.0 ± 5.0	Carry et al. (2021)
(88) Thisbe	221.0 ± 2.0	Alí-Lagoa et al. (2020)	218.2 ± 7.4	Herald et al. (2020)
(93) Minerva	167.0 ± 3.0	Alí-Lagoa et al. (2020)	162.3 ± 1.7	Herald et al. (2020)
(94) Aurora	$158.8^{+6.7}_{-0.0}$	Hung et al. (2022)	193.5 ± 6.2	Herald et al. (2020)
(95) Arethusa	$131.1^{+5.2}_{-4.5}$	Hung et al. (2022)	147.0 ± 1.4	Herald et al. (2020)
(99) Dike	66.5 ± 0.9	Hanuš et al. (2018)	69.0 ± 3.0	Herald et al. (2020)
(107) Camilla	245.0 ± 25.0	Delbo' et al. (2015)	225.4 ± 19.8	Herald et al. (2020)
(109) Felicitas	85.0 ± 6.0	MacLennan & Emery (2019)	84.5 ± 2.7	Herald et al. (2020)
(121) Hermione	220.0 ± 22.0	Delbo' et al. (2015)	191.5 ± 0.5	Herald et al. (2020)
(130) Elektra	197.0 ± 20.0	Delbo' et al. (2015)	201.0 ± 2.0	Fuksa et al. (2023)
(135) Hertha	$73.45^{+4.6}_{-4.5}$	Hung et al. (2022)	79.3 ± 2.5	Herald et al. (2020)
(152) Atala	57.5 ± 1.8	Hanuš et al. (2018)	65.0 ± 8.0	Ďurech et al. (2011)
(158) Koronis	$34.75^{+4.4}_{-1.9}$	Hung et al. (2022)	38.0 ± 5.0	Ďurech et al. (2011)
(159) Aemilia	137.0 ± 8.0	Marciniak et al. (2018)	132.0 ± 2.0	Herald et al. (2020)
(166) Rhodope	$48.1^{+1.9}_{-2.3}$	Hung et al. (2022)	50.0 ± 3.6	Herald et al. (2020)
(167) Urda	41.15 ± 0.8	Hanuš et al. (2018)	47.5 ± 15.0	Ďurech et al. (2011)
(187) Lamberta	$126.8^{+3.8}_{-1.4}$	Hung et al. (2022)	141.5 ± 0.5	Herald et al. (2020)
(192) Nausikaa	87.95 ± 3.6	Hung et al. (2022)	95.7 ± 1.7	Herald et al. (2020)
(199) Byblis	$66.0^{+2.2}_{-0.8}$	Hung et al. (2022)	53.0 ± 5.0	Herald et al. (2020)
(208) Lacrimosa	40.4 ± 0.7	MacLennan & Emery (2019)	44.5 ± 0.5	Herald et al. (2020)
(234) Barbara	$44.1^{+1.9}_{-0.7}$	Hung et al. (2022)	45.9 ± 1.0	Tanga et al. (2015)
(276) Adelheid	$102.25^{+8.0}_{-4.9}$	Hung et al. (2022)	121.3 ± 5.0	Herald et al. (2020)
(306) Unitas	56.0 ± 1.0	Delbo' et al. (2015)	51.0 ± 5.0	Ďurech et al. (2011)
(328) Gudrun	$103.55^{+3.2}_{-0.6}$	Hung et al. (2022)	103.3 ± 2.5	Herald et al. (2020)
(329) Svea	78.0 ± 4.0	Marciniak et al. (2018)	73.3 ± 2.5	Herald et al. (2020)
(334) Chicago	$146.55^{+8.8}_{-1.6}$	Hung et al. (2022)	179.3 ± 2.9	Herald et al. (2020)
(347) Pariana	$46.35^{+1.7}_{-2.2}$	Hung et al. (2022)	52.3 ± 4.5	Herald et al. (2020)
(349) Dembowska	155.8 ± 7.1	Yu et al. (2017)	149.0 ± 1.0	Herald et al. (2020)
(350) Ornamenta	$116.0^{+3.1}_{-3.7}$	Hung et al. (2022)	119.0 ± 5.0	Herald et al. (2020)

(Continued on next page...)

Table A.1: continued.

Target	D_{tpm}	references$_{TPM}$	D_{occ}	references$_{occ}$
(360) Carlova	$114.1^{+3.3}_{-0.7}$	Hung et al. (2022)	135.0 ± 3.0	Hanuš et al. (2017)
(365) Corduba	$83.5^{+3.5}_{-3.6}$	Hung et al. (2022)	94.5 ± 0.5	Herald et al. (2020)
(372) Palma	$166.85^{+9.2}_{-10.3}$	Hung et al. (2022)	183.2 ± 13.1	Herald et al. (2020)
(380) Fiducia	72.0 ± 8.0	Marciniak et al. (2019)	73.0 ± 1.0	Herald et al. (2020)
(381) Myrrha	$111.35^{+4.9}_{-4.2}$	Hung et al. (2022)	$134.8^{+45.3}_{-12.8}$	Podlewska-Gaca et al. (2020)
(404) Arsinoe	$91.6^{+3.4}_{-2.3}$	Hung et al. (2022)	95.7 ± 3.3	Herald et al. (2020)
(423) Diotima	200.0 ± 4.0	Alí-Lagoa et al. (2020)	205.7 ± 8.4	Herald et al. (2020)
(426) Hippo	$108.2^{+6.3}_{-6.7}$	Hung et al. (2022)	$125.5^{+11.5}_{-6}$	Marciniak et al. (2023)
(433) Eros	17.8 ± 0.5	Delbo' et al. (2015)	17.0 ± 5.0	Herald et al. (2020)
(439) Ohio	$67.85^{+2.7}_{-3.8}$	Hung et al. (2022)	74.0^{+3}_{-8}	Marciniak et al. (2023)
(441) Bathilde	$66.5^{+2.5}_{-2.6}$	Hung et al. (2022)	$76.05^{+45.25}_{-10.0}$	Podlewska-Gaca et al. (2020)
(458) Hercynia	$33.8^{+1.5}_{-0.0}$	Hung et al. (2022)	37.0 ± 1.0	Herald et al. (2020)
(464) Megaira	69.56 ± 6.38	MacLennan & Emery (2021)	$76.5^{+2.5}_{-8.5}$	Marciniak et al. (2023)
(468) Lina	69.0 ± 10.0	Marciniak et al. (2019)	65.7 ± 1.9	Herald et al. (2020)
(532) Herculina	207.3 ± 12.0	Delbo' et al. (2015)	191.0 ± 4.0	Hanuš et al. (2017)
(580) Selene	$47.35^{+1.2}_{-1.9}$	Hung et al. (2022)	49.5 ± 0.5	Herald et al. (2020)
(657) Gunlod	$38.3^{+2.8}_{-2.7}$	Hung et al. (2022)	$38.0^{+2.5}_{-2}$	Marciniak et al. (2023)
(694) Ekard	109.5 ± 1.5	Delbo' et al. (2015)	101.3 ± 2.5	Herald et al. (2020)
(695) Bella	$41.4^{+0.9}_{-1.9}$	Hung et al. (2022)	49.5 ± 1.5	Herald et al. (2020)
(757) Portlandia	32.95 ± 0.5	Hanuš et al. (2018)	36.0 ± 5.0	Herald et al. (2020)
(791) Ani	$86.5^{+1.3}_{-0.0}$	Hung et al. (2022)	80.0 ± 5.6	Herald et al. (2020)
(834) Burnhamia	67.0 ± 7.0	Marciniak et al. (2019)	65.0 ± 2.8	Herald et al. (2020)
(849) Ara	$72.1^{+1.7}_{-2.3}$	Hung et al. (2022)	73.0 ± 3.0	Hanuš et al. (2017)
(925) Alphonsina	$58.15^{+2.4}_{-2.2}$	Hung et al. (2022)	58.0 ± 0.8	Herald et al. (2020)
(3200) Phaethon	5.1 ± 0.2	Hanuš et al. (2016)	5.3 ± 0.4	Herald et al. (2020)

Notes. If one value was provided or a specific pole was preferred, the value is included directly in this table. In cases where solutions for two poles were reported in the literature without distinction, their respective sizes are averaged here, and the maximum uncertainty is adopted.

Appendix B: Chi-squared plots vs. thermal inertia

Plots of $\chi^2_{\rm red}$ versus thermal inertia for various levels of surface roughness described by $\bar{\theta}$ (symbol coded) and optimised diameter (colour coded). Plots present the results for one pole solution since the results for the mirror-pole solution were similar.

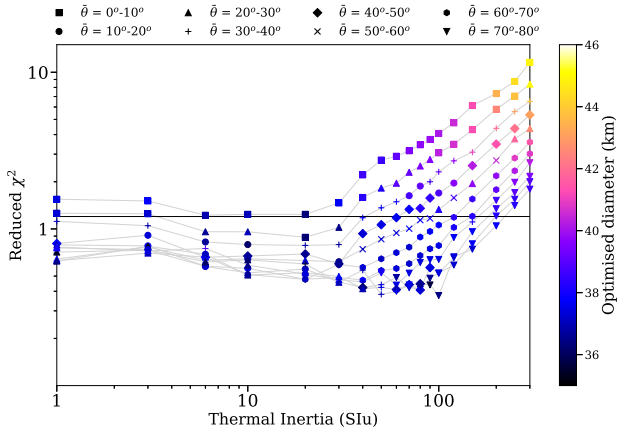

Fig. B.1: (215) Oenone: reduced χ^2 vs. Γ. The horizontal line represents the threshold for accepting a solution based on thermal data. The plot corresponds to pole solution 1.

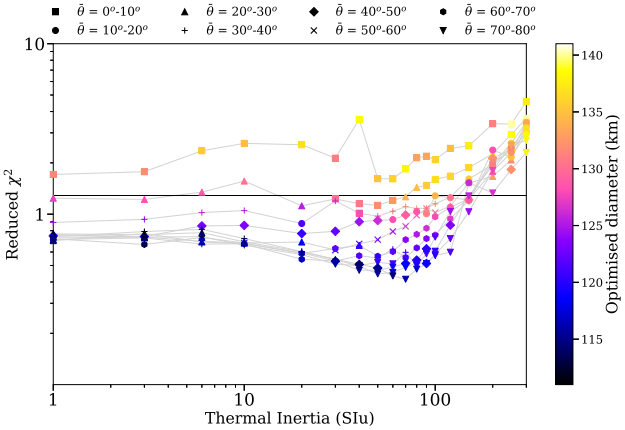

Fig. B.2: (279) Thule: reduced χ^2 vs. Γ for pole 1.

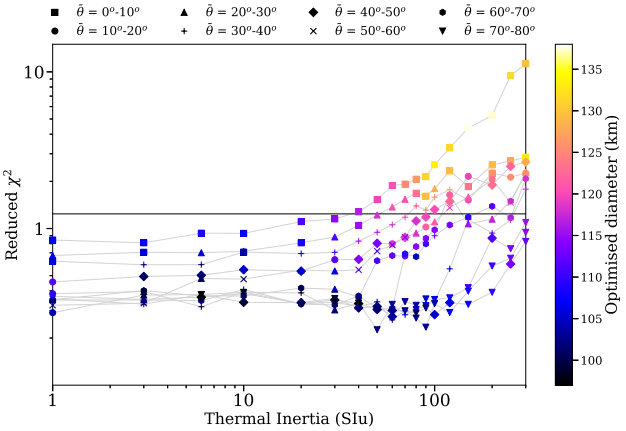

Fig. B.3: (357) Ninina: reduced χ^2 vs. Γ for pole 1.

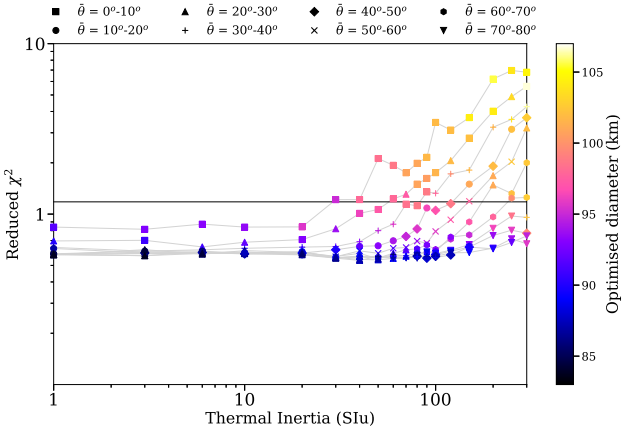

Fig. B.4: (366) Vincentina: reduced χ^2 vs. Γ for pole 1.

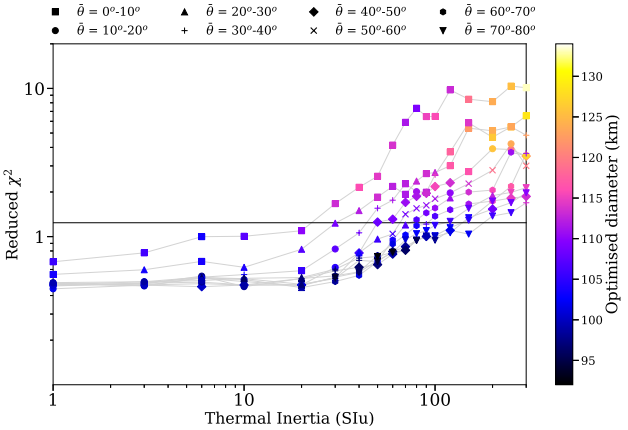

Fig. B.5: (373) Melusina: reduced χ^2 vs. Γ for pole 2.

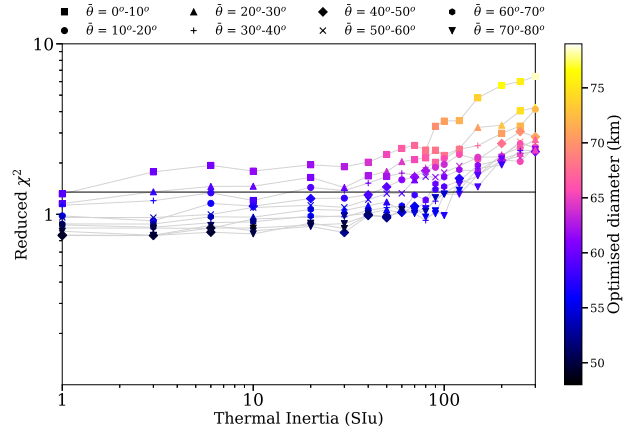

Fig. B.6: (395) Delia: reduced χ^2 vs. Γ for pole 1.

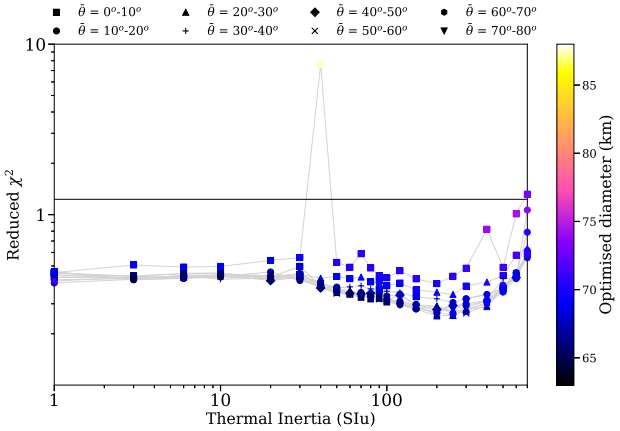

Fig. B.7: (429) Lotis: reduced χ^2 vs. Γ for pole 1.

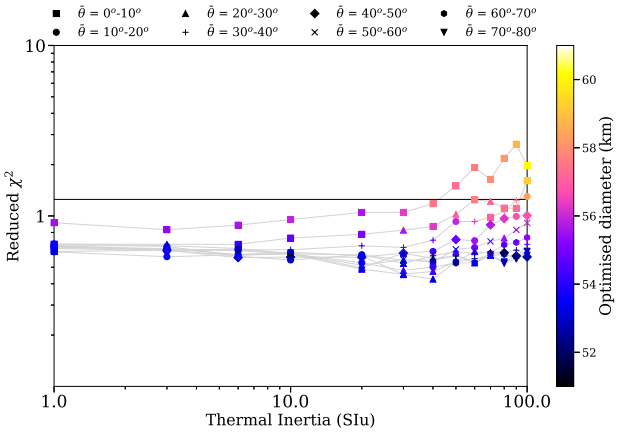

Fig. B.8: (527) Euryanthe: reduced χ^2 vs. Γ for pole 2.

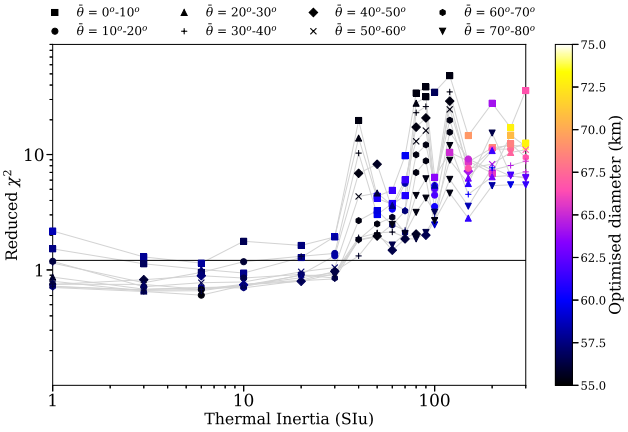

Fig. B.9: (541) Deborah: reduced χ^2 vs. Γ for pole 2.

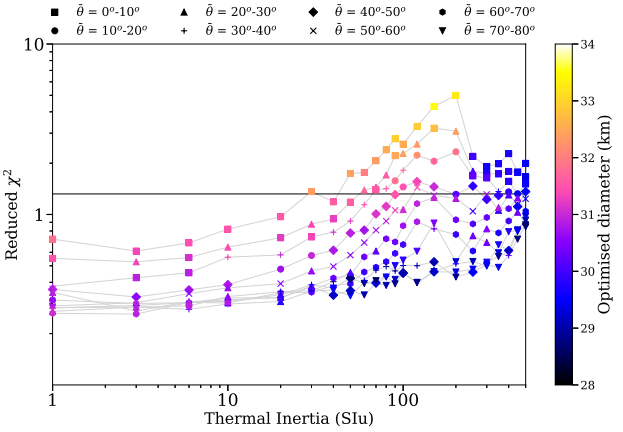

Fig. B.10: (672) Astarte: reduced χ^2 vs. Γ for pole 1.

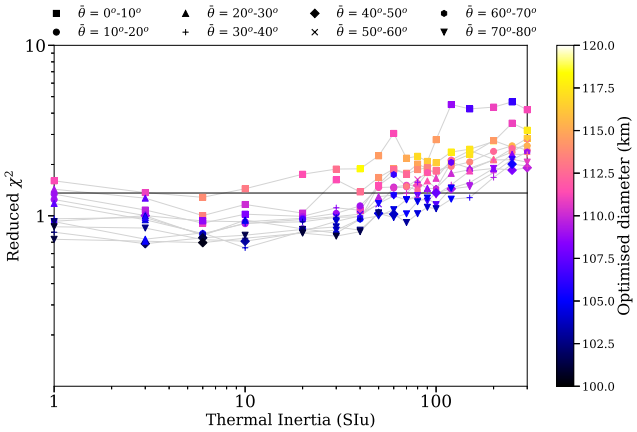

Fig. B.11: (814) Tauris: reduced χ^2 vs. Γ for pole 1.

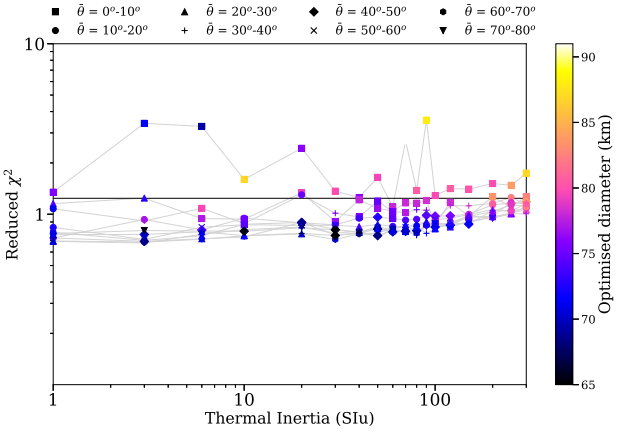

Fig. B.12: (859) Bouzareah: reduced χ^2 vs. Γ for pole 1.

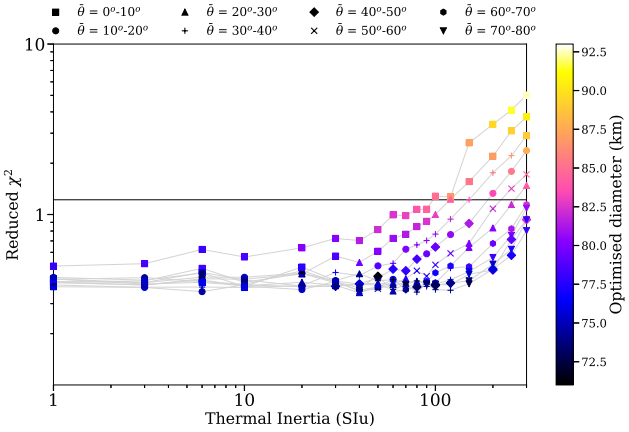

Fig. B.13: (907) Rhoda: reduced χ^2 vs. Γ for pole 1.

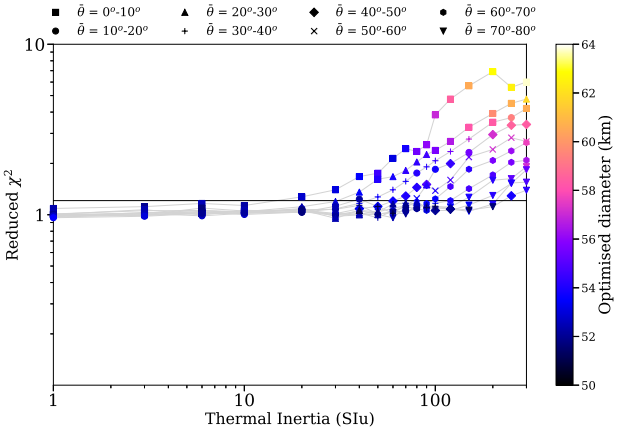

Fig. B.14: (931) Whittemora: reduced χ^2 vs. Γ for pole 2.

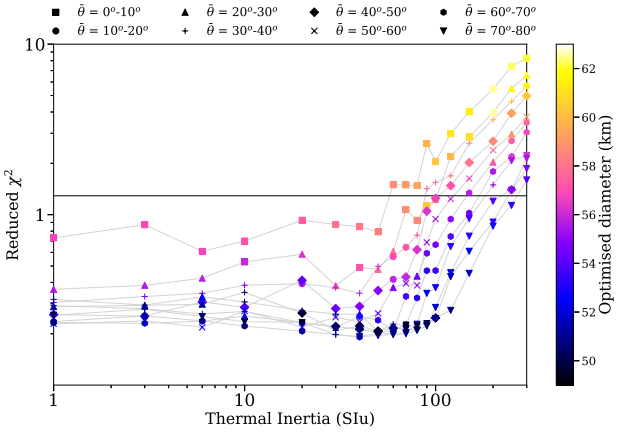

Fig. B.15: (1062) Ljuba: reduced χ^2 vs. Γ for pole 2.

Appendix C: Example fits to light curves in the visible range

Model fit to light curves in the visible range obtained from Kepler and TESS spacecrafts (Figures C.1–C.10) for the preferred pole solution (see Table 5). When no pole solution was preferred, the fit for pole 1 is shown. Fit to the whole light curve dataset can be viewed in the DAMIT database.

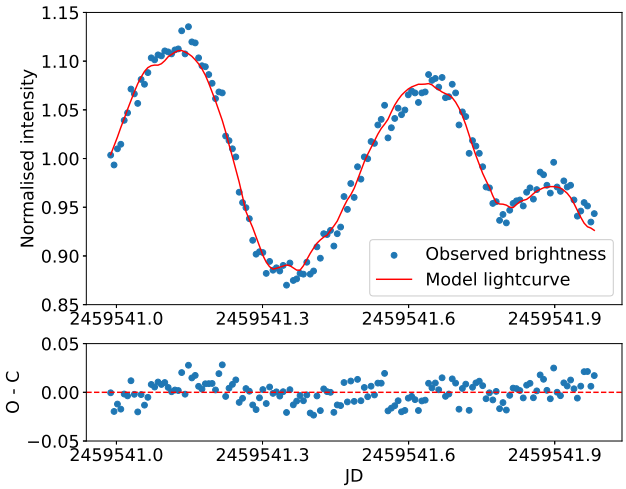

Fig. C.1: (215) Oenone model light curve fit (red line) to visible data from TESS spacecraft (blue points)

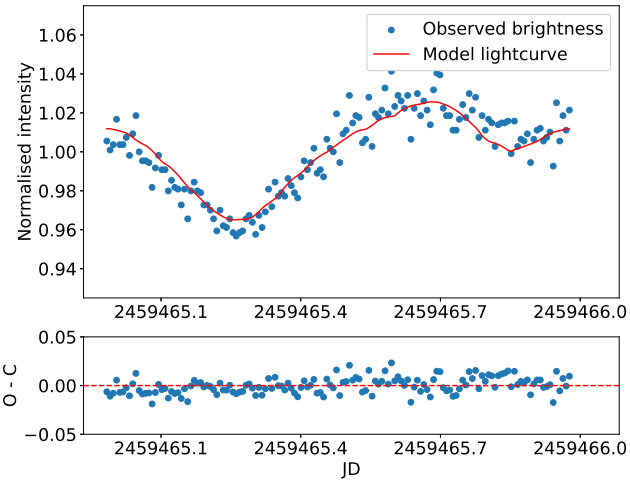

Fig. C.2: (279) Thule model fit to TESS data

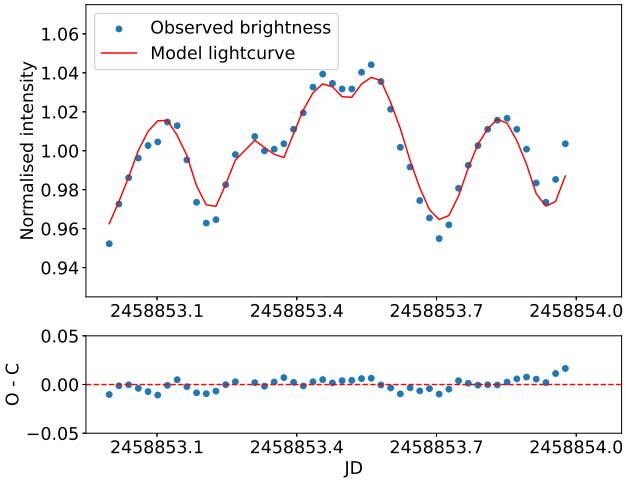

Fig. C.3: (366) Vincentina model fit to TESS data

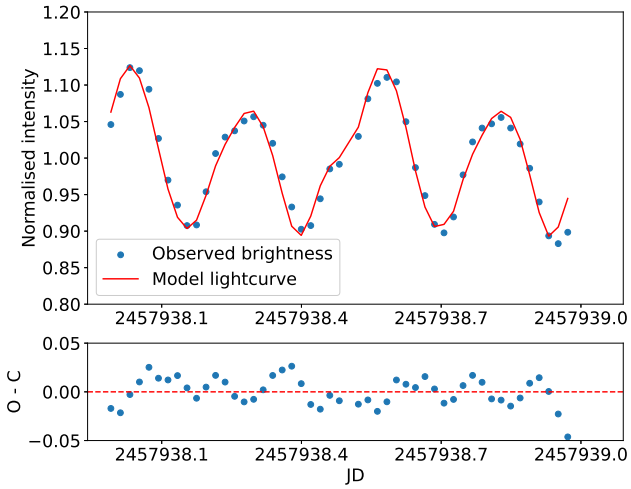

Fig. C.4: (373) Melusina model fit to Kepler data

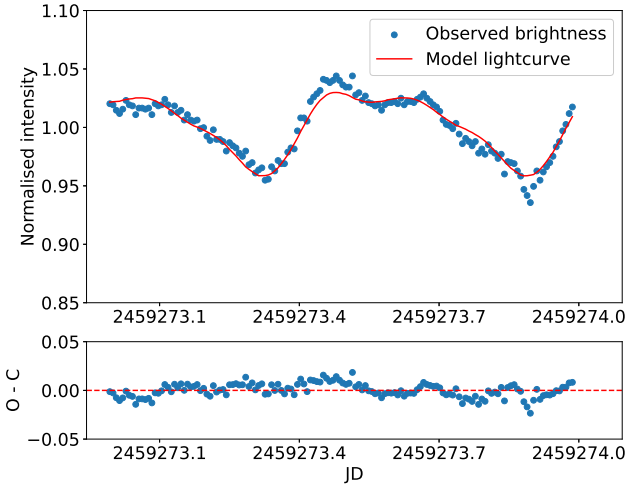

Fig. C.5: (429) Lotis model fit to TESS data

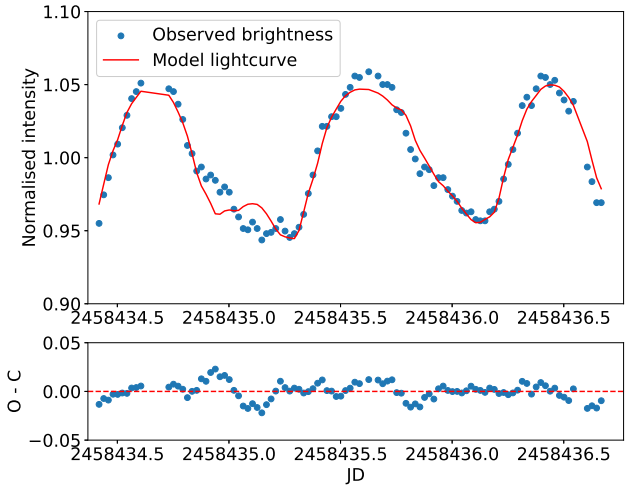

Fig. C.6: (527) Euryanthe model fit to TESS data

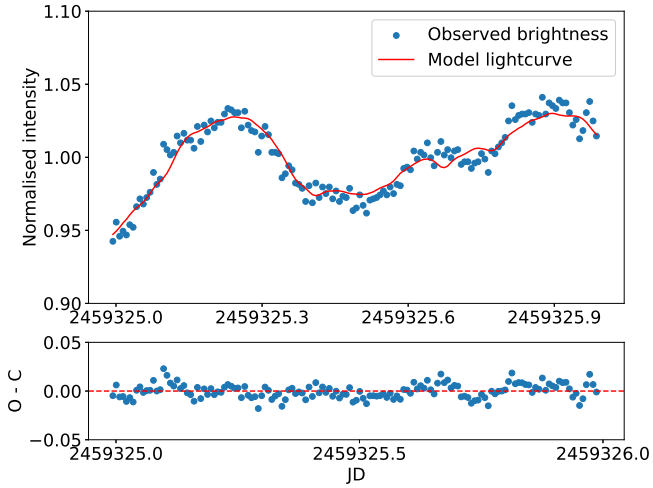

Fig. C.7: (541) Deborah model fit to TESS data

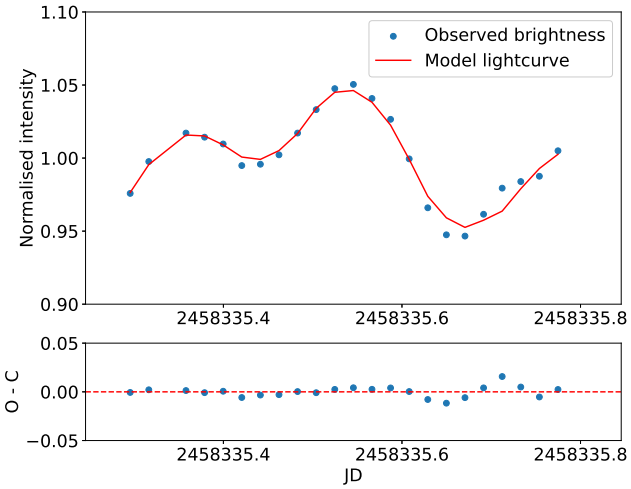

Fig. C.8: (672) Astarte model fit to TESS data

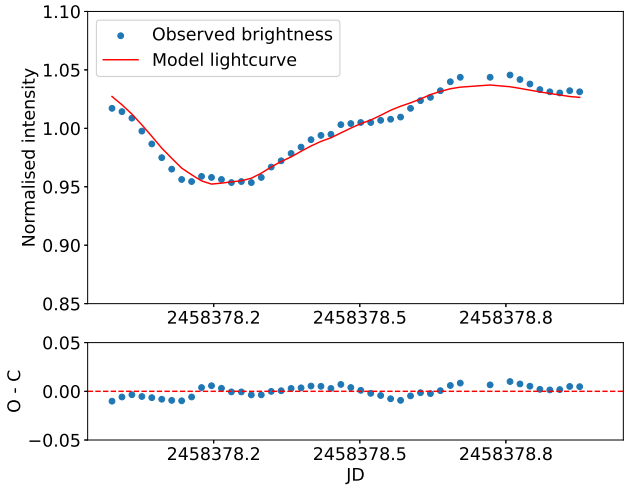

Fig. C.9: (1062) Ljuba model fit to Kepler data

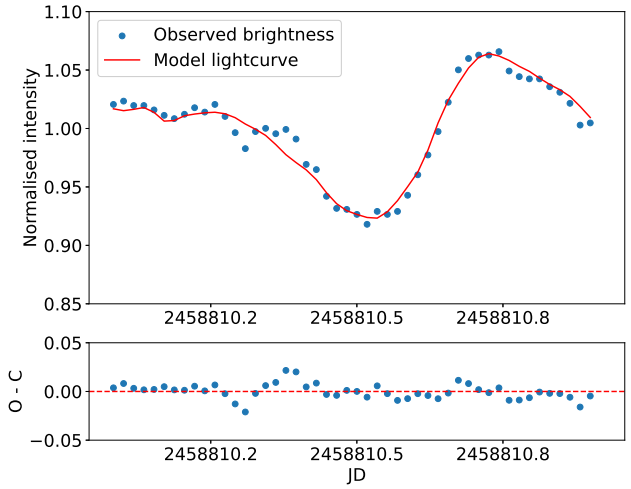

Fig. C.10: (1062) Ljuba model fit to TESS data

Appendix D: Model fits to thermal light curves

Model fit to non-saturated WISE thermal light curves (Figures D.1–D.21) for the preferred pole solution (see Table 5). When no pole solution was preferred, the fit for pole 1 is shown.

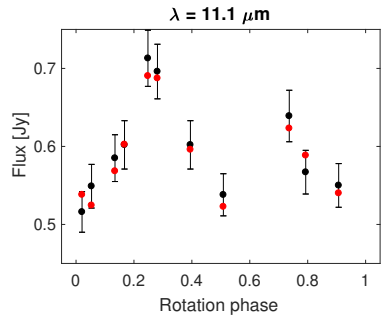

Fig. D.1: (215) Oenone model flux (red points) compared with data point (black) from the W3 band from WISE spacecraft.

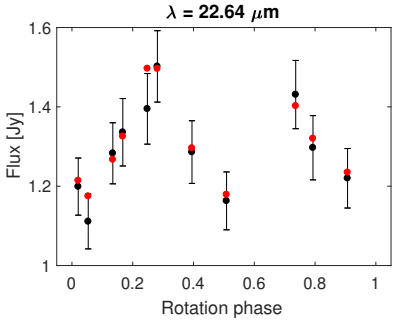

Fig. D.2: (215) Oenone, W4 band.

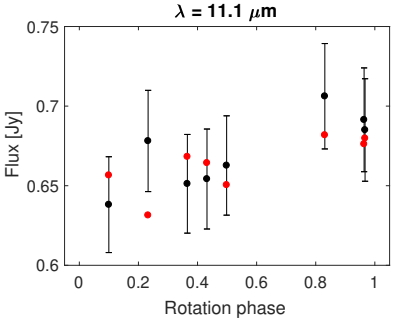

Fig. D.3: (279) Thule, W3 band.

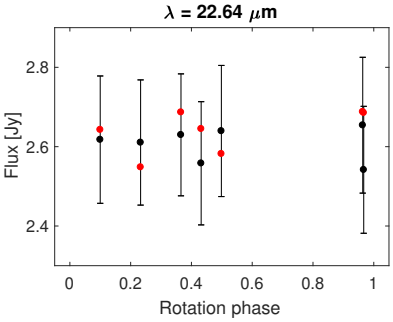

Fig. D.4: (279) Thule, W4 band.

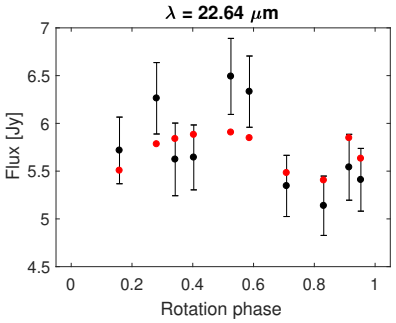

Fig. D.5: (357) Ninina, W4 band.

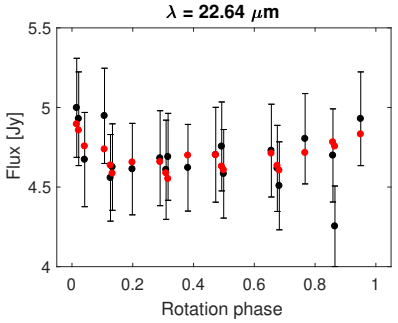

Fig. D.6: (366) Vincentina, W4 band.

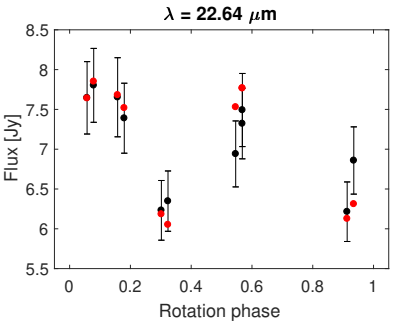

Fig. D.7: (373) Melusina, W4 band.

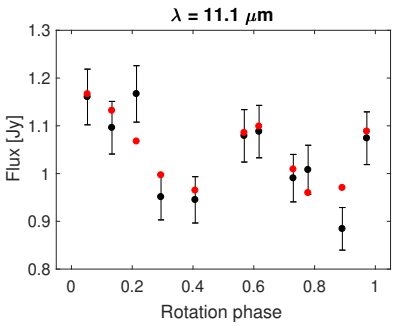

Fig. D.8: (395) Delia, W3 band.

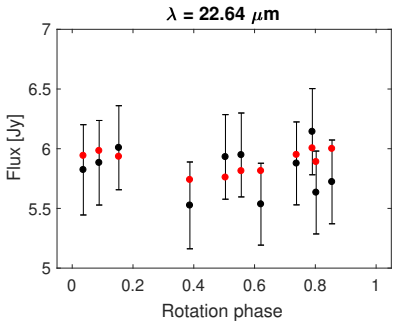

Fig. D.9: (429) Lotis, W4 band.

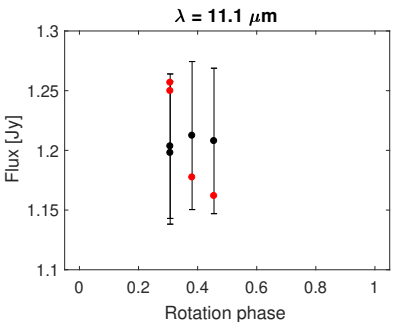

Fig. D.10: (527) Euryanthe, W3 band.

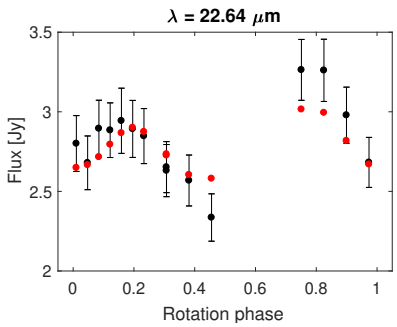

Fig. D.11: (527) Euryanthe, W4 band.

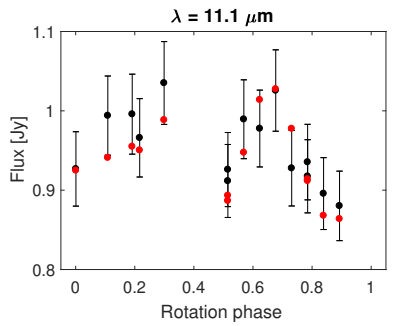

Fig. D.12: (541) Deborah, W3 band.

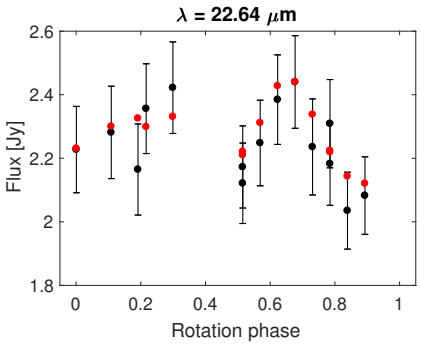

Fig. D.13: (541) Deborah, W4 band.

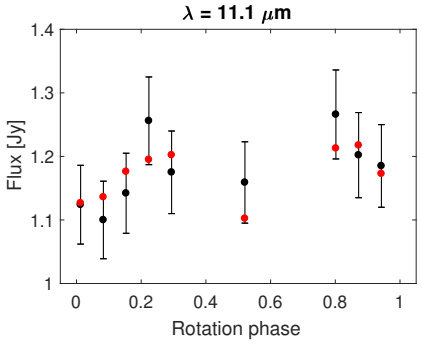

Fig. D.14: (672) Astarte, W3 band.

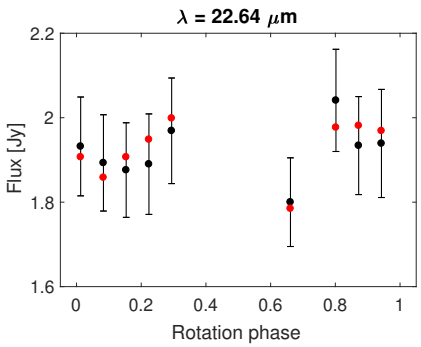

Fig. D.15: (672) Astarte, W4 band.

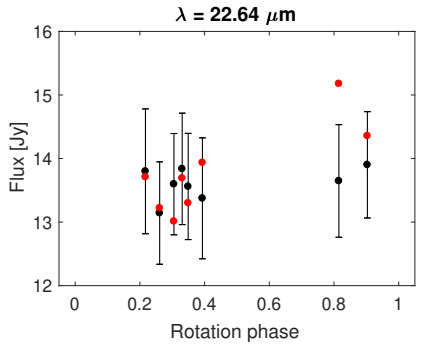

Fig. D.16: (814) Tauris, W4 band.

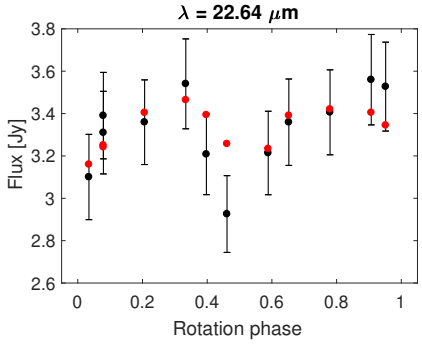

Fig. D.17: (859) Bouzareah, W4 band.

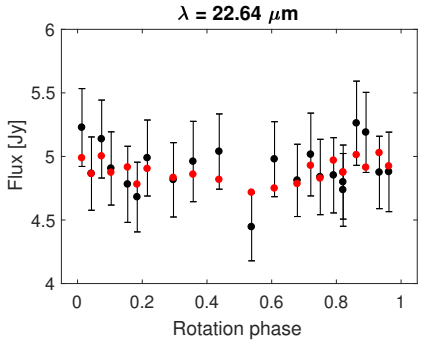

Fig. D.18: (907) Rhoda, W4 band.

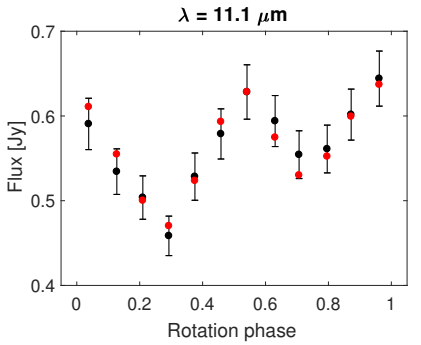

Fig. D.19: (931) Whittemora , W3 band.

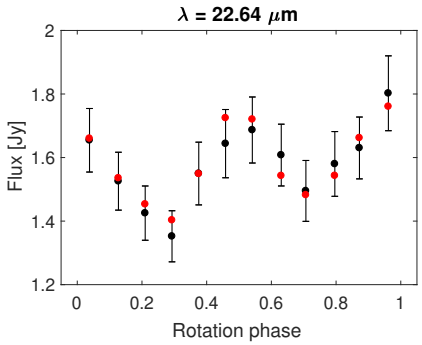

Fig. D.20: (931) Whittemora, W4 band.

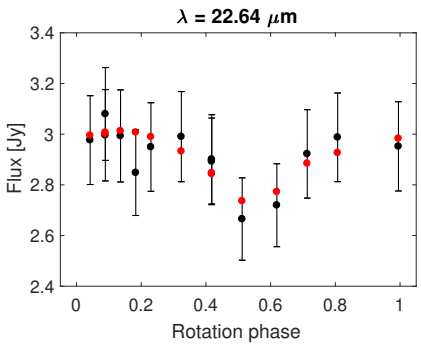

Fig. D.21: (1062) Ljuba, W4 band.

Appendix E: Occultation fits

Instantaneous silhouettes of asteroid models derived here with the light curve inversion, fitted on the fundamental plane to the chords from stellar occultations (Figures E.1 to E.13). The scale is in kilometres. Blue contour by default is for pole 1 shape solution, and magenta for pole 2, unless one of them is preferred – then this one one is shown with the solid contour, and less preferred in dashed contour. Continuous black lines join photoelectrically determined occultation timings, creating more reliable chords than those from visual observations marked with dashed black lines. The dotted lines are for negative (non-detection) observations. The grey segments show the chord uncertainties from the occultation timings, while the red segment shows the distance covered by the asteroid shadow in a given time.

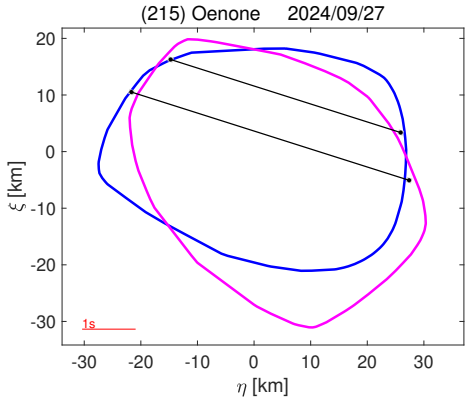

Fig. E.1: Occultation fits for asteroid (215) Oenone

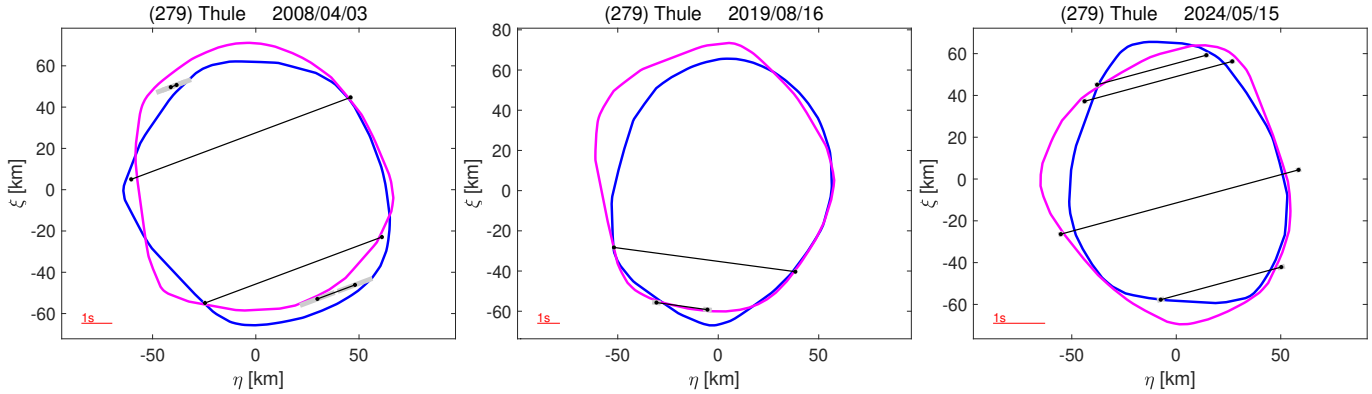

Fig. E.2: Occultation fits for asteroid (279) Thule

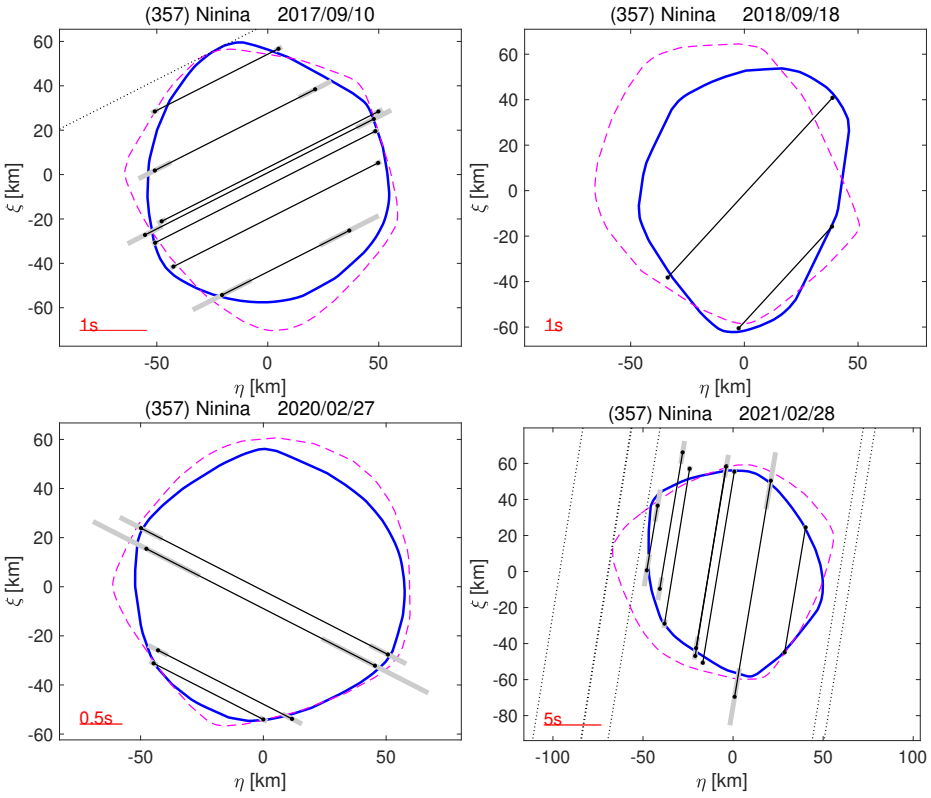

Fig. E.3: Occultation fits for asteroid (357) Ninina. The pole 1 shape model is preferred.

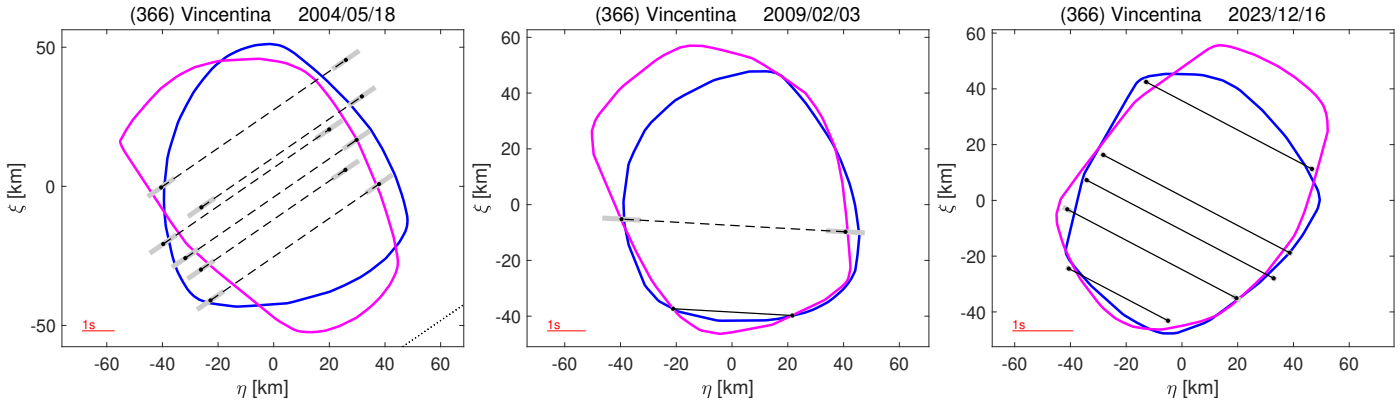

Fig. E.4: Occultation fits for asteroid (366) Vincentina

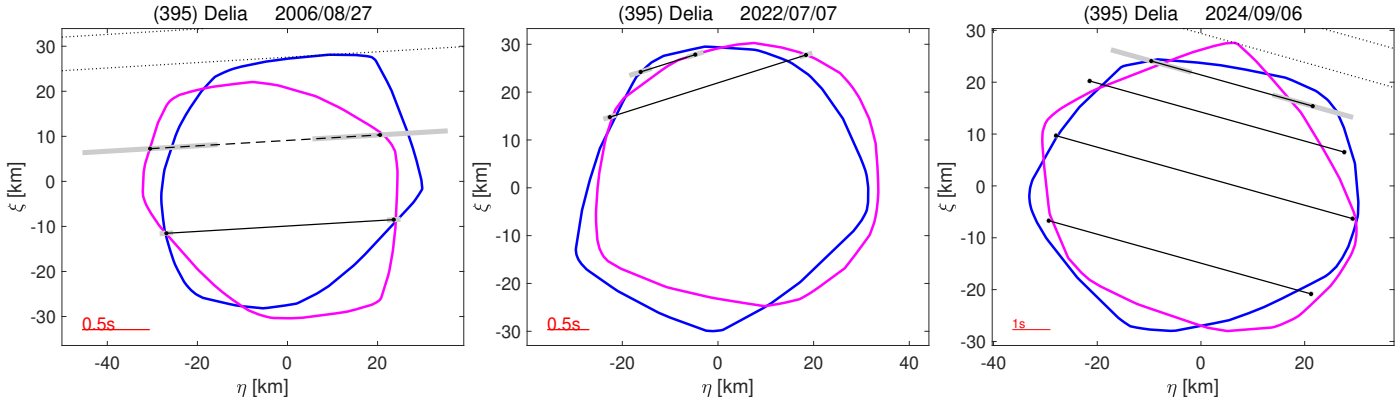

Fig. E.5: Occultation fits for asteroid (395) Delia

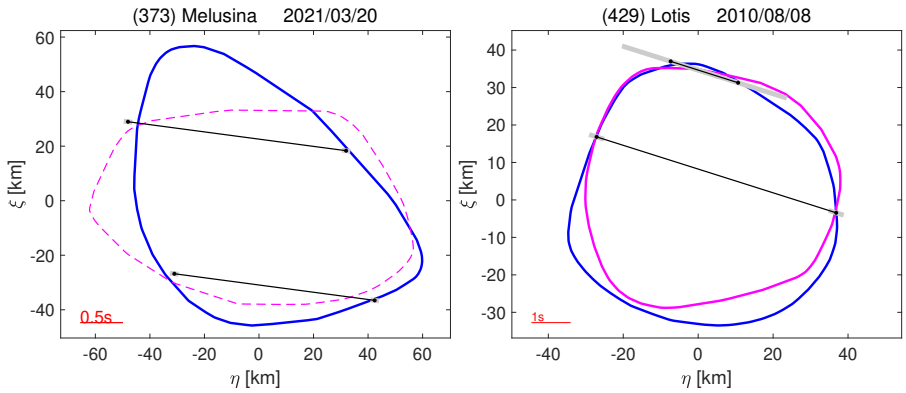

Fig. E.6: Occultation fits for asteroids (373) Melusina and (429) Lotis. The preferred pole for Melusina is pole 2 (blue contour). For Lotis the slightly preferred solution (pole 2) is also marked in blue.

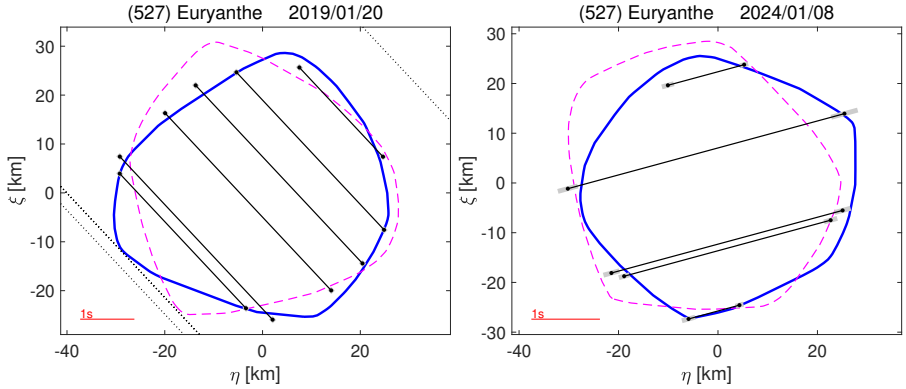

Fig. E.7: Occultation fits for asteroid (527) Euryanthe. Pole 2 (blue contour) is preferred.

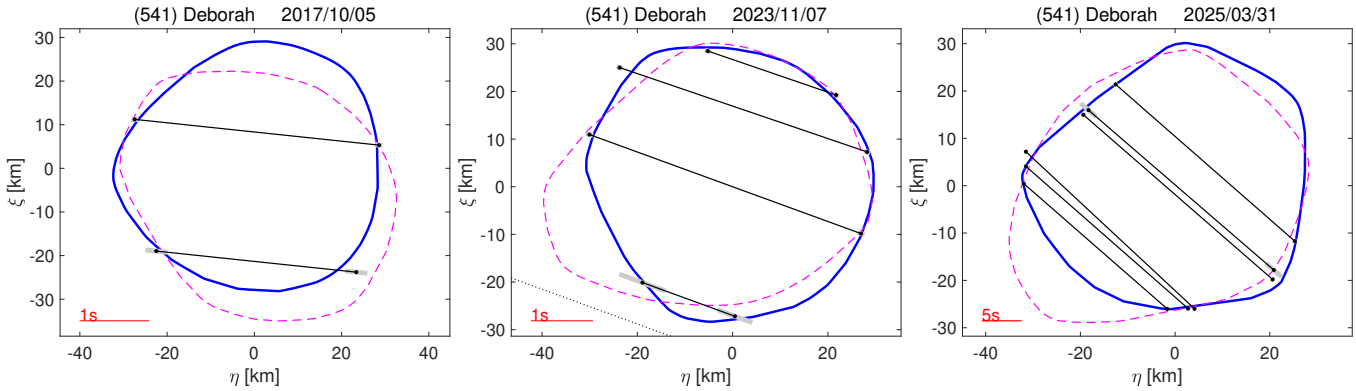

Fig. E.8: Occultation fits for asteroid (541) Deborah. Pole 2 (blue contour) is preferred.

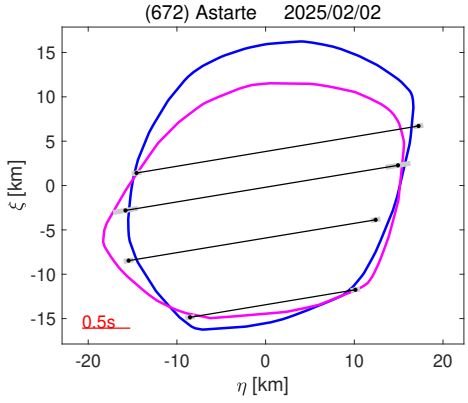

Fig. E.9: Occultation fits for asteroid (672) Astarte. Blue contour is for pole 2.

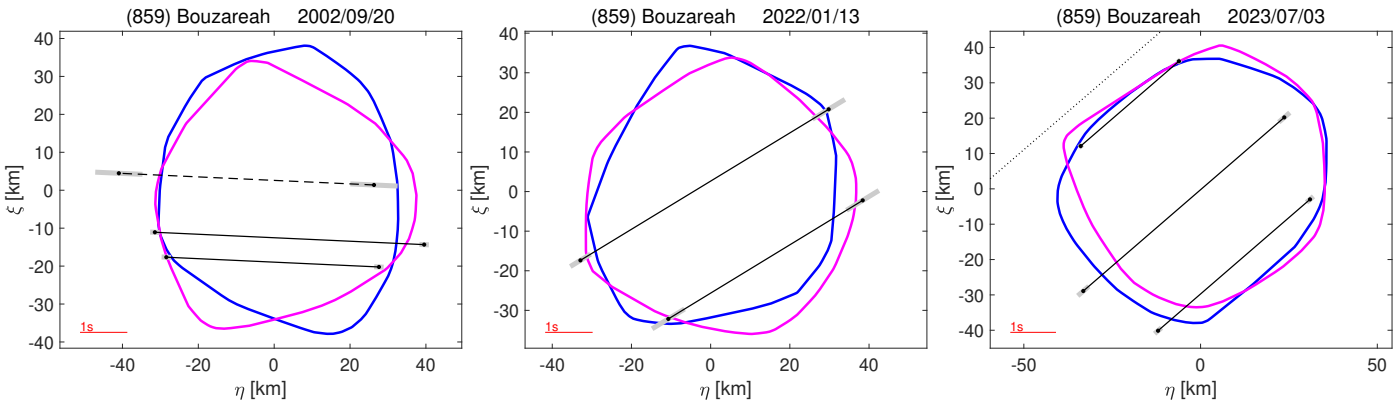

Fig. E.10: Occultation fits for asteroid (859) Bouzareah

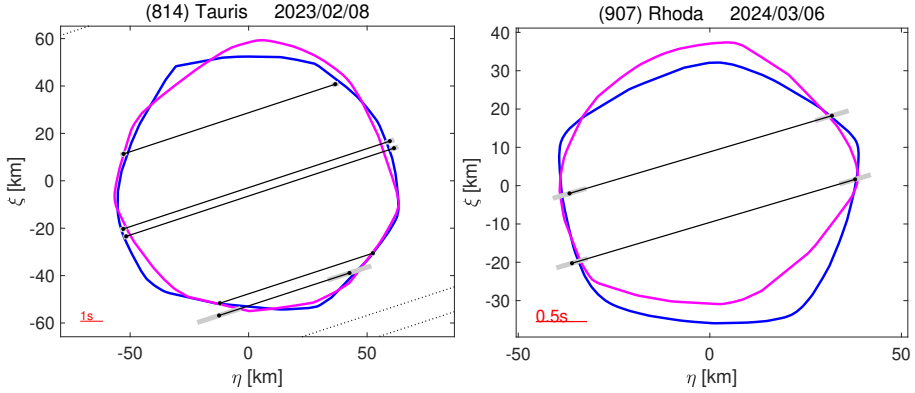

Fig. E.11: Occultation fits for asteroids (814) Tauris and (907) Rhoda. The blue contour is for pole 2 in the case of Rhoda.

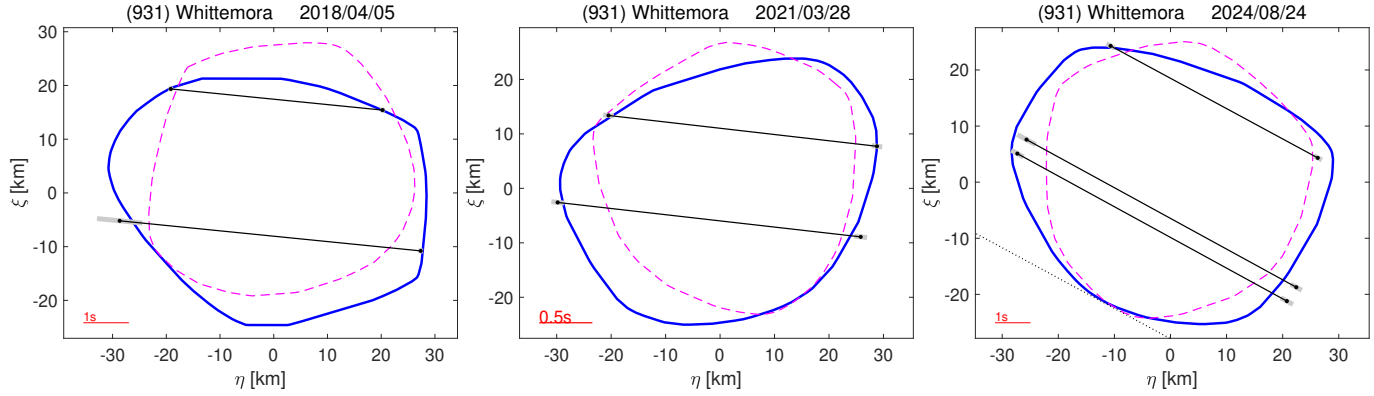

Fig. E.12: Occultation fits for asteroid (931) Whittemora. Pole 2 is preferred (blue contour).

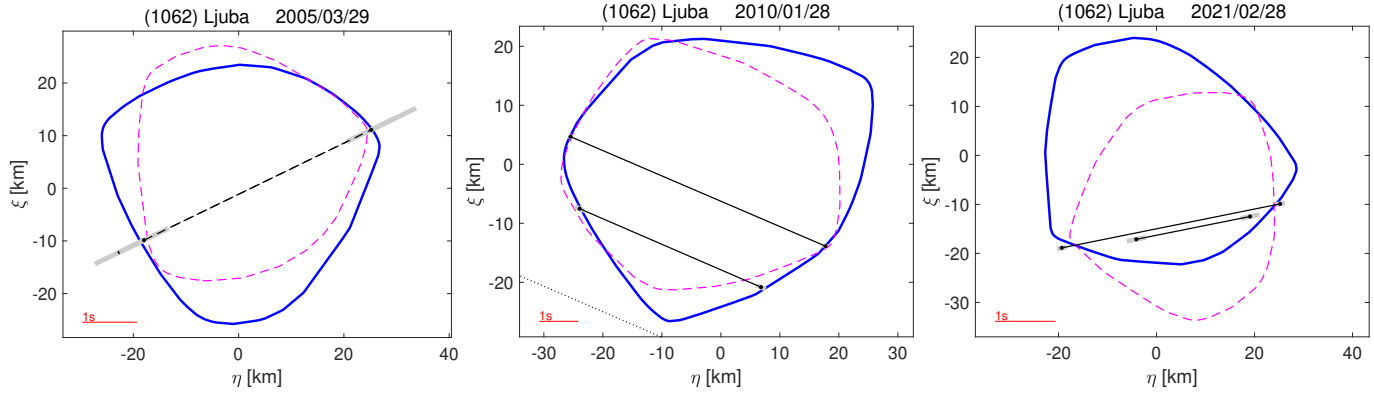

Fig. E.13: Occultation fits for asteroid (1062) Ljuba. Pole 2 is preferred (blue contour).

The Planetary Science Journal, 6:60 (9pp), 2025 March https://doi.org/10.3847/PSJ/adb28b

Thermophysical Model of (269) Justitia—Main Belt Asteroid Possibly Implanted from Trans-Neptunian Region

Anna Marciniak[1], Antoine Choukroun[1], Julia Perła[1], Waldemar Ogłoza[2], Robert Szakáts[3,4], Pierre Antonini[5], Raoul Behrend[5], Géza Csörnyei[6], Marek Dróżdż[2], Marcel Fauvaud[7,8], Stéphane Fauvaud[7,8], Adrian Jones[9], Dong-Heun Kim[10], Myung-Jin Kim[11], Viktor Kudak[12], Iga Mieczkowska[1], Erika Pakštienė[13], Vasyl Perig[12], and Eda Sonbas[14,15]

[1] Astronomical Observatory Institute, Faculty of Physics and Astronomy, Adam Mickiewicz University, Słoneczna 36, 60-286 Poznań, Poland
[2] Mount Suhora Observatory, University of the National Education Commission, Podchorążych 2, 30-084, Cracow, Poland
[3] Konkoly Observatory, HUN-REN Research Centre for Astronomy and Earth Sciences, Konkoly Thege 15-17, H-1121 Budapest, Hungary
[4] CSFK, MTA Centre of Excellence, Budapest, Konkoly Thege Miklós út 15-17, H-1121, Hungary
[5] Geneva Observatory, CH-1290 Sauverny, Switzerland
[6] Konkoly Observatory, Research Centre for Astronomy and Earth Sciences, Eötvös Loránd Research Network (ELKH), H-1121 Budapest, Konkoly Thege Miklós út 15-17, Hungary
[7] Observatoire du Bois de Bardon, 16110 Taponnat, France
[8] Association T60, Observatoire Midi-Pyrénées, 14, avenue Edouard Belin, 31400 Toulouse, France
[9] British Astronomical Association, Burlington House, Piccadilly, Mayfair, W1J 0DU, London, UK
[10] Chungbuk National University, 1, Chungdae-ro, Seowon-gu, Cheongju-si, Chungcheongbuk-do, Republic of Korea
[11] Korea Astronomy and Space Science Institute, 776 Daedeok-daero, Yuseong-gu, Daejeon 34055, Republic of Korea
[12] Laboratory of Space Researches, Uzhhorod National University, Daleka st. 2a, 88000, Uzhhorod, Ukraine
[13] Institute of Theoretical Physics and Astronomy, Vilnius University, Saulėtekio al. 3, 10257 Vilnius, Lithuania
[14] Department of Physics, Adıyaman University, Adıyaman 02040, Türkiye
[15] Astrophysics Application and Research Center, Adıyaman University, Adıyaman 02040, Türkiye
Received 2024 June 20; revised 2024 September 24; accepted 2024 October 16; published 2025 March 18

Abstract

Asteroid Justitia is a special main-belt object, being an extremely red body with a steeper spectral slope than any other D-type asteroid. Conversely, its spectral and polarimetric properties resemble organics-rich Centaurs and trans-Neptunian objects. For this reason, it was chosen as a main target of the MBR Explorer space mission. It is crucial for space mission planning and operations to have in advance the best estimate of the target size, spin, shape, and properties of the surface. In particular, the size determination was in high demand before the extensive stellar occultation campaign in 2023 August, for station deployment and observation planning. We utilized multiple lightcurves from our campaign on slow rotators and from the literature to reconstruct the spin and shape of Justitia via lightcurve inversion. Then we applied the Convex Inversion Thermophysical Model to simultaneously optimize the fit to visible lightcurves and to thermal data from infrared space observatories. We present here the pair of most precise physical models of Justitia possible before the occultation campaign, with similar properties of both solutions. The size range of Justitia was narrowed here to 55–60 km, so by a factor of 4 compared with previous estimates, and also the shape model's resolution was improved. An estimate of thermal inertia and surface roughness was also obtained, with implications for surface texture and regolith properties.

Unified Astronomy Thesaurus concepts: Asteroids (72); Asteroid surfaces (2209); Asteroid rotation (2211)

Materials only available in the online version of record: data behind figure, figure set

1. Introduction

Asteroid (269) Justitia studied by spectroscopy revealed unusual features. In the research of F. E. DeMeo et al. (2009) and S. Hasegawa et al. (2021), this D-type asteroid was found to have an extremely red surface color and a much steeper spectral slope than any other D-type asteroid (the red spectrum meaning increased reflectance toward longer wavelengths). The recent classification scheme of asteroid spectra by M. Mahlke et al. (2022) actually separates the extreme, red-sloped objects into a new "Z-class". Justitia, and (203) Pompeja, distinctively stand out of their taxonomy, looking clearly out of place. Their spectra are much more typical for the outer solar system trans-Neptunian and Centaur objects of RR and IR class, rich in organics (S. Hasegawa et al. 2021). To create a surface with such an extremely red spectrum requires a presence of complex organic matter. For such matter to be created, ices of volatile organic matter are necessary, like methanol and methane (C. Sagan & B. N. Khare 1979), although the signatures of such (fresh) ices are today absent from their surface spectra due to organic ice reddening. This implies that objects bearing such compounds must have formed beyond the snow line of certain volatile organics, while objects with bluer surface spectra (BB and BR type) formed inside of this line (P. Vernazza & P. Beck 2017).

Moreover, asteroid (269) Justitia has been found to display quite unusual polarimetric properties (R. Gil-Hutton & E. Garcìa-Migani 2017). Similarly to a Centaur Chariklo and the dark side of Saturn's moon Iapetus, it has the smallest depth of negative polarization branch of all bodies ever subjected to polarimetric studies, and also a very small angle of minimum polarization. Such properties put it close to dark F-type asteroids and icy objects, yet far from D-type Jupiter Trojans.

All these findings strongly suggest that asteroid Justitia has been formed in the outer solar system and later was transported

to the main belt during the planetary migration era (A. Morbidelli et al. 2005; K. Tsiganis et al. 2005; D. Vokrouhlický et al. 2016). The fact that objects of such properties are so rare in the inner solar system would be a simple consequence of their origin in the farther regions of the outer solar system, as compared to, e.g., D-type Jupiter Trojan asteroids, believed to evolve from BR-type trans-Neptunian objects (S. Hasegawa et al. 2021).

As such, this object provides a unique opportunity to study outer solar system objects in situ without a lengthy space mission. Its relatively good accessibility (middle main belt), together with unique features, providing constraints on solar system formation and dynamic evolution, were the main drivers of the recently announced Mohammed bin Rashid (MBR) Explorer space mission (G. Filacchione et al. 2023; A. Raponi et al. 2023) of the United Arab Emirates (UAE),[16] also known as the Emirates Mission to the Asteroid Belt. The mission launch is scheduled for 2028 March. The spacecraft is planned to visit seven asteroids and attempt to land on Justitia in the year 2034. This mission is well in line with the white paper advocating the need for a space mission to a primitive main-belt asteroid (P. Vernazza et al. 2022).

The science objectives of the MBR Explorer mission are, among others, to provide new insights into the dynamical evolution of small main-belt asteroids and to help investigate how icy small bodies physically evolve across the solar system. One of the principal goals of the mission is to determine the geological history, interior structure, and ice content of the target asteroids (M. R. El-Maarry et al. 2023). These general science goals are going to be achieved with the four instrument main payload: a visible narrow-angle framing camera, a midwavelength infrared (IR) imaging spectrometer, an IR spectrometer, and an IR imager (H. Reed et al. 2023). Using these instruments, the mission in particular is going to determine the asteroids' mineralogy, including hydrated minerals, and their organic materials content; derive the surface regolith properties; characterize the diurnal surface temperature and its temporal variability; determine the thermophysical properties of the outer surface layers; and characterize the potential landing zones on (269) Justitia (G. Filacchione et al. 2023).

Since the announcement of the mission, the scientific interest in Justitia has started to grow. For example, a promising stellar occultation by Justitia has been predicted for 2023 August 31, and an extensive campaign has been organized, with over 50 observers engaged (see M. W. Buie et al. 2025).

By a fortunate coincidence, we had been observing Justitia within our photometric campaign targeted at slow rotators (A. Marciniak et al. 2015) for a few years already when the mission to this asteroid was announced. During this campaign, we have been gathering dense rotational lightcurves of a few tens of asteroids with periods within a range of 12–60 hr, to construct their spin and shape models and put them into scale via thermophysical modeling and stellar occultations (see, e.g., A. Marciniak et al. 2021, 2023). At the request of the occultation team gathered around the event in 2023 August, we attempted to determine the size of Justitia, to help with the planning of the station deployment. Previous size determinations of this asteroid ranged from 46.56 ± 1.655 km (E. L. Ryan & C. E. Woodward 2010) to 64.92 ± 0.590 km (J. R. Masiero et al. 2012), with the newest determination of 60.94 ± 13.950 (J. R. Masiero et al. 2020), complicating the occultation campaign planning that aimed at dense and uniform coverage of the predicted asteroid shadow.

Combining lightcurves from our slow rotators program with the data from the literature, we successfully reconstructed Justitia's spin and shape, first basing this exclusively on relative lightcurves. Later we combined these lightcurves with thermal data in a joint approach that resulted in a comprehensive model of the spin, shape, size, and thermal inertia of Justitia. This model provided the size in a much narrower range than published before, allowing for an optimal station deployment plan and contributing to the success of the occultation campaign (M. W. Buie et al. 2025).

In the following section, we briefly describe previous photometric studies on Justitia and our program targeting slow rotators. The next section outlines the methods used for spin and shape reconstruction, followed by the thermophysical modeling description and the results. Section 4 summarizes the work and outlines prospects for the utilization of our results.

2. Photometric Observations

Long before Justitia was chosen as a target of a space mission, it was part of our program targeting slow rotators. These are asteroids whose spin and shape models were often unavailable, due to observing selection effects. Their long rotation periods, in the range of 12–60 hr, often coupled with small amplitudes of lightcurves, make them challenging targets largely avoided by previous studies (A. Marciniak et al. 2015). Due to the scarcity of dense lightcurves, construction of their spin and shape models was hampered, and as a consequence this bias made them underrepresented in the sample of well-studied asteroids, considering their actual, abundant occurrence (see, e.g., A. Pál et al. 2020).

Our photometric observing campaign targeted at slow rotators is described in detail in A. Marciniak et al. (2015). In the case of Justitia, stations from Turkey, Lithuania, Hungary, Poland, Ukraine, the UK, France, and South Korea provided data that resulted in almost full coverage of Justitia's 33 hr period in all three attempted apparitions. Telescopes with diameters from 30 to 60 cm equipped with CCD cameras were used, and the observations were made mostly through R but also L filters. They were long (3–9 hr), continuous exposure series of the field with the asteroid and comparison stars, resulting in precise, dense lightcurves. The key issue in the campaign targeting slow rotators is the observers' coordination for efficient phase coverage and duplicate avoidance. It was achieved with an internal web planning service displaying visible targets, their rotation phases already covered, and those available during a given night from a particular observing site. Some duplication of lightcurve fragments was actually desirable, especially spaced by a few weeks, since the repeating lightcurve features facilitate better constraining the rotation period, but also track the small lightcurve morphology changes due to shadowing effects. The raw CCD frames have been corrected for bias, dark frame, and flat field, and the aperture photometry was applied using various software. When, due to asteroid brightness, short exposures have been used, to avoid oversampling a point binning was applied so that the number of data points per period stayed between 100 and 200.

Figures 5–6 present the composite lightcurves from three apparitions obtained within this study. Table 2 presents the observing runs' circumstances, the observers, and their sites.

[16] MBR Explorer was named after Sheikh Mohammed bin Rashid Al Maktoum, the vice president and prime minister of UAE.

Previously, lightcurves of Justitia have been published by M. A. Barucci et al. (1992), F. Pilcher (2016), and T.-S. Yeh et al. (2020). The rotation period of 16.5 hr from the first and last of these works was found to be twice as long by F. Pilcher (2016), which has been confirmed by our observations.

3. Modeling Asteroid Justitia

By another lucky coincidence, in mid-2023 the overall set of Justitia lightcurves from our program and the literature turned out to be just sufficient for spin and shape reconstruction. Also, there existed a rich set of thermal data from infrared observatories. All this combined allowed us to determine the size of this body just in time for the occultation campaign on 2023 August 31.

First, we used exclusively the relative lightcurves in the visible for an initial spin and shape reconstruction through the lightcurve inversion method (M. Kaasalainen & J. Torppa 2001; M. Kaasalainen et al. 2001). The shape model in this method is a convex polyhedron parameterized by a spherical harmonics series. When the method is fed with data from sufficiently varied viewing geometries, it quickly converges to a unique solution. We constrained both the period and the spin solution for Justitia this way, with its pole mirror counterpart, due to the unavoidable symmetry of the problem. Since the majority of main-belt asteroids have low orbital inclinations, the appearance of their lightcurves would be insensitive to a mirror-flip of the spin axis by 180° in longitude. This ambiguity can only be broken for asteroids with orbital inclination higher than ∼20°. In the case of Justitia, its orbit inclination to the ecliptic I is $5\overset{\circ}{.}5$, so the spin and shape ambiguity is inevitable.

The lightcurves are well fitted by the models practically down to the noise level (0.010 mag; see Figure 7 in the Appendix). There existed a previous spin and shape model of Justitia, based exclusively on sparse-in-time data (J. Ďurech et al. 2020). Our spin solutions are similar to it, but due to the usage of dense lightcurves, our initial shape model is less angular. However, the stretch of this initial model along the "z"-axis is not well constrained from the lightcurve inversion alone.

In the next step, we added one of two sparse photometric data sets from the ATLAS survey (J. L. Tonry et al. 2018), used by J. Ďurech et al. (2020). These calibrated data well constrained the stretch of the shape model along the rotation axis, since they are sensitive to the absolute dimensions of the asteroid cross section. Then we gathered all available thermal data for Justitia, downloading them from the Infrared Database[17] (R. Szakáts et al. 2020). They were obtained at 12, 25, and 60 μm (IRAS survey; G. Neugebauer et al. 1984); 9 and 18 μm (Akari survey; F. Usui et al. 2011), and 22.6 μm (Wide-field Infrared Survey Explorer (WISE) survey; E. L. Wright et al. 2010). Data obtained by WISE at 11.1 μm were partially saturated and could not be used.

We utilized these data in a joint approach to optimize the asteroid parameters and shape simultaneously to fit the visible lightcurves, sparse data, and thermal flux measurements. This method is called the Convex Inversion Thermophysical Model (CITPM) and has been introduced by J. Ďurech et al. (2017) and verified on multiple targets by A. Marciniak et al. (2021). In parallel to the same convex inversion algorithms described above, the CITPM method also uses the standard Thermophysical Model (TPM) approach introduced by J. S. V. Lagerros (1996, 1997, 1998) and widely used in multiple thermophysical studies (see M. Delbo' et al. 2015 for the review). The algorithm solves the one-dimensional heat diffusion equation to find the temperature of each surface element and its infrared flux at the time of each thermal measurement. There are hundreds of such surface elements, whose contribution is added for the overall flux. The parameters characterizing each element are thermal inertia, surface roughness (described by spherical-section craters of opening angle from 10° to 90° and fraction of surface coverage from 0% to 100%), and a light scattering law in the form of the Hapke model (B. Hapke 1981, 1984, 1986). Parameters of the Hapke model are optimized to fit the phase curve. For emissivity, we used a standard value of 0.9 (see, e.g., L. F. Lim et al. 2005). The main point in the CITPM usage is to find the best weight between visible and thermal data so that the final model optimally fits both types of data. Still, making the initial, convex inversion model based on lightcurves only was a necessary step. The CITPM method, due to the multitude of fitted parameters, is not able to scan the whole parameter space for the best period and spin axis position. Thus, the spin parameters from the convex inversion are a required input for the CITPM.

4. Results

Applying the CITPM we obtained a much smoother, more realistic shape model of Justitia than from lightcurve inversion alone, and a precise size determination with an estimate of thermal inertia and surface roughness. The resulting model parameters are presented in Table 1. The spin axis is far from the ecliptic plane and the rotation is retrograde, as indicated by the negative values of β_p. Size is now constrained to the narrow range of 55–60 km, where CITPM solutions even 2 km beyond this range provided a much poorer fit to thermal data. Shape models for both spin solutions are presented as viewed from three sides in Figure 1. In addition, Figure 2 shows the fit of both model solutions to a normalized phase curve, while Figures 7 and 8 show the model fit to lightcurves in the visible, and the fit to all the thermal data, respectively. It can be seen that this model well fits both types of data with very small deviations of model lightcurves from the observed ones (0.0128 mag) and a small reduced $\chi^2 = 0.29$ for the infrared data fit (all values discussed here are for pole 1 solution, those for the mirror solution being similar; see Table 1). Geometric albedo is also well constrained to 0.058 ± 0.006.

Unlike the size and albedo, the thermal inertia is usually determined with a large uncertainty, and so is the case here: for pole 1 it is 41^{+110}_{-40} SI units, where most of the solutions with free thermal inertia tended to concentrate below 50 SI units. A large uncertainty here might be due to the relatively large variations in Justitia heliocentric distance (full range of the order of 0.6 au at the mean value of 2.74 au), while there is a dependence of thermal inertia on heliocentric distance, due to different temperatures (S. J. Keihm 1984; M. Mueller et al. 2010). Figure 4 present the results from multiple loops over various levels of surface roughness, run for thermal inertia varied by 10 SI units[18] in each step. In Table 1 we also present the thermal inertia corrected to 1 au (87 SI units) for direct

[17] https://ird.konkoly.hu/

[18] $\mathrm{J\,m^{-2}\,s^{-1/2}\,K^{-1}}$.

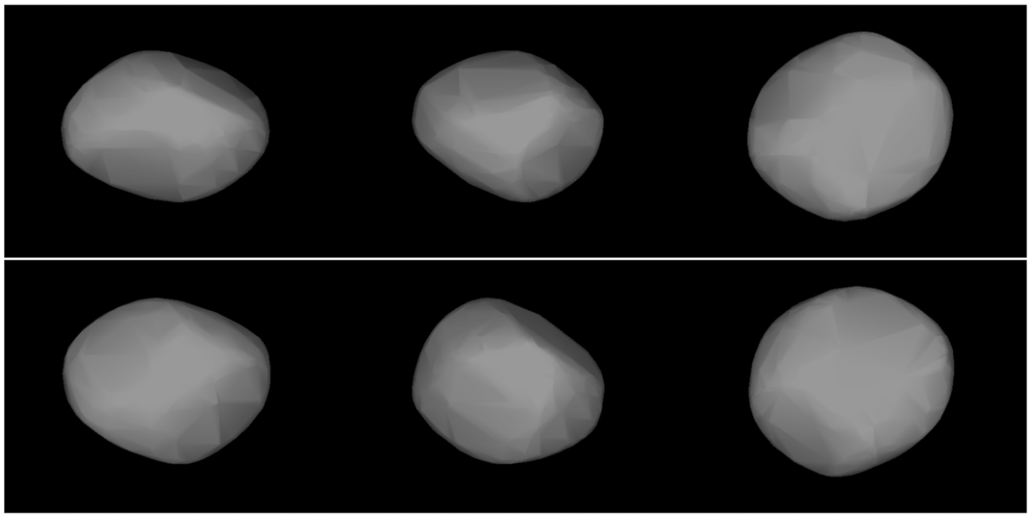

Figure 1. Shape models of asteroid (269) Justitia from the CITPM: solution for pole 1 (top) and pole 2 (bottom). Shapes are displayed in three views, left to right: two equatorial views, 90° apart, and a pole-on view.

Table 1
Physical Properties of Asteroid Justitia and Information on the Data Set Used

Parameter	Value
Number of apparitions (calendar years)	7 (1984–2022)
Number of lightcurves	52
Number of IRAS, Akari, and WISE thermal data points	12, 10, 15
Average heliocentric distance (au)	2.74 ± 0.30
Pole 1 solution	
λ_{p1} (deg)	73 ± 11
β_{p1} (deg)	−81 ± 15
Sidereal period (hr)	33.12962 ± 0.00001
Deviations from visible lightcurves (mag)	0.0128
Infrared $\chi^2_{\rm red}$	0.29
Equivalent sphere diameter (km)	58 ± 2
Albedo	0.058 ± 0.006
Thermal inertia (SIu)	41^{+110}_{-40}
Thermal inertia at 1 au (SIu)	87
Pole 2 solution	
λ_{p2} (deg)	254 ± 8
β_{p2} (deg)	−68 ± 12
Sidereal period (hr)	33.12962 ± 0.00001
Deviations from visible lightcurves (mag)	0.0124
Infrared $\chi^2_{\rm red}$	0.27
Equivalent sphere diameter (km)	56^{+4}_{-1}
Albedo	0.059 ± 0.007
Thermal inertia (SIu)	53^{+100}_{-52}
Thermal inertia at 1 au (SIu)	113

Note. The first two rows contain the number of apparitions when lightcurves were obtained, calendar years, and the number of separate lightcurves. The next part details the infrared data set: the number of points provided by space observatories IRAS, Akari, and WISE, respectively, and an average heliocentric distance of thermal infrared observations $r_{\rm hel}$ with the standard deviation. Next follow the model parameters for two mirror solutions: J2000 ecliptic coordinates λ_p, β_p of the spin axis, sidereal rotation period P, and the deviation of model fit from those lightcurves (including fit to sparse data). The next rows present the reduced chi-square of the best fit ($\chi^2_{\rm red}$) to infrared data, the surface-equivalent size D, geometric albedo p_V, thermal inertia Γ in J m^{-2} s$^{-1/2}$ K^{-1} SI units (SIu), and thermal inertia normalized to 1 au calculated according to the equation $\Gamma_{1\ \rm au} = \Gamma(r)r^{0.75}$, following B. Rozitis et al. (2018).

comparisons with other studies of asteroid thermal inertia. Consistent with the small or medium thermal inertia value, the surface roughness is very high in our study, as the two quantities are usually anticorrelated. However, thermal skin depth calculated according to the formula from J. R. Spencer et al. (1989) is only 5 mm for Justitia, implying small regolith grain sizes.

Finally, since the main trigger of this work was an upcoming stellar occultation campaign, we generated the on-sky views of our newly cleated models. Figure 3 presents both solutions of Justitia's shape as on-sky views phased for the anticipated occultation moment on 2023 August 31 at 10:56 UT.

Our results have much wider applications: the reliable size and albedo constraints with the knowledge of thermal inertia and surface roughness of asteroid Justitia is going to facilitate the MBR Explorer mission planning, in situ operations, and landing. Also, the wealth of data obtained during the mission compared to premission results are going to provide a ground truth for asteroid studies based on remote sensing.

5. Discussion and Conclusions

Motivated by the planned space mission and upcoming favorable occultation event, we successfully attempted spin and shape reconstruction of the unusual D-type main-belter Justitia from lightcurves. Additionally, we also studied this body in the thermal aspect, which allowed us to obtain a good size estimate of 58 ± 2 km, pinpointing it to a much narrower range than the sizes available from previous studies (46.56–64.92 km). Previous size determinations of Justitia were based on the Simple Thermal Model (STM) (E. F. Tedesco et al. 2002), IRAS-STM model; (E. L. Ryan & C. E. Woodward 2010), and NEATM (e.g., J. R. Masiero et al. 2012), which use spherical shape approximation and other simplifying assumptions concerning the asteroid spin and thermophysical parameters to fit sparse thermal measurements. Here we provide detailed spin and shape solutions applied in a more sophisticated thermophysical model, free from such assumptions. As such, our model is the first full spin, shape, and size solution for asteroid Justitia, consistent with all the data used for its construction: a rich set of dense lightcurves, calibrated brightness measurements, and thermal infrared data. Connected to size, previously published

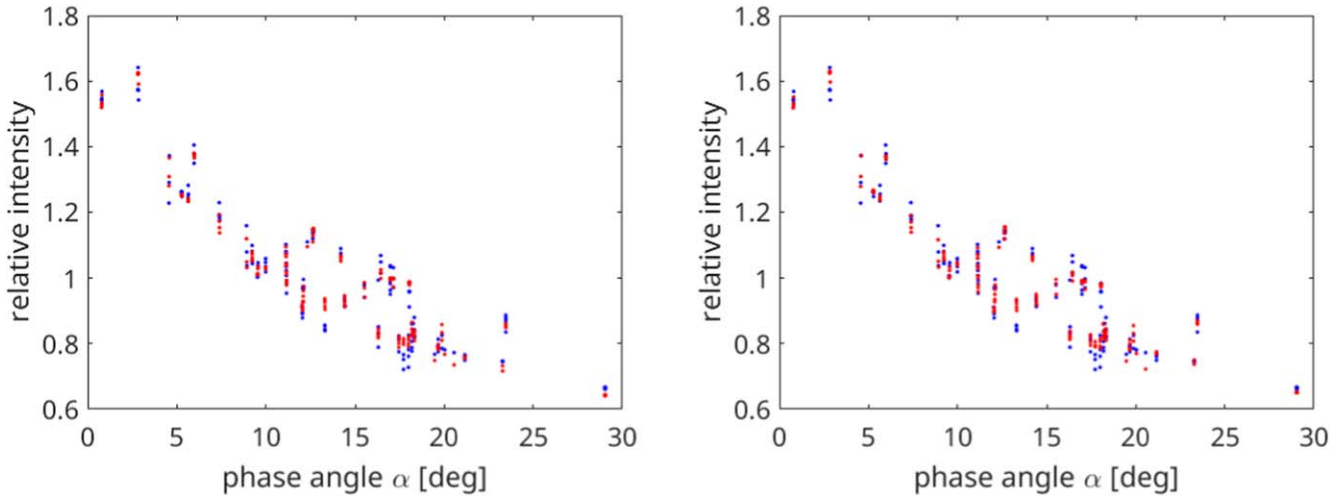

Figure 2. The model fit to normalized phase curve of (269) Justitia resulting from the CITPM: solution for pole 1 (left) and pole 2 (right). Calibrated brightness measurements have to be normalized in the modeling process in order not to overweight other types of data.

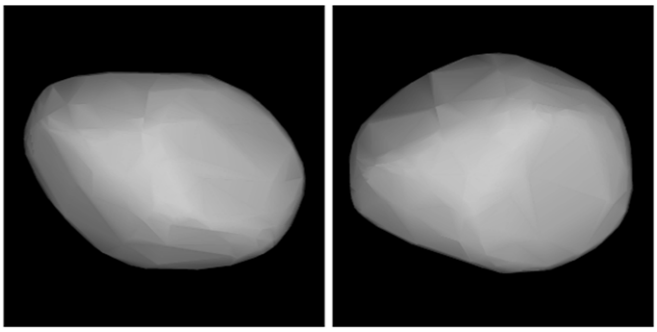

Figure 3. On-sky views of Justitia shape models from the CITPM phased for the 2023 August 31 occultation moment at 10:56 UT. North is up and east is left. Left plot: shape model for pole 1; right plot: same for pole 2 (see Table 1).

albedo values for Justitia were in a rather wide range from 0.061 (J. R. Masiero et al. 2012) to 0.130 (E. L. Ryan & C. E. Woodward 2010). Our value for albedo turns out to be even smaller (0.058 ± 0.006), consistent with the hypothesized origin of Justitia in the trans-Neptunian region of icy bodies, with a surface covered with darker organic material, later darkened even more by the organic ice reddening processes. Relatively small to medium thermal inertia supports a long history of the surface being influenced by micrometeorite bombardment, resulting in a layer of fine regolith on the surface. The thermal solution also suggests a high surface roughness, with a thermal skin depth of 5 mm.

As opposed to a previous sparse-data model published by J. Ďurech et al. (2020), our high-resolution shape model of Justitia has a more realistic, smooth appearance, free from sharp edges and large planar sections, characteristic of models based on sparse-in-time data. Such data apparently do not contain full information on the whole shape. Still, models constructed on them are good at correctly reproducing spin axis position and sidereal period (J. Hanuš et al. 2016). The spin solution found by J. Ďurech et al. (2020) is $\lambda_{p1} = 71°$, $\beta_{p1} = -79°$, and $\lambda_{p2} = 251°$, $\beta_{p2} = -69°$, with $P_{\rm sid} = 33.129$ hr, placing the spin axis a few degrees from our solution and having consistent, though less precise, sidereal period of rotation (see Table 1). Also, our study resulted in a shape model with well-determined stretch along the rotation axis, which has been a persisting weakness of shape models reconstructed from relative lightcurves only, as was the case in an initial version of our model.

Our model of the Justitia asteroid already proved useful for the occultation campaign planning and will be important for the MBR Explorer mission operations and science results. The initial results from the occultation campaign confirm our findings. They also clearly reject one of the mirror shape solutions, while confirming the other, thus breaking the spin ambiguity. For a detailed description of the occultation campaign and results see the accompanying paper by M. W. Buie et al. (2025).

Acknowledgments

We are grateful to Vadim Nikitin for contacting us with the occultation team, which motivated us to model asteroid Justitia just in time to support the occultation campaign planning. We thank Josef Ďurech for enabling us to phase the new model of Justitia through the DAMIT service.

This work was supported by the National Science Centre, Poland, through grant No. 2020/39/O/ST9/00713. R.S. has received funding from the K-138962 grant of the National Research, Development and Innovation Office (NKFIH, Hungary). This paper was partially based on observations obtained at Sobaeksan Optical Astronomy Observatory (SOAO), which is operated by the Korea Astronomy and Space Science Institute (KASI). E.P. acknowledges the Europlanet 2024 RI project funded by the European Union's Horizon 2020 Research and Innovation Programme (grant agreement No. 871149).

Appendix
Additional Figures and Tables

Plots of the reduced infrared χ^2 versus thermal inertia (Figure 4), composite lightcurves in the visible from three apparitions (Figures 5 and 6), example fit of Justitia model to visible lightcurves (Figure 7), and infrared model fluxes compared to measured fluxes (Figure 8). Details of the observing campaign are given in Table 2.

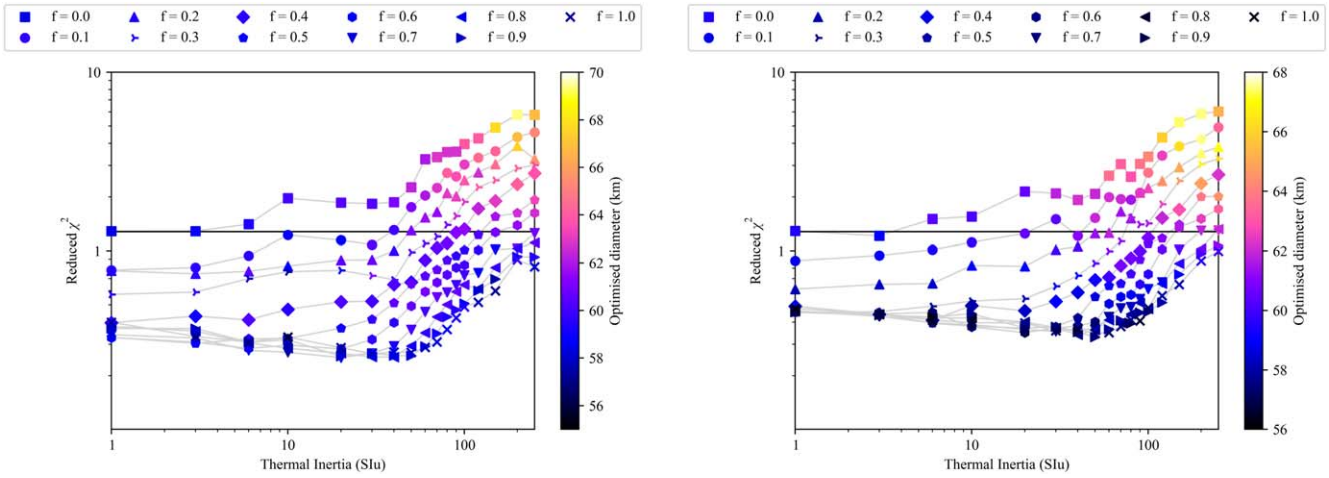

Figure 4. Reduced infrared χ^2 values vs. thermal inertia for various combinations of surface roughness (symbol coded) and optimized diameters of the equivalent surface sphere (color coded). Solutions for pole 1 (left) and for pole 2 (right). Due to the multitude of parameters, for surface roughness only the surface element coverage is shown (f), while the opening angle of spherical-section craters ranged from 10° to 90°. Higher opening angles provided better fit to thermal data.

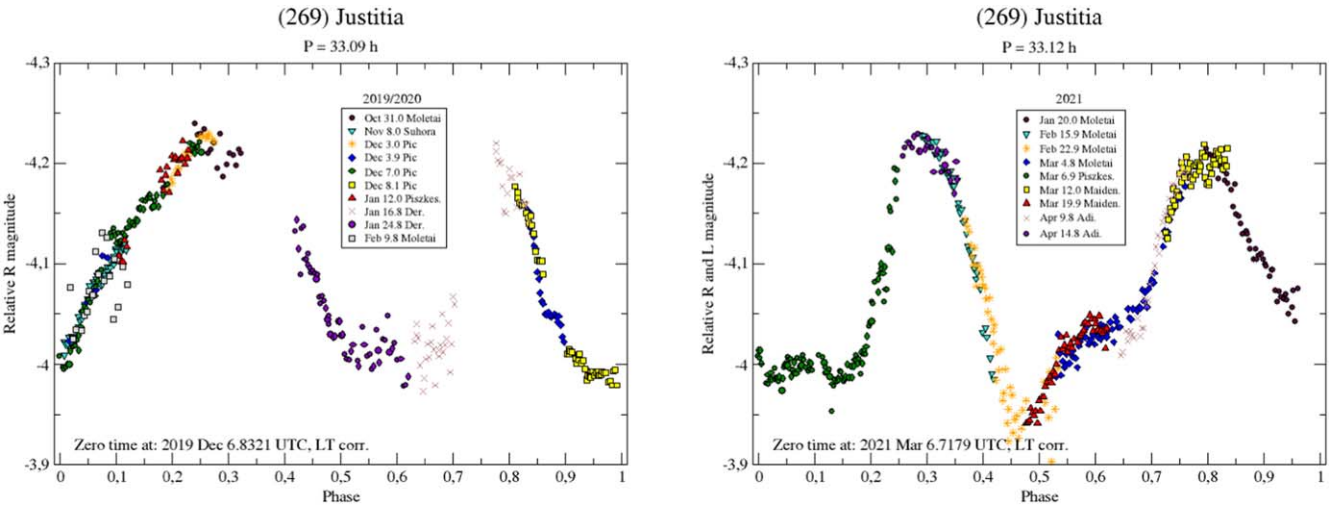

Figure 5. Composite lightcurves of (269) Justitia from the verge of the years 2019 and 2020 (left) and from the year 2021 (right).

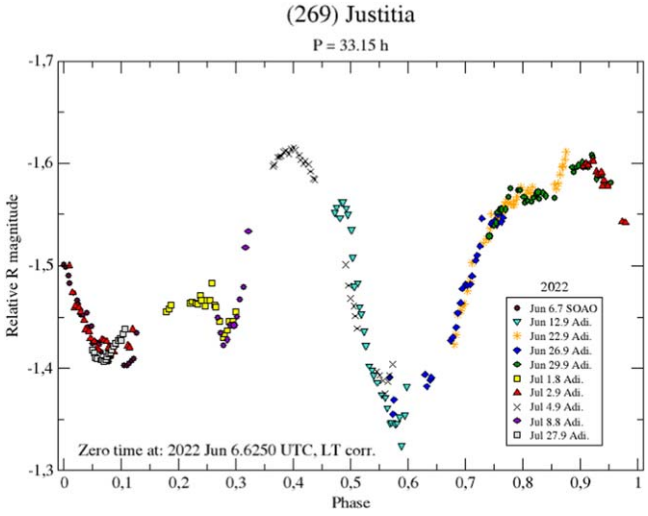

Figure 6. Composite lightcurve of (269) Justitia from the year 2022.

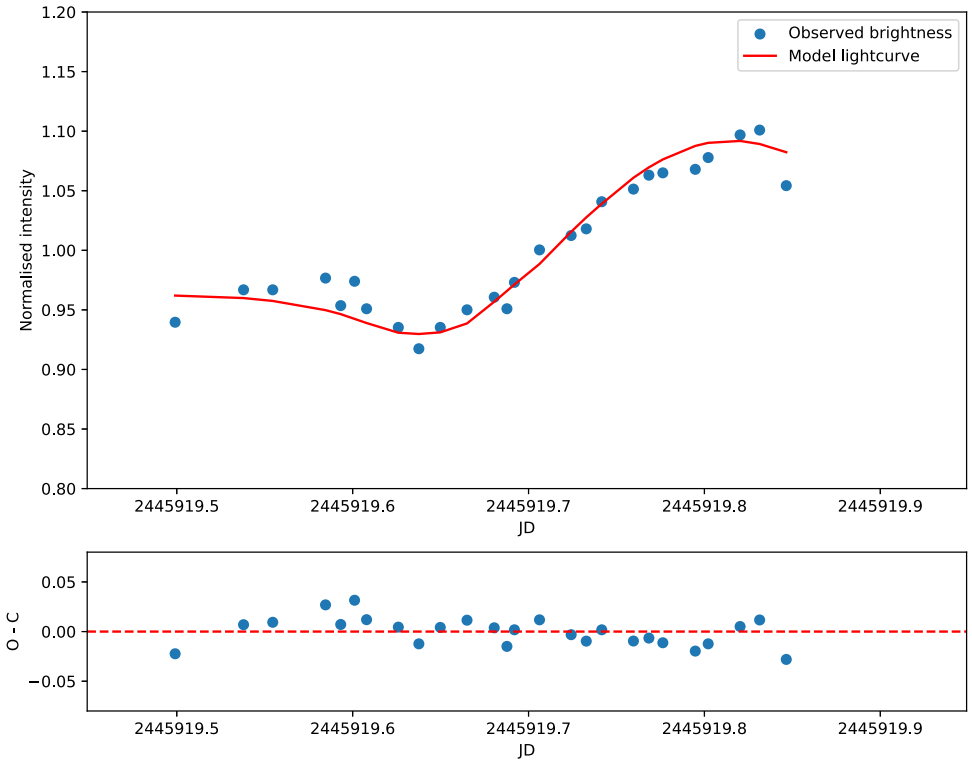

Figure 7. Example fit of Justitia model to visible lightcurves. Due to a slow rotation (33 hr period), each lightcurve covers only a small portion of the full period. (The data used to create this figure are available in the online article.)
(The complete figure set (51 images) is available in the online article.)

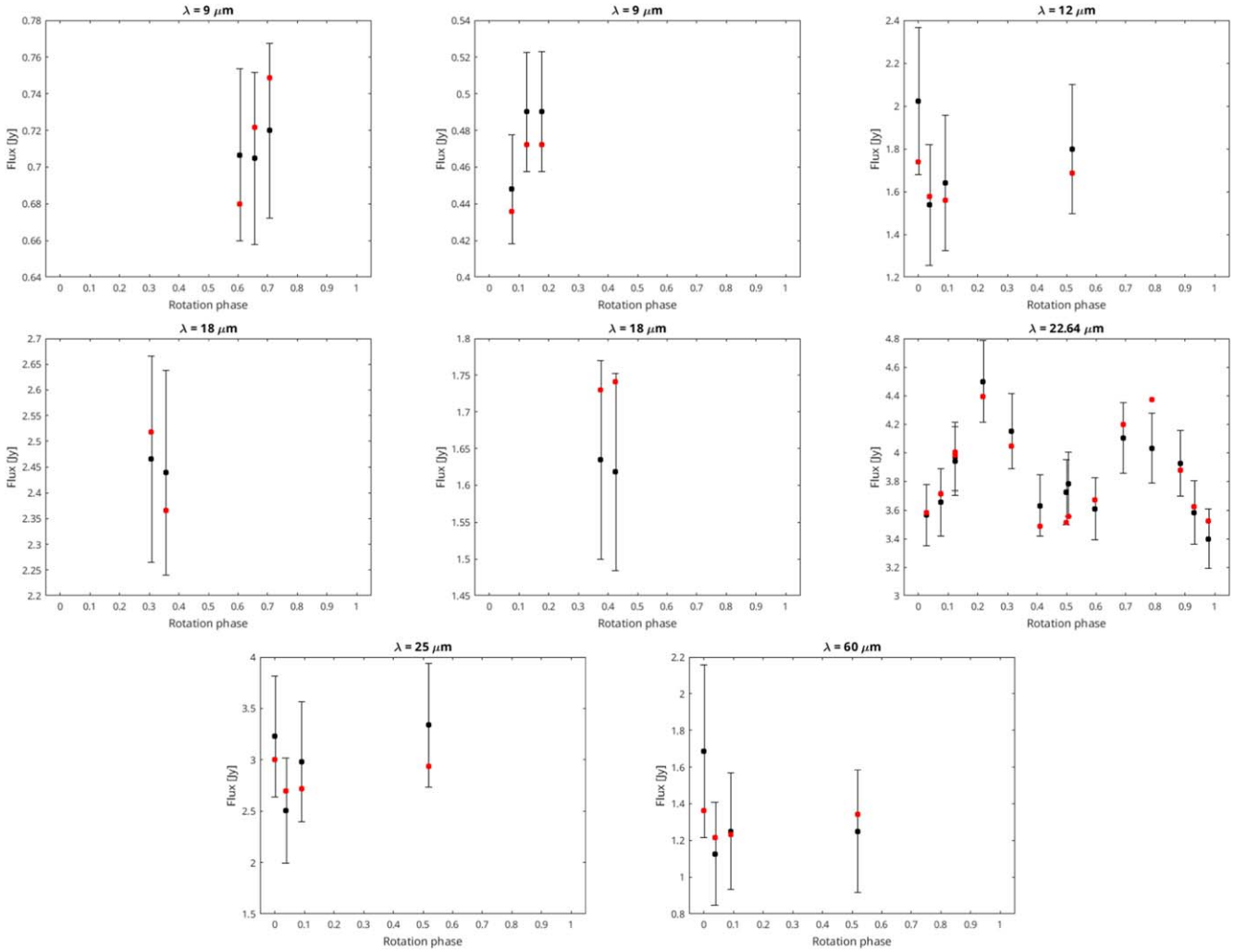

Figure 8. Asteroid Justitia infrared model fluxes (red circles) compared to measured fluxes in various bands indicated in each plot (black circles). Infrared measurements spaced by more than 100 days are shown in separate plots.

Table 2
Details of the Photometric Campaign for (269) Justitia

Date	N_{lc}	λ (deg)	Phase Angle (deg)	Observer	Site
1984 Aug 6.2–1984 Aug 15.2	5	296–297	8–13	M. A. Barucci et al. (1992)	ESO, La Silla, Chile
2006 Dec 11.9–2006 Dec 13.9	2	43	12	P. Antonini, R. Behrend	Observatoire des Hauts Patys, France
2015 Nov 21.4–2016 Jan 3.2	11	85–94	2–11	F. Pilcher (2016)	Organ Mesa Observatory, NM, USA
2017 Feb 26.7–2017 Mar 2.7	5	162–163	0–2	T.-S. Yeh et al. (2020)	Purple Mountain Observatory, PR China
2019 Oct 31.0–2020 Feb 9.8	2	66–79	13–18	E. Pakštienė	Molėtai, Lithuania
2019 Nov 8.0	1	78	10	M. Dróżdż	Mount Suhora, Poland
2019 Dec 3.0–2019 Dec 8.1	4	72–73	3	S. Fauvaud, M. Fauvaud	Pic du Midi Observatory, France
2020 Jan 12.0	1	66	13	G. Csörnyei	Piszkéstető, Hungary
2020 Jan 16.8–2020 Jan 24.8	2	65–65	14–16	V. Kudak, V. Perig	Derevivka, Ukraine
2021 Jan 20.0–2021 Mar 4.8	4	137–147	2–9	E. Pakštienė	Molėtai, Lithuania
2021 Mar 6.9	1	137	10	R. Szakáts	Piszkéstető, Hungary
2021 Mar 12.0–2021 Mar 19.9	2	135–136	12–14	A. Jones	Maidenhead, UK
2021 Apr 9.8–2021 Apr 14.8	2	134–135	19–20	W. Ogłoza	Adiyaman, Turkey
2022 Jun 6.7	1	287	15	D.-H. Kim, M.-J. Kim	SOAO, South Korea
2022 Jun 12.9–2022 Jul 27.9	9	278–286	4–13	W. Ogłoza	Adiyaman, Turkey

Note. Table shows observing dates, number of lightcurves, range of ecliptic longitudes of the target, Sun–target–observer phase angles, the observer's name (or paper citation in cases of published data), and the observing site. SOAO stands for Sobaeksan Optical Astronomy Observatory.

References

Barucci, M. A., di Martino, M., & Fulchignoni, M. 1992, AJ, 103, 1679
Buie, M. W., AlMazmi, H., Hayne, P., et al. 2025, Occultation based Size and Shape of (269) Justitia, PSJ, 6, 61
Delbo', M., Mueller, M., Emery, J. P., Rozitis, B., & Capria, M. T. 2015, in Asteroid Thermophysical Modeling, ed. W. F. Botte, F. E. DeMeo, & P. Michel (Tucson, AZ: Univ. Arizona Press), 107
DeMeo, F. E., Binzel, R. P., Slivan, S. M., & Bus, S. J. 2009, Icar, 202, 160
Ďurech, J., Delbo', M., Carry, B., Hanuš, J., & Alí-Lagoa, V. 2017, A&A, 604, A27
Ďurech, J., Tonry, J., Erasmus, N., et al. 2020, A&A, 643, A59
El-Maarry, M. R., Landis, M. E., Capaccioni, F., & Filacchione, G. 2023, in LPI Contribution, 2851 (Houston, TX: Lunar and Planetary Inst.), 2385
Filacchione, G., Ciarniello, M., De Sanctis, M. C., et al. 2023, in LPI Contribution, 2851 (Houston, TX: Lunar and Planetary Inst.), 2157
Gil-Hutton, R., & Garcìa-Migani, E. 2017, A&A, 607, A103
Hanuš, J., Ďurech, J., Oszkiewicz, D. A., et al. 2016, A&A, 586, A108
Hapke, B. 1981, JGR, 86, 3039
Hapke, B. 1984, Icar, 59, 41
Hapke, B. 1986, Icar, 67, 264
Hasegawa, S., Marsset, M., DeMeo, F. E., et al. 2021, ApJL, 916, L6
Kaasalainen, M., & Torppa, J. 2001, Icar, 153, 24
Kaasalainen, M., Torppa, J., & Muinonen, K. 2001, Icar, 153, 37
Keihm, S. J. 1984, Icar, 60, 568
Lagerros, J. S. V. 1996, A&A, 310, 1011
Lagerros, J. S. V. 1997, A&A, 325, 1226
Lagerros, J. S. V. 1998, A&A, 332, 1123
Lim, L. F., McConnochie, T. H., Bell, J. F., & Hayward, T. L. 2005, Icar, 173, 385
Mahlke, M., Carry, B., & Mattei, P. A. 2022, A&A, 665, A26
Marciniak, A., Ďurech, J., Alí-Lagoa, V., et al. 2021, A&A, 654, A87
Marciniak, A., Ďurech, J., Choukroun, A., et al. 2023, A&A, 679, A60
Marciniak, A., Pilcher, F., Oszkiewicz, D., et al. 2015, P&SS, 118, 256
Masiero, J. R., Mainzer, A. K., Bauer, J. M., et al. 2020, PSJ, 1, 5
Masiero, J. R., Mainzer, A. K., Grav, T., et al. 2012, ApJL, 759, L8
Morbidelli, A., Levison, H. F., Tsiganis, K., & Gomes, R. 2005, Natur, 435, 462
Mueller, M., Marchis, F., Emery, J. P., et al. 2010, Icar, 205, 505
Neugebauer, G., Habing, H. J., van Duinen, R., et al. 1984, ApJL, 278, L1
Pál, A., Szakáts, R., Kiss, C., et al. 2020, ApJS, 247, 26
Pilcher, F. 2016, MPBu, 43, 135
Raponi, A., Filacchione, G., Ciarniello, M., et al. 2023, in LPI Contribution, 2851 (Houston, TX: Lunar and Planetary Inst.), 2450
Reed, H., Al Ameri, M. O., Landis, M. E., et al. 2023, in LPI Contribution, 2851 (Houston, TX: Lunar and Planetary Inst.), 2366
Rozitis, B., Green, S. F., MacLennan, E., & Emery, J. P. 2018, MNRAS, 477, 1782
Ryan, E. L., & Woodward, C. E. 2010, AJ, 140, 933
Sagan, C., & Khare, B. N. 1979, Natur, 277, 102
Spencer, J. R., Lebofsky, L. A., & Sykes, M. V. 1989, Icar, 78, 337
Szakáts, R., Müller, T., Alí-Lagoa, V., et al. 2020, A&A, 635, A54
Tedesco, E. F., Noah, P. V., Noah, M., & Price, S. D. 2002, AJ, 123, 1056
Tonry, J. L., Denneau, L., Heinze, A. N., et al. 2018, PASP, 130, 064505
Tsiganis, K., Gomes, R., Morbidelli, A., & Levison, H. F. 2005, Natur, 435, 459
Usui, F., Kuroda, D., Müller, T. G., et al. 2011, PASJ, 63, 1117
Vernazza, P., & Beck, P. 2017, in Planetesimals: Early Differentiation and Consequences for Planets, ed. L. T. Elkins-Tanton & B. P. Weiss (Cambridge: Cambridge Univ. Press), 269
Vernazza, P., Beck, P., Ruesch, O., et al. 2022, ExA, 54, 1051
Vokrouhlický, D., Bottke, W. F., & Nesvorný, D. 2016, AJ, 152, 39
Wright, E. L., Eisenhardt, P. R. M., Mainzer, A. K., et al. 2010, AJ, 140, 1868
Yeh, T.-S., Li, B., Chang, C.-K., et al. 2020, AJ, 160, 73

A&A, 679, A60 (2023)
https://doi.org/10.1051/0004-6361/202346191

Astronomy & Astrophysics

Scaling slowly rotating asteroids with stellar occultations*

A. Marciniak[1], J. Ďurech[2], A. Choukroun[1], J. Hanuš[2], W. Ogłoza[3], R. Szakáts[4,5], L. Molnár[4,5,6,7], A. Pál[4,5,8], F. Monteiro[9], E. Frappa[10], W. Beisker[11], H. Pavlov[11], J. Moore[12], R. Adomavičienė[13], R. Aikawa[14], S. Andersson[11], P. Antonini[15], Y. Argentin[11], A. Asai[14], P. Assoignon[11], J. Barton[12], P. Baruffetti[11], K. L. Bath[11], R. Behrend[15], L. Benedyktowicz[11], L. Bernasconi[16], G. Biguet[17], M. Billiani[11], D. Błażewicz[11], R. Boninsegna[11], M. Borkowski[11], J. Bosch[18], S. Brazill[12], M. Bronikowska[1], A. Bruno[17], M. Butkiewicz-Bąk[1], J. Caron[15], G. Casalnuovo[11], J. J. Castellani[11], P. Ceravolo[12], M. Conjat[11], P. Delincak[11], J. Delpau[11], C. Demeautis[15], A. Demirkol[19], M. Dróżdż[3], R. Duffard[20], C. Durandet[17], D. Eisfeldt[12], M. Evangelista[9], S. Fauvaud[21,17], M. Fauvaud[21,17], M. Ferrais[22], M. Filipek[11], P. Fini[11], K. Fukui[14], B. Gährken[11], S. Geier[23,24], T. George[12], B. Goffin[11], J. Golonka[19], T. Goto[14], J. Grice[25], K. Guhl[11], K. Halíř[11], W. Hanna[26], M. Harman[11], A. Hashimoto[14], W. Hasubick[11], D. Higgins[27], M. Higuchi[14], T. Hirose[14], R. Hirsch[1], O. Hofschulz[11], T. Horaguchi[14], J. Horbowicz[1], M. Ida[14], B. Ignácz[4,5], M. Ishida[14], K. Isobe[14], E. Jehin[28], B. Joachimczyk[19], A. Jones[29], J. Juan[11], K. Kamiński[1], M. K. Kamińska[1], P. Kankiewicz[30], H. Kasebe[14], B. Kattentidt[11], D.-H. Kim[31,32], M.-J. Kim[32], K. Kitazaki[14], A. Klotz[11], M. Komraus[19], I. Konstanciak[1], R. Könyves-Tóth[4,5], K. Kouno[14], E. Kowald[11], J. Krajewski[1], G. Krannich[11], A. Kreutzer[11], A. Kryszczyńska[1], J. Kubánek[11], V. Kudak[33], F. Kugel[15], R. Kukita[14], P. Kulczak[1], D. Lazzaro[9], J. Licandro[23,34], F. Livet[17], P. Maley[12,35], N. Manago[14], J. Mánek[11], A. Manna[11], H. Matsushita[14], S. Meister[11], W. Mesquita[9], S. Messner[12], J. Michelet[17], J. Michimani[9], I. Mieczkowska[1], N. Morales[20], M. Motyliński[19], M. Murawiecka[1], J. Newman[26], V. Nikitin[12], M. Nishimura[14], J. Oey[36], D. Oszkiewicz[1], M. Owada[14], E. Pakštienė[13], M. Pawłowski[1], W. Pereira[9], V. Perig[33], J. Perła[1], F. Pilcher[37], E. Podlewska-Gaca[1], J. Polák[11], T. Polakis[38], M. Polińska[1], A. Popowicz[39], F. Richard[17], J. J Rives[17], T. Rodrigues[9], Ł. Rogiński[1], E. Rondón[9], M. Rottenborn[11], R. Schäfer[11], C. Schnabel[11], O. Schreurs[11], A. Selva[11], M. Simon[11], B. Skiff[40], M. Skrutskie[41], J. Skrzypek[1], K. Sobkowiak[1], E. Sonbas[42], S. Sposetti[11], P. Stuart[12], K. Szyszka[19], K. Terakubo[14], W. Thomas[12], P. Trela[1], S. Uchiyama[14], M. Urbanik[11], G. Vaudescal[11], R. Venable[12], Ha. Watanabe[14], Hi. Watanabe[14], M. Winiarski[3,†], R. Wróblewski[1], H. Yamamura[14], M. Yamashita[14], H. Yoshihara[14], M. Zawilski[11], P. Zelený[43,11], M. Żejmo[44], K. Żukowski[1], and S. Żywica[19]

(Affiliations can be found after the references)

Received 20 February 2023 / Accepted 28 August 2023

ABSTRACT

Context. As evidenced by recent survey results, the majority of asteroids are slow rotators (spin periods longer than 12 h), but lack spin and shape models because of selection bias. This bias is skewing our overall understanding of the spins, shapes, and sizes of asteroids, as well as of their other properties. Also, diameter determinations for large (>60 km) and medium-sized asteroids (between 30 and 60 km) often vary by over 30% for multiple reasons.

Aims. Our long-term project is focused on a few tens of slow rotators with periods of up to 60 h. We aim to obtain their full light curves and reconstruct their spins and shapes. We also precisely scale the models, typically with an accuracy of a few percent.

Methods. We used wide sets of dense light curves for spin and shape reconstructions via light-curve inversion. Precisely scaling them with thermal data was not possible here because of poor infrared datasets: large bodies tend to saturate in WISE mission detectors. Therefore, we recently also launched a special campaign among stellar occultation observers, both in order to scale these models and to verify the shape solutions, often allowing us to break the mirror pole ambiguity.

Results. The presented scheme resulted in shape models for 16 slow rotators, most of them for the first time. Fitting them to chords from stellar occultation timings resolved previous inconsistencies in size determinations. For around half of the targets, this fitting also allowed us to identify a clearly preferred pole solution from the pair of two mirror pole solutions, thus removing the ambiguity inherent to light-curve inversion. We also address the influence of the uncertainty of the shape models on the derived diameters.

Conclusions. Overall, our project has already provided reliable models for around 50 slow rotators. Such well-determined and scaled asteroid shapes will, for example, constitute a solid basis for precise density determinations when coupled with mass information. Spin and shape models in general continue to fill the gaps caused by various biases.

Key words. minor planets, asteroids: general – techniques: photometric

* Lighcurves are available at the CDS via anonymous ftp to cdsarc.cds.unistra.fr (130.79.128.5) or via https://cdsarc.cds.unistra.fr/viz-bin/cat/J/A+A/679/A60

1. Introduction

One of the ultimate aims of asteroid research is to obtain density determinations that would enable studies of their internal structure (micro- and macroporosity), and mineralogical composition in order to link meteorites with their parent bodies. Asteroids larger than 100 km in diameter are considered primitive and largely unchanged since their formation (Morbidelli et al. 2009), while smaller ones are seen as remnants of collisional disruptions and reaccumulations, with substantial macroporosity (Carry 2012).

Sizes of asteroids, a necessary prerequisite to deriving conclusions as to internal structure and density where mass is available, are not easy to determine. Accurate size determinations are of vital importance, as their relative error is tripled in density determinations, while to clearly distinguish between the different mineralogies of asteroid interiors, the density needs to be known with 20% precision (Carry 2012). In the majority of cases, asteroid sizes are calculated from a known value of absolute magnitude, and an assumed geometric albedo (Harris & Harris 1997), which leads to large uncertainties in the derived diameter, namely at the level of 20%–30% for main-belt asteroids, and reaching over 50% in some cases (Tanga et al. 2013)[1]. The solution is to use infrared measurements: in the visible light, a small target with a highly reflective surface is equally as bright as a large target with a dark surface. However, in the infrared, the two objects appear substantially different. A visually dark object, due to its smaller albedo, absorbs most of the solar radiation, and is heated to higher temperatures than its visually brighter counterpart (Harris & Lagerros 2002). Therefore, thermal data combined with absolute brightness in the visible light enable us to put tight constraints on the object size, typically reducing the uncertainty to 5–10% (Delbo' et al. 2015), but only if spin and shape model is available. Without a model, the accuracy of this method is greatly reduced. Also, this method is limited to objects with rich thermal datasets from multiple space observatories. For example, large objects of around 100 km in diameter tend to be saturated in W3 and/or W4 bands (11.1 and 22.64 μm respectively) of the WISE mission (Wright et al. 2010), and so data from WISE cannot be used in their thermophysical modelling (Delbo' et al. 2015). The diameters of these targets must therefore be determined with other methods.

A somewhat complementary method that enables large asteroid surfaces to be imaged and their shapes and sizes to be determined is high-resolution imaging with the state-of-the-art adaptive optics systems used with modern deconvolution techniques. A recent large programme at the VLT using the SPHERE/ZIMPOL instrument provided detailed shapes and accurate sizes for around 40 main-belt asteroids representing all of the main taxonomic classes (see e.g. Vernazza et al. 2021). This technique, although spectacular, is nevertheless limited to the relatively nearby and large asteroids.

Another powerful technique for measuring sizes of asteroids is the stellar occultation timing analysis (Herald et al. 2020), which is almost completely independent of their size or distance. Asteroids in their on-sky paths sometimes cross background stars, casting a shadow on the Earth surface. Observations of these rare events from a few separate sites within the predicted shadow path – thanks to precise timings – enable almost direct asteroid size measurements in kilometers. The target silhouette can also be outlined by the occultation, which can be used to verify the shape models (Ďurech et al. 2011). Such events sometimes lead to discoveries of asteroid satellites or rings (Gault et al. 2022; Ortiz et al. 2017), enabling mass determinations. An important advantage of this technique is the possibility to break the symmetry between two mirror pole solutions, which is inherent to photometric light-curve inversions of asteroids orbiting close to the ecliptic plane (Kaasalainen & Lamberg 2006).

A desirable situation would be to have at least three occultation chords for each event (Ďurech et al. 2011). A dense network of ground-based observatories is therefore required, such as the network built within the Lucky Star project[2], the RECON network[3] (Buie & Keller 2016), or the wide and well-organised regional networks of the International Occultation Timing Association[4]. With *Gaia* catalogues available (Gaia Collaboration 2021), the accuracy of occultation predictions has substantially improved (Tanga et al. 2022), and is expected to improve even more with the release of the full *Gaia* catalogue. Now there is a unique opportunity for successful observations, since both stellar positions and asteroid orbits are determined with unprecedented accuracy, resulting in most reliable occultation predictions to date. There is a time-window in which to take this opportunity, because over the following decades both quantities will start to deteriorate because of uncertainties in stellar proper motions and perturbations of asteroid orbits.

The vast majority of asteroid shape models published today are scale-free, approximate shape representations, because the focus is mainly on determining their spin parameters (see e.g. Hanuš et al. 2018; Ďurech et al. 2020). These shape models, given their angular appearance with sharp edges and large planar areas, tend to be problematic when used in further applications such as thermophysical modelling or fitting their silhouettes to stellar occultations (Hanuš et al. 2016), with the main outcome of both being diameter determinations.

In parallel, the targets on which most of these studies have focused do not necessarily represent all of the various populations of main-belt asteroids (Marciniak et al. 2015). Most of the spin and shape asteroid models available today are for relatively fast-rotating targets, while the TESS mission, for example, revealed that slow rotators (bodies rotating with periods of longer than 12 h) strongly dominate in all asteroid populations at various sizes (e.g. around 5700 objects out of 9900 in the TESS DR1 sample[5], Pál et al. 2020).

Motivated by the trends described above, our survey (see e.g. Marciniak et al. 2018) is designed to reconstruct precise spin and three-dimensional shape models for the most challenging, slowly rotating asteroids, and to determine their sizes with the best available methods (thermophysical modelling, and/or stellar occultation fitting). Thanks to this survey, we now have the most accurate shape models and size values to date for over 30 such asteroids (Marciniak et al. 2021). In this work, we present a further 16 slow rotators, most of which previously lacked shape models or even good-quality light curves. Unlike our previous targets (published in Marciniak et al. 2018, 2019, 2021), these 16 asteroids could not be reliably scaled using thermal data because of the poor quality of the infrared datasets existing for them. Here, we therefore focus on scaling them using stellar occultations.

Section 2 describes our two observing campaigns, which target these bodies: one to obtain their light curves in multiple

[1] https://mp3c.oca.eu/

[2] http://lesia.obspm.fr/lucky-star/

[3] http://tnorecon.net/

[4] https://occultations.org/

[5] https://archive.konkoly.hu/pub/tssys/dr1/

apparitions, and another to observe them in stellar occultations. Sections 3 and 4 present the methods we used for shape reconstruction and to fit the models to stellar occultation chords. Section 5 presents asteroid spin and shape models, verified and scaled using occultation fitting, which in many cases enabled us to identify a preferred pole solution. A final section summarises our findings and presents future plans, with possible applications of our results.

2. Observing campaigns

2.1. Photometric campaign for dense light curves

Our wide photometric campaign, which is described in detail in Marciniak et al. (2015), is motivated by the lack of a good-quality representation of the main-belt asteroid population as a whole by spin and shape models. As expected, models have mainly been constructed for targets for which this process is relatively straightforward, while others have been left behind. Therefore, we focused on asteroids with long periods and low amplitudes in order to counterbalance this unequal distribution. Later, slow rotators were shown to be important targets for thermal studies, as it has been speculated that they might allow us to study deeper surface regolith layers (see Harris & Drube 2016, 2020; Marciniak et al. 2021, for discussions). Furthermore, as evident from the results from *Kepler* (Molnár et al. 2018; Kalup et al. 2021) and confirmed by TESS missions (Pál et al. 2020), the main focus in asteroid physical studies should be on slow rotators.

The light-curve campaign for slow rotators relies on a wide, relatively uniformly distributed, and efficiently coordinated network of small telescopes of up to 1m in diameter (Table B.1 in the Appendix presents the observing runs, sites, and participating observers). This allows full coverage of the light curves of targets with rotation periods reaching 60 h within a reasonable time-frame. Data collection took a long time, partly because of the long periods of our targets, but also because of the paucity of previous data, which meant it was necessary to observe each target in five or more apparitions in order to obtain a unique spin and shape model using the convex inversion method by Kaasalainen et al. (2001). Wherever possible, our light curves are supplemented with data from the *Kepler* and TESS missions, and from previous ground-based observations, resulting in dense light curves (see Table B.1 in the Appendix for references), mostly through the ALCDEF database[6].

2.2. Stellar occultation campaign

In October 2020, we launched an auxiliary campaign for slow rotators. Although some of them have previously been observed in stellar occultations, the results were mostly single positive chord observations, which are unusable for precise scaling (Herald et al. 2019). Therefore, in cooperation with the European Section of the International Occultation Timing Association (IOTA/ES), we started an occultation campaign for 'Neglected Asteroids'[7]. Later, this campaign gained its separate tag in the Occult Watcher Cloud[8], a tool widely used for occultation planning and coordination. The aim is to register multi-chord stellar occultations for slow rotators from our target list. In contrast to the light-curve campaign, where hundreds of hours on-target are needed, occultation events require observations of only one or 2 min, as they last only a few seconds. This means that good coordination and timing are even more important than in the light-curve campaign. The occultation predictions were made using the JPL Horizons database for asteroid orbits[9], and *Gaia* EDR3[10] for star positions. Although these events are rare, the campaign has already resulted in a dozen or so successful occultation observations, with the number of positive chords per event reaching nine (see e.g. the events from the years 2021 and 2022 in Figs. A.6 and A.14).

Archival occultation data were downloaded from the Planetary Data System (PDS) archive[11] (Herald et al. 2019), and more recent ones were obtained from the archive of the Occult programme[12], or directly from the regional IOTA coordinators, who perform data evaluation and vetting in order to achieve good-quality and consistent occultation results. Most of the occultation observers are amateur astronomers, which makes this campaign a good example of a successful professional–amateur, or 'pro–am', collaboration. Table B.2 provides the observer names and site locations for each occultation event used here.

3. Convex inversion with shape regularisation

The majority of asteroid models presented in this work were constructed using the common convex inversion method of Kaasalainen & Torppa (2001); Kaasalainen et al. (2001). When light-curve data are sufficiently abundant to uniquely determine the sidereal rotation period and the pole direction, the shape model reconstructed from the Gaussian image is usually such that its rotation axis z is very close to the principal axis of the inertia tensor with the largest moment of inertia. Shapes that fit the data but strongly violate this condition have to be rejected as physically unacceptable solutions of the inverse problem. However, in some cases the data are so abundant that it is clear that, although the solution is correct, the shape is not physically acceptable. By 'squeezing' the shape along the rotation axis, the inertia tensor can be changed in such a way that its greatest axis is close to the rotation axis. However, this can only be done after the best-fit model is found, and we must also check whether or not this shrinking along the rotation axis affects the light-curve fit significantly.

When working with the Gaussian image during the optimisation, the shape is not known and we cannot regularise it to obtain the maximum moment of inertia around the rotation axis. However, even without computing the inertia tensor precisely, the shapes that are not rotating along the shortest axis are elongated along the z axis. This elongation means that the cross-section viewed from the pole direction is smaller than that from the equatorial view (xy plane). Although the 3D shape is not available during optimisation, the areas of surface facets and their normals are known, and so their projections can be computed. The regularisation term R that we introduce is

$$R = \frac{\sum_{i=1}^{N} \sigma_i \left(|\hat{\boldsymbol{n}}_i \cdot \hat{\boldsymbol{x}}| + |\hat{\boldsymbol{n}}_i \cdot \hat{\boldsymbol{y}}|\right)}{2 \sum_{i=1}^{N} \sigma_i |\hat{\boldsymbol{n}}_i \cdot \hat{\boldsymbol{z}}|}, \tag{1}$$

[6] https://alcdef.org
[7] https://www.iota-es.de/neglected_asteroids.html
[8] https://cloud.occultwatcher.net/
[9] https://ssd.jpl.nasa.gov/horizons/
[10] https://www.cosmos.esa.int/web/gaia/earlydr3
[11] http://sbn.psi.edu/pds/resource/occ.html
[12] http://www.lunar-occultations.com/iota/occult4.htm

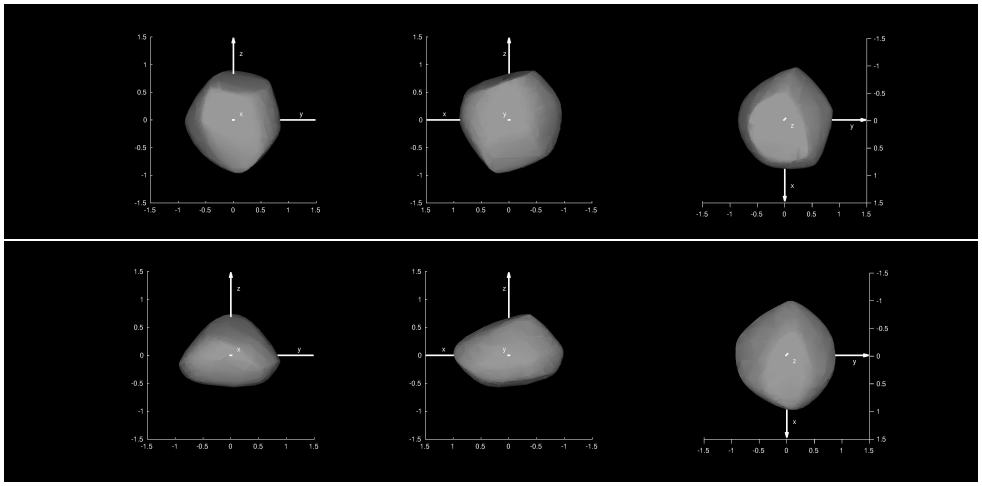

Fig. 1. Two versions of shape model 2 for (566) Stereoskopia: without shape regularisation (top) and with regularisation applied (bottom), using the same starting parameters otherwise. The three views show, from left to right: two equatorial views separated by 90°in phase, and the pole-on view. We note that the pole-on silhouettes generally agree between two versions of the shape model, as it is the equatorial cross-section that most effectively influences the light curves.

where $\hat{\boldsymbol{n}}_i$ are unit normals to surface elements of areas σ_i, and $\hat{\boldsymbol{x}}, \hat{\boldsymbol{y}}, \hat{\boldsymbol{z}}$ are unit vectors along the coordinate axes; the summation is over all N surface elements. The more extended the shape along the z axis, the higher R, and so the penalty function that is added to the χ^2 is R^2 times some weight w. By increasing w, the shape model is forced to have projected areas along the x and y axes that are smaller than along the z axis, which makes it more oblate and ensures physically correct rotation. This way, we were able to produce physically realistic shapes for (439) Ohio and (566) Stereoskopia, for which the standard light-curve inversion without regularisation led to unphysical shapes. With regularisation, the fit to the data remained almost the same (RMS changed from 0.0073 to 0.0074 for the example shown in Fig. 1), meaning that the dimension along the rotation axis was not constrained by the data, and the regularisation helped to produce realistic shapes without affecting the fit. A 'negative regularisation' mentioned in the following section means using the regularisation term $1/R^2$, which produces more stretched shapes when needed.

4. Occultation fitting

As mentioned in Sect. 1, shape models derived from photometry do not carry information about the size; they are scale-free. We scaled them using the same approach as Ďurech et al. (2011) and recently Marciniak et al. (2021). The positions of the observers detecting an occultation were projected on the fundamental plane, which is the plane crossing the geocenter and is perpendicular to the direction from the asteroid to the star. We then computed the orientation of the shape model for the mean time of occultation and projected it also to the fundamental plane. Because the time span of occultation timings is usually much shorter than the rotation period of the asteroid, the rotation is neglected, and the silhouette is assumed to be constant. The size of the asteroid and the relative position of its projection on the fundamental plane with respect to chords are three parameters optimised to converge to the best agreement between the projection of the asteroid shape and occultation chords. The goodness of the fit is described by a standard χ^2 measure with timing uncertainties taken into account.

The uncertainty of the derived size is affected by many factors: the number of occultation events, the number of chords in individual occultations and their distribution across the silhouette, the timing errors of individual chords, and the uncertainty on the projection of the asteroid (and therefore the uncertainty on its shape and spin state). When there are several occultations by one asteroid with many chords covering the whole projected disc, the RMS residual in kilometers is one estimation of the size uncertainty (see the last column in Table 1).

However, the uncertainty on the sizes of the asteroids determined in this way does not take into account the uncertainty on the models themselves. The main problem is that relative light curves supporting the models are largely insensitive to a vertical dimension of the shape model, as the ratio between the biggest and smallest projected area in a given aspect remains similar regardless of this dimension. To tackle this problem, we used the ability of inertia regularisation to influence the vertical stretch of the derived models. We created ten versions of each model, with both positive and negative regularisations, creating flatter and rounder shapes that would still fit the light curves at a similar level to the nominal solution, and at the same time remaining physical (rotating around the shortest axis) and realistic (e.g. not being extremely thin). Models fitting the light curves within 10% RMS of the best-fit solution are accepted following Kaasalainen et al. (2001). With tens of light curves and thousands of photometric points, the 10% increase in RMS is really an extreme limit and is the upper boundary for 'acceptable' models, as shown by the example in Fig. 2. The upper model is the nominal one, without inertia regularisation, while the bottom one was created with a relatively high level of regularisation. The other model fitted the light curves within 7% of the best solution (RMS of 0.0117 vs. 0.0110 for the best fit) and is already unrealistically flattened. Another approach relates the χ^2 limit to the number of data points (see e.g. Hanuš et al. 2021; Ďurech et al. 2022, Appendix A).

Those variations of each model have been fitted to occultations as well, resulting in a pool of plausible sizes. This also revealed the shape versions fitting the occultations with substantially higher RMS, or not fitting some chords at all. In some cases, this strengthened the case for a preference for one of two pole solutions, where all the versions of shape for one pole

Table 1. Spin parameters and sizes of asteroid models obtained in this work.

Asteroid	Pole		P	Observing span	N_{app}	N_{lc}	D	D RMS
	λ_p(°)	β_p(°)	(h)	(yr)			(km)	(km)
(70) Panopaea	42 ± 5	+27 ± 3	15.80440 ± 0.00002	1980–2019	7	122	128 ± 7	7
	240 ± 6	+26 ± 4	15.80439 ± 0.00001				128^{+7}_{-11}	7
(275) Sapientia	85 ± 11	−10 ± 18	14.93045 ± 0.00005	1998–2018	7	38	98^{+6}_{-11}	6
	264 ± 4	**−1 ± 20**	**14.93045 ± 0.00005**				$\mathbf{103}^{+6}_{-7}$	6
(275) Sapientia (ADAM)	82 ± 8	−11 ± 17	14.93044 ± 0.00005	1998–2018	7	38	100 ± 1	–
	260 ± 7	**−2 ± 20**	**14.93044 ± 0.00005**				**100 ± 1**	–
(286) Iclea	**31 ± 5**	**+13 ± 4**	**15.36120 ± 0.00004**	2002–2019	9	52	$\mathbf{86}^{+13}_{-7}$	**2**
	196 ± 5	+44 ± 7	15.36114 ± 0.0007				69^{+3}_{-12}	3
(326) Tamara	**79 ± 1**	**−3 ± 3**	**14.46130 ± 0.0005**	1981–2019	9	69	$\mathbf{77}^{+5}_{-10}$	**5**
	242 ± 1	−36 ± 3	14.46136 ± 0.0004				81 ± 9	9
(412) Elisabetha	3 ± 20	+17 ± 7	19.65610 ± 0.00003	1990–2021	7	77	119 ± 9	9
	191 ± 23	**+52 ± 8**	**19.65618 ± 0.00004**				$\mathbf{97}^{+7}_{-14}$	**4**
(426) Hippo	62 ± 55	−49 ± 20	67.5038 ± 0.0005	1993–2021	7	103	129^{+19}_{-8}	6
	223 ± 80	**−89 ± 17**	**67.5041 ± 0.0005**				**122 ± 4**	**4**
(439) Ohio	**308 ± 50**	**−61 ± 7**	**37.46726 ± 0.00005**	1984–2022	10	66	$\mathbf{74}^{+3}_{-8}$	**2**
(464) Megaira	47 ± 2	+16 ± 5	12.878572 ± 0.000002	1979–2020	9	85	76^{+3}_{-6}	3
	236 ± 5	+38 ± 10	12.878572 ± 0.000002				76^{+2}_{-11}	2
(464) Megaira (ADAM)	45 ± 3	+13 ± 5	12.878573 ± 0.000001	1979–2020	9	85	75 ± 1	–
	234 ± 4	+34 ± 14	12.878573 ± 0.000001				79 ± 1	–
(476) Hedwig	**49 ± 4**	**+60 ± 7**	**27.2403 ± 0.0006**	1982 – 2018	6	58	$\mathbf{116}^{+6}_{-16}$	**6**
	218 ± 4	+36 ± 4	27.2404 ± 0.0005				122 ± 10	10
(524) Fidelio	52 ± 50	+76 ± 6	14.171031 ± 0.000005	2005–2019	6	31	66 ± 5	5
	186 ± 25	**+54 ± 10**	**14.171042 ± 0.000005**				**67 ± 3**	**3**
(530) Turandot	42 ± 3	+28 ± 5	19.95240 ± 0.00009	1986–2019	8	62	89 ± 11	11
	226 ± 9	**+54 ± 10**	**19.95231 ± 0.000009**				**89 ± 6**	**6**
(530) Turandot (ADAM)	39 ± 6	+31 ± 11	19.95239 ± 0.00009	1986–2019	8	62	89 ± 2	–
	223 ± 9	**+60 ± 9**	**19.95232 ± 0.000009**				**89 ± 2**	–
(551) Ortrud	149 ± 35	−63 ± 9	17.41924 ± 0.00003	2006–2021	7	88	85 ± 11	11
	305 ± 30	−66 ± 8	17.41921 ± 0.00002				86 ± 10	10
(566) Stereoskopia	**164 ± 15**	**−2 ± 2**	**12.08466 ± 0.00006**	1990–2022	6	35	**148 ± 8**	**8**
	338 ± 9	−13 ± 2	12.08463 ± 0.00003				148 ± 11	11
(657) Gunlod	127 ± 25	+61 ± 6	15.92872 ± 0.00003	1984–2022	6	47	37 ± 3	3
	252 ± 50	**+51 ± 20**	**15.92870 ± 0.00004**	1984–2022	6	47	$\mathbf{39}^{+2}_{-1}$	**1**
(738) Alagasta	67 ± 7	−47 ± 5	17.8888 ± 0.0005	2015–2020	5	41	56 ± 6	6
	246 ± 10	−41 ± 8	17.8889 ± 0.0006				54 ± 4	4
(806) Gyldenia	34 ± 12	+39 ± 2	16.85695 ± 0.00003	2010–2021	8	63	57 ± 8	8
	235 ± 15	+42 ± 5	16.85699 ± 0.00007				55 ± 4	4

Notes. The columns contain asteroid name, J2000 ecliptic coordinates λ_p, β_p of the spin axis solution, and the sidereal rotation period P, with the mirror pole solution in the second row. The following columns provide the main characteristics of the light-curve dataset (same for both pole solutions): observing span in calendar years, number of apparitions (N_{app}) and number of light curves (N_{lc}.) The last two columns give volume-equivalent diameter D and its RMS residual from the stellar occultation fitting. Boldface highlights the solution preferred by means of occultation fits. See Sect. 4 for the discussion on diameter uncertainties.

resulted in a similar value for the size and a consistently small RMS of the fit, while for the other pole the sizes varied substantially, and the RMS was high. Such cases are described in more detail in the following section.

The key point here was to check whether the range of sizes derived in this way would be higher or smaller than the nominal RMS of the occultation fit, which is mainly governed by the occultation timing uncertainties. When it was higher, it

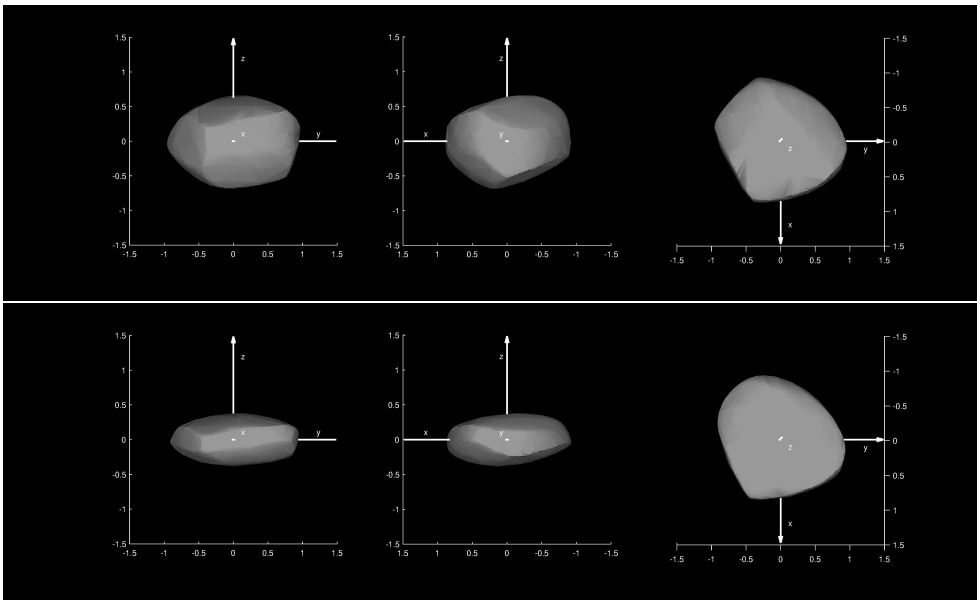

Fig. 2. Two versions of shape model 2 for (412) Elisabetha. The high-regularisation model (bottom) still fits the light curves on formally acceptable level, but is unrealistically flat. See Sect. 4 for discussion.

replaced the nominal RMS value as a measure of diameter uncertainty in Table 1. However, when the range of sizes was smaller than the RMS of the fit, this meant that the uncertainty here was dominated by the occultation timing errors or the convex approximation of the shape.

5. Results

We used the rich datasets of dense light curves from our campaign (see Figs. C.1–C.77) for spin and shape modelling with the classical light-curve inversion method – or its slight variation with shape regularisation – in order to make non-physical models rotate in a physical manner around the axis of largest inertia (see Sect. 3). Table 1 summarises the spin parameters and diameters determined in this work. The fit of the shape models to occultation chords can be seen in Figs. 3–A.17. A good fit has manifold benefits: primarily it serves to scale the models in kilometers, but it also verifies the shape features, and often clearly points to the solution that must be close to the real one, making its mirror counterpart less probable. We should note that the asteroid sizes determined here are diameters of volume-equivalent spheres, while sizes determined from infrared measurements are for surface-equivalent spheres. In any case, the difference between the two diameters for the same shape model is at the level of 5% or less, which is smaller than the uncertainty on the models themselves, especially with NEATM spherical shape approximation. It is therefore justified to directly compare sizes determined with the two methods, without any scaling factors.

In parallel, in a few justified cases (275 Sapientia, 464 Megaira, 530 Turandot) where the occultation results suggest the presence of non-convex shape features, we additionally used the all-data asteroid modelling (ADAM, Viikinkoski et al. 2015) method for shape reconstruction. This technique uses both light curves and occultation timings as input data in a single optimisation process. The results are presented in Figs. 5, A.1, A.8, and A.12 and in Table 1. They can be compared with the respective shape models constructed with traditional convex inversion without occultations; and fitted to occultations later (Figs. 4, A.7, and A.11). The determined sizes and spin parameters are consistent between the two methods, while ADAM shapes show a slightly better fit to the occultations, as expected. The size uncertainties for ADAM shape models presented in Table 1 come from the scatter of solutions and are clearly underestimated.

For each model, Table 1 presents the spin axis ecliptic coordinates, with the sidereal period of rotation, together with the uncertainties on each parameter. The table also contains details of the light-curve datasets, and the volume-equivalent diameters with uncertainties based on the deviation of the shape model silhouettes from the occultation chord ends, or on the scatter of sizes for various versions of the same shape, whichever source dominated the error budget. The preferred pole solutions after occultation fitting are marked in boldface. In Figs. 3–A.17, lesser preferred solutions are marked with dashed magenta contours, and the solid blue contours mark the preferred solutions. In the case of only slightly preferred solutions, both contours are solid lines, but the preferred solution is still shown in blue. In some cases, the preference seems to be based on single chords, but it is the duration rather than the chord absolute position that is the deciding factor in such cases The duration of the occultation events is usually recorded correctly, while the gross timing error might shift the whole chord, but does not change its length. There are of course exceptions to this rule; see the discussion on (275) Sapientia in Sect. 5. In the cases with no preference for the spin solution, both coloured contours are again solid; see the text and figure captions for details.

Additionally, Table 2 contains the range of previously determined sizes, with the source references. Please note the diversity of the literature diameters, differing by 50% for some targets between different works. Below we describe all targets in more detail.

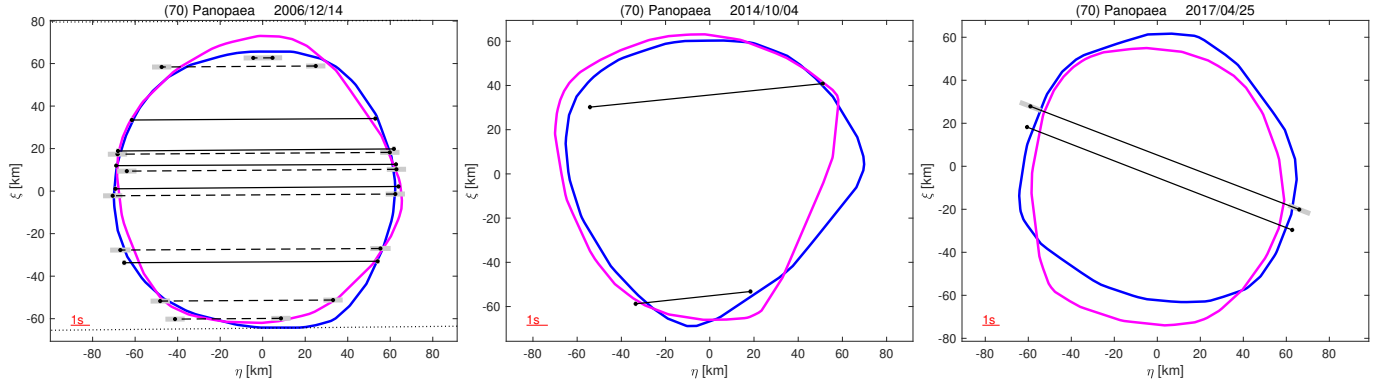

Fig. 3. (70) Panopaea model fit to occultation chords shown in the fundamental plane. North is up and west is right. Dashed lines mark visual observations, as opposed to video or photoelectric ones marked with solid lines. Grey segments correspond to timing uncertainties. Blue contour: Instantaneous silhouette of shape model 1 (see Table 1). Magenta: Same but for model 2. In this case, occultations show no preference for any of the models.

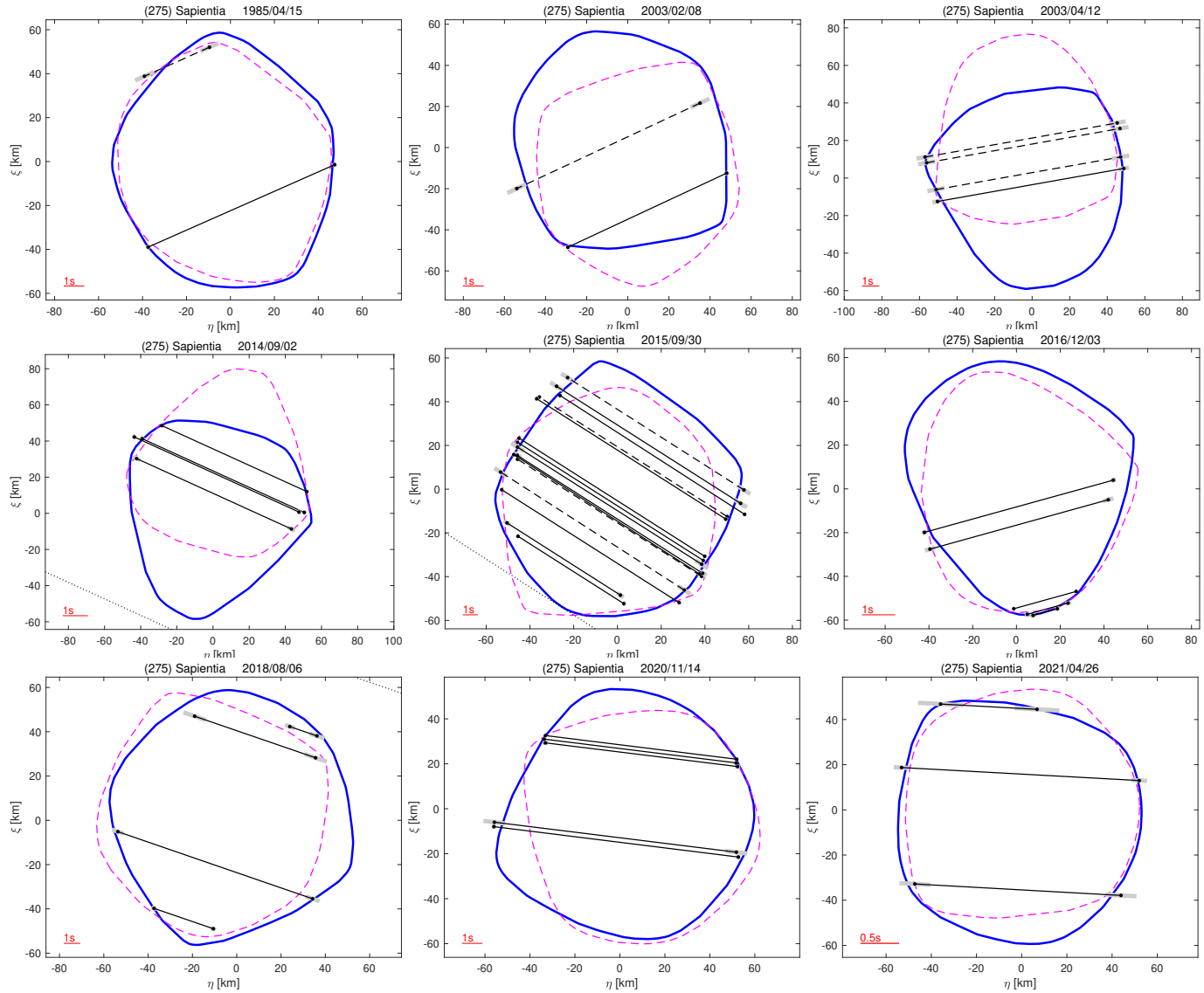

Fig. 4. (275) Sapientia model fit to occultation chords. Here, model 2 is preferred (blue solid contour).

Table 2. Previously published diameters for the asteroids studied here.

Asteroid	D_{min} (km)	D_{min} reference	D_{max} (km)	D_{max} reference
(70) Panopaea	105.17 ± 2.797	Ryan & Woodward (2010)	162.63 ± 1.280	Masiero et al. (2012)
(275) Sapientia	89.05 ± 25.310	Masiero et al. (2020)	124.59 ± 35.830	Masiero et al. (2021)
(286) Iclea	81.31 ± 2.762	Ryan & Woodward (2010)	125.20 ± 40.850	Masiero et al. (2021)
(326) Tamara	63.30 ± 14.530	Masiero et al. (2021)	116.98 ± 36.530	Masiero et al. (2021)
(412) Elisabetha	76.38 ± 2.114	Ryan & Woodward (2010)	111.12 ± 22.220	Alí-Lagoa et al. (2018)
(426) Hippo	107.33 ± 4.405	Ryan & Woodward (2010)	137.56 ± 1.080	Masiero et al. (2012)
(439) Ohio	69.53 ± 2.060	Ryan & Woodward (2010)	86.86 ± 0.750	Masiero et al. (2012)
(464) Megaira	56.93 ± 15.508	Masiero et al. (2017)	91.81 ± 31.750	Masiero et al. (2021)
(476) Hedwig	106.15 ± 27.050	Nugent et al. (2016)	138.49 ± 0.970	Masiero et al. (2012)
(524) Fidelio	61.71 ± 26.030	Nugent et al. (2016)	83.26 ± 4.093	Ryan & Woodward (2010)
(530) Turandot	75.88 ± 19.520	Masiero et al. (2021)	89.50 ± 17.900	Alí-Lagoa et al. (2018)
(551) Ortrud	65.91 ± 14.860	Nugent et al. (2016)	86.04 ± 4.731	Ryan & Woodward (2010)
(566) Stereoskopia	134.00 ± 6.627	Masiero et al. (2011)	190.08 ± 7.909	Ryan & Woodward (2010)
(657) Gunlod	31.44 ± 8.570	Masiero et al. (2020)	46.59 ± 3.149	Ryan & Woodward (2010)
(738) Alagasta	55.36 ± 1.867	Ryan & Woodward (2010)	77.94 ± 24.740	Nugent et al. (2016)
(806) Gyldenia	56.43 ± 3.098	Ryan & Woodward (2010)	83.10 ± 0.740	Masiero et al. (2012)

Notes. Minimum and maximum diameters are given with their uncertainties and references. For the full list, see the MP3C database.

5.1. (70) Panopaea

Our result for the spin and shape of Panopaea (see Table 1) closely agrees with the one recently published by Hanuš et al. (2021). Three multi-chord occultations were available for Panopaea, one of them with a particularly rich set of 13 positive chords (see Fig. 3). However, many of these were visual observations, and the chords had unrealistically small error bars. All errors have been changed here to 0.05 s for photoelectric and video observations, and to 0.5 s for visual observations. Both shape solutions are consistent with the occultations, resulting in a size determination of 128 km with very small uncertainty of a few percent (Table 1). Previous literature diameter determinations for Panopaea varied widely from 105 km to 163 km (Table 2), and were mostly based on the NEATM model (Harris 1998), which approximates the body shape with a sphere.

5.2. (275) Sapientia

There were seven pre-existing occultation observations for this target (one with 16 chords), and our Neglected Asteroids campaign adds another two events. From the full set of nine events, four chords had to be removed because of their clear inconsistency with the remaining ones: there must have been large errors on either the duration or the absolute timing. The fitting to occultations clearly points at pole 2 as the preferred solution (Table 1), which is especially evident from the fit to occultations from years 2015, 2020, and 2021 (see Fig. 4). The size is determined with high accuracy (7%).

With such a rich set of occultations, and some of them suggesting non-convex shape features, the ADAM method was also applied. The resulting shape for pole 2 shows a slightly better fit to all occultations simultaneously (see Figs. 5 and A.1), but the fit is still not perfect. In particular, the four-chord event from the year 2018 cannot be fittted by any of the models, even though here we allow the occultations to influence the shape. The northernmost chord probably has an underestimated duration (this event is actually annotated 'short low drop event in noisy recording') or it points to some small shape feature below the resolution of the ADAM shape reconstruction procedure. The size of Sapientia found with the ADAM method (100 km) is consistent with that described above, and the scatter of possible sizes shrank to a mere 1%. Previous size determinations for Sapientia were somewhat less discrepant than for Panopaea, ranging from 89 to 124 km (Table 2).

5.3. (286) Iclea

Although the fit to the only available three-chord occultation for Iclea only slightly favours the pole 1 solution (see Fig. A.2), the sizes from the fitting for both solutions are clearly discrepant: the size for pole 2 solution is much smaller than the size for the pole 1 solution (69 vs. 86 km), and is also inconsistent with all the previous sizes determined using infrared data (81–125 km, see Table 2). Also, pole 1 spin parameters are confirmed by the results of Ďurech et al. (2020); this is the only solution for the pole of Iclea. Considering all of the above, we think that our solution for pole 2 (Table 1) can be safely rejected.

5.4. (326) Tamara

There exists an extremely wide range of literature diameters for Tamara (see Table 2): from 63 km to as much as 117 km, an almost two-fold difference. This might be due to the relatively unusual orbit of Tamara given that it is a main-belt asteroid, with an eccentricity of 0.19, and an inclination of 23°. As a consequence, thermal measurements of Tamara must have been taken at substantially varied heliocentric distances, complicating thermal analysis. Our result, being independent of thermal aspects, resolves these inconsistencies, pinpointing the diameter of this body to 77^{+5}_{-10} km. The first pole solution is preferred based on the quality of the occultation fit (Fig. A.3), with the RMS being almost twice as low as in any version of model 2. Also, the spin solution found here is in good agreement with that from Hanuš et al. (2021).

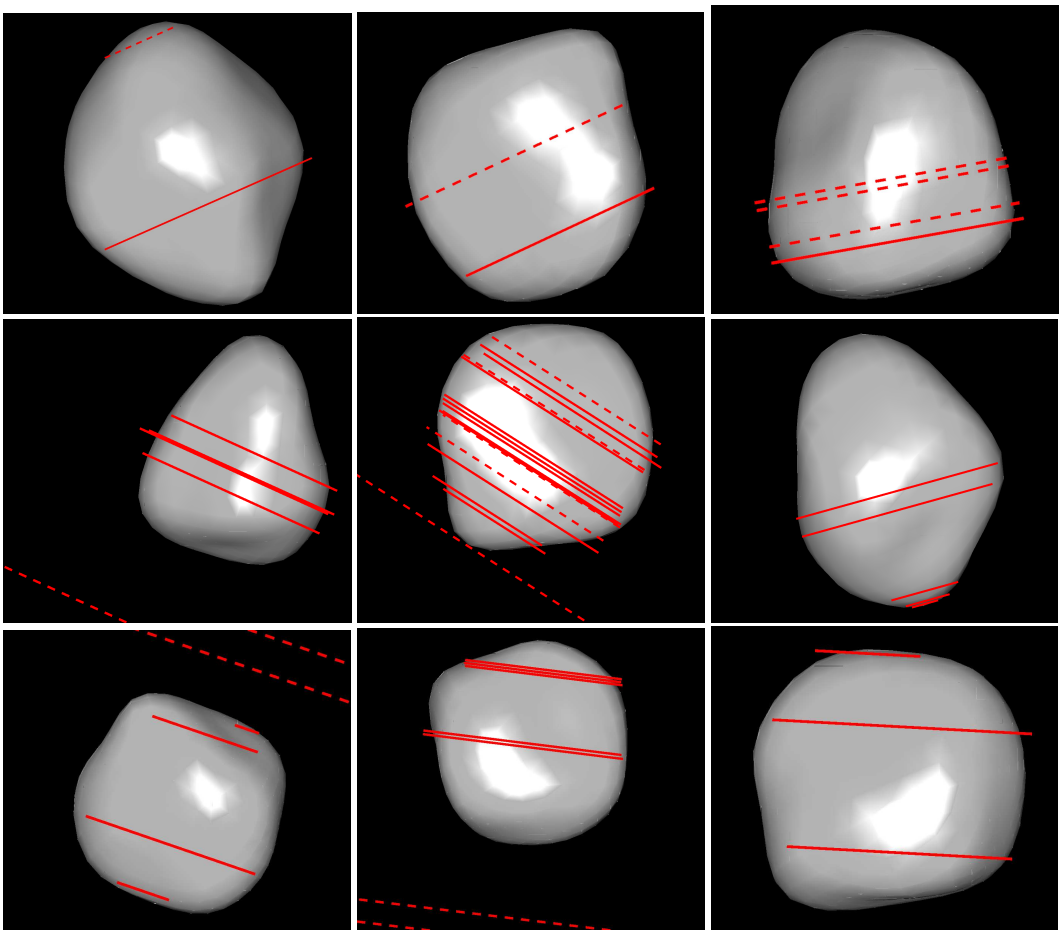

Fig. 5. (275) Sapientia, ADAM solution pole 1, shown with occultation chords used to construct the model. Occultation events are the same as in Fig. 4.

5.5. (412) Elisabetha

The model 2 solution for Elisabetha is a much better fit to the occultations than any version of model 1 (compare the events from years 2011 and 2016 between the two poles in Fig. A.4), and therefore model 2 is our preferred solution (Table 1). Our size determination (97^{+7}_{-14} km) confirms previous determinations (76–112 km), which tended towards larger values (see Table 2, and MP3C database).

5.6. (426) Hippo

For Hippo we obtained two pole solutions from light-curve inversion; however, the second pole (see Table 1) was at the verge of rejection on the basis of the RMS fit to the light curves, which was almost 10% higher than for the first pole. See Sect. 4 for a discussion of this threshold. Our spin solutions roughly agree with those published by Hanuš et al. (2021) and Ďurech et al. (2019), in terms of pole latitude and period but disagree with the pole longitude for model 2 presented by these authors.

We decided to fit both shape solutions to the rich set of occultations; see Fig. A.5. Surprisingly, it is the shape connected to pole solution 2 (blue contour in Fig. A.5) that fits most of the occultations better than solution 2, especially the richest one from 27 December 2021. We therefore consider the pole 1 solution to be lesser probable (dashed magenta contour), even though it provided a formally better fit to light curves. The size determined here (122 ± 4 km) is close to the middle of the size range found in the literature (Table 2).

5.7. (439) Ohio

Our research into the asteroid Ohio is a success in multiple ways. First, we have been able to correct a previously accepted rotation period, identifying a period of around 37.46 h as the correct one (Marciniak et al. 2015), instead of 19.2 h which persisted for decades in the asteroid Light-Curve Database (Warner et al. 2009). Later, after gathering sufficient light-curve data over multiple apparitions, we managed to obtain its physically rotating model, which was possible thanks to regularisation added to light-curve inversion routines. There was only a single pole solution (Table 1) on the level of light-curve inversion, as the mirror pole solution gave a much poorer fit to light curves. This is facilitated by a relatively high orbital inclination of 19° for Ohio. Our spin solution is ~30° and ~50° away in spin axis latitude and longitude, respectively, from the pole 2 solution provided by Ďurech et al. (2018).

Later, in March 2022, we coordinated observers around two stellar occultation events (resulting in 6 and 9 positive chords, including one grazing event observed by the first author), where there were no previously recorded multi-chord events (i.e. containing more than three positive chords). In the end, our shape model was fitted to these occultations, presenting a very good-quality fit (see Fig. A.6). Thanks to the quality of both the model

and the occultation timings, the shape was precisely scaled with small residual RMS. The only small discrepancies between the model and the chords from the last occultation probably reveal the shape resolution limits of a classical light-curve inversion.

5.8. (464) Megaira

The fit to occultations for Megaira is puzzling: Model 2 gives a somewhat better fit than model 1 (Fig. A.7), but it always leaves the southernmost chord outside the profile. Some variations of the shape for model 1 can fit that chord, but they then lead to a clearly poorer fit to the remaining chords. The situation is similar when modelling this target with the ADAM algorithm (Fig. A.8). In summary, model 2 is slightly preferred, but cannot fit all the chords. Previously published sizes range from 57 to 92 km. Our determination results in sizes of 75–79 km.

5.9. (476) Hedwig

Both pole solutions for Hedwig agree with those found by Hanuš et al. (2021), but the pole 1 solution is clearly the preferred one by the fit to almost all of the six occultations, especially to the event from the year 2000 (see Fig. A.9). The diameter we determine (116^{+6}_{-16} km) is around the mean of the range of previous determinations (106–138 km, Table 2.)

5.10. (524) Fidelio

Pole 2 (see Table 1) is preferred by occultations here (Fig. A.10). This solution is also confirmed by the value for β_p found by Ďurech et al. (2020) and the full spin solution by Hanuš et al. (2021). The size determined here (67 ± km) is closer to the lower end of the range of literature sizes (62–83 km).

5.11. (530) Turandot

The occultation set for Turandot contained a few discrepant chords, and so we had to remove four chords from the first event in the year 2006, and completely leave out the second three-chord event from that year due to strong mutual inconsistencies among the chords. The remaining set allowed us to clearly identify one of two pole solutions as the preferred one (see Fig. A.11), especially in the ADAM version of the model. With the ADAM model for pole 2, the southernmost chord of the 2006 event is finally fitted, revealing a non-convex feature on the shape (Fig. A.12). Both methods gave the same size for the two models, of namely 89 km, while previous determinations were in the narrow range from 76 to 89 km. Our spin latitude found with the ADAM method is almost 30° away from the value found by Hanuš et al. (2021) using convex inversion.

5.12. (551) Ortrud

The occultation event for Ortrud from July 2021 contains problematic, mutually inconsistent chords (Fig. A.13). Because it is hard to identify the erroneous chords, we keep them all for the scaling. This results in larger RMS residuals for the diameter (12%). Previous determinations ranged from 66 to 86 km (see Table 2), while ours are around 85 km, confirming the upper values.

5.13. (566) Stereoskopia

One of the best covered occultations for Stereoskopia was observed within our campaign (see the event from 2021 in Fig. A.14). As the shape solutions tended to be non-physical and unstable here, we used the regularisation, and tried a few versions of the shape model for each of the two pole solutions. We adopted the one that gave the best fit to occultations. All the shape fits for pole 1 were clearly superior to any shape fits for pole 2. Still, no shape was able to fit all the chords from the event in 2021. This might be due to insufficient information on the shape contained in the light curves of this low-pole asteroid (see very low $|\beta_p|$ values in Table 1). Some light curves were obtained in pole-on geometries, and therefore showed hardly any brightness variations.

There were large discrepancies in literature diameter determinations for Stereoskopia, which range from 134 to 190 km. The value found here (148 km) is consistent with lower of these values, and in spite of the imperfect fit, has an RMS of only 5–7%.

5.14. (657) Gunlod

The values for both pole coordinates for Gunlod are roughly consistent with the ones determined previously by Ďurech et al. (2019), although the poles found here have notably higher (~20°) values of β_p, which are closer to the values found by Hanuš et al. (2021). The fit to the only multi-chord occultation by Gunlod prefers pole 2 solution (see Fig. A.15), however that preference is based on only one chord, and a smaller RMS value for the diameter (Table 1). Literature size determinations for Gunlod range from 31 to 46 km, while this work places its diameter in the middle of this range (37–39 km).

5.15. (738) Alagasta

The fit to occultations shows that the solution for pole 2 of Alagasta is slightly better, but still imperfect (Fig. A.16). Sizes from the literature are from 55 to 78 km, while the size determined here is 55 ± 5 km, confirming the values at the lower end of this range.

5.16. (806) Gyldenia

The spin solution for asteroid Gyldenia is within a few degrees of that found by Ďurech et al. (2019). The pole 2 solution seems to better fit the only available occultation (Fig. A.17), as also evidenced by the smaller RMS residual for the volume-equivalent size determined in this way (Table 1). Still, this solution also fails to fit the longest occultation chord. On the other hand, pole 1 has difficulty in fitting the short chord at the edge of the shape; although the fitting of such small chords is problematic in general. Previous diameter determinations range from 56 to 83 km (Table 2), and the diameter presented here is 55–57 km, which is consistent with the lowest of the published values.

6. Conclusions and future prospects

Our project and comprehensive approach has provided almost 50 high-quality scaled models (Marciniak et al. 2018, 2019, 2021) for poorly studied but large and ubiquitous asteroids, including 16 presented here. Two observing campaigns – for light curves and occultations – were carried out by a wide network of collaborators and involved many amateur astronomers, bringing

new people to the field. We are going to continue the occultation campaign, and to a lesser extent, also the one for time-series photometry, as the latter is gradually being replaced by wide ground-based and space-based sky surveys. As so many asteroids have poorly determined sizes, stellar occultations are the best technique to reliably determine the sizes of a large number of targets from all groups, especially in the era of the *Gaia* mission.

Our precise determinations of spins, shapes, and sizes for many, previously largely omitted targets enrich and complement the available sample of modelled asteroids[13] (Ďurech et al. 2010). Our set includes asteroids belonging to a few asteroid families that are believed to form in catastrophic disruptions of larger parent bodies. Current theories of collisional evolution of the Solar System predict a steady number of existing asteroid families throughout history, but observational evidence contradicts this prediction (Brož et al. 2013). The key to solving this inconsistency is to determine family ages by deciphering the drift rate of family members from the centre. This can be done by studying the V-shaped dependence of the inverse size $1/D$ on the proper semimajor axis $a_{\rm p}$ (Vokrouhlický et al. 2006). Among the many potential applications, our improved size determinations and spin properties can facilitate better predictions of the thermally driven drift of the asteroids within their families.

Acknowledgements. We thank an anonymous referee, whose comments led to a substantial improvement of this paper. This work was supported by the National Science Centre, Poland, through grant no. 2020/39/O/ST9/00713 This project has been supported by the Lendület grant LP2012-31 of the Hungarian Academy of Sciences and by the KKP-137523 Élvonal grant of the Hungarian Research, Development and Innovation Office (NKFIH). The work of JĎ and JH was supported by the grant 20-08218S of the Czech Science Foundation, and by the Erasmus programme of the European Union under grant number 2020-1-CZ01-KA203-078200. A. Pál and R. Szakáts have received funding from the K-138962 grant of the National Research, Development and Innovation Office (NKFIH, Hungary). Erika Pakštienė and Rūta Urbonavičiūtė acknowledge the Europlanet 2024 RI project funded by the European Union's Horizon 2020 Research and Innovation Programme (Grant agreement No. 871149). Data from Observatório Astronômico do Sertão de Itaparica (OASI, Itacuruba) have been obtained with the 1-m telescope, a facility operated by the IMPACTON project of the Observatório Nacional, Brazil. F.M., E.R., M.E., W.M., W.P. and J.M. would like to thank CNPq, FAPERJ (E-26/201.877/2020 and E-26/204.602/2021) and CAPES for their support through diverse fellowships (Brazilian funding agencies). Support by CNPq (310964/2020-2) and FAPERJ (E-26/202.841/2017 and E-26/201.001/2021) is acknowledged by D.L. We acknowledge financial support from the State Agency for Research of the Spanish MCIU through the "Center of Excellence Severo Ochoa" award to the Instituto de Astrofísica de Andalucía (SEV-2017-0709). Funding from Spanish projects PID2020-112789GB-I00 from AEI and Proyecto de Excelencia de la Junta de Andalucía PY20-01309 is acknowledged. This work uses data obtained from the Asteroid Light-Curve Data Exchange Format (ALCDEF) database, which is supported by funding from NASA grant 80NSSC18K0851. This work is based on data provided by the Minor Planet Physical Properties Catalogue (MP3C) of the Observatoire de la Côte d'Azur. Based on observations made with the Mercator Telescope, operated on the island of La Palma by the Flemmish Community, at the Spanish Observatorio del Roque de los Muchachos of the Instituto de Astrofísica de Canarias. Based on observations obtained with the MAIA camera, which was built by the Institute of Astronomy of KU Leuven, Belgium, thanks to funding from the European Research Council under the European Community's Seventh Framework Programme (FP7/2007-2013)/ERC grant agreement no 227224 (PROSPERITY, PI: Conny Aerts) and from the Research Foundation – Flanders (FWO) grant agreement G.0410.09. The CCDs of MAIA were developed by e2v in the framework of the ESA Eddington space mission project; they were offered by ESA on permanent loan to KU Leuven (Raskin et al. 2013). This article is based on observations obtained at the Observatório Astronômico do Sertão de Itaparica (OASI, Itacuruba) of the Observatório Nacional, Brazil. The Joan Oró Telescope (TJO) of the Montsec Astronomical Observatory (OAdM) is owned by the Catalan Government and operated by the Institute for Space Studies of Catalonia (IEEC). This article is based on observations made in the Observatorios de Canarias del IAC with the 0.82 m IAC80 telescope operated on the island of Tenerife by the Instituto de Astrofísica de Canarias (IAC) in the Observatorio del Teide. This article is based on observations made with the SARA telescopes (Southeastern Association for Research in Astronomy), whose nodes are located at the Observatorios de Canarias del IAC on the island of La Palma in the Observatorio del Roque de los Muchachos; Kitt Peak, AZ under the auspices of the National Optical Astronomy Observatory (NOAO); and Cerro Tololo Inter-American Observatory (CTIO) in La Serena, Chile. This project uses data from the SuperWASP archive. The WASP project is currently funded and operated by Warwick University and Keele University, and was originally set up by Queen's University Belfast, the Universities of Keele, St. Andrews, and Leicester, the Open University, the Isaac Newton Group, the Instituto de Astrofisica de Canarias, the South African Astronomical Observatory, and by STFC. TRAPPIST-South is a project funded by the Belgian Fonds (National) de la Recherche Scientifique (F.R.S.-FNRS) under grant PDR T.0120.21. TRAPPIST-North is a project funded by the University of Liège, in collaboration with the Cadi Ayyad University of Marrakech (Morocco). Funding for the *Kepler* and K2 missions are provided by the NASA Science Mission Directorate. The data presented in this paper were obtained from the Mikulski Archive for Space Telescopes (MAST). STScI is operated by the Association of Universities for Research in Astronomy, Inc., under NASA contract NAS5-26555. Support for MAST for non-HST data is provided by the NASA Office of Space Science via grant NNX09AF08G and by other grants and contracts. Data from Pic du Midi Observatory have been obtained with the 0.6-m telescope, a facility operated by Observatoíre Midi Pyrénées and Association T60, an amateur association. This research is partly based on observations obtained with the 60-cm Cassegrain telescope (TC60) and 90-cm Schmidt-Cassegrain telescope (TSC90) of the Institute of Astronomy of the Nicolaus Copernicus University in Toruń. We acknowledge the contributions of the occultation observers who have provided the observations in the dataset. Most of those observers are affiliated with one or more of: European Asteroidal Occultation Network (EAON), International Occultation Timing Association (IOTA), International Occultation Timing Association European Sect. (IOTA/ES), Japanese Occultation Information Network (JOIN), and Trans Tasman Occultation Alliance (TTOA).

[13] https://astro.troja.mff.cuni.cz/projects/damit/

References

Alí-Lagoa, V., Müller, T. G., Usui, F., & Hasegawa, S. 2018, A&A, 612, A85
Alkema, M. S. 2013, Minor Planet Bull., 40, 215
Binzel, R. P. 1987, Icarus, 72, 135
Binzel, R. P., & Sauter, L. M. 1992, Icarus, 95, 222
Brož, M., Morbidelli, A., Bottke, W. F., et al. 2013, A&A, 551, A117
Buie, M. W., & Keller, J. M. 2016, AJ, 151, 73
Carry, B. 2012, Planet. Space Sci., 73, 98
Delbo', M., Mueller, M., Emery, J. P., Rozitis, B., & Capria, M. T. 2015, Asteroid Thermophysical Modeling, 107
Denchev, P. 2000, Planet. Space Sci., 48, 987
di Martino, M., Dotto, E., Cellino, A., Barucci, M. A., & Fulchignoni, M. 1995, A&AS, 112, 1
Ďurech, J., Sidorin, V., & Kaasalainen, M. 2010, A&A, 513, A46
Ďurech, J., Kaasalainen, M., Herald, D., et al. 2011, Icarus, 214, 652
Ďurech, J., Hanuš, J., & Alí-Lagoa, V. 2018, A&A, 617, A57
Ďurech, J., Hanuš, J., & Vančo, R. 2019, A&A, 631, A2
Ďurech, J., Tonry, J., Erasmus, N., et al. 2020, A&A, 643, A59
Ďurech, J., Vokrouhlický, D., Pravec, P., et al. 2022, A&A, 657, A5
Gaia Collaboration (Brown, A. G. A., et al.) 2021, A&A, 649, A1
Gault, D., Nosworthy, P., Nolthenius, R., Bender, K., & Herald, D. 2022, Minor Planet Bull., 49, 3
Hainaut-Rouelle, M. C., Hainaut, O. R., & Detal, A. 1995, A&AS, 112, 125
Hanuš, J., Ďurech, J., Oszkiewicz, D. A., et al. 2016, A&A, 586, A108
Hanuš, J., Delbo', M., Alí-Lagoa, V., et al. 2018, Icarus, 299, 84
Hanuš, J., Pejcha, O., Shappee, B. J., et al. 2021, A&A, 654, A48
Harris, A. W. 1998, Icarus, 131, 291
Harris, A. W., & Drube, L. 2016, ApJ, 832, 127
Harris, A. W., & Drube, L. 2020, ApJ, 901, 140
Harris, A. W., & Harris, A. W. 1997, Icarus, 126, 450
Harris, A. W., & Lagerros, J. S. V. 2002, in Asteroids III (Tucson: University of Arizona Press), 205
Harris, A. W., & Young, J. W. 1989, Icarus, 81, 314
Harris, A. W., Young, J. W., Dockweiler, T., et al. 1992, Icarus, 95, 115
Herald, D., Frappa, E., Gault, D., et al. 2019, Asteroid Occultations V3.0, NASA Planetary Data System
Herald, D., Gault, D., Anderson, R., et al. 2020, MNRAS, 499, 4570
Higgins, D. 2011, Minor Planet Bull., 38, 41
Kaasalainen, M., & Torppa, J. 2001, Icarus, 153, 24
Kaasalainen, M., & Lamberg, L. 2006, Inverse Probl., 22, 749
Kaasalainen, M., Torppa, J., & Muinonen, K. 2001, Icarus, 153, 37
Kalup, C. E., Molnár, L., Kiss, C., et al. 2021, ApJS, 254, 7
Koff, R. A. 2006, Minor Planet Bull., 33, 31

Lagerkvist, C. I., Hahn, G., Magnusson, P., & Rickman, H. 1987, A&AS, 70, 21
Lagerkvist, C. I., Magnusson, P., Debehogne, H., et al. 1992, A&AS, 95, 461
Marciniak, A., Pilcher, F., Oszkiewicz, D., et al. 2015, Planet. Space Sci., 118, 256
Marciniak, A., Pilcher, F., Oszkiewicz, D., et al. 2016, in 37th Meeting of the Polish Astronomical Society, 3, eds. A. Różańska, & M. Bejger, 84
Marciniak, A., Bartczak, P., Müller, T., et al. 2018, A&A, 610, A7
Marciniak, A., Alí-Lagoa, V., Müller, T. G., et al. 2019, A&A, 625, A139
Marciniak, A., Ďurech, J., Alí-Lagoa, V., et al. 2021, A&A, 654, A87
Masiero, J. R., Mainzer, A. K., Grav, T., et al. 2011, ApJ, 741, 68
Masiero, J. R., Mainzer, A. K., Grav, T., et al. 2012, ApJ, 759, L8
Masiero, J. R., Nugent, C., Mainzer, A. K., et al. 2017, AJ, 154, 168
Masiero, J. R., Mainzer, A. K., Bauer, J. M., et al. 2020, Planet. Sci. J., 1, 5
Masiero, J. R., Mainzer, A. K., Bauer, J. M., et al. 2021, Planet. Sci. J., 2, 162
Mohamed, R. A., Krugly, Y. N., & Lupishko, D. F. 1995, AJ, 109, 1877
Molnár, L., Pál, A., Sárneczky, K., et al. 2018, ApJS, 234, 37
Morbidelli, A., Bottke, W. F., Nesvorný, D., & Levison, H. F. 2009, Icarus, 204, 558
Nugent, C. R., Mainzer, A., Bauer, J., et al. 2016, AJ, 152, 63
Ortiz, J. L., Santos-Sanz, P., Sicardy, B., et al. 2017, Nature, 550, 219
Pál, A., Szakáts, R., Kiss, C., et al. 2020, ApJS, 247, 26
Pilcher, F. 2014, Minor Planet Bull., 41, 250
Pilcher, F. 2015, Minor Planet Bull., 42, 38
Pilcher, F. 2016, Minor Planet Bull., 43, 135
Pilcher, F. 2019, Minor Planet Bull., 46, 360
Pilcher, F., Benishek, V., Bonamico, R., et al. 2021, Minor Planet Bull., 48, 4
Polakis, T. 2021a, Minor Planet Bull., 48, 394
Polakis, T. 2021b, Minor Planet Bull., 48, 23
Raskin, G., Bloemen, S., Morren, J., et al. 2013, A&A, 559, A26
Ryan, E. L., & Woodward, C. E. 2010, AJ, 140, 933
Schober, H. J., & Schroll, A. 1985, A&AS, 62, 187
Schroll, A., & Schober, H. J. 1983, A&AS, 53, 77
Stephens, R. D. 2012, Minor Planet Bull., 39, 226
Tanga, P., Delbo, M., & Gerakis, J. 2013, in AAS/Division for Planetary Sciences Meeting Abstracts, 45, 208.29
Tanga, P., Pauwels, T., Mignard, F., et al. 2022, A&A, 674, A12
Vernazza, P., Ferrais, M., Jorda, L., et al. 2021, A&A, 654, A56
Viikinkoski, M., Kaasalainen, M., & Durech, J. 2015, A&A, 576, A8
Vokrouhlický, D., Brož, M., Bottke, W. F., Nesvorný, D., & Morbidelli, A. 2006, Icarus, 182, 118
Warner, B. D. 2007, Minor Planet Bull., 34, 72
Warner, B. D., Harris, A. W., & Pravec, P. 2009, Icarus, 202, 134
Waszczak, A., Chang, C.-K., Ofek, E. O., et al. 2015, AJ, 150, 75
Wright, E. L., Eisenhardt, P. R. M., Mainzer, A. K., et al. 2010, AJ, 140, 1868

[1] Astronomical Observatory Institute, Faculty of Physics, Adam Mickiewicz University, Słoneczna 36, 60-286 Poznań, Poland
e-mail: am@amu.edu.pl
[2] Astronomical Institute, Faculty of Mathematics and Physics, Charles University, V Holešovičkách 2, 180 00 Prague 8, Czech Republic
[3] Mt. Suhora Observatory, Pedagogical University, Podchorążych 2, 30-084 Cracow, Poland
[4] Konkoly Observatory, Research Centre for Astronomy and Earth Sciences, Eötvös Loránd Research Network (ELKH), 1121 Budapest, Konkoly Thege Miklós út 15–17, Hungary
[5] CSFK, MTA Centre of Excellence, Budapest, Konkoly Thege Miklós út 15–17, 1121, Hungary
[6] MTA CSFK Lendület Near-Field Cosmology Research Group, Hungary
[7] ELTE Eötvös Loránd University, Institute of Physics, 1117, Pázmány Péter sétány 1/A, 1117 Budapest, Hungary
[8] Astronomy Department, Eötvös Loránd University, Pázmány P. s. 1/A, 1171 Budapest, Hungary
[9] Observatório Nacional, R. Gen. José Cristino 77, São Cristóvão, 20921-400, Rio de Janeiro, RJ, Brazil
[10] EURASTER, 8 rue du Tonnelier, 46100 Faycelles, France
[11] International Occultation Timing Association/European Section, Am Brombeerhag 13, 30459 Hannover, Germany
[12] International Occultation Timing Association (IOTA), PO Box 7152, WA 98042, USA
[13] Institute of Theoretical Physics and Astronomy, Vilnius University, Saulėtekio al. 3, 10257 Vilnius, Lithuania
[14] Japanese Occultation Information Network, Japan
[15] Geneva Observatory, 1290 Sauverny, Switzerland
[16] Les Engarouines Observatory, 84570 Mallemort-du-Comtat, France
[17] Association T60, Observatoire Midi-Pyrénées, 14 avenue Édouard Belin, 31400 Toulouse, France
[18] Collonges Observatory, 90 allée des Résidences, 74160 Collonges, France
[19] Institute of Astronomy, Faculty of Physics, Astronomy and Informatics, Nicolaus Copernicus University in Toruń, ul. Grudziądzka 5, 87-100 Toruń, Poland
[20] Departamento de Sistema Solar, Instituto de Astrofísica de Andalucía (CSIC), Glorieta de la Astronomía s/n, 18008 Granada, Spain
[21] Observatoire du Bois de Bardon, 16110 Taponnat, France
[22] Arecibo Observatory, University of Central Florida, HC-3 Box 53995, Arecibo, PR 00612, USA
[23] Instituto de Astrofísica de Canarias, C/ Vía Lactea, s/n, 38205 La Laguna, Tenerife, Spain
[24] Gran Telescopio Canarias (GRANTECAN), Cuesta de San José s/n, 38712, Breña Baja, La Palma, Spain
[25] Open University, School of Physical Sciences, The Open University, MK7 6AA, UK
[26] Trans-Tasman Occultation Alliance (TTOA), Wellington, PO Box 3181, New Zealand
[27] Hunters Hill Observatory, 7 Mawalan Street, Ngunnawal, ACT 2913, Australia
[28] Space sciences, Technologies and Astrophysics Research Institute, Université de Liège, Allée du Août 4000 Liège, Belgium
[29] British Astronomical Association, Burlington House, Piccadilly, Mayfair, London W1J 0DU, UK
[30] Institute of Physics, Jan Kochanowski University, ul. Uniwersytecka 7, 25-406 Kielce, Poland
[31] Chungbuk National University, 1, Chungdae-ro, Seowon-gu, Cheongju-si, Chungcheongbuk-do, Republic of Korea
[32] Korea Astronomy and Space Science Institute, 776 Daedeok-daero, Yuseong-gu, Daejeon 34055, Korea
[33] Laboratory of Space Researches, Uzhhorod National University, Daleka st. 2a, 88000, Uzhhorod, Ukraine
[34] Departamento de Astrofísica, Universidad de La Laguna – ULL, Tenerife, Spain
[35] NASA Johnson Space Center Astronomical Society, Houston, TX 77058, USA
[36] Blue Mountains Observatory, 94 Rawson Parade, Leura NSW 2780, Australia
[37] Organ Mesa Observatory, 4438 Organ Mesa Loop, Las Cruces, NM 88011, USA
[38] Command Module Observatory, 121 W. Alameda Dr., Tempe, AZ 85282, USA
[39] Silesian University of Technology, Department of Electronics, Electrical Engineering and Microelectronics, Akademicka 16, 44-100 Gliwice, Poland
[40] Lowell Observatory, 1400 West Mars Hill Road, Flagstaff, AZ 86001, USA
[41] Department of Astronomy, University of Virginia, Charlottesville, VA 22904, USA
[42] Department of Physics, Adiyaman University, 02040 Adiyaman, Turkey
[43] Observatory, Vsetínská 78, 757 01 Valašské Meziříčí, Czech Republic
[44] Kepler Institute of Astronomy, University of Zielona Góra, Lubuska 2, 65-265 Zielona Góra, Poland

Appendix A: Additional figures

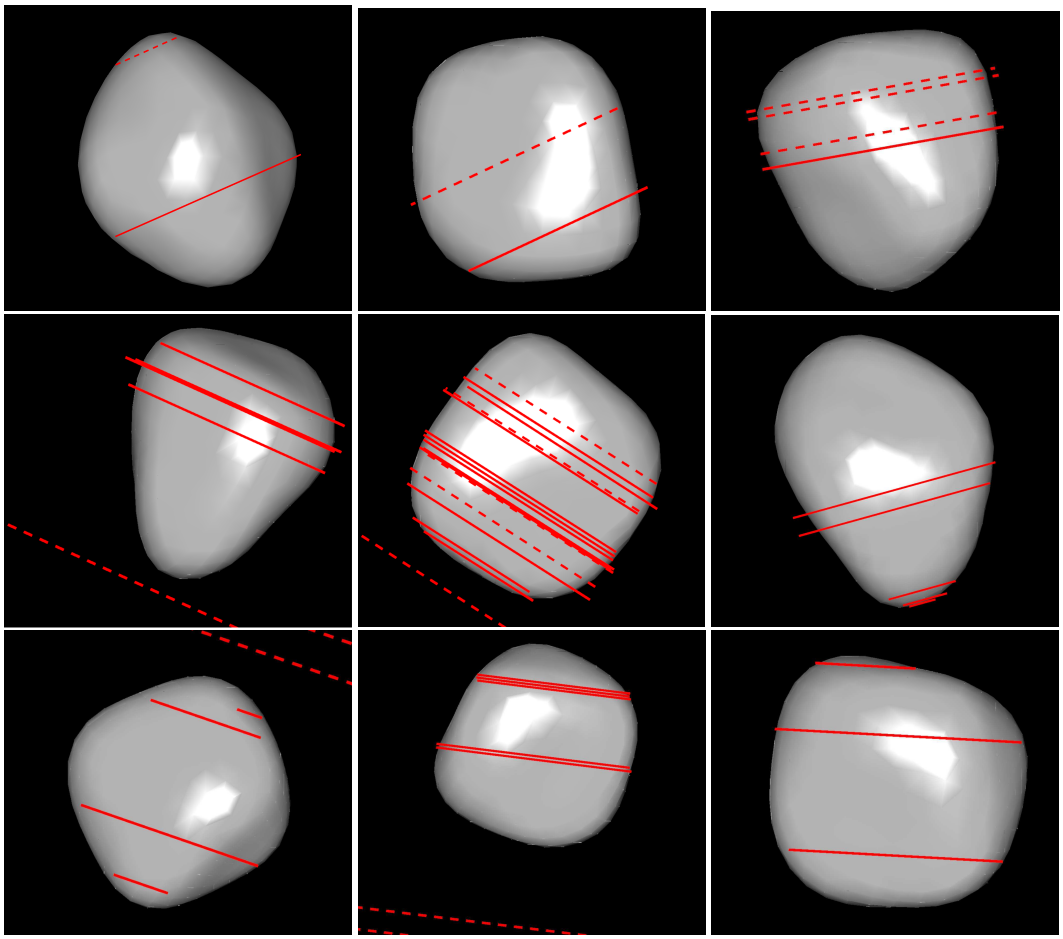

Fig. A.1: (275) Sapientia ADAM solution pole 2, shown with occultation chords used to construct the model. Occultation events are the same as in Fig. 4.

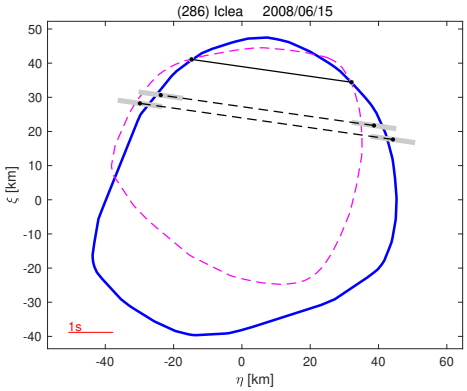

Fig. A.2: (286) Iclea model fit to occultation chords. Pole 2 (dashed contour) is rejected as inconsistent with all previous size determinations.

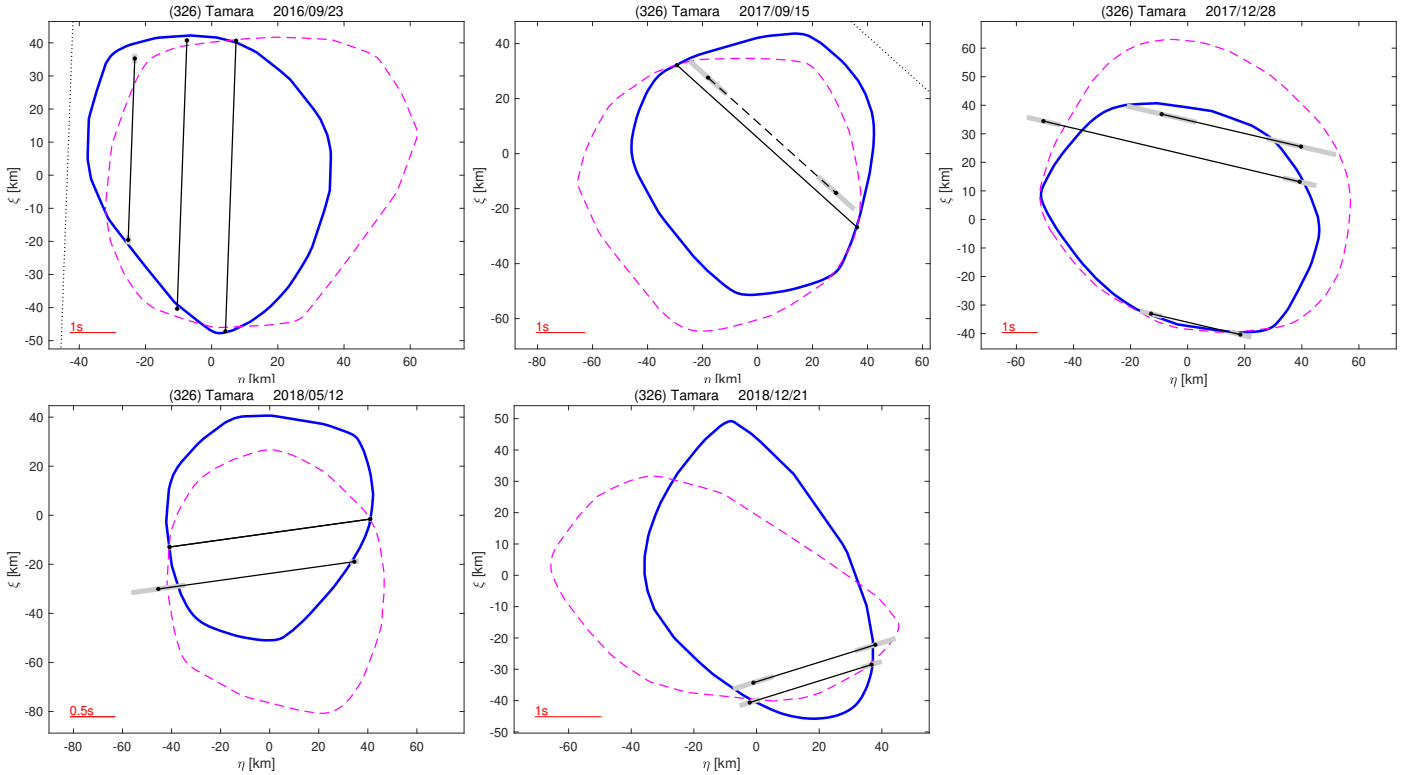

Fig. A.3: (326) Tamara model fit to occultation chords. Pole 1 is preferred (solid contour).

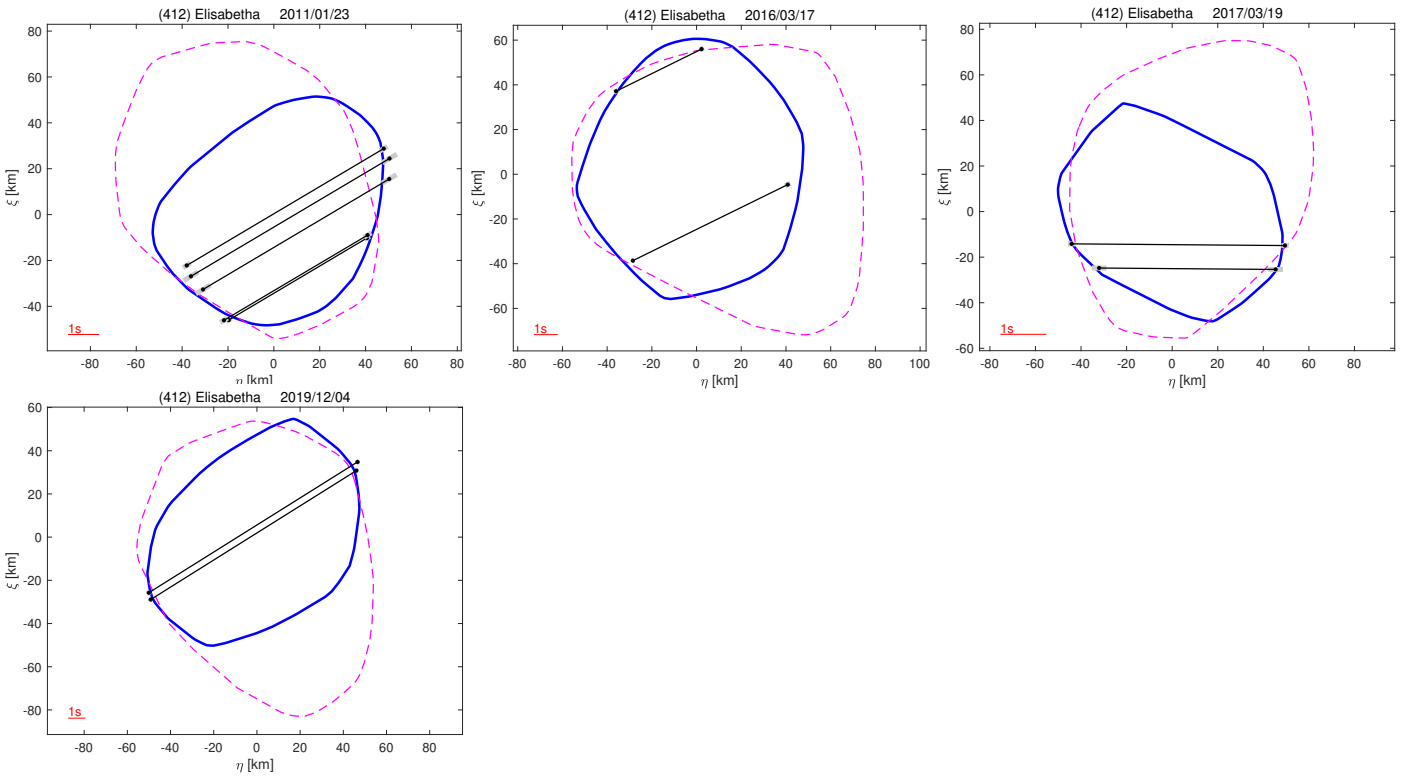

Fig. A.4: (412) Elisabetha model fit to occultation chords. Pole 2 is preferred (solid contour).

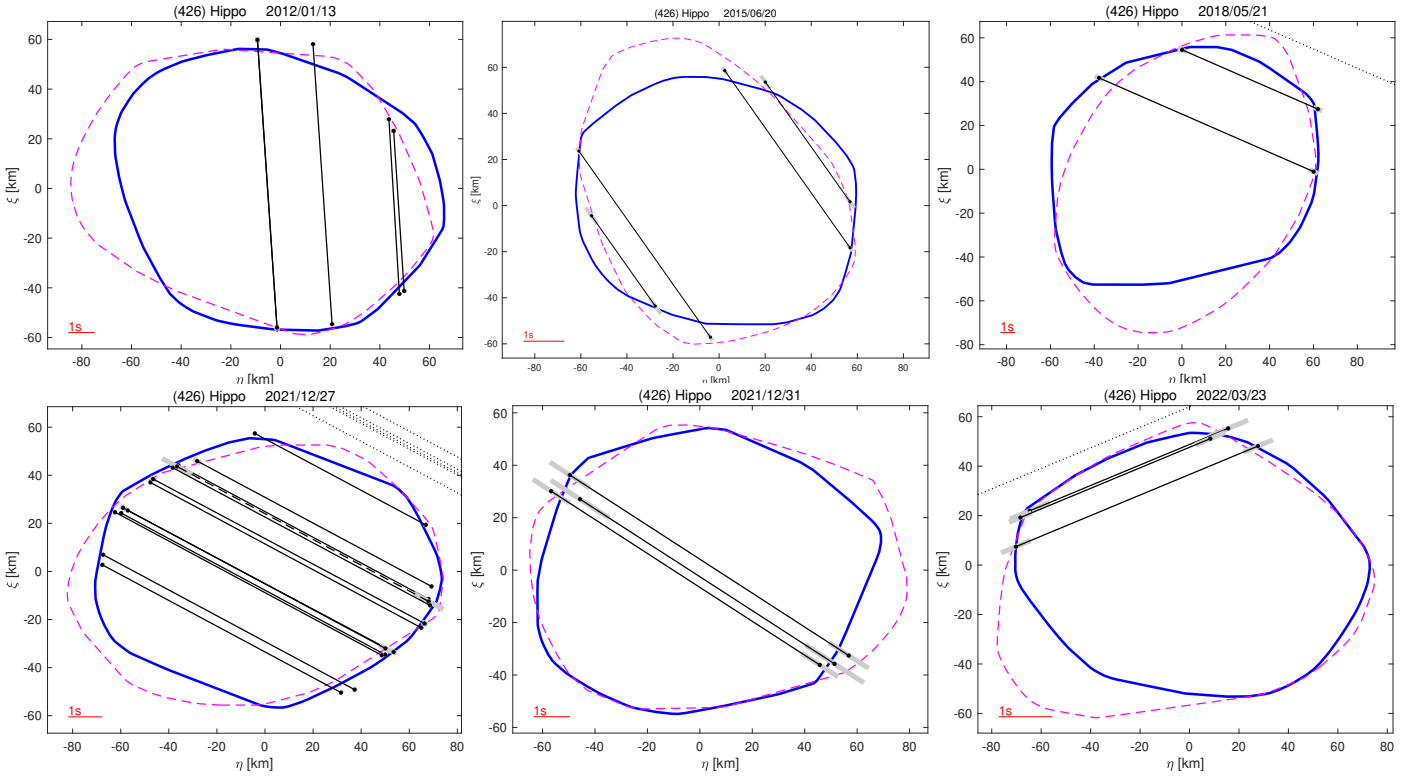

Fig. A.5: (426) Hippo model fit to occultation chords. Pole 2 is preferred (solid contour).

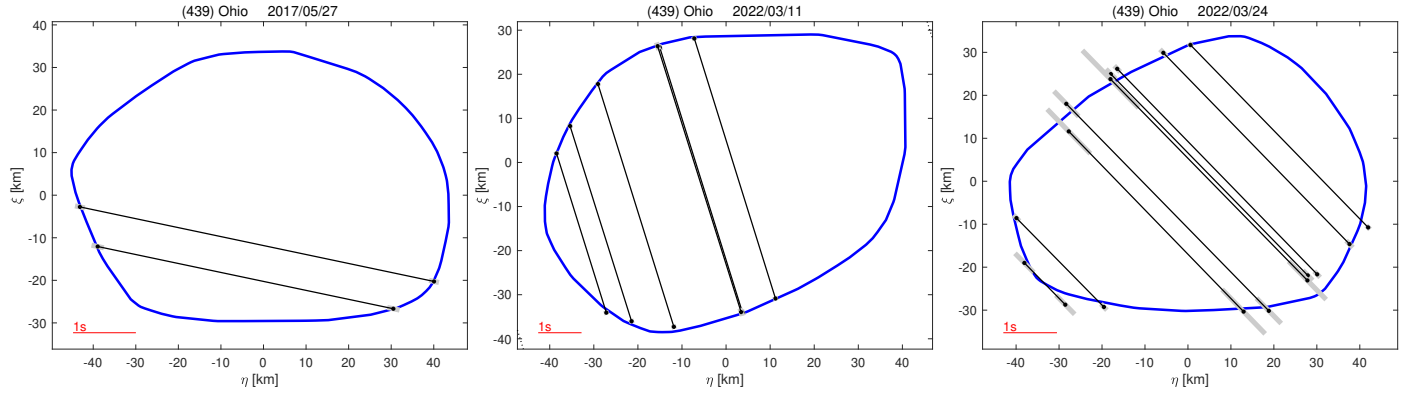

Fig. A.6: (439) Ohio model fit to occultation chords.

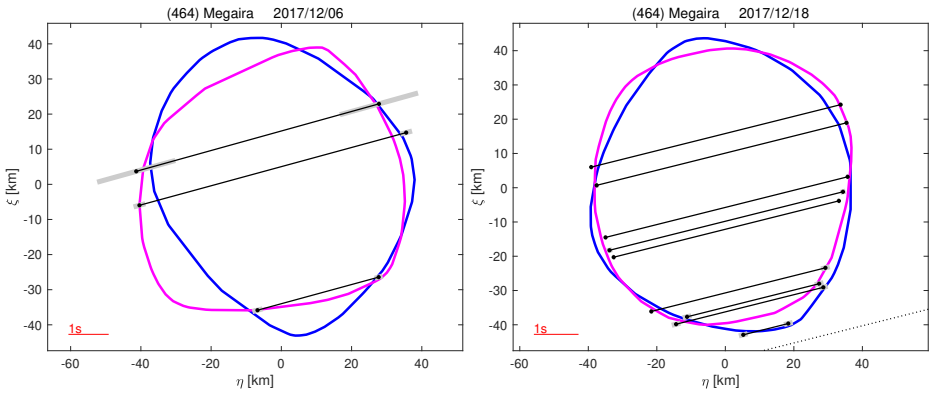

Fig. A.7: (464) Megaira model fit to occultation chords: pole 1 (blue), and pole 2 (magenta).

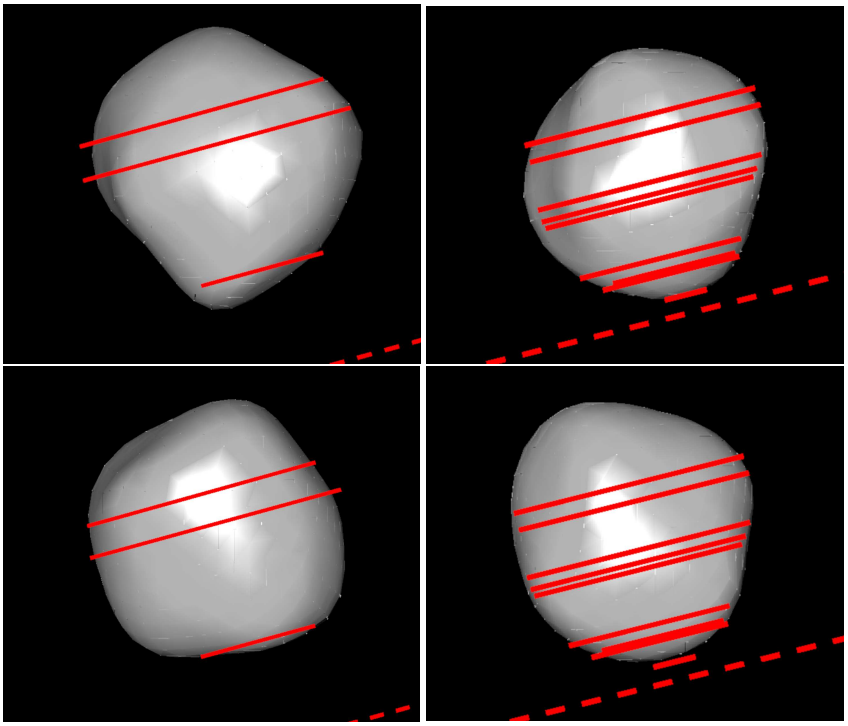

Fig. A.8: (464) Megaira ADAM solution pole 1 (top row), pole 2 (bottom row), shown with occultation chords used to construct the models. Occultation events same as in Fig. A.7.

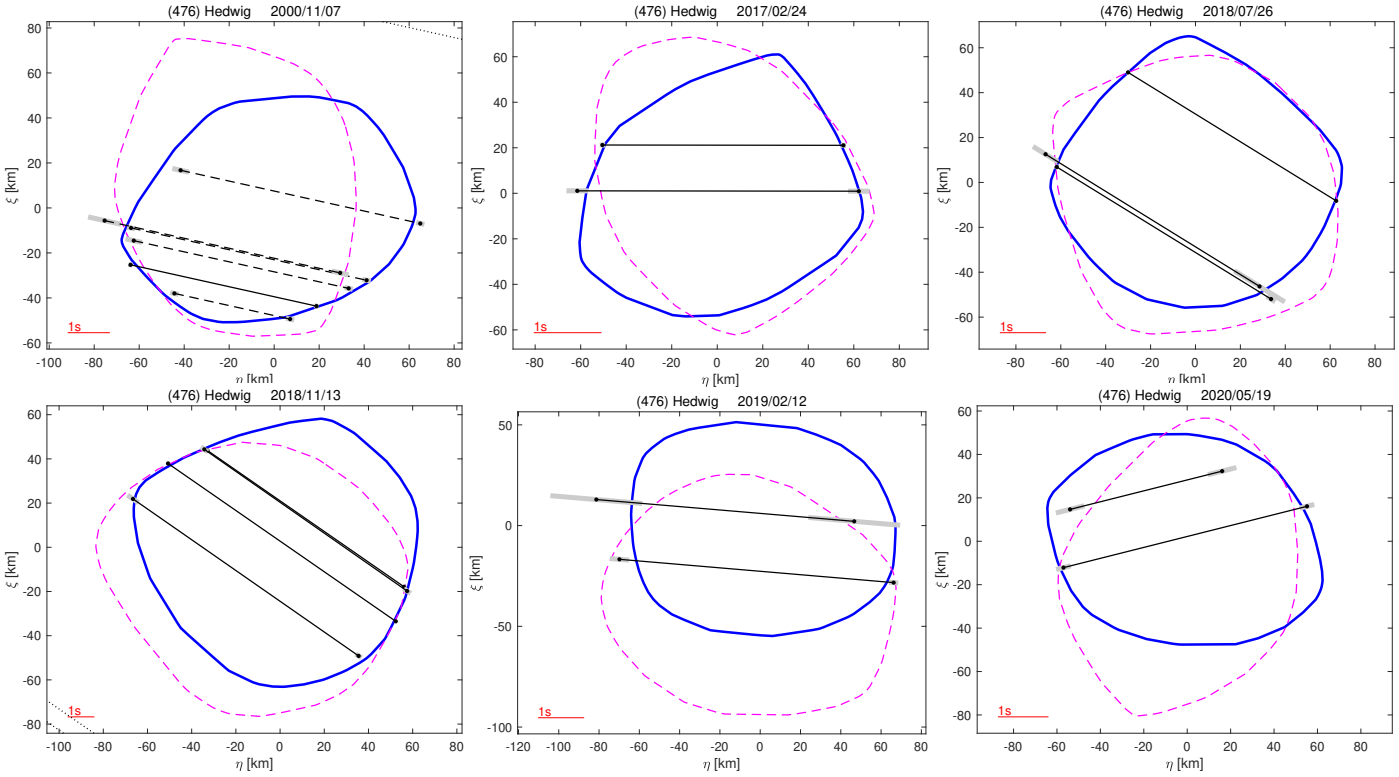

Fig. A.9: (476) Hedwig model fit to occultation chords. Pole 1 is preferred (solid contour).

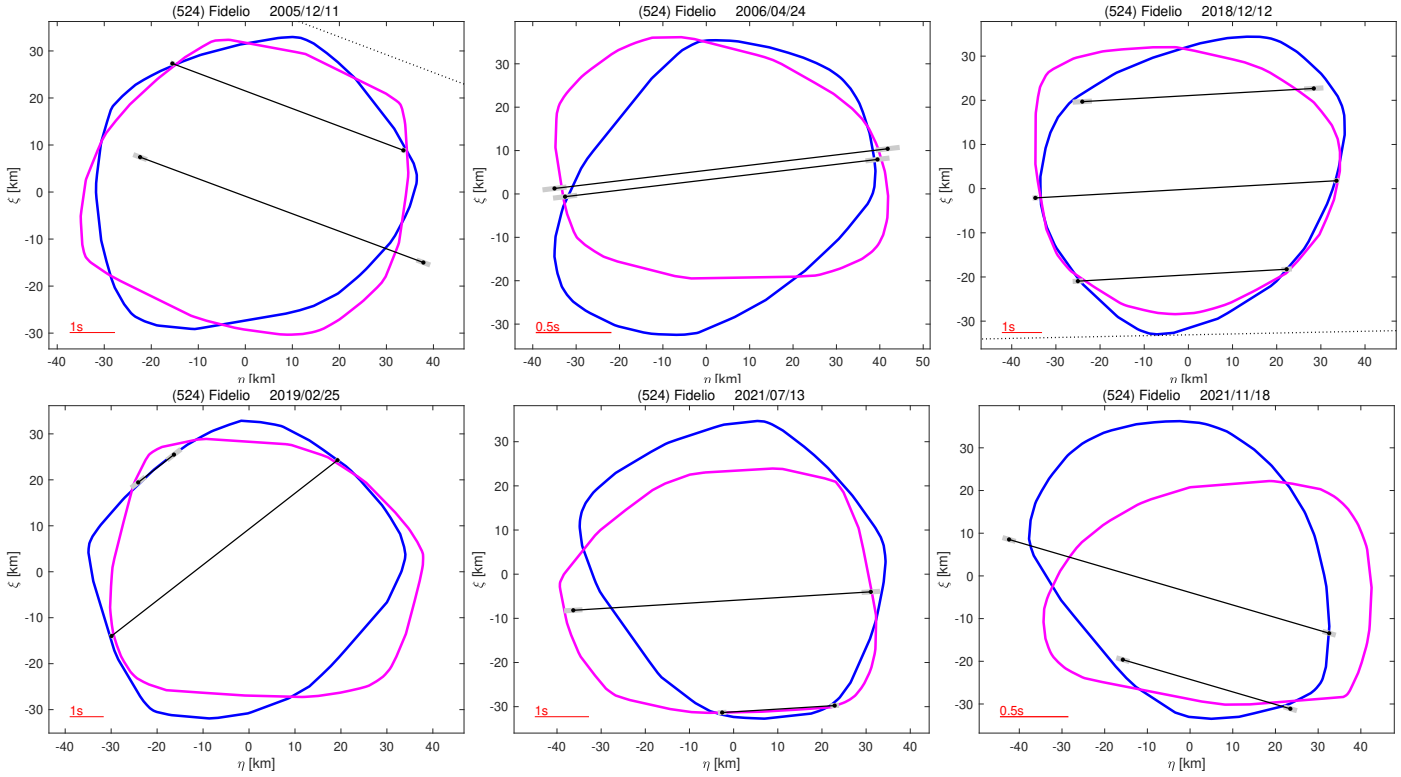

Fig. A.10: (524) Fidelio model fit to occultation chords. Pole 2 is preferred (blue contour).

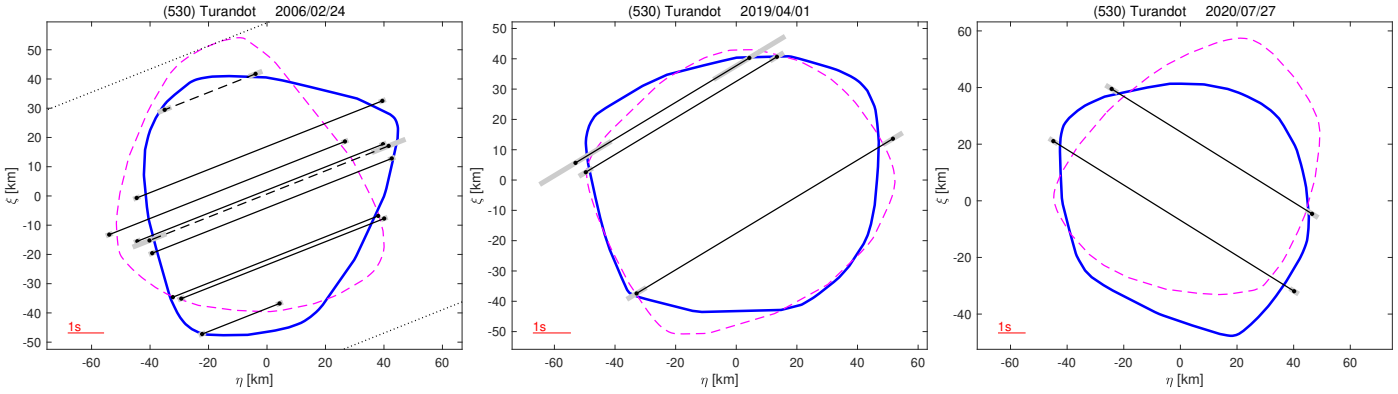

Fig. A.11: (530) Turandot model fit to occultation chords. Pole 2 is preferred (solid contour).

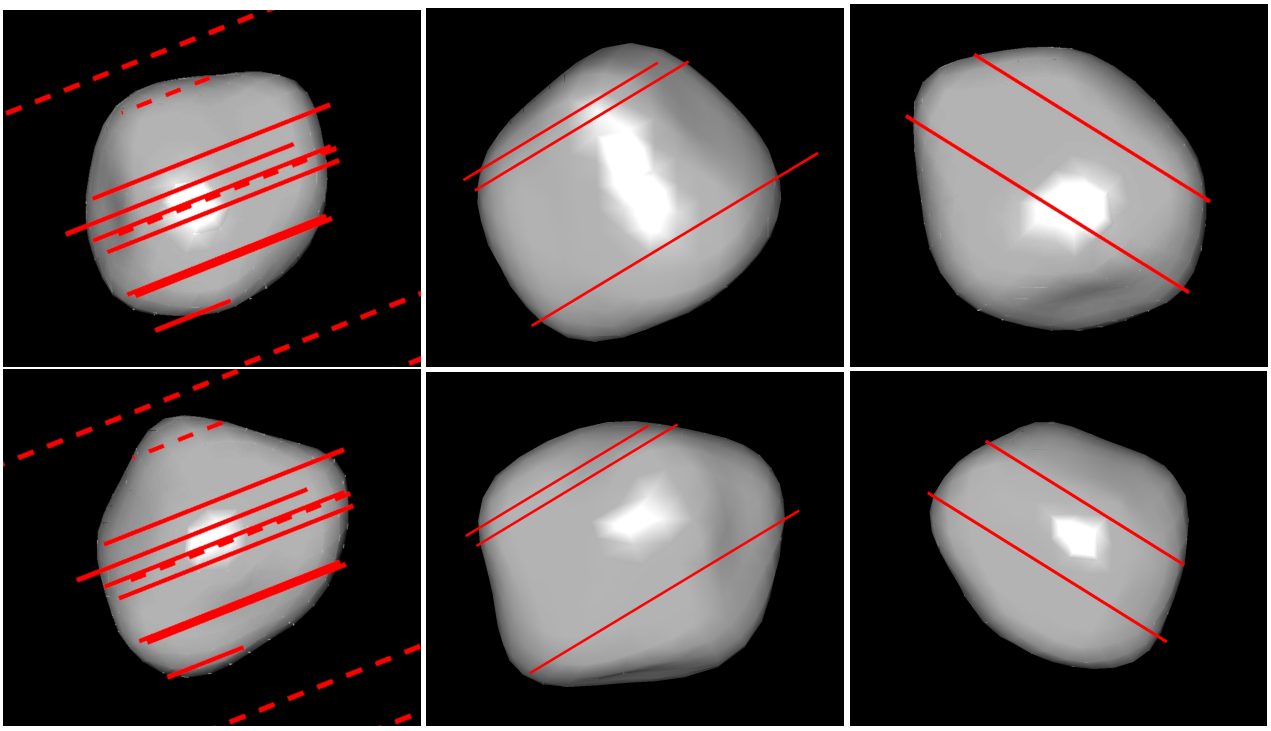

Fig. A.12: (530) Turandot ADAM solution pole 1 (top row), pole 2 (bottom row), shown with occultation chords used to construct the models. Occultation events same as in Fig. A.11.

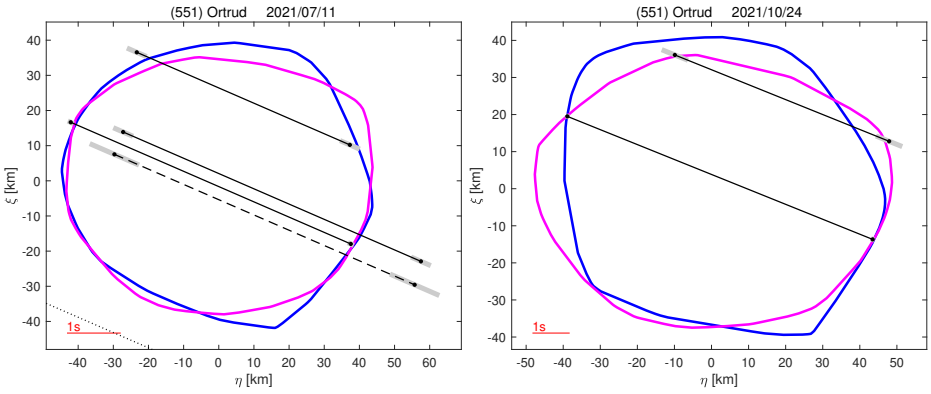

Fig. A.13: (551) Ortrud model fit to occultation chords: pole 1 (blue), and pole 2 (magenta).

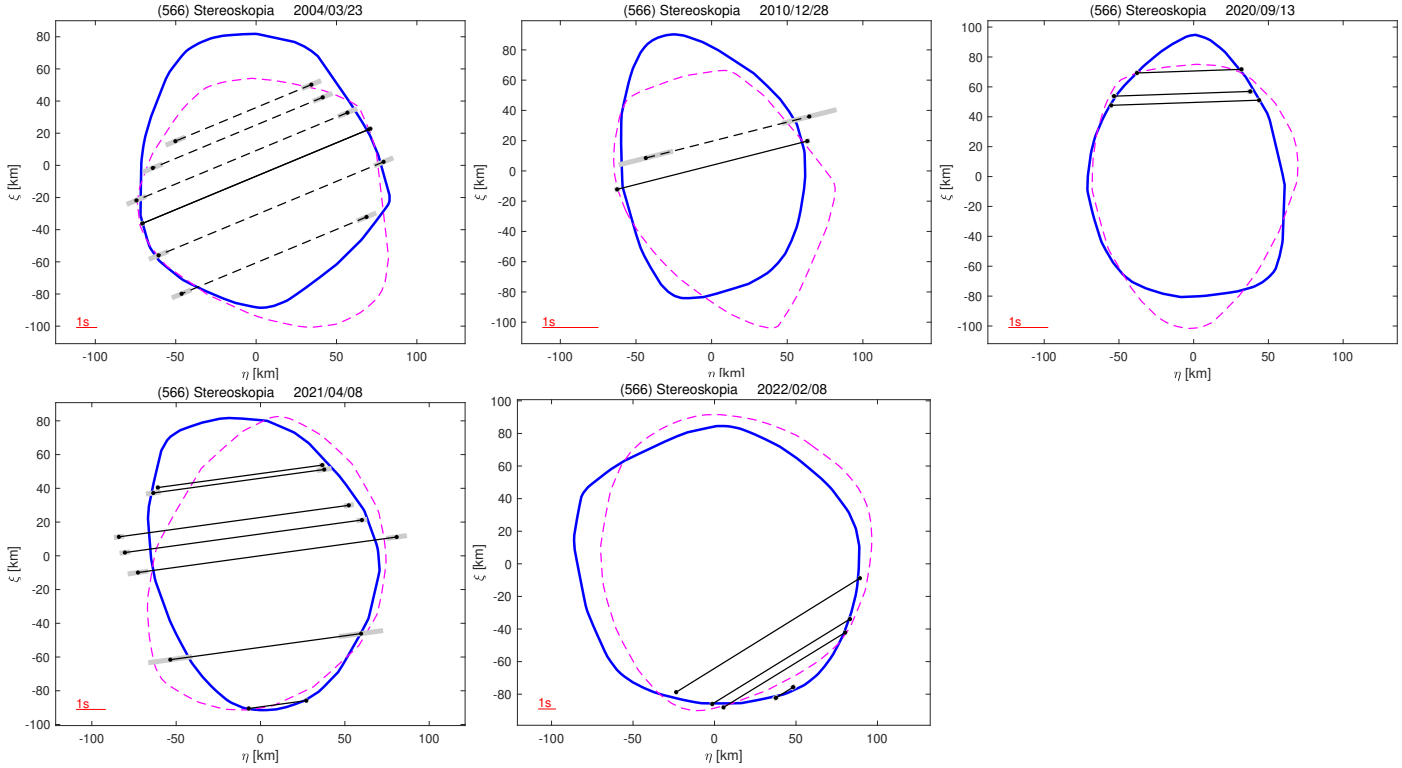

Fig. A.14: (566) Stereoskopia model fit to occultation chords. Pole 1 is preferred (solid contour).

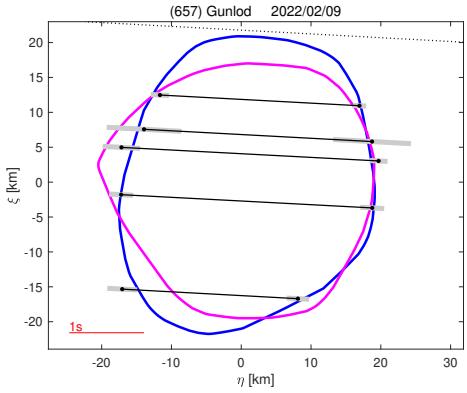

Fig. A.15: (657) Gunlod model fit to occultation chords. Pole 2 is preferred (blue contour).

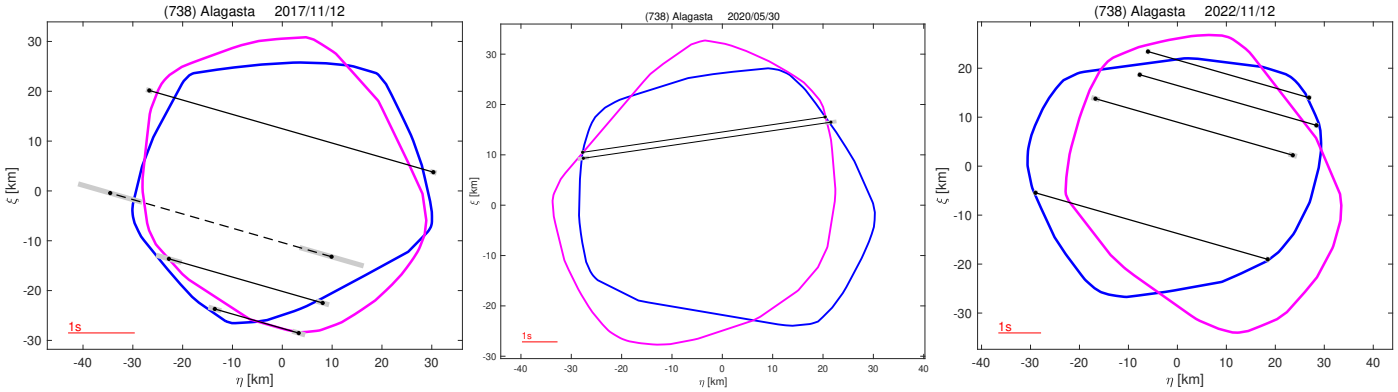

Fig. A.16: (738) Alagasta model fit to occultation chords: pole 2 (blue), and pole 1 (magenta).

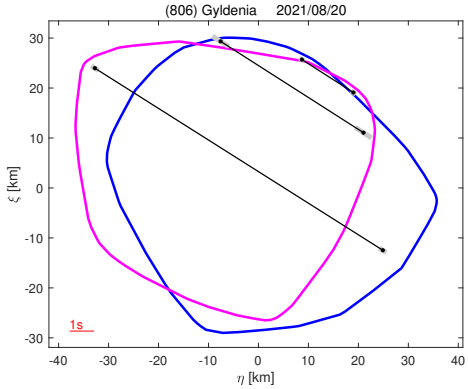

Fig. A.17: (806) Gyldenia model fit to occultation chords: pole 1 (blue), and pole 2 (magenta).

Appendix B: Observing campaign details

This section contains summarised details of all time-series observations used for the modelling (Table B.1), and the list of stellar occultation event observers and sites (Table B.2).

Table B.1: Details of all photometric observations for light curves: observing dates, number of light curves, range of ecliptic longitudes of the target, and sun-target-observer phase angles, observer name (or paper citation in case of published data), and the observing site. Some data come from robotic telescopes, in which case there is no observer specified. For data from the TESS spacecraft, N_{lc} denotes the number of days of continuous observations. CSSS stands for Center for Solar System Studies, CTIO - Cerro Tololo Interamerican Observatory, e-EyE - Entre Encinas y Estrellas, ESO - European Southern Observatory, OASI - Observatório Astronômico do Sertão de Itaparica, ORM - Roque de los Muchachos Observatory, OT - Observatorio del Teide, and SOAO - Sobaeksan Optical Astronomy Observatory.

Date	N_{lc}	λ [deg]	Phase angle [deg]	Observer	Site
70 Panopaea					
1980 08 20 - 1980 08 21	2	329 - 330	10	Harris & Young (1989)	Mountain Observatory, CA, USA
1980 09 05	1	326	12	Schroll & Schober (1983)	Table Mountain Observatory, CA, USA
2006 09 23 - 2006 12 24	22	48 - 63	3 - 20	-	Super WASP
2014 09 11 - 2014 12 30	15	353 - 3	8 - 24	Marciniak et al. (2015)	Montsec, Catalonia, Spain; Bisei Spaceguard Center, Japan
2015 10 27 - 2015 12 18	16	103 - 108	7 - 19	Marciniak et al. (2016)	Borowiec, Poland; Organ Mesa Observatory, NM, USA; Montsec, Catalonia, Spain
2016 01 04	1	99	4	F. Pilcher	Organ Mesa Observatory, NM, USA
2016 12 26 - 2017 01 30	10	181 - 184	16 - 19	T. Polakis, B. Skiff	Tempe, AZ, USA
2017 01 27 - 2017 03 28	2	174 - 184	7 - 17	V. Kudak, V. Perig	Derenivka, Ukraine
2017 03 26	1	175	6	A. Marciniak	Borowiec, Poland
2018 06 26 - 2018 10 16	20	313 - 324	14 - 25	B. Skiff	Lowell Observatory, AZ, USA
2018 07 26 - 2018 08 17	24	317 - 321	10 - 13	Pál et al. (2020)	TESS spacecraft
2019 09 05 - 2019 10 16	3	84 - 90	19 - 21	M. Dróżdż	Suhora, Poland
2019 09 17	1	87	21	E. Pakštienė	Molėtai Astronomical Observatory, Lithuania
2019 09 26 - 2019 10 25	3	88 - 90	17 - 21	W. Ogłoza	Adiyaman, Turkey
2019 12 16	1	82	3	R. Szakáts	Piszkéstető, Hungary
275 Sapientia					
1998 01 01 - 1998 01 03	2	82	7 - 8	Denchev (2000)	Rozhen National Observatory, Bulgaria
2007 01 01 - 2007 01 10	5	56	14 - 17	Warner (2007)	CSSS - Palmer Divide Station, CO USA
2013 04 23	1	249	14	F. Pilcher	Organ Mesa Observatory, NM, USA
2014 07 25 - 2014 09 10	8	329 - 338	2 - 11	Pilcher (2015)	Organ Mesa Observatory, NM, USA
2015 09 28 - 2015 11 20	5	40 - 49	3 - 13	Pilcher (2016)	Organ Mesa Observatory, NM, USA
2016 12 4 - 2017 01 09	4	154 - 159	18 - 24	R. Hirsch, A. Marciniak, Butkiewicz - Bąk	Borowiec, Poland
2017 01 18	1	159	16	A. Marciniak	CTIO, Chile
2017 01 25 - 2017 01 30	6	158	11 - 13	T. Polakis, B. Skiff	Tempe, AZ, USA
2017 01 29	1	158	11	V. Kudak, V. Perig	Derenivka, Ukraine
2018 05 15	1	289	9	M.-J. Kim, D.-H. Kim	SOAO, South Korea
2018 05 17 - 2018 05 18	2	292	17	K. Kamiński	Winer, AZ, USA
2018 05 26	1	287	4	S. Geier	Kitt Peak Observatory, AZ, USA
2018 06 08	1	290	11	S. Geier	ORM, La Palma, Spain
286 Iclea					
2002 05 30	1	230	9	J. G. Bosch	Collonges Observatory, France
2003 08 02	1	311	3	L. Bernasconi	Observatoire des Engarouines, France
2007 04 13 - 2007 04 24	6	176 - 177	9 - 12	R. Hirsch, M. K. Kamińska, K. Kamiński, A. Marciniak, M. Polińska	Borowiec, Poland
2007 04 17	1	177	10	P. Kankiewicz	Kielce, Poland
2013 04 08 - 2013 05 19	6	201	6 - 13	M. Bronikowska, K. Sobkowiak, M. Murawiecka, R. Hirsch	Borowiec, Poland
2014 05 20 - 2014 08 12	7	272 - 285	13 - 14	A. Marciniak, P. Trela, I. Konstanciak, R. Hirsch	Borowiec, Poland
2014 05 24	1	285	13	K. Kamiński	Winer, AZ, USA
2014 08 10 - 2014 08 17	4	272 - 273	14 - 15	-	Montsec, Catalonia, Spain
2015 09 06 - 2015 10 03	8	353 - 359	4 - 7	-	Montsec, Catalonia, Spain
2016 11 13 - 2017 02 27	5	72 - 82	8 - 18	J. Horbowicz, M. Butkiewicz - Bąk, A. Marciniak, R Hirsch	Borowiec, Poland
2017 01 07	1	74	11	S. Geier	Kitt-Peak, AZ, USA
2017 01 22	1	73	14	R. Hirsch	CTIO, Chile
2017 12 30 - 2018 04 19	3	145 - 159	13 - 16	A. Marciniak, K. Żukowski, J. Horbowicz	Borowiec, Poland
2018 02 15	1	151	2	V. Kudak, V. Perig	Derenivka. Ukraine
2019 04 18 - 2019 04 25	2	225 - 226	8 - 9	M. K. Kamińska, M. Pawłowski	Borowiec, Poland
2019 05 07	1	222	8	D.-H. Kim, M.-J. Kim	SOAO, South Korea
2019 05 24	1	219	10	K. Kamiński	Winer, AZ, USA
2019 06 01 - 2019 06 02	2	218	11	S. Fauvaud	Le Bois de Bardon Observatory, France
326 Tamara					
1981 09 20 - 1981 09 27	3	7 - 9	9 - 10	Harris et al. (1992)	Table Mountain Observatory, CA, USA
1991 04 27	1	233	10	Hainaut-Rouelle et al. (1995)	ESO, La Silla, Chile
2006 11 17 - 2006 12 22	10	32 - 37	7 - 19	-	Super WASP
2009 05 07 - 2009 05 29	5	317 - 326	32	Higgins (2011)	Hunters Hill Observatory, Australia
2012 04 19 - 2012 06 09	24	189 - 194	9 - 28	F. Kugel, J. Caron	Observatoire de Dauban, France
2015 04 05 - 2015 04 09	2	121 - 122	23	V. Kudak, V. Perig	Derenivka, Ukraine
2015 04 13 - 2015 05 16	3	122 - 131	23 - 24	W. Ogłoza	Suhora, Poland
2015 04 29 - 2015 05 2	3	126	24	P. Kulczak	Borowiec, Poland
2016 05 25 - 2016 10 30	6	287 - 315	22 - 31	S. Geier, A. Marciniak	CTIO, Chile
2017 09 25 - 2017 12 18	8	76 - 87	10 - 22	-	Montsec, Catalonia, Spain
2019 02 17 - 2019 05 02	2	197 - 198	17 - 20	V. Kudak, V. Perig	Derenivka, Ukraine
2019 02 19	1	198	20	M. K. Kamińska	Borowiec, Poland
2019 02 19	1	198	20	S. Fauvaud, J. J. Rives, G. Biguet	Pic du Midi Observatory, France

Date	N_{lc}	λ [deg]	Phase angle [deg]	Observer	Site
412 Elisabetha					
1990 08 22 - 1990 08 29	6	328-329	5-6	Lagerkvist et al. (1992)	ESO, La Silla, Chile
2012 05 10 - 2012 05 18	7	231-233	7	Stephens (2012)	Rancho Cucamonga, CA USA
2016 02 25 - 2016 03 10	2	163-166	7	K. Kamiński	Winer, AZ, USA
2016 03 4 - 2016 04 3	4	158-164	7-14	V. Kudak, V. Perig	Derenivka, Ukraine
2017 06 19 - 2017 07 17	7	271-277	2-8	F. Pilcher	Organ Mesa Observatory, NM, USA
2018 09 4 - 2018 10 5	11	10-17	7-13	-	Montsec, Catalonia, Spain
2018 10 4 - 2018 10 17	15	8-11	7-9	Pál et al. (2020)	TESS spacecraft
2019 11 21 - 2020 04 17	3	105 - 111	13 - 21	W. Ogłoza	Adiyaman, Turkey
2020 02 8	1	97	14	A. Marciniak	Borowiec, Poland
2020 03 27	1	100	21	R. Szakáts	Piszkéstető, Hungary
2021 02 18 - 2021 02 20	3	217	20	D.-H. Kim, M.-J. Kim	Mt. Lemmon, USA
2021 02 18	1	217	20	D.-H. Kim, M.-J. Kim	SOAO, South Korea
2021 02 21 - 2021 04 23	5	210 - 217	8 - 20	W. Ogłoza	Adiyaman, Turkey
2021 02 23	1	217	20	W. Ogłoza	Suhora, Poland
2021 02 25	1	218	19	V. Kudak, V. Perig	Derenivka, Ukraine
2021 02 26 - 2021 04 24	5	210-218	8-19	A. Jones	Maidenhead, UK
2021 03 10	1	218	17	S. Fauvaud, A. Bruno	Pic du Midi, France
2021 04 19 - 2021 04 21	3	211-212	8	Polakis (2021a)	Tempe, AZ USA
426 Hippo					
1993 02 15	1	126	8	Mohamed et al. (1995)	Astronomical Observatory, Kharkiv, Ukraine
2008 03 01 - 2008 04 11	7	155 - 163	6 - 17	J. Oey, D. Higgins	Leura, Australia
2015 08 05 - 2015 10 27	7	349 - 3	7 - 14	P. Kulczak, A. Marciniak, R. Hirsch, M. Butkiewicz - Bąk	Borowiec, Poland
2015 09 08 - 2015 09 24	10	354 - 358	6 - 7	-	Montsec, Catalonia, Spain
2016 09 27 - 2016 11 29	4	80 - 83	9 - 19	R. Hirsch, J. Horbowicz	Borowiec, Poland
2016 10 26 - 2016 12 28	11	73 - 85	8 - 16	-	Montsec, Catalonia, Spain
2016 12 26 - 2017 01 18	9	71 - 74	10 - 15	T. Polakis, B. Skiff	Tempe, AZ, USA
2017 01 07	1	72	13	W. Ogłoza	Suhora, Poland
2019 06 27 - 2019 07 17	15	289 - 293	4 - 7	Pál et al. (2020)	TESS spacecraft
2020 07 23 - 2020 07 24	2	9	17	S. Fauvaud, F. Livet, J. J. Rives	Pic de Château-Renard, France
2020 08 10	1	9	15	M. Żejmo	Suhora, Poland
2020 08 20 - 2020 08 21	2	8 - 9	12 - 13	V. Kudak, V. Perig	Derenivka, Ukraine
2020 08 28 - 2020 09 16	9	4 - 8	7 - 11	Pilcher et al. (2021)	Organ Mesa Observatory, NM, USA
2020 09 20 - 2020 09 30	9	1 - 3	7	Polakis (2021b)	Tempe, AZ, USA
2020 11 29	1	355	17	W. Ogłoza	Adiyaman, Turkey
2021 09 07	1	86	20	A. Pál	Piszkéstető, Hungary
2021 09 12 - 2021 10 31	7	87 - 93	17 - 20	E. Pakštienė, R. Urbonavičiūtė	Molėtai Astronomical Observatory, Lithuania
2021 10 01 - 2021 12 04	9	89 - 93	9 - 20	A. Popowicz	Otívar, Spain
2021 10 30 - 2021 11 12	2	93	14 - 17	V. Kudak, V. Perig	Derenivka, Ukraine
2021 12 03 - 2021 12 05	3	89	9	M. Żejmo	e-Eye, Spain
439 Ohio					
1984 03 02 - 1984 03 05	4	192 - 193	9 - 10	Lagerkvist et al. (1987)	ESO, Chile
2014 08 21 - 2014 11 20	12	344 - 356	5 - 18	Marciniak et al. (2015)	Borowiec, Poland; Montsec, Spain; Winer, AZ, USA
2015 11 30 - 2015 12 09	6	74 - 76	8	F. Pilcher	Organ Mesa Observatory, NM, USA
2016 01 26 - 2016 01 27	2	67	17	K. Kamiński	Winer, AZ, USA
2017 03 09	1	166	5	A. Marciniak	CTIO, Chile
2017 03 14 - 2017 03 20	3	164 - 165	6 - 7		Montsec, Catalonia, Spain
2017 04 04	1	161	11	R. Hirsch	Borowiec, Poland
2018 04 22 - 2018 05 24	10	236 - 242	5 - 16	K. Żukowski, R. Hirsch, J. Skrzypek, J. Horbowicz	Borowiec, Poland
2018 05 31 - 2018 06 20	3	231 - 234	7 - 12	R. Szakáts, R. Könyves - Tóth	Piszkéstető, Hungary
2019 07 30 - 2019 10 15	7	303 - 310	7 - 18	R. Szakáts, B. Ignácz,	Piszkéstető, Hungary
2019 08 08 - 2019 09 06	2	303 - 308	8 - 13	-	OAdM, Montsec, Catalonia, Spain
2019 09 14	1	302	14	J. Skrzypek	Borowiec, Poland
2020 08 15 - 2020 09 12	4	32	13 - 18	R. Szakáts	Piszkéstető, Hungary
2020 09 18 - 2020 09 19	2	31	11	W. Ogłoza	Suhora, Poland
2020 09 21	1	31	10	A. Marciniak	Borowiec, Poland
2020 09 24 - 2020 10 23	3	25 - 31	2 - 9	W. Ogłoza	Adiyaman, Turkey
2020 10 10	1	28	4	A. Jones	Maidenhead, UK
2021 12 01	1	125	17	M. Żejmo	e-Eye, Spain
2022 01 10	1	119	9	M. Komraus, L. Rogiński, K. Szyszka, S. Żywica	Piwnice, Poland
2022 03 27	1	112	19	K. Kamiński	Winer, AZ, USA

Date	N_{lc}	λ [deg]	Phase angle [deg]	Observer	Site
464 Megaira					
1979 10 28	1	29	8	Harris & Young (1989)	Table Mountain Observatory, USA
2007 09 11 - 2007 09 23	8	1 - 3	8 - 10	J. Oey	Australia
2010 04 02 - 2010 07 01	24	182 - 189	4 - 18	Waszczak et al. (2015)	Mt. Palomar, CA, USA
2014 02 18	1	145	3	J. Horbowicz	Borowiec, Poland
2015 04 22 - 2015 05 24	3	203 - 208	4 - 11	P. Kulczak, A. Marciniak	Borowiec, Poland
2015 05 20	1	204	10	M. Żejmo	Adiyaman, Turkey
2015 06 02 - 2015 06 16	5	201-202	14 - 17	K. Kamiński	Winer, AZ, USA
2015 06 17	1	201	17	-	Montsec, Catalonia, Spain
2016 04 27	1	299	22	S. Geier	ORM, La Palma, Spain
2016 05 24 - 2016 07 27	2	296 - 303	4 - 20	A. Marciniak	OT, Tenefie, Spain
2016 06 14	1	304	15	K. Kamiński	Winer, AZ, USA
2016 07 01 - 2016 07 16	5	299 - 302	3 - 9	-	Montsec, Catalonia, Spain
2016 08 26	1	291	16	A. Marciniak	CTIO, Chile
2017 09 17 - 2017 09 23	7	91 - 93	24	T. Polakis, B. Skiff	Tempe, AZ, USA
2017 10 18	1	97	22	J. Skrzypek	Borowiec, Poland
2017 10 28 - 2017 11 15	6	97 - 98	15 - 20	-	Montsec, Catalonia, Spain
2018 12 09 - 2019 01 11	2	171 - 173	15 - 17	R. Szakáts	Piszkéstető, Hungary
2019 01 05	1	173	16	R. Duffard, N. Morales	La Sagra, Spain
2019 02 17 - 2019 04 18	2	159 - 170	7 - 13	J. Skrzypek, M. Pawłowski	Borowiec, Poland
2019 02 28 - 2019 03 25	7	162 - 167	4 - 7	Pilcher (2019)	Organ Mesa Observatory, NM, USA
2019 03 12	1	165	4	E. Pakštienė	Molėtai Astronomical Observatory, Lithuania
2020 03 22	1	238	15	M.-J. Kim, D.-H. Kim	SOAO, South Korea
2020 04 02 - 2020 04 29	2	233 - 237	6 - 13	R. Szakáts	Piszkéstető, Hungary
2020 04 17 - 2020 05 14	2	230 - 235	4 - 9	W. Ogłoza	Adiyaman, Turkey
476 Hedwig					
1982 03 27 - 1982 04 01	6	223	13 - 14	Schober & Schroll (1985)	-
2013 08 07 - 2013 12 27	12	321 - 336	5 - 22	K. Sobkowiak, A. Marciniak, R. Hirsch, D. Oszkiewicz	Borowiec, Poland
2014 09 17	1	77	21	P. Kankiewicz	Kielce, Poland
2014 10 05 - 2015 02 19	7	65 - 79	4 - 20	R. Hirsch, J. Horbowicz, M. Polińska, A. Marciniak	Borowiec, Poland
2014 10 18 - 2014 10 19	2	79	17	K. Kamiński	Winer, AZ, USA
2016 01 13 - 2016 03 27	7	157 - 169	10 - 17	-	Montsec, Catalonia, Spain
2016 01 20 - 2016 01 25	4	169	14 - 16	K. Kamiński	Winer, AZ, USA
2017 05 25 - 2017 06 03	2	285 - 286	13 - 16	K. Kamiński	Winer, AZ, USA
2017 06 19 - 2017 07 12	4	278 - 283	1 - 6	E. Jehin	TRAPPIST-S
2017 07 24	1	275	11	-	Montsec, Catalonia, Spain
2017 08 06	1	274	16	S. Geier	OT, Tenerife, Spain
2017 10 02	1	280	24	S. Geier	Kitt Peak, AZ, USA
2018 09 11	2	48	18 - 19	S. Fauvaud	Le Bois de Bardon Observatory, France
2018 09 09 - 2018 10 31	6	42 - 48	6 - 20	J. Skrzypek, R. Hirsch, A. Marciniak, M. K. Kamińska	Borowiec Observatory, Poland
2018 10 04 - 2018 10 04	2	47	13 - 14	S. Fauvaud, J. Michelet, F. Richard	Pic du Midi Observatory, France
524 Fidelio					
2005 10 25 - 2005 11 02	5	78 - 79	16 - 19	Koff (2006)	Antelope Hills Observatory, CO, USA
2013 09 30 - 2013 10 30	5	348 - 351	10 - 20	D. Oszkiewicz, R. Hirsch, A. Marciniak	Borowiec, Poland
2014 11 24 - 2015 04 21	4	126 - 137	7 - 23	A. Marciniak, K. Sobkowiak, J. Horbowicz	Borowiec, Poland
2015 02 17	1	127	8	V. Kudak, V. Perig	Derenivka, Ukraine
2015 02 18 - 2015 02 20	2	127	9	S. Fauvaud, C. Durandet, F. Livet, J. J. Rives	Pic du Midi Observatory, France
2016 04 26 - 2016 04 30	2	224	4 - 5	S. Geier	ORM, La Palma, Spain
2016 05 10 - 2016 05 23	2	218 - 221	5 - 9	S. Geier, A. Marciniak	OT, Tenerife, Spain
2017 08 03	1	314	2	S. Geier	OT, Tenerife, Spain
2017 10 06	1	307	21	S. Geier	ORM, La Palma, Spain
2017 10 31	1	311	23	A. Marciniak	CTIO, Chile
2018 09 28	1	96	26	M. Dróżdż	Suhora, Poland
2018 10 06	1	98	25	S. Fauvaud, J. Michelet, F. Richard	Pic du Midi Observatory, France
2018 10 17 - 2019 02 17	4	90 - 103	20 - 25	M. K. Kamińska, R. Hirsch, M. Pawłowski, J. Krajewski	Borowiec, Poland
2019 04 15	1	102	23	R. Szakáts	Piszkéstető, Hungary
530 Turandot					
1986 07 12 - 1986 07 27	3	318 - 320	5 - 12	di Martino et al. (1995)	ESO, La Silla, Chile
2002 04 19 - 2002 05 13	3	209 - 214	4 - 7	C. Demeautis	Village-Neuf Observatory, France
2005 01 04 - 2005 02 03	6	62	12 - 17	P. Antonini	Observatoire des Hauts Patys, France
2014 05 31 - 2014 06 30	16	265 - 271	3 - 8	Pilcher (2014)	Organ Mesa Observatory, NM, USA
2014 06 10 - 2014 06 22	4	267 - 269	3 - 5	-	Montsec, Catalonia, Spain
2015 09 20 - 2016 01 03	8	29 - 41	5 - 15	M. Butkiewicz - Bąk, P. Kulczak, A. Marciniak, R. Hirsch, K. Żukowski	Borowiec, Poland
2016 01 22 - 2016 02 03	4	33 - 36	19	K. Kamiński	Winer, AZ, USA
2016 12 07 - 2016 12 11	4	114	9 - 10	S. Fauvaud, M. Fauvaud, F. Richard	Pic du Midi Observatory, France
2016 12 09	1	114	9	S. Geier	ORM, La Palma, Spain
2018 01 26 - 2018 03 018	3	153 - 162	6 - 9	K. Kamiński	Winer, AZ, USA
2018 03 15	1	154	6	M. Dróżdż	Suhora, Poland
2019 06 02	1	217	14	V. Kudak, V. Perig	Derenivka, Ukraine
2019 04 01 - 2019 04 14	4	211 - 214	4 - 7	A. Marciniak, M. Pawłowski, K. Żukowski	Borowiec, Poland
2019 04 02	1	214	7	E. Pakštienė	Molėtai Astronomical Observatory, Lithuania
2019 04 02 - 2019 04 04	2	213 - 214	6 - 7	W. Ogłoza	Suhora, Poland
2019 05 09	1	206	7	M.-J. Kim, D.-H. Kim	SOAO, South Korea

Date	N_{lc}	λ [deg]	Phase angle [deg]	Observer	Site
551 Ortrud					
2006 11 10 - 2006 12 08	8	46 - 51	1 - 11	-	Super WASP
2015 06 30	1	302	7	A. Marciniak	OT, Tenerife, Spain
2015 07 07 - 2015 09 13	8	291 - 301	1 - 16	-	Montsec, Catalonia, Spain
2016 08 31 -2016 11 25	15	21 - 33	8 - 18	Marciniak et al. (2018)	Borowiec, Poland; Organ Mesa, NM, USA; Tempe, AZ, USA
2018 01 08 - 2018 04 17	4	136 - 147	5 - 19	R. Hirsch, J. Skrzypek, A. Marciniak	Borowiec, Poland
2019 03 28 - 2019 04 29	10	224 - 229	2 - 12	-	OAdM, Montsec, Catalonia, Spain
2019 04 10	1	227	8	D.-H. Kim, M.-J. Kim	SOAO, South Korea
2020 05 23 - 2020 05 25	2	297	14 - 15	K. Kamiński	Winer, AZ, USA
2019 05 24	1	219	7	K. Kamiński	Winer, AZ, USA
2020 07 17 - 2020 08 13	4	285 - 289	2 - 11	W. Ogłoza	Adiyaman, Turkey
2021 08 21 - 2021 10 11	33	13 - 20	0 - 16	-	TESS spacecraft
2021 12 06	1	8	19	M. Żejmo	e-Eye, Spain
566 Stereoskopia					
1990 02 24 - 1990 02 25	2	108	12	Binzel & Sauter (1992)	McDonald Observatory, TX, USA
2006 10 24 - 2006 11 16	6	328 - 331	17 - 19	D. J. Higgins	Australia
2017 09 12 - 2017 09 19	8	235 - 236	14 - 15	-	Kepler Spacecraft
2019 09 04 - 2019 10 01	3	25 - 28	6 - 14	M. Dróżdż	Suhora, Poland
2019 09 23 - 2019 11 04	3	19 - 27	5 - 9	W. Ogłoza	Adiyaman, Turkey
2020 01 23 - 2020 01 23	1	24	19	V. Kudak, V. Perig	Derenivka, Ukraine
2020 10 16 - 2021 01 10	4	106 - 113	1 - 18	W. Ogłoza	Adiyaman, Turkey
2020 11 04	1	113	17	A. Jones	Maidenhead, UK
2022 02 27 - 2022 03 20	3	166 - 170	2 - 4	E. Pakštienė, R. Urbonavičiūtė	Molėtai Astronomical Observatory, Lithuania
2022 03 01 - 2022 03 12	2	168 - 170	2 - 3	J. Golonka, M. Motyliński, K. Szyszka, B. Joachimczyk, A. Demirkol	Piwnice, Poland
2022 03 26	1	165	6	A. Jones	Maidenhead, UK
2022 04 22	1	162	12	W. Ogłoza	Adiyaman, Turkey
657 Gunlod					
1984 02 09	1	121	8	Binzel (1987)	McDonald Observatory. TX, USA
2015 07 03	1	323	14	A. Marciniak	OT, Tenerife, Spain
2015 08 04	1	317	3	M. Żejmo	Adiyaman, Turkey
2015 09 05 - 2015 09 13	4	310 - 311	11 - 14	-	Montsec, Catalonia, Spain
2016 10 05	1	51	13	A. Marciniak	ORM, La Palma, Spain
2016 10 07 - 2016 10 09	2	50	12	R. Szakáts	Piszkéstető, Hungary
2016 10 08 - 2016 10 10	2	50	12	R. Duffard, N. Morales	La Sagra, Spain
2016 12 27	1	37	18	M.-J. Kim, D.-H. Kim	SOAO, South Korea
2018 02 26 - 2018 04 21	5	153 - 160	5 - 22	K. Żukowski, J. Skrzypek	Borowiec, Poland
2020 10 09 - 2021 02 04	2	26 - 27	6 - 19	R. Szakáts	Piszkéstető, Hungary
2020 10 21	1	23	6	K. Kamiński	Winer, AZ, USA
2020 10 22 - 2020 10 27	3	22 - 23	6 - 7	W. Ogłoza	Suhora, Poland
2020 10 24	1	23	6	W. Ogłoza	Adiyaman, Turkey
2021 10 21 - 2021 11 28	16	126 - 135	22 - 23	-	TESS spacecraft
2021 11 13	1	132	23	M. Dróżdż	Suhora, Poland
2021 12 13 - 2022 01 11	2	133 - 136	9 - 19	M. Żejmo	e-EYE, Spain
2021 12 29	1	135	14	E. Pakštienė, R. Urbonavičiūtė	Molėtai Astronomical Observatory, Lithuania
2022 01 06 - 2022 01 07	2	134	10 - 11	D.-H. Kim, M.-J. Kim	SOAO, South Korea
738 Alagasta					
2015 06 05 - 2015 06 09	2	244 - 245	3 - 5	-	Montsec, Catalonia, Spain
2015 06 11 - 2015 07 04	7	241 - 244	6 - 13	W. Ogłoza, M. Winiarski	Suhora, Poland
2015 07 20	1	240	17	M. Żejmo	Adiyaman, Turkey
2016 09 06 - 2016 09 11	2	323 - 324	6 - 8	-	Montsec, Catalonia, Spain
2016 09 20 - 2016 10 06	4	321 - 322	11 - 14	J. Licandro, A. Marciniak	ORM, La Palma, Spain
2016 10 29	1	322	17	A. Marciniak	CTIO, Chile
2017 10 15 - 2017 12 09	9	36 - 47	3 - 12	-	Montsec, Catalonia, Spain
2018 12 05 - 2019 02 24	2	120 - 132	12 - 17	K. Żukowski, M. Pawłowski	Borowiec, Poland
2019 01 05 - 2019 02 11	4	122 - 129	6 - 8	M.-J. Kim, D.-H. Kim	SOAO, South Korea
2019 01 10	1	128	6	V. Kudak, V. Perig	Derenivka, Ukraine
2020 03 16 - 2020 04 23	4	221 - 226	3 - 15	R. Szakáts	Piszkéstető, Hungary
2020 04 18 - 2020 06 13	4	214 - 222	3 - 15	W. Ogłoza	Adiyaman, Turkey

Date	N_{lc}	λ [deg]	Phase angle [deg]	Observer	Site
806 Gyldenia					
2010 07 25 - 2010 12 08	9	38 - 47	4 - 18	Waszczak et al. (2015)	Mt. Palomar, CA, USA
2013 03 05 - 2013 05 08	9	210 - 211	2 - 15	Marciniak et al. (2015)	Borowiec, Poland; Organ Mesa Observatory, NM, USA
2013 04 07 - 2013 04 18	9	212 - 214	2 - 6	Alkema (2013)	-
2015 06 28	1	0	17	A. Marciniak	OT, Tenerife, Spain
2015 09 11 - 2015 11 01	5	348 - 356	5 - 13	-	Montsec, Catalonia, Spain
2015 11 12	1	348	15	R. Duffard, N. Morales	La Sagra, Spain
2016 10 04	1	67	15	A. Marciniak	ORM, La Palma, Spain
2016 10 07 - 2016 10 09	3	67	14	R. Szakáts	Piszkéstető, Hungary
2016 10 11 - 2016 10 30	3	65 - 67	8 - 13	R. Duffard, N. Morales	LaSagra, Spain
2016 10 29	1	65	8	A. Marciniak	CTIO, Chile
2018 02 13	1	143	7	M.-J. Kim, D.-H. Kim	SOAO, South Korea
2018 02 13 - 2018 03 19	4	138 - 143	7 - 14	J. Skrzypek, R. Hirsch	Borowiec, Poland
2018 03 17	1	138	13	K. Kamiński	Winer, AZ, USA
2019 04 30 - 2019 05 21	4	230 - 234	3 - 5	K. Kamiński	Winer, AZ, USA
2019 05 06 - 2019 05 07	2	233	2	D.-H. Kim, M.-J. Kim	SOAO, South Korea
2020 09 17 - 2020 09 20	5	299	14 - 15	F. Monteiro, W. Mesquita, W. Pereira, M. Evangelista, E. Rondón, J. Michimani, D. Lazzaro, T. Rodrigues	OASI, Itacuruba, Brasil
2021 09 08 - 2021 11 25	4	4 - 15	8 - 15	M. Dróżdż	Suhora, Poland

(70) Panopaea, 2006-12-14	
S. Herchak	Mesa, AZ
B. Roberts	Shady Grove, MS
B. Richardson	Hewitt, TX
J. Barton	Robinson, TX
R. Nugent	Centerville, TX
D. Craig Smith	Ozona, TX
M. McCants	Oakalla, TX
D. Dunham	McComb, MS
W. Aulenbacher	L. Bunshannon, TX
D. Nye	Marfa, TX
P. Maley	Madisonville, TX
D. Rask	Huntsville, TX
D. Clark	Providence, TX
K. Drake	Willis, TX
P. Nolan	Mountain Home, TX
A. Sanchez-Ibarra	Sonora, MX
B. Cudnik	Houston, TX
R. Frakenberger	San Antonio, TX
(70) Panopaea, 2014-10-04	
J. Broughton	Eagleby, AU
G. Bolt	Perth, AUS
(70) Panopaea, 2014-04-25	
A. Olsen	Urbana, IL
P. Maley	Marana, AZ
J. Moore	Blackwell, OK
(275) Sapientia, 1985-04-15	
A. Olsen	Urbana, IL
P. Maley	Marana, AZ
J. Moore	Blackwell, OK
(275) Sapientia, 2003-02-08	
R. Venable	Pelham, USA
D. Rowley	North Henderson, NC
(275) Sapientia, 2003-04-12	
J. Nosaka	Masuda: Shimane, JP
M. Uchiyama	Owase: Mie, JP
I. Yamanihi, Naoko Kaifu et al	JP
M. Yamanishi	Yuasa: Wakayama, JP
(275) Sapientia, 2014-09-02	
J. Rovira	ES
J. Juan	ES
E. Frappa, A. Klotz	FR
C. Perelló, A. Selva	ES
P. Baruffetti	IT
M. Bachini	IT
(275) Sapientia, 2015-09-30	
C. Hills	GB
S. Clarke	GB
J. Warell	SE
C. Hooker	GB
S. Kidd	GB
T. Haymes	GB
A. Jones	GB
M. Charron	GB
D. Arditti	GB
H. Paulus	DE
T. Law	GB
H. Denzau	DE
P. Denyer	GB
P. Carson	GB
M. Jennings	GB
E. Edens	NL
(275) Sapientia, 2016-12-03	
O. Klös	DE
V. Přibáň	CZ
K. Halíř	CZ
M. Rottenborn	CZ
J. Polák	Cz
(275) Sapientia, 2018-08-06	
G. Vaudescal, A. Cazaux	FR
P. Lindner	DE
C. Schnabel	ES
B. Kattentidt	DE
G. Dangl	AT
J. Polák	CZ
(275) Sapientia, 2020-11-14	
G. Vaudescal	FR
E. Frappa, A. Klotz	FR
M. Conjat	FR
A. Manna	CH
S. Sposetti	CH
G. Casalnuovo	IT
A. Kreutzer, R. Schäfer	AT
M. Billiani	FR
(275) Sapientia, 2021-04-26	
T. George	Scottsdale, AZ
P. Stuart	Clear Lake Shores, TX
S. Brazill	Georgetown, TX
(286) Iclea, 2008-06-15	
D. Lowe	Mt. Mee, AU
J. Bradshaw, A. Beck	Samford, AU
P. Anderson	The Gap, Qld, AU
D. Breadsell	Toowoomba, AU
(326) Tamara, 2016-09-23	
J. Broughton	Reedy Creek, AU
J. Broughton	Brunswick Heads, AU
J. Broughton	Ballina, AU
J. Broughton	Broadwater, AU

Table B.2: List of stellar occultation observers and locations of their observing sites. Source: Occult programme.

(326) Tamara, 2017-09-15	
D. Breit	Morgan Hill, CA
R. Nolthenius	Paicine, CA
J. Bardecker	Gardnerville, NV
(326) Tamara, 2017-12-28	
H. De Groot	NL
E. Conseil	FR
T. Janík	CZ
R. Boninsegna	BE
(326) Tamara, 2018-05-12	
B. Leonard	Sherman, TX
M. Smith	Sherman, TX
K. Cobble	Princeton, TX
(326) Tamara, 2018-12-21	
A. Manna	CH
S. Sposetti	CH
(412) Elisabetha, 2011-01-23	
M. Ida	Higashiomi, Shiga, JP
M. Ishida	Koka, Shiga, JP
A. Asai	Inabe, Mie, JP
H. Watanabe et al	Inabe, mie, JP
M. Owada	Hamamatsu, Shizuoka, JP
(412) Elisabetha, 2016-03-17	
P. Delincak	SK
B. Gährken	DE
M. Korec	SK
(412) Elisabetha, 2017-03-19	
A. Ossola	CH
A. Manna	CH
(412) Elisabetha, 2019-12-04	
P. Baruffetti	IT
S. Donati	IT
(426) Hippo, 2012-01-13	
D. Ewald	DE
G. Wortmann, K. Walzel	DE
W. Rothe	DE
O. Canales, F. Campos	ES
E. Frappa, M. Lavayssière	FR
P. Lindner	DE
C. Schnabel, J. Juan	ES
J. Rovira	ES
A. Selva	ES
(426) Hippo, 2015-06-20	
R. Baldridge	Los Altos Hills, CA
T. Swift	Davis, CA
J. Bardecker	Gardnerville, NV
C. McPartlin	Santa Barbara, CA

(426) Hippo, 2018-05-21	
J. Broughton	Tumbulgum, AU
J. Broughton	Brunswick Heads, AU
J. Broughton	Ballina, AU
(426) Hippo, 2021-12-27	
H. Yoshihara	Soja, Okayama, JP
M. Yamashita	Ikeda, Osaka, JP
T. Goto	Yamada Higashi, JP
M. Higuchi	Shigokamachi, JP
M. Nishimura	Kitakuzuhacho, JP
H. Kasebe	Osaka, JP
A. Asai	Kuwana, Mie, JP
A. Hashimoto	Chichibu, Saitama, JP
H. Watanabe, H. Watanabe	Tsu, Mie, JP
M. Ishida	Tsu, Mie, JP
R. Aikawa	Sakasdo, Saitama, JP
M. Ida	Tsu, Mie, JP
R. Kukita	Nabekura, JP
T. Horaguchi	Tsukuba, JP
K. Fukui	Nagakunidai, JP
K. Kouno	Miyazaki, JP
K. Terakubo	Kokubunji, Tokyo, JP
K. Kitazaki	Musashino, Tokyo, JP
S. Uchiyama	Kashiwa, Chiba, JP
T. Hirose	Ohtaku, Tokyo, JP
M. Owada	Hamamatsu, Shizuoka, JP
(426) Hippo, 2021-12-31	
A. Selva	ES
J. Juan	ES
C. Schnabel	ES
(426) Hippo, 2022-03-23	
J. Mánek	CZ
J. Kubánek	CZ
K. Halíř	CZ
M. Rottenborn	CZ
J. Polák	CZ
E. Kowald	AT
B. Kattentidt	DE
(439) Ohio, 2017-05-27	
D. Gault	Hawkesbury Heights, AU
T. Barry	Penrith, AU
D. Herald	Murrumbateman:nsw, AU
J. Newman	Flynn:act, AU
(439) Ohio, 2022-03-11	
P. Zelený	CZ
P. Delincak	SK
M. Urbanik	SK
M. Zawilski	PL
L. Benedyktowicz	PL
M. Borkowski	PL
M. Filipek	PL
M. Harman	SK
D. Błażewicz	PL

(439) Ohio, 2022-03-24	
O. Schreurs	BE
B. Goffin	BE
R. Boninsegna, P. Assoignon	BE
K. Guhl	DE
O. Hofschulz	DE
S. Andersson	DE
J. Delpau	FR
M. Borkowski	PL
A. Marciniak	PL

(464) Megaira, 2017-12-06	
G. Lyzenga	Altadena, CA
J. Moore	Tulsa, OK
C. Ellington	Edmond, OK
P. Maley	Congress, AZ

(464) Megaira, 2017-12-18	
H. Tomioka	Hitachi, Ibaraki, JP
H. Watanabe	Tarui, Gifu, JP
S. Uchiyama	Hamamatsu, Shizuoka, JP
A. Asai	Inabe, Mie, JP
H. Watanabe	Inabe, Mie, JP
M. Owada	Hamamatsu, Shizuoka, JP
M. Ishida	Moriyama, Shiga, JP
Y. Ikari	Moriyama, Shiga, JP
T. Ito	Suzuka, Mie, JP
H. Yamamura	Tsu, Mie, JP
M. Ida	Tsu, Mie, JP

(476) Hedwig, 2000-11-07	
N. Quinn	GB
J. Moellmann	DE
D. Ewald	DE
N. Wünsche	DE
M. Dentel	DE
S. Andersson, M. Haupt	DE
P. Enskonatus	DE
J. A. Berdejo	ES
J. Grados	ES

(476) Hedwig, 2017-02-24	
B. Loader	Nelson, NZL
G. McKay	Blenheim

(476) Hedwig, 2018-07-26	
P. Delincak	SK
J. Kubánek	HU
M. Jarmoc	PL

(476) Hedwig, 2018-11-13	
C. Perelló, A. Selva	ES
C. Perelló, A. Selva	ES
J. Rovira	ES
J. Rovira	ES
S. Meister	CH
A. Ossola	CH
S. Sposetti	CH
J. Polák	CZ
M. Rottenborn	CZ
C. Weber	DE
C. Weber	DE

(476) Hedwig, 2019-02-12	
E. Frappa	FR
M. Conjat	FR

(476) Hedwig, 2020-05-19	
P. Le Cam	FR
E. Frappa	FR
E. Frappa, A. Klotz	FR

(524) Fidelio, 2005-12-11	
R. Gonçalves	PT
O. Canales, J. L. Marco	ES
R. Poncy	FR
P. Bernascolle	FR

(524) Fidelio, 2006-04-24	
H. Denzau	DE
W. Rothe	DE
T. Janík	CZ
V. Přibáň	CZ
J. Vilagi, L. Kornos	SK
G. Dangl	AT
E. Frappa, A. Klotz	Tarot, Calern, FR
J. Lecacheux	FR

(524) Fidelio, 2018-12-12	
E. Frappa, A. Klotz	Grasse, FR
R. Venable	Lovejoy, GA
R. Venable	Griffin, GA
R. Venable	Barnesville, GA
V. Tsamis, A. Tserionis et al.	Ellinogermaniki, GR

(524) Fidelio, 2019-02-25	
R. Reaves	Parker, AZ
P. Maley	Dateland, AZ

(524) Fidelio, 2021-07-13	
J. Newman	Flynn, Act, AU
W. Hanna	Yass, Nswn AU

(524) Fidelio, 2021-11-18	
R. Venable	Chester, GA
R. Venable	Tarversvillle, GA

(530) Turandot, 2006-02-24	
S. Jamieson	Eagle, WI
S. Ballaron	Lake Villa, IL
C. Bueter	Gas City, IN
D. Drake	Indian Head Park, IL
D. Dunham	Gaston, IN
G. Samolyk	Shirland, IL
B. Oldham	Pelham, NC
D. Oesper	Dodgeville, WI
S. Messner	Harvest Moon Obs, MN
R. Huziak	Saskatoon:sk, CAN
P. Maley et al	Cincinnati, OH
D. Dunham	Fisher, IN
J. Armor	Villa Hilles, KY
M. Hoskinson	Vilna Alberta, CAN
G. Stone	Lorborn:sk, CAN
D. Carton	Dark Sky Obs, CAN
O. Piechowski	Versailles, KY
D. Breit	Martinez, CA

(530) Turandot, 2019-04-01	
P. Maley	Carefree, AZ
T. George	Scottsdale, AZ
W. Thomas	Florence, AZ

(530) Turandot, 2020-07-27	
S. Preston	Medina, WA
D. Gamble	Summerland, BC

(551) Ortrud, 2021-07-11	
A. Asai	Inabe, Mie, JP
H. Yamamura	Suzuka, Mie, JP
K. Isobe	Uda, Mie, JP
A. Hashimoto	Chichibu, Saitama, JP
M. Owada	Hammatsu, Shizuoka, JP

(551) Ortrud, 2021-10-24	
J. Barton	Robinson, TX
D. Eisfeldt	Waco, TX

(566) Stereoskopia, 2004-03-23	
T. Janík	CZ
D. Naillon	FR
H. McGee	GB
A. Christou, D. Asher	GB
J. Lecacheux	FR
T. Midavaine, O. Dechambre et al	FR
B. Christophe, J. M. Vugnon	FR
L. Parmeggiani	FR
G. Kirby	GB

(566) Stereoskopia, 2010-12-28	
H. Tomioka	Hitachie, Ibaraki, JP
R. Aikawa	Sakado, Saitama, JP
K. Kitazaki	Musashino, Tokyo, JP
M. Owada	Hamamatsu, Shizuoka, JP
H. Watanabe	Inabe, Mie, JP

(566) Stereoskopia, 2020-09-13	
H. Watanabe	Tarui: Gifu, JP
H. Yamamura	Wanouchi: Gifu, JP
A. Asai	Inabe: Mie, JP

(566) Stereoskopia, 2021-04-08	
R. Boninsegna	BE
K. L. Bath	DE
S. Meister	CH
M. Simon	DE
W. Hasubick	DE
G. Krannich	DE
B. Gährken	DE
B. Kattentidt	DE

(566) Stereoskopia, 2022-02-08	
P. Ceravolo	Osoyoos, CAN
V. Nikitin	Boulder, CO
S. Messner	Jefferson, TX
M. Skrutskie	Nederland, CO

(657) Gunlod, 2022-02-09	
J. J. Castellani	FR
P. Baruffetti	IT
M. Conjat	FR
M. Conjat	FR
G. Vaudescal	FR
Y. Argentin	FR
P. Fini	IT

(738) Alagasta, 2017-11-12	
M. Kashiwagura	Ōe, Yamagata, JP
H. Togashi	Ōe, Yamagata, JP
I. Otsuki	Date, Fukushima, JP
K. Hosoi	Miharu, Fukushima, JP
A. Hashimoto	Ono, Fukushima, JP
H. Yamamura	Hodatsushimizu, Ishikawa, JP
M. Ida	Kahoku, Ishikawa, JP
M. Ishida	Kanazawa, Ishikawa, JP
H. Tomioka	Hitachi, Ibaraki, JP
A. Yaeza	Hitachi, Ibaraki, JP
A. Asai	Inabe, Mie, JP
H. Watanabe	Inabe, Mie, JP
Y. Ikari	Moriyama, Shiga, JP

(738) Alagasta, 2020-05-30	
J. Bourgeois	BE
F. Van Den Abbeel	BE
O. Schreurs, E. Fernandez	BE
J. M. Winkel	NL
J. Polák	CZ
M. Rottenborn	CZ
J. Kubánek	CZ

(738) Alagasta, 2022-11-12	
K. Kitazaki	Musashino, Tokyo, JP
Ha. Watanabe, Hi. Watanabe	Tamaki, JP
M. Owada	Hamamatsu, Shizuoka, JP
H. Matsushita	Shima, Mie, JP
N. Manago	Kamitonda, Wakayama, JP

(806) Gyldenia, 2021-08-20	
W. Thomas	Florence, AZ
P. Maley	Toltec, AZ
S. Messner	Hudson, WI

Appendix C: Light curves

Composite light curves presenting new data for target asteroids (Figures C.1 - C.77).

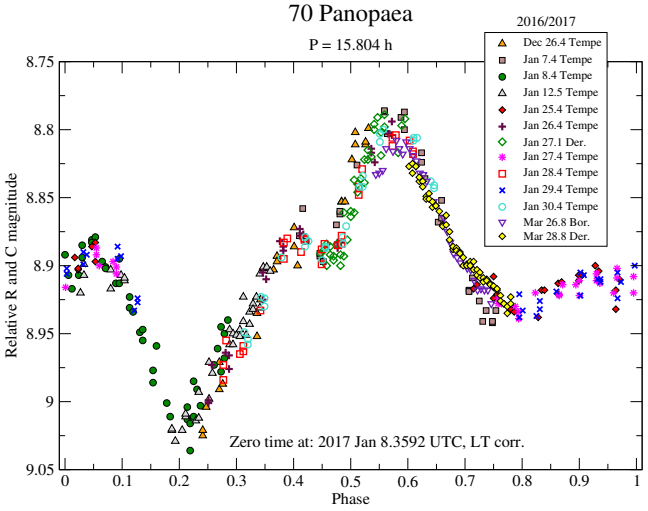

Fig. C.1: Composite light curve of (70) Panopaea from the years 2016-2017.

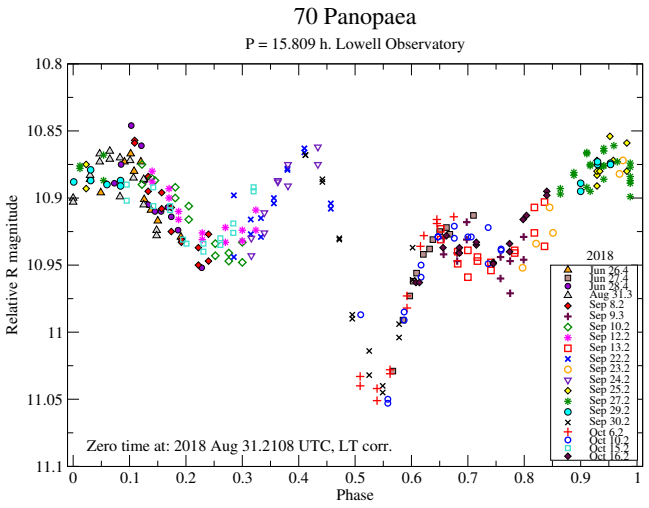

Fig. C.2: Composite light curve of (70) Panopaea from the year 2018.

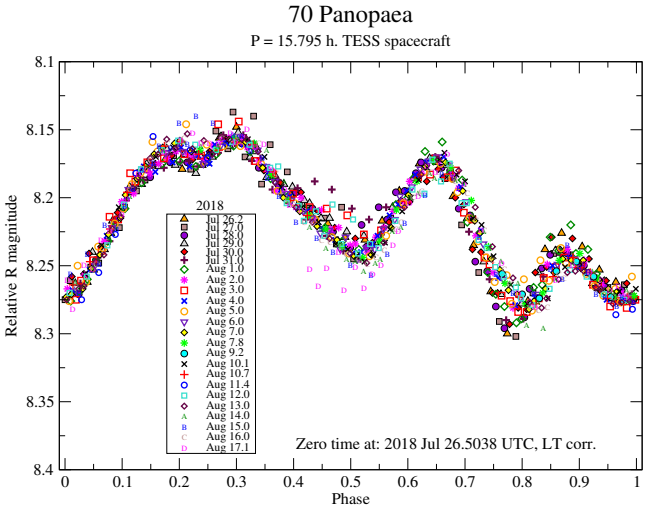

Fig. C.3: Composite light curve of (70) Panopaea from the year 2018 observed by TESS spacecraft.

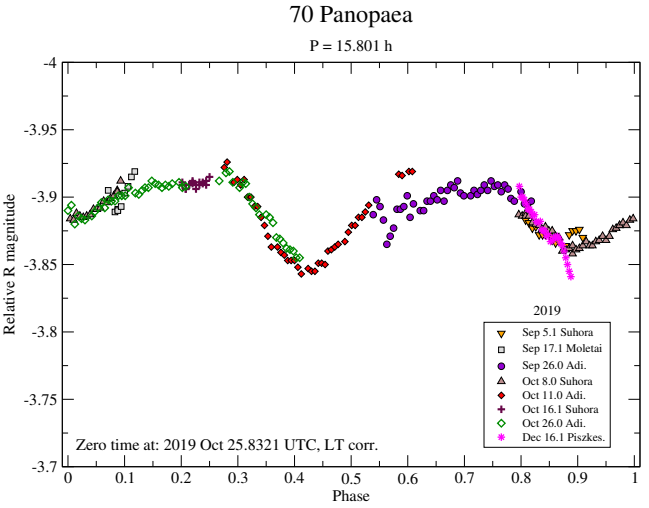

Fig. C.4: Composite light curve of (70) Panopaea from the year 2019.

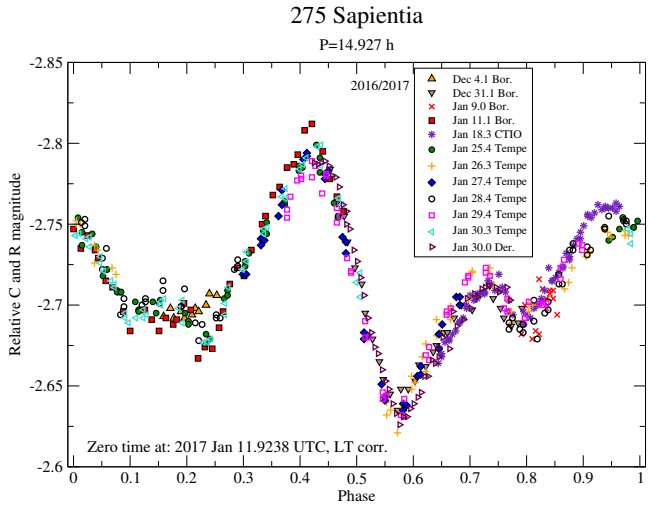

Fig. C.5: Composite light curve of (275) Sapientia from the years 2016-2017.

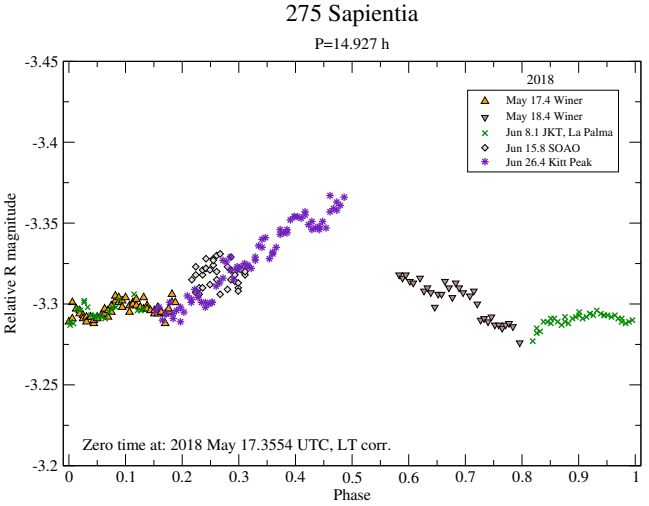

Fig. C.6: Composite light curve of (275) Sapientia from the year 2018.

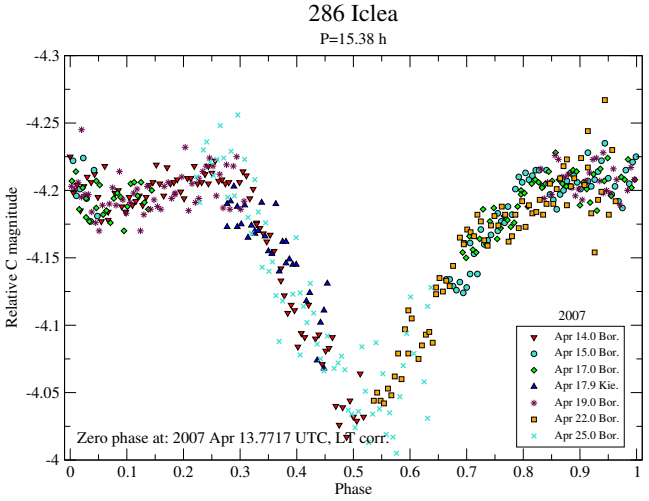

Fig. C.7: Composite light curve of (286) Iclea from the year 2007.

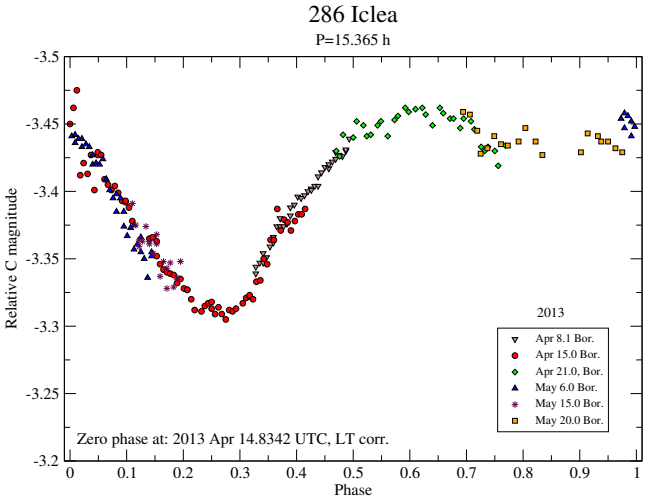

Fig. C.8: Composite light curve of (286) Iclea from the year 2013.

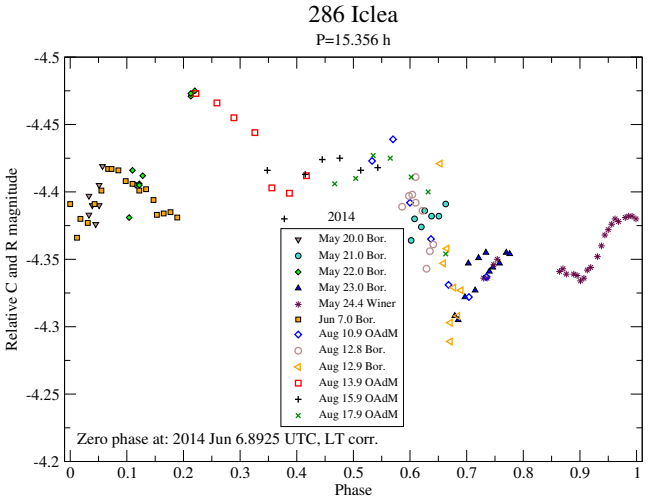

Fig. C.9: Composite light curve of (286) Iclea from the year 2014.

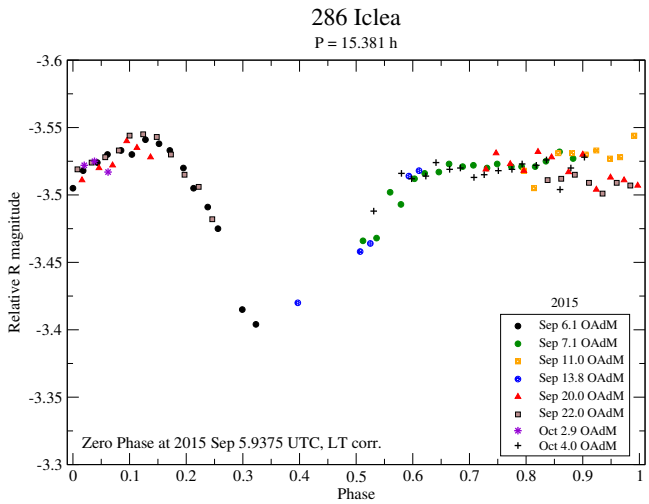

Fig. C.10: Composite light curve of (286) Iclea from the year 2015.

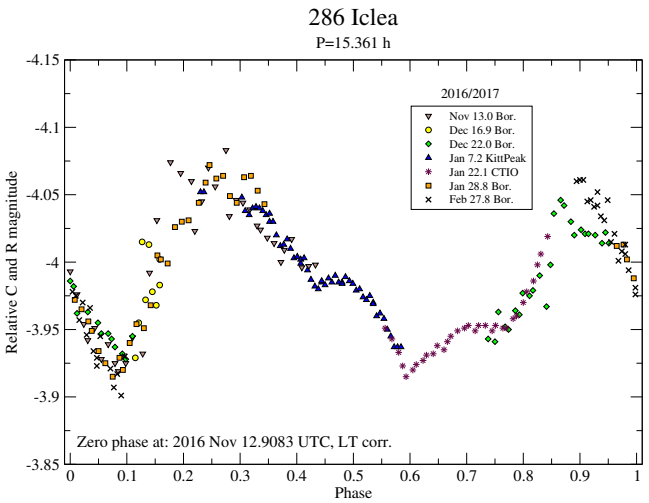

Fig. C.11: Composite light curve of (286) Iclea from the years 2016-2017.

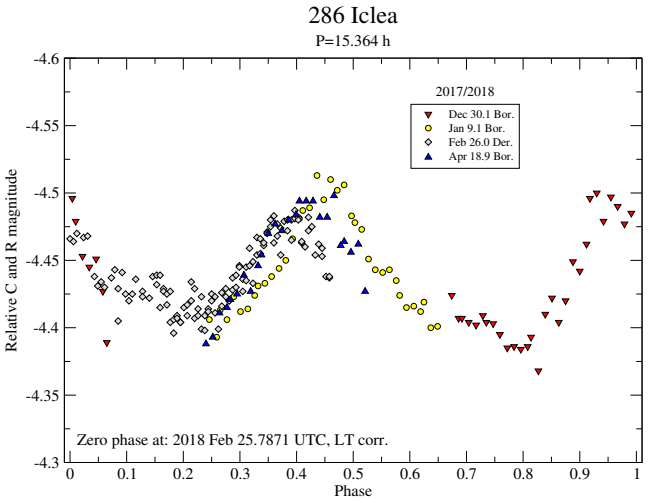

Fig. C.12: Composite light curve of (286) Iclea from the years 2017-2018.

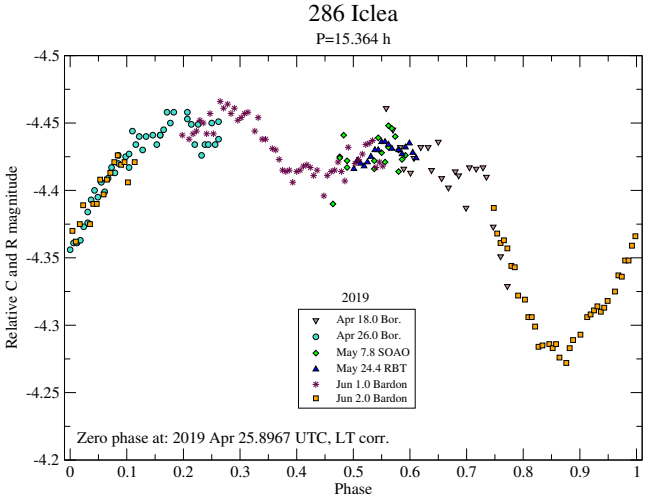

Fig. C.13: Composite light curve of (286) Iclea from the year 2019.

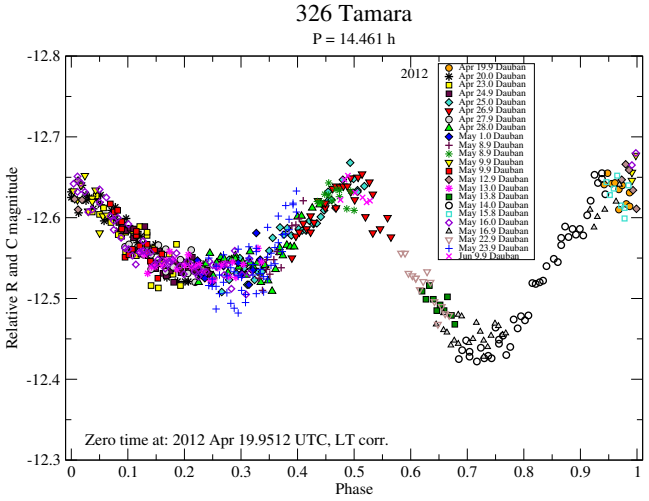

Fig. C.14: Composite light curve of (326) Tamara from the year 2012.

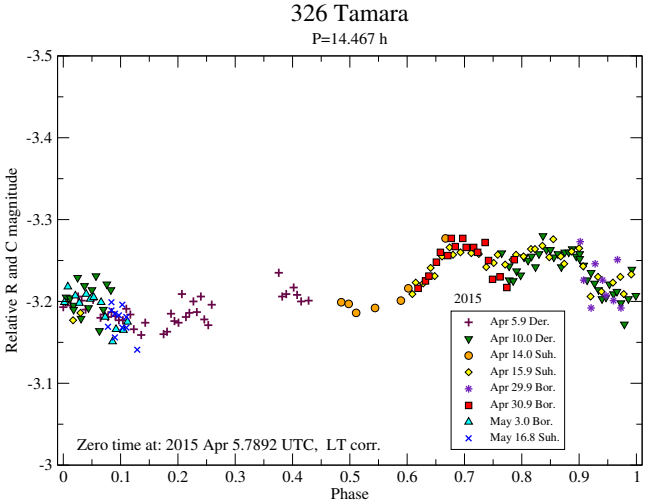

Fig. C.15: Composite light curve of (326) Tamara from the year 2015.

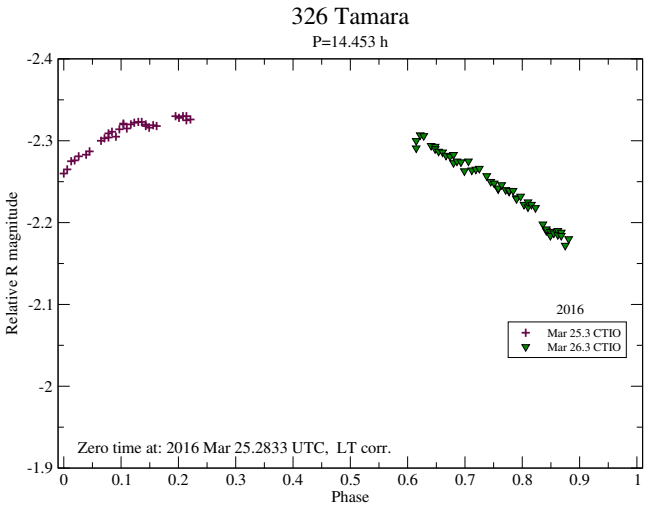

Fig. C.16: Composite light curve of (326) Tamara from March 2016.

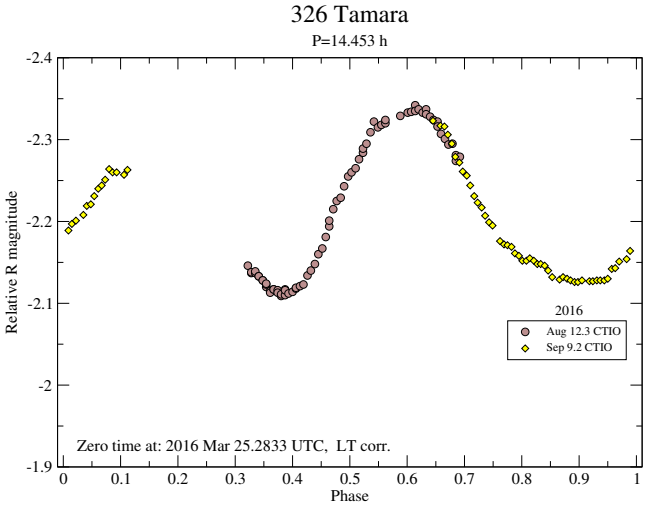

Fig. C.17: Composite light curve of (326) Tamara August-September 2016.

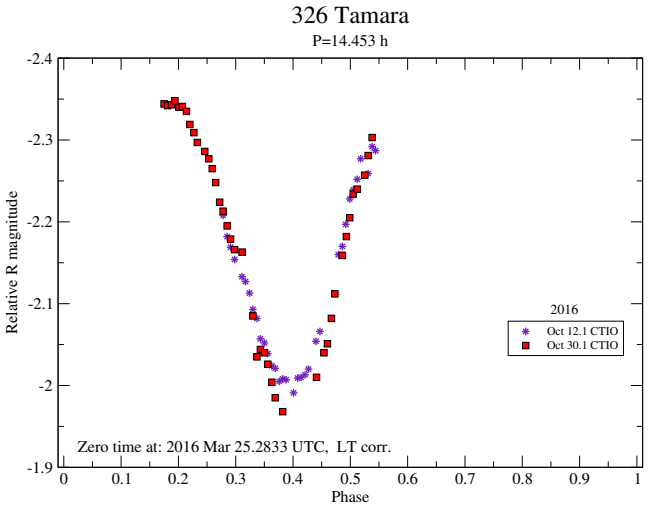

Fig. C.18: Composite light curve of (326) Tamara from October 2016. Data in 2016 were gathered in greatly varied phase angles and ecliptic longitudes, preventing the creation of one composite light curve (see Fig. C.16, and C.17).

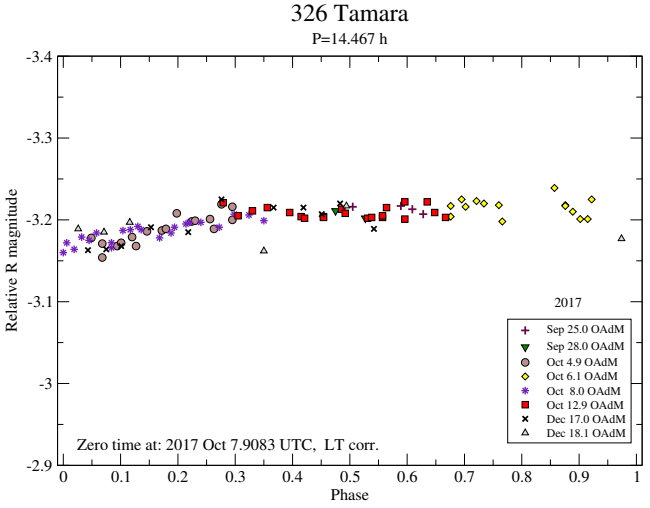

Fig. C.19: Composite light curve of (326) Tamara from the year 2017.

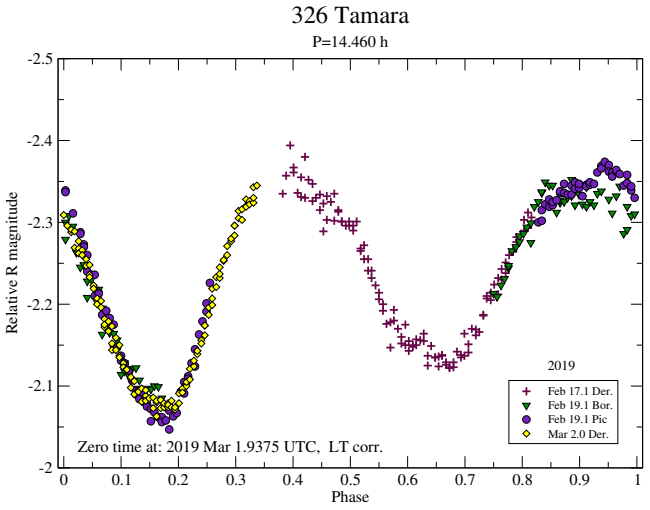

Fig. C.20: Composite light curve of (326) Tamara from the year 2019.

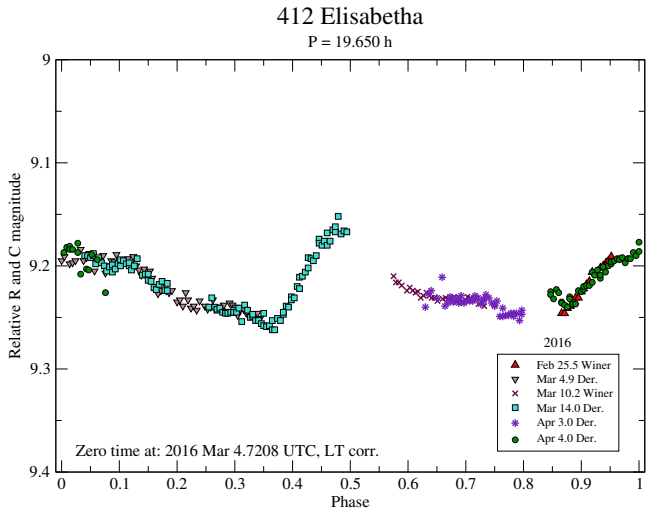

Fig. C.21: Composite light curve of (412) Elisabetha from the year 2016.

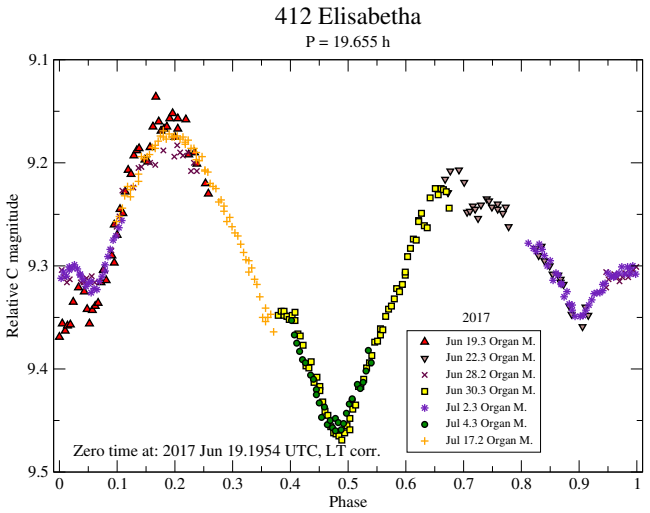

Fig. C.22: Composite light curve of (412) Elisabetha from the year 2017.

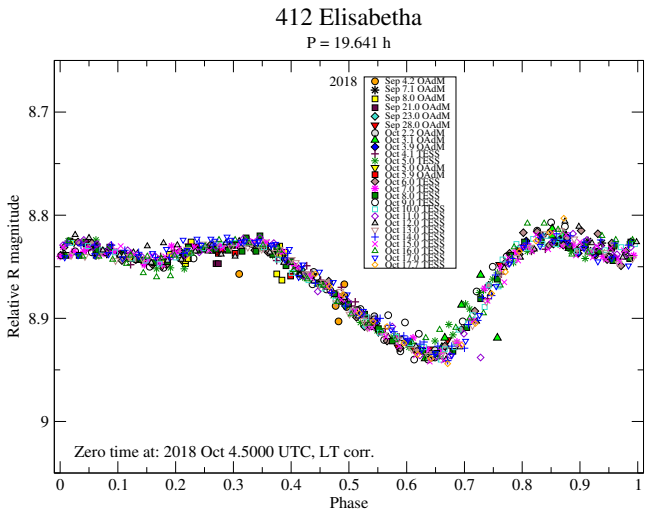

Fig. C.23: Composite light curve of (412) Elisabetha from the year 2018.

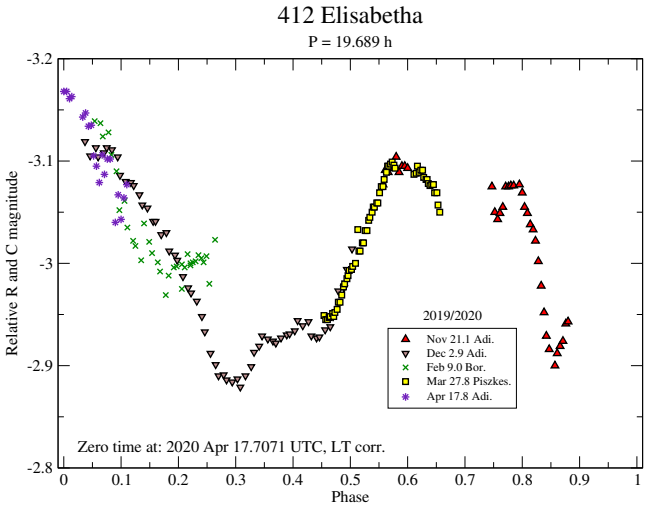

Fig. C.24: Composite light curve of (412) Elisabetha from the years 2019-2020.

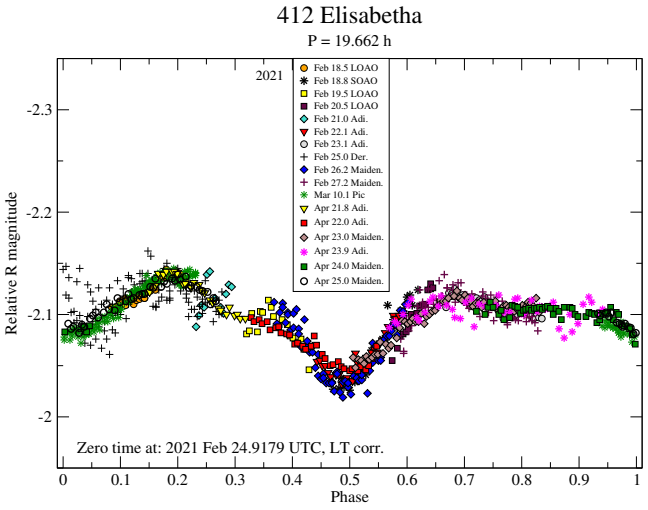

Fig. C.25: Composite light curve of (412) Elisabetha from the year 2021.

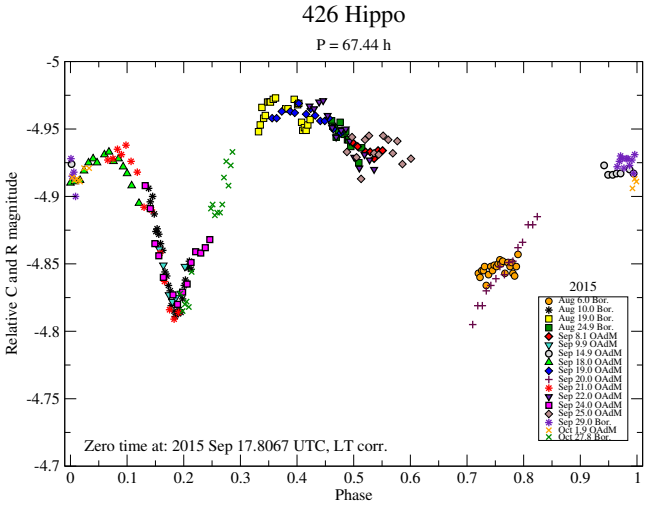

Fig. C.26: Composite light curve of (426) Hippo from the year 2015.

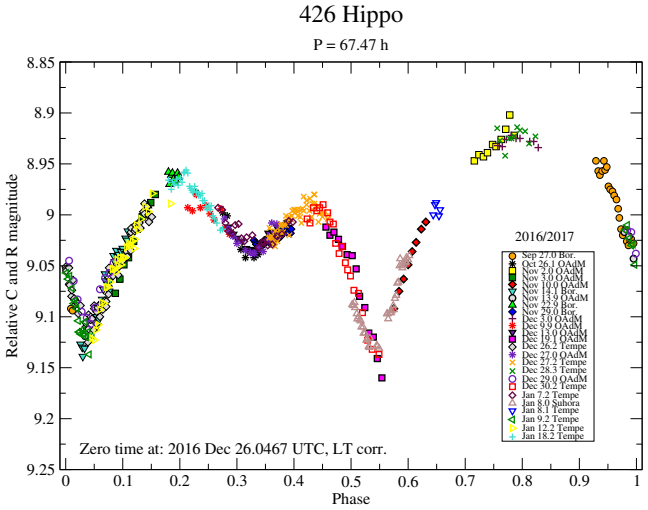

Fig. C.27: Composite light curve of (426) Hippo from the years 2016-2017.

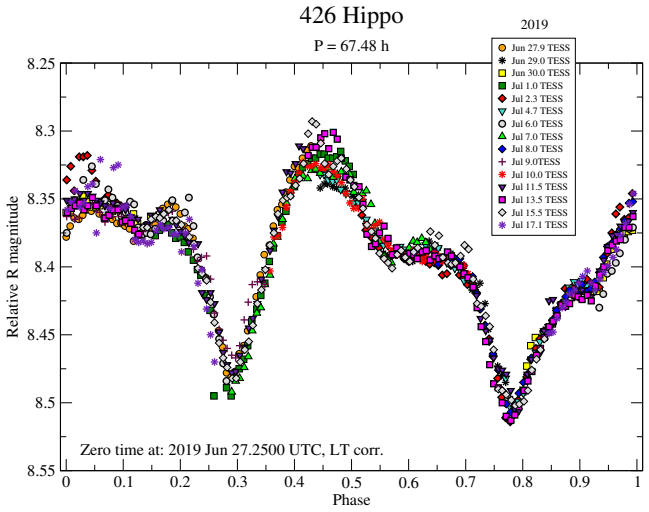

Fig. C.28: Composite light curve of (426) Hippo from the year 2019 observed by TESS spacecraft.

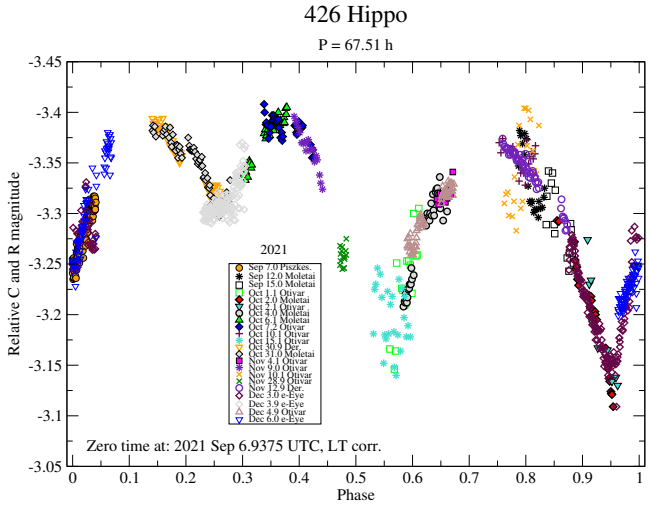

Fig. C.29: Composite light curve of (426) Hippo from the year 2021.

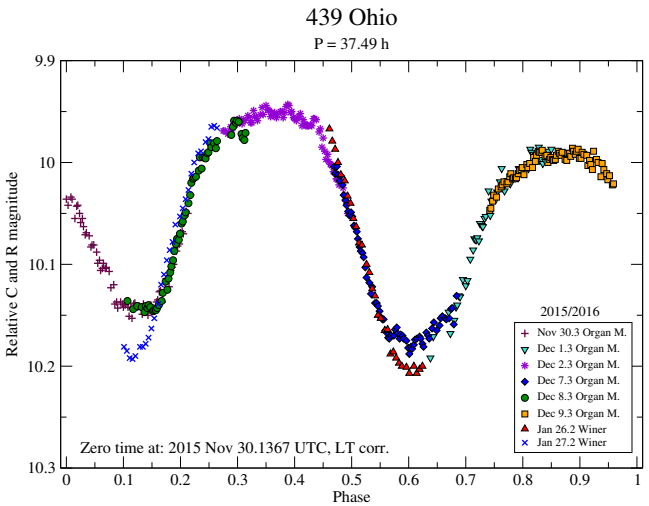

Fig. C.30: Composite light curve of (439) Ohio from the years 2015-2016.

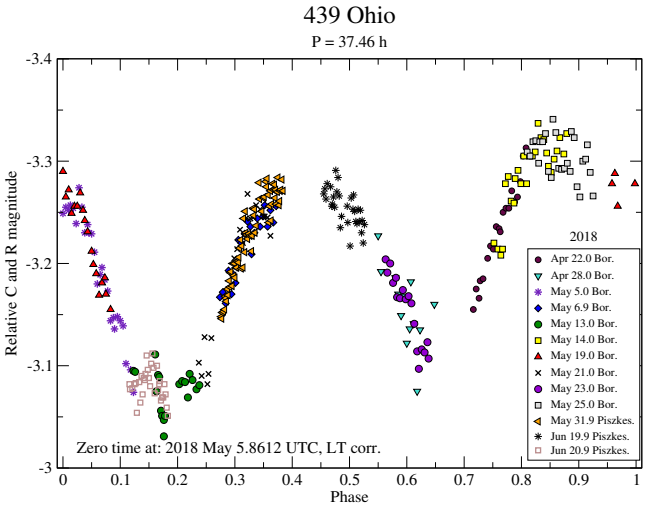

Fig. C.31: Composite light curve of (439) Ohio from the year 2018.

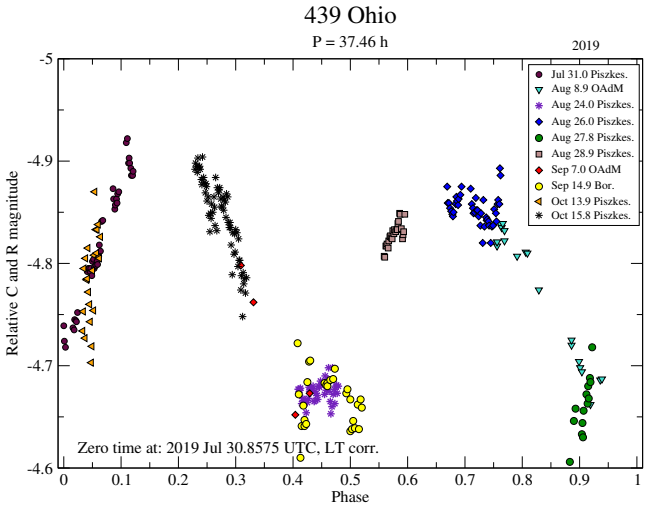

Fig. C.32: Composite light curve of (439) Ohio from the year 2019.

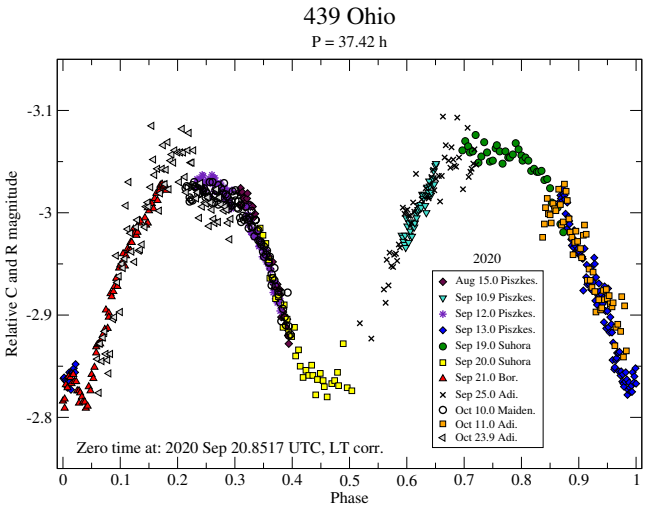

Fig. C.33: Composite light curve of (439) Ohio from the year 2020.

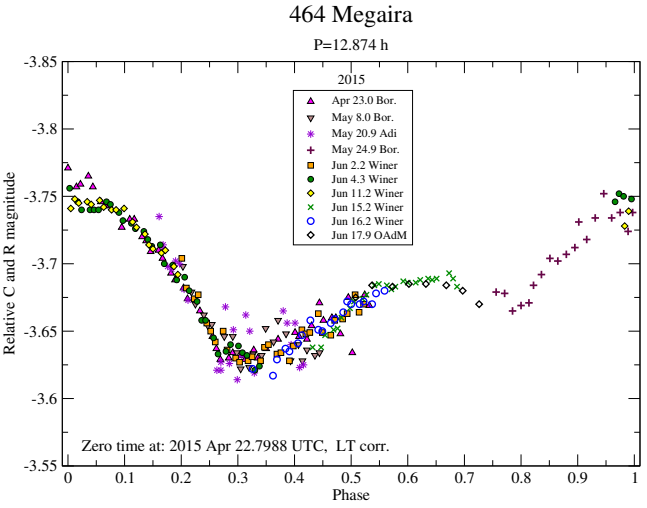

Fig. C.34: Composite light curve of (464) Megaira from the year 2015.

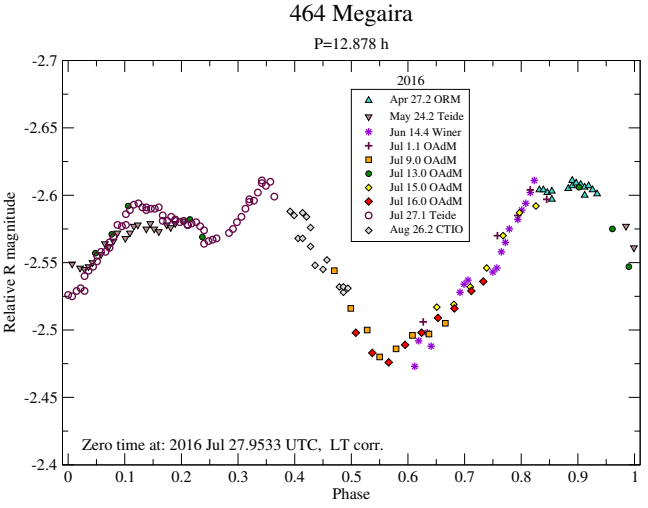

Fig. C.35: Composite light curve of (464) Megaira from the year 2016.

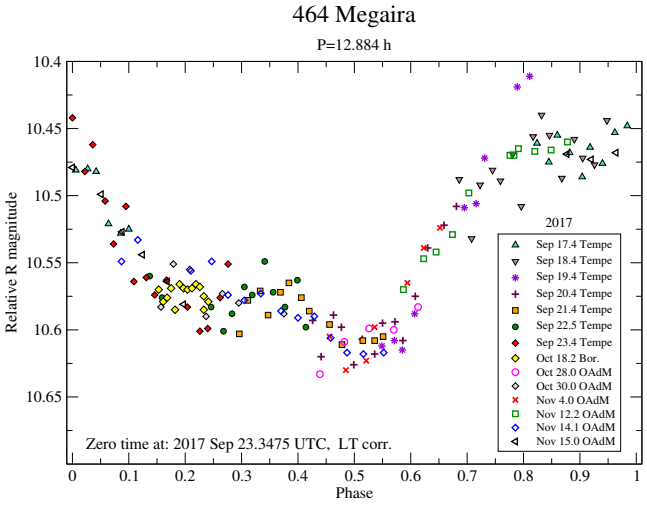

Fig. C.36: Composite light curve of (464) Megaira from the year 2017.

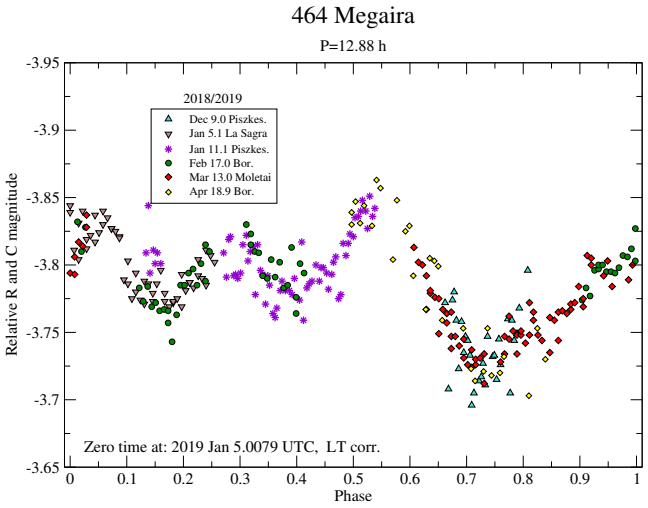

Fig. C.37: Composite light curve of (464) Megaira from the years 2018-2019.

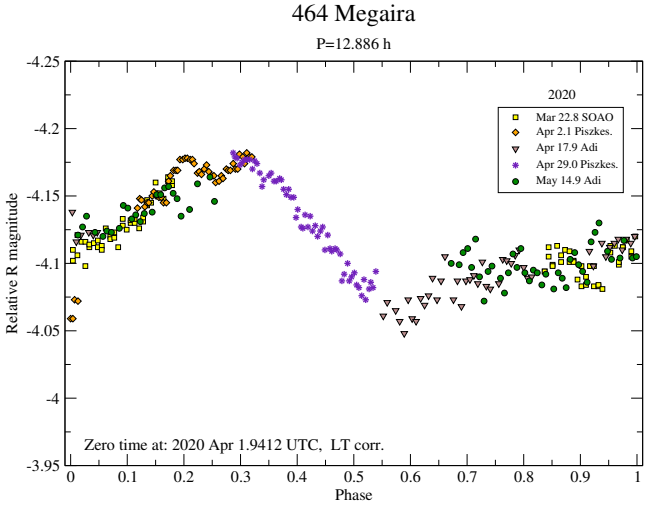

Fig. C.38: Composite light curve of (464) Megaira from the year 2020.

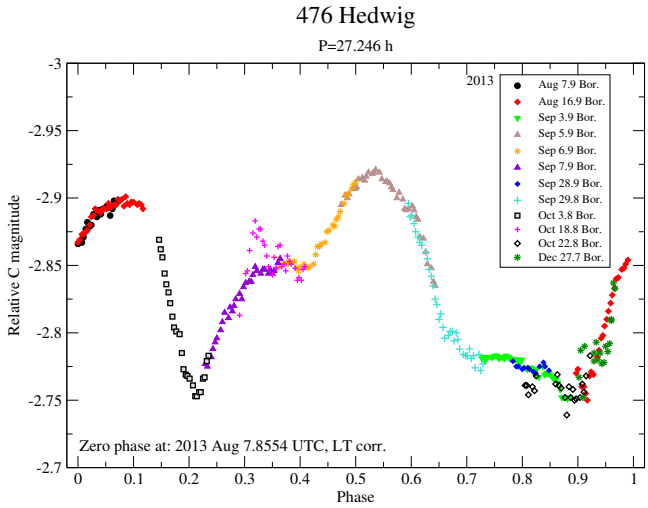

Fig. C.39: Composite light curve of (476) Hedwig from the year 2013.

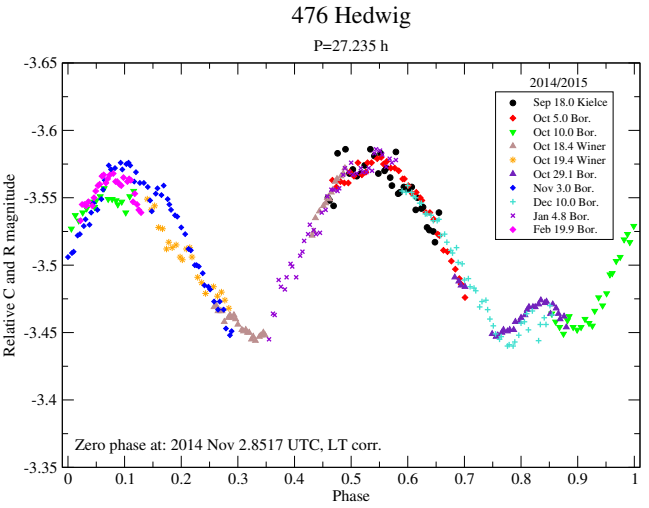

Fig. C.40: Composite light curve of (476) Hedwig from the years 2014-2015.

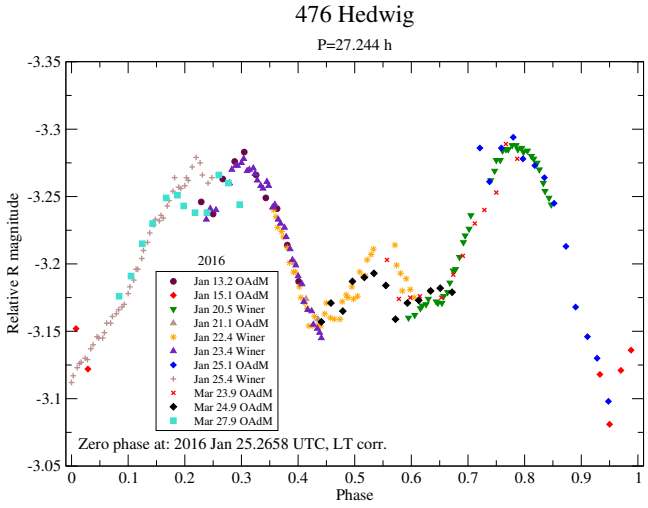

Fig. C.41: Composite light curve of (476) Hedwig from the year 2016.

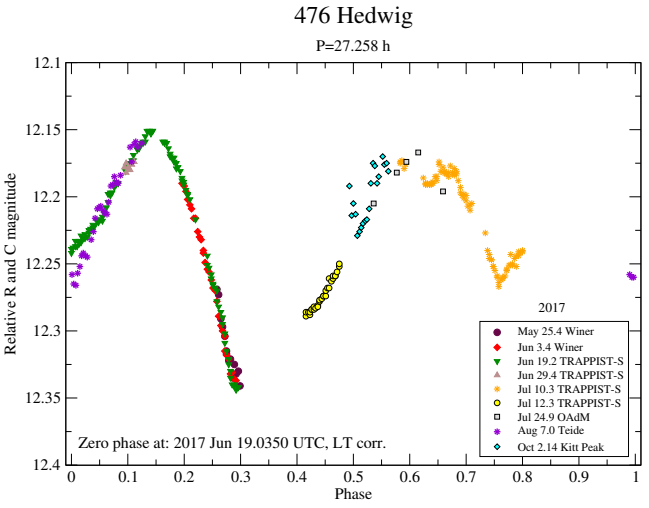

Fig. C.42: Composite light curve of (476) Hedwig from the year 2017.

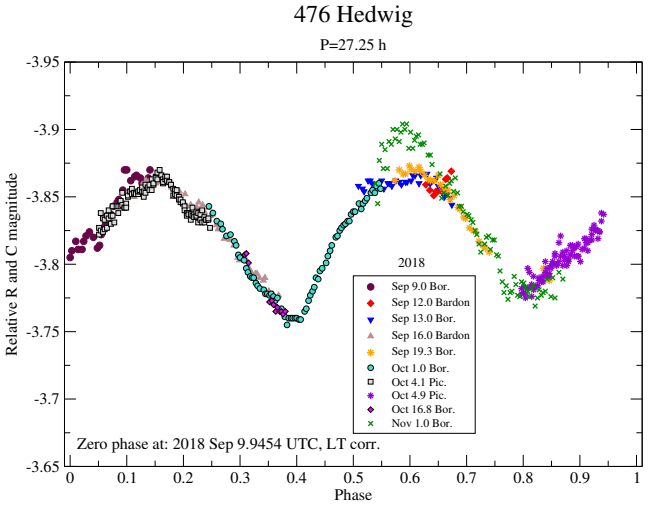

Fig. C.43: Composite light curve of (476) Hedwig from the year 2018.

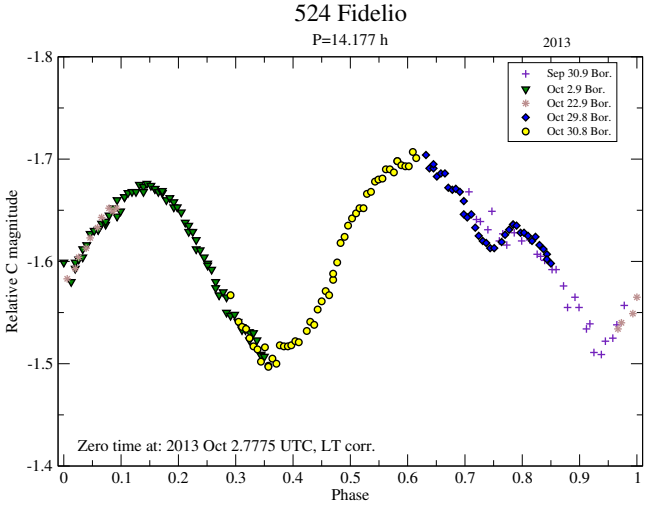

Fig. C.44: Composite light curve of (524) Fidelio from the year 2013.

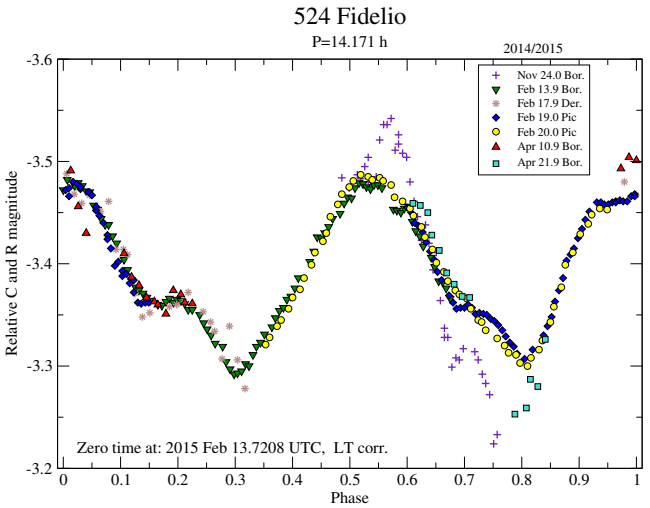

Fig. C.45: Composite light curve of (524) Fidelio from the years 2014-2015.

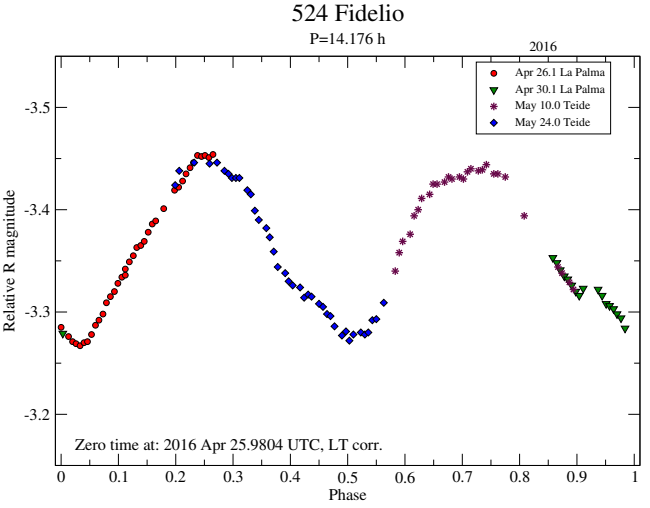

Fig. C.46: Composite light curve of (524) Fidelio from the year 2016.

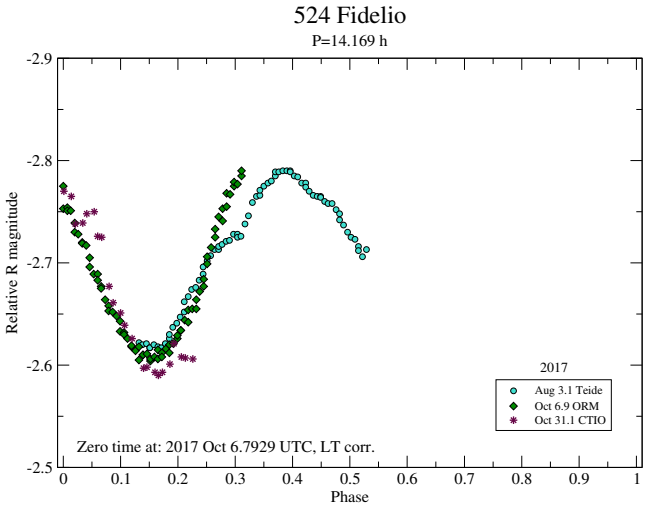

Fig. C.47: Composite light curve of (524) Fidelio from the year 2017.

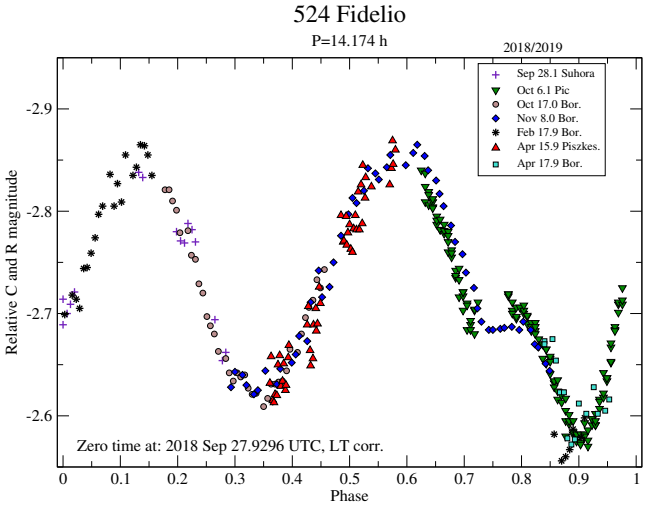

Fig. C.48: Composite light curve of (524) Fidelio from the years 2018-2019.

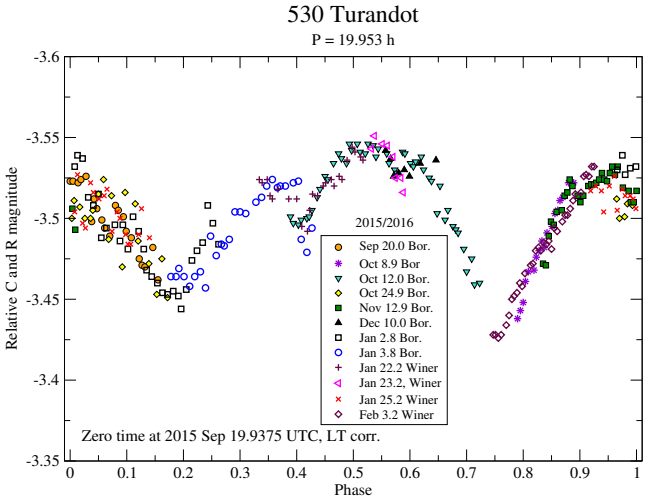

Fig. C.49: Composite light curve of (530) Turandot from the years 2015-2016.

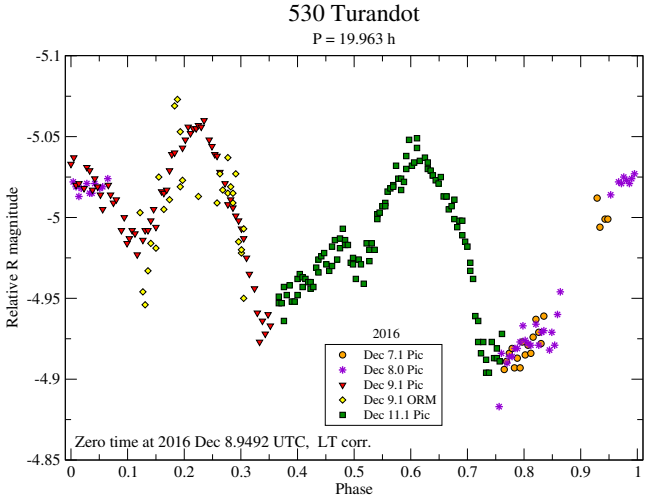

Fig. C.50: Composite light curve of (530) Turandot from the year 2016.

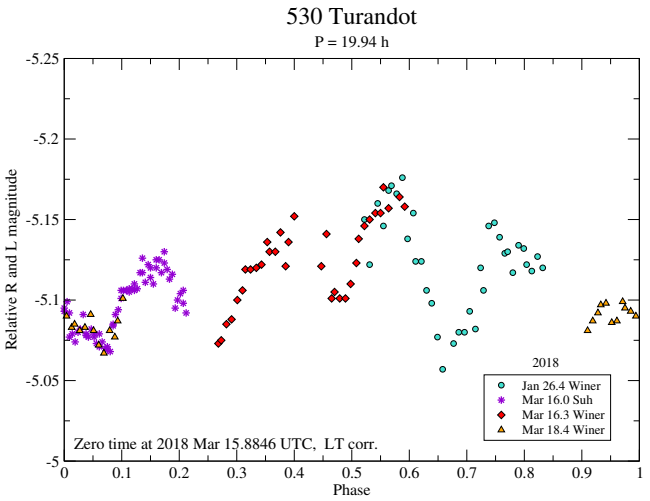

Fig. C.51: Composite light curve of (530) Turandot from the year 2018.

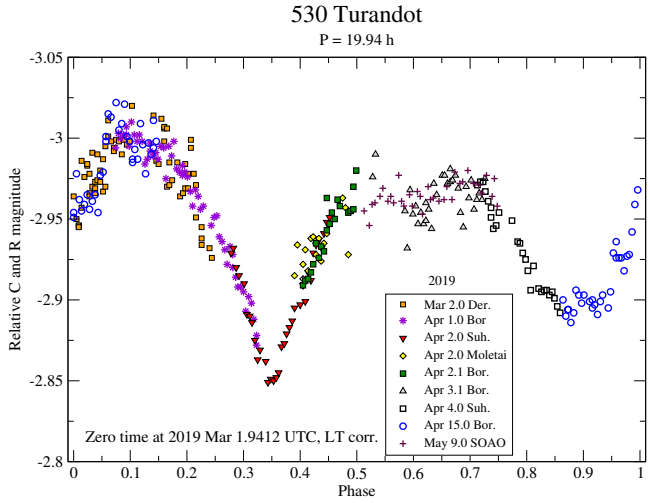

Fig. C.52: Composite light curve of (530) Turandot from the year 2019.

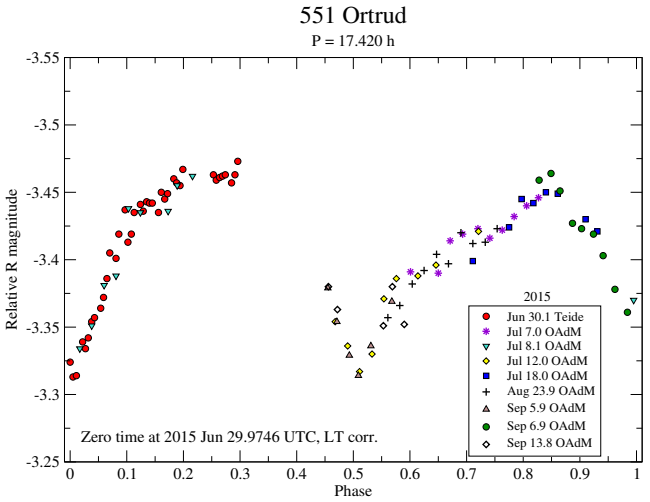

Fig. C.53: Composite light curve of (551) Ortrud from the year 2015.

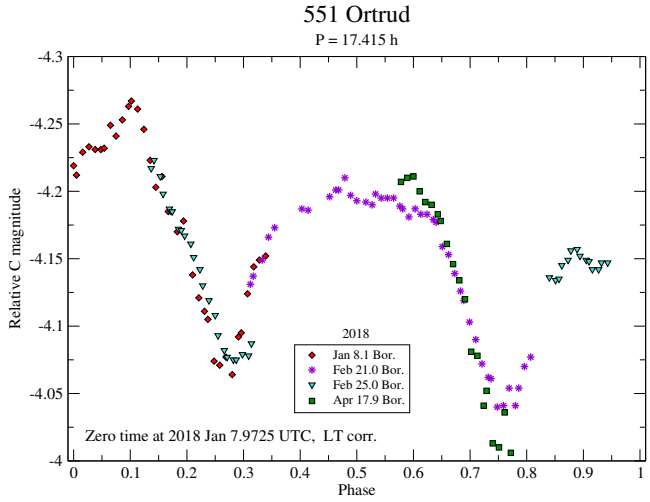

Fig. C.54: Composite light curve of (551) Ortrud from the year 2018.

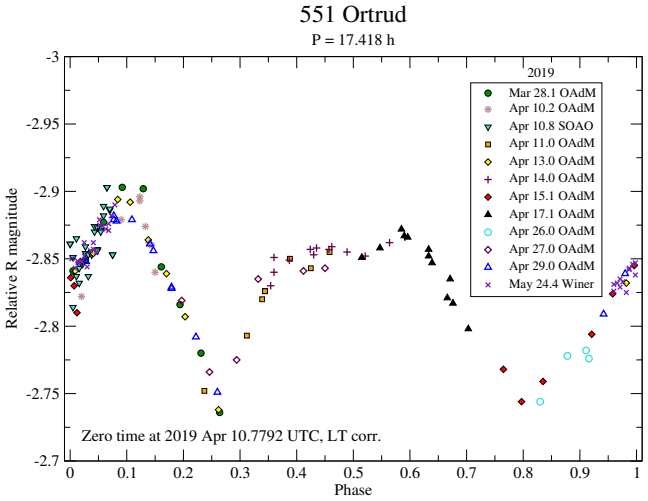

Fig. C.55: Composite light curve of (551) Ortrud from the year 2019.

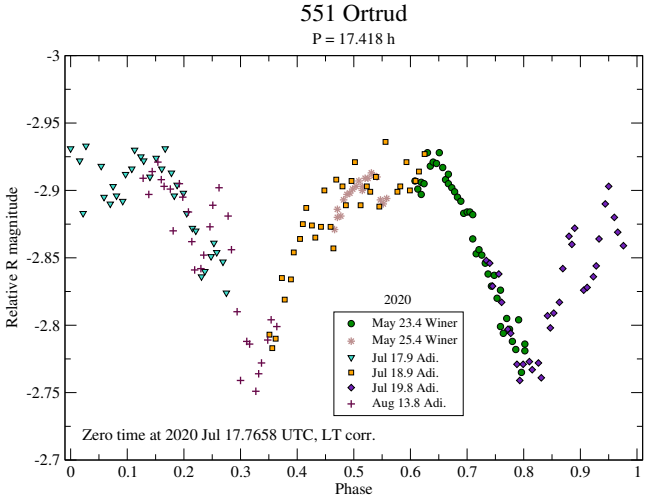

Fig. C.56: Composite light curve of (551) Ortrud from the year 2020.

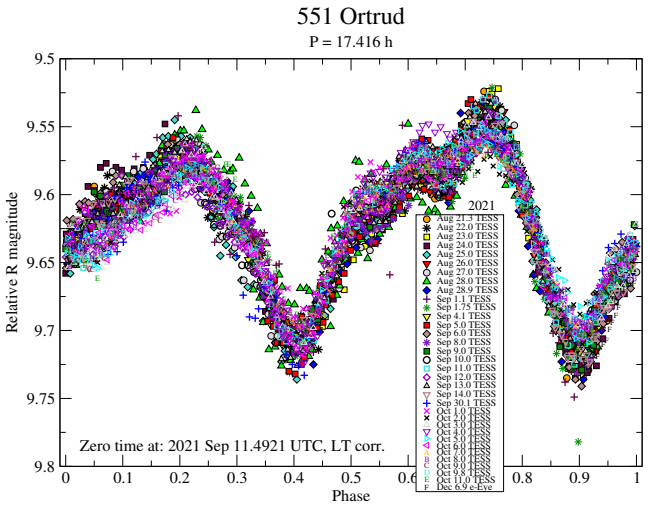

Fig. C.57: Composite light curve of (551) Ortrud from the year 2021, observed mainly from TESS spacecraft.

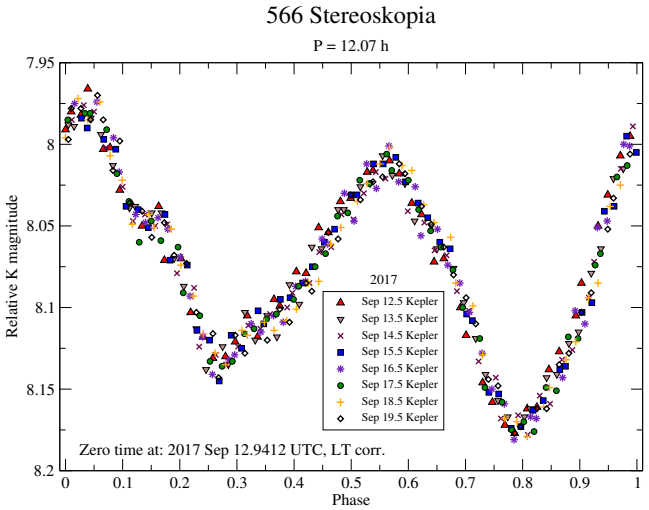

Fig. C.58: Composite light curve of (566) Stereoskopia from the year 2017, observed by Kepler mission.

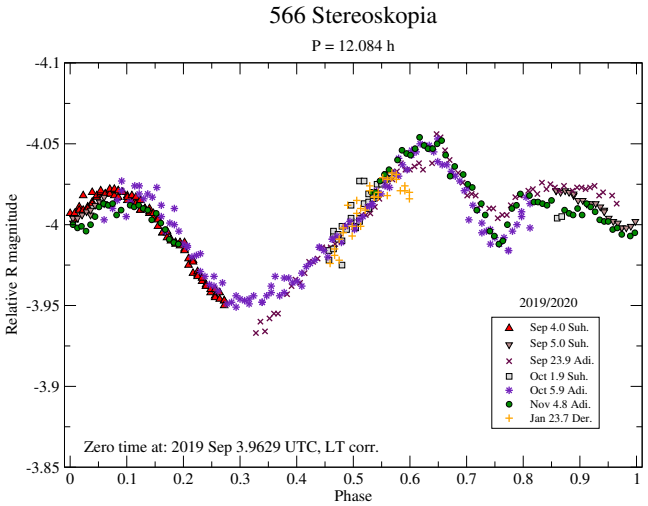

Fig. C.59: Composite light curve of (566) Stereoskopia from the years 2019-2020.

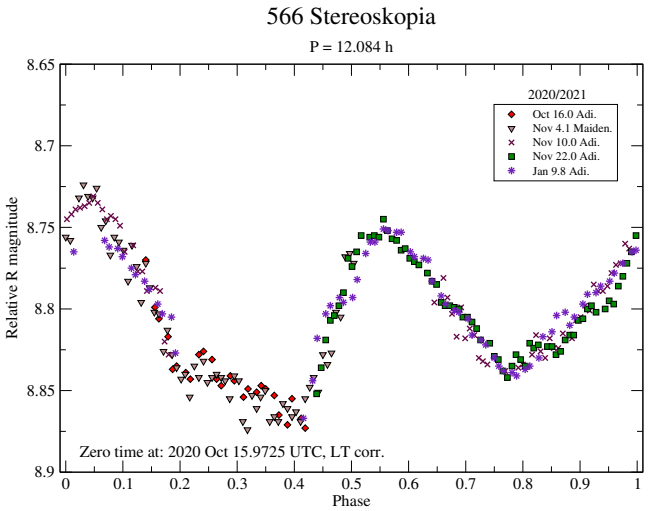

Fig. C.60: Composite light curve of (566) Stereoskopia from the years 2020-2021.

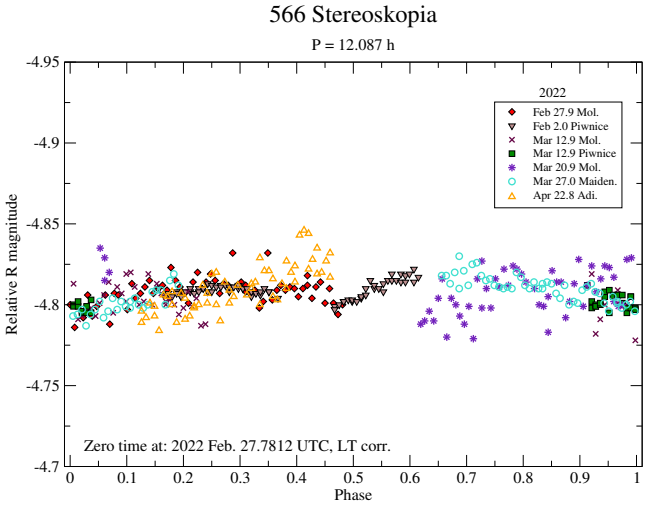

Fig. C.61: Composite light curve of (566) Stereoskopia from the year 2022.

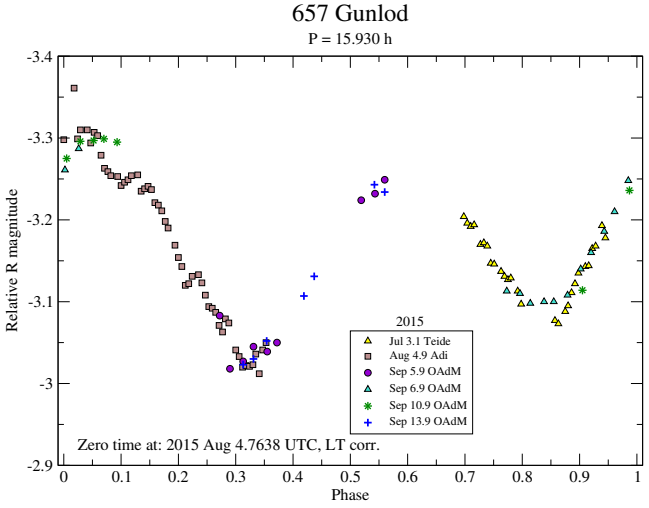

Fig. C.62: Composite light curve of (657) Gunlod from the year 2015.

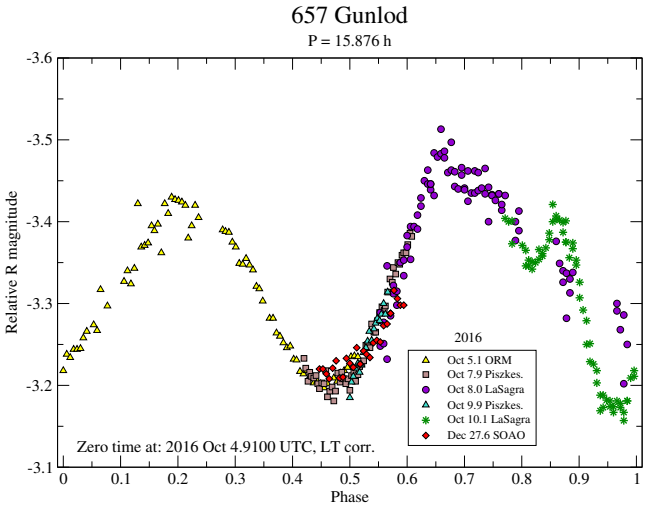

Fig. C.63: Composite light curve of (657) Gunlod from the year 2016, observed mainly from TESS spacecraft.

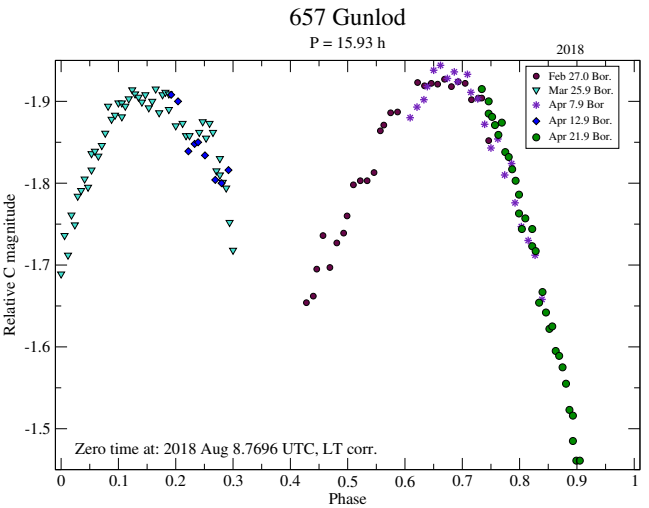

Fig. C.64: Composite light curve of (657) Gunlod from the year 2018, observed by Kepler mission.

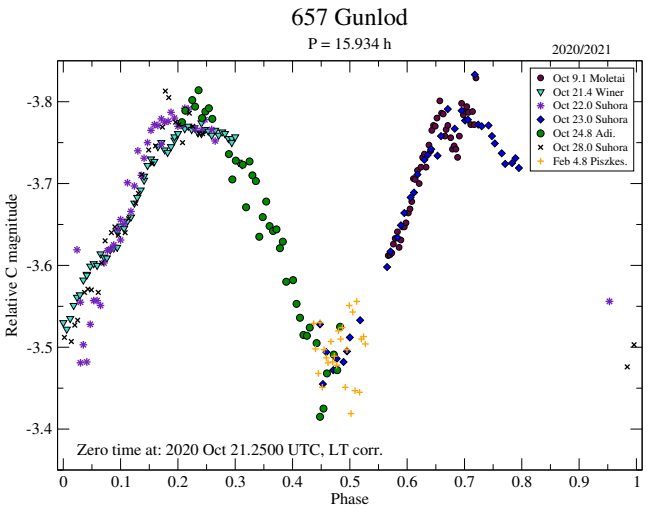

Fig. C.65: Composite light curve of (657) Gunlod from the year 2020.

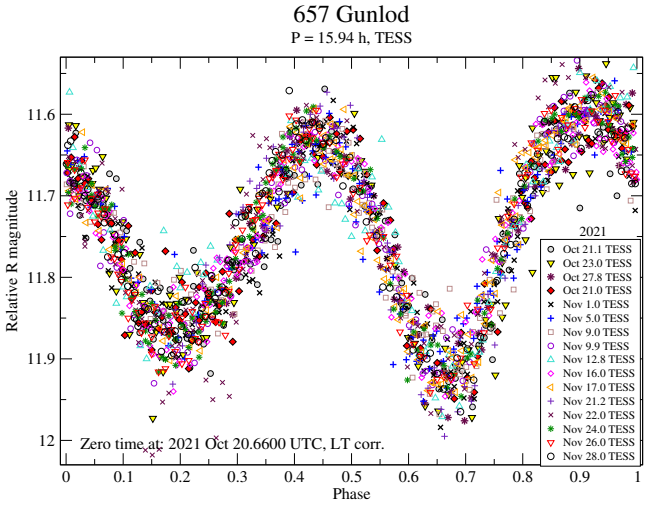

Fig. C.66: Composite light curve of (657) Gunlod from the year 2021 from TESS spacecraft.

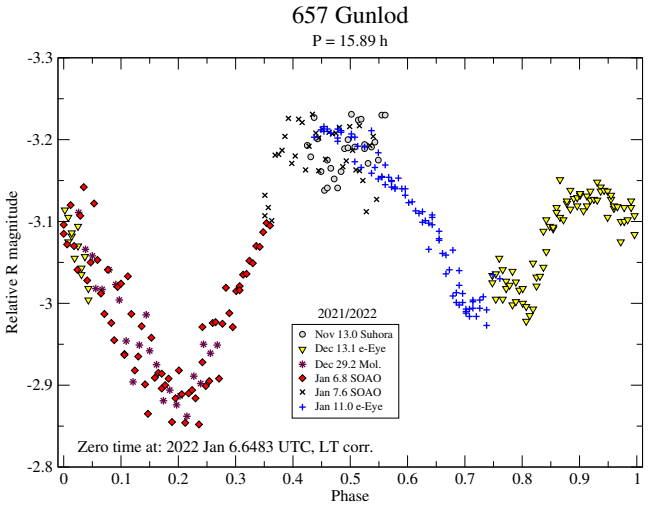

Fig. C.67: Composite light curve of (657) Gunlod from the years 2021-2022. Given the different character of the light curve caused by slightly different viewing geometry, it could not be folded with the light curve from Fig. C.66.

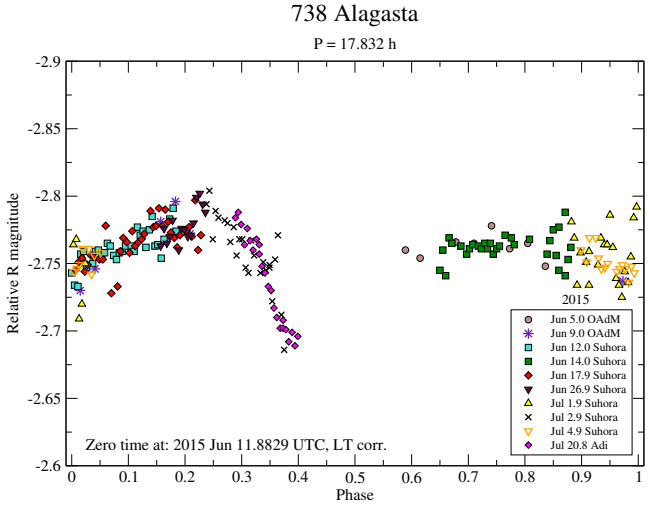

Fig. C.68: Composite light curve of (738) Alagasta from the year 2015.

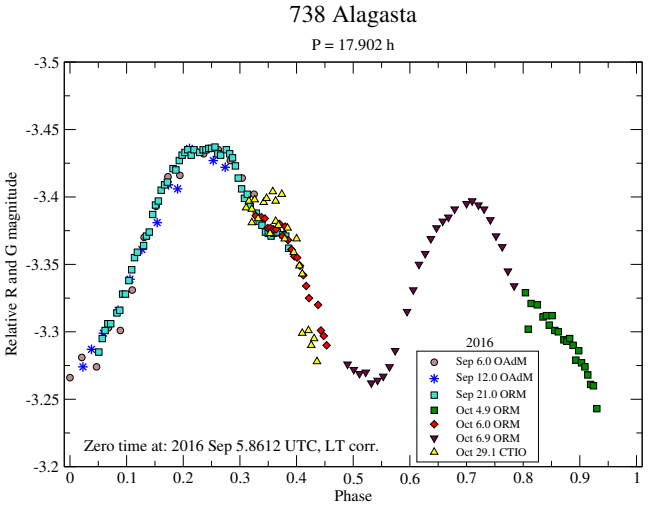

Fig. C.69: Composite light curve of (738) Alagasta from the year 2016.

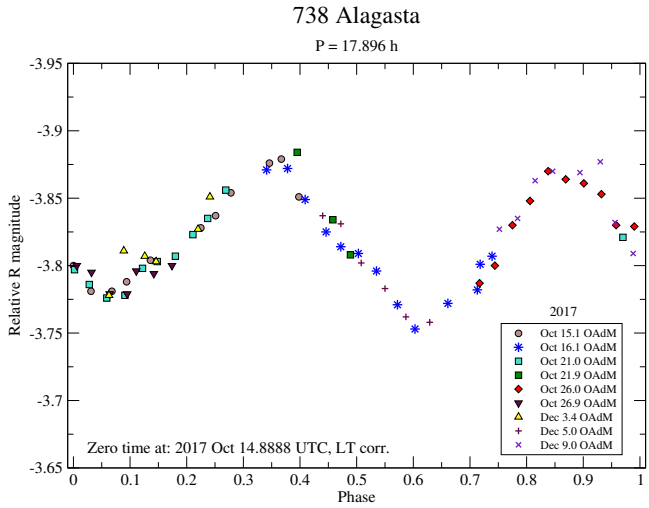

Fig. C.70: Composite light curve of (738) Alagasta from the year 2017.

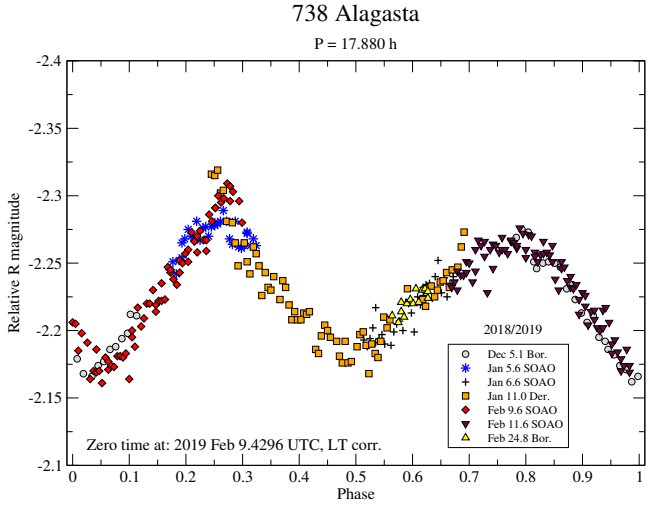

Fig. C.71: Composite light curve of (738) Alagasta from the years 2018-2019.

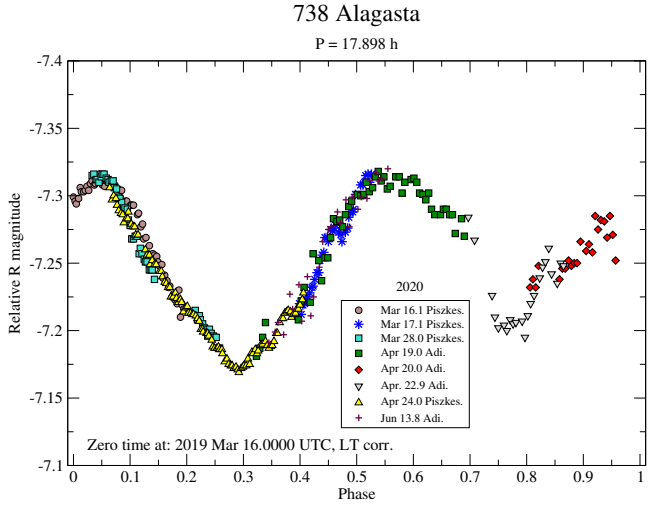

Fig. C.72: Composite light curve of (738) Alagasta from the year 2020.

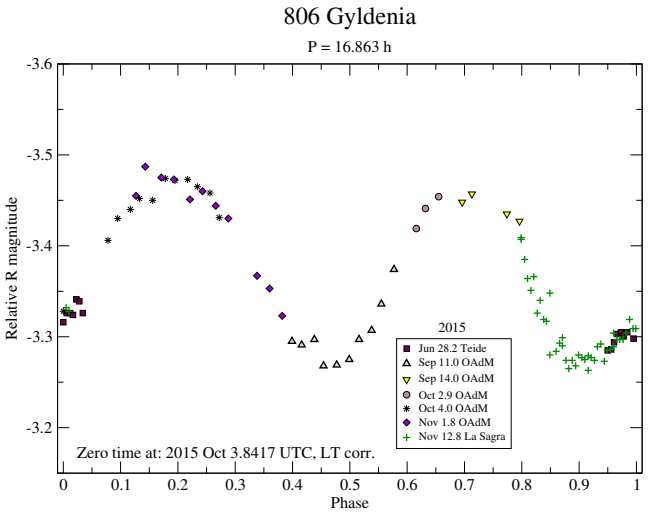

Fig. C.73: Composite light curve of (806) Gyldenia from the year 2015.

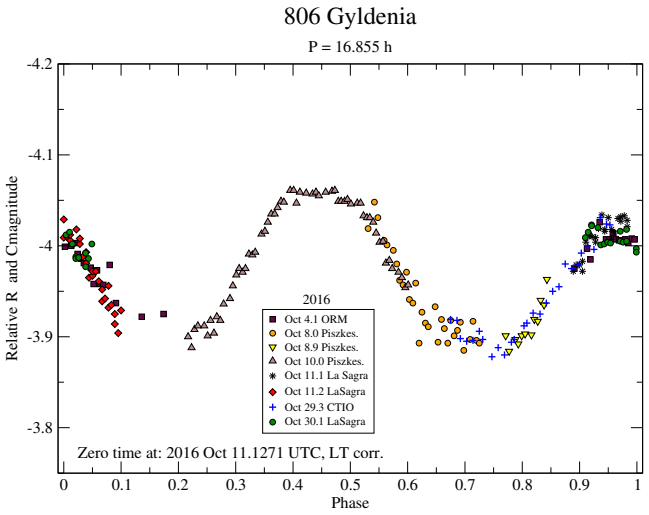

Fig. C.74: Composite light curve of (806) Gyldenia from the year 2016.

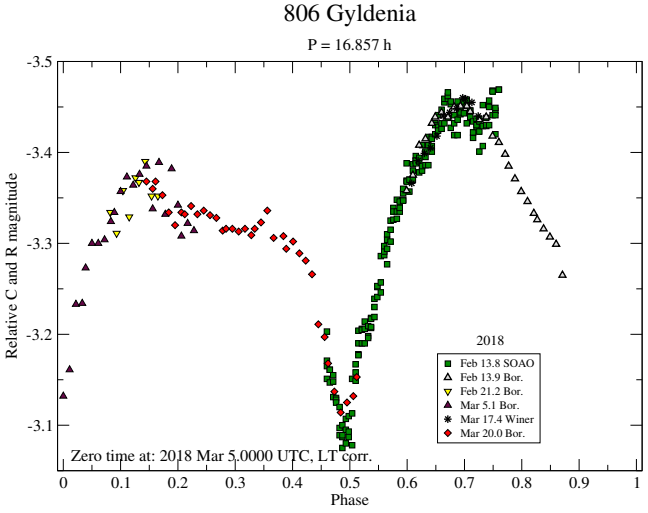

Fig. C.75: Composite light curve of (806) Gyldenia from the year 2018.

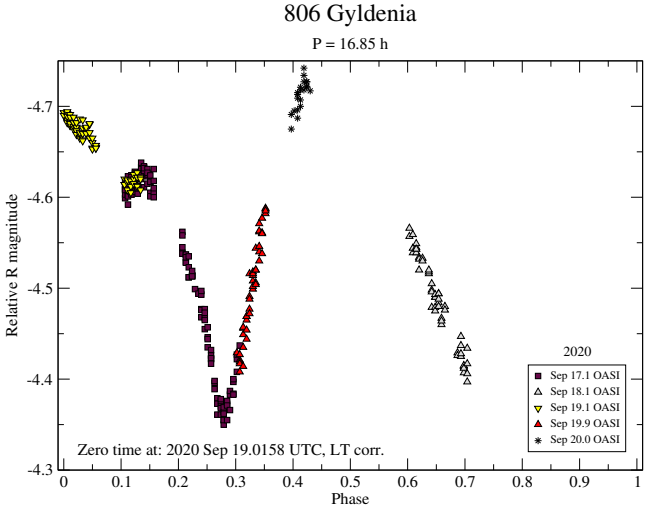

Fig. C.76: Composite light curve of (806) Gyldenia from the year 2020.

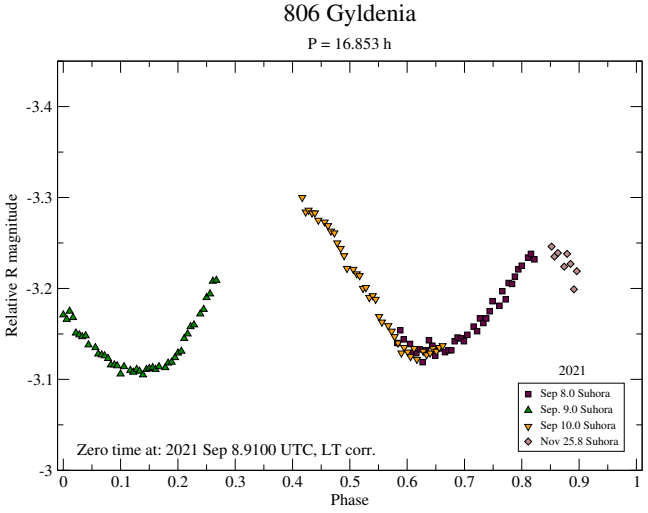

Fig. C.77: Composite light curve of (806) Gyldenia from the year 2021.

Opis rozprawy doktorskiej:

Imię i nazwisko autora pracy	Antoine Choukroun
Adres e-mail, telefon autora pracy	antoine-spartan@hotmail.fr +48 797 128 432
Imię i nazwisko promotora lub promotorów pracy	Anna Marciniak
Wydział	Wydział Fizyki i Astronomii UAM
Instytut/Zakład	Instytut Obserwatorium Astronomiczne UAM
Tytuł pracy w jęz. polskim	Rozmiary i własności cieplne planetoid
Tytuł pracy w jęz. angielskim	Sizes and thermal properties of asteroids
Język pracy	angielski
Słowa kluczowe w jęz. polskim (max 5)	planetoidy - fotometria - model termofizyczny - zakrycia gwiazdowe - średnice planetoid
Słowa kluczowe w jęz. angielskim (max 5)	asteroids - photometry - thermophysical model - stellar occultations - asteroid diameters
Streszczenie pracy w jęz. polskim (max 1400 znaków)	Planetoidy zawierają w sobie cenny zapis historii Układu Słonecznego, lecz własności wielu z nich są słabo poznane. Dokładne rozmiary są niezbędne do wyznaczania gęstości i struktury wewnętrznej, jednak publikowane wartości często różnią się o ponad 30%. Praca łączy fotometrię, modelowanie termofizyczne i zakrycia gwiazd w ramach dwóch długoterminowych kampanii. Przeanalizowano piętnaście planetoid pasa głównego metodą modelowania termofizycznego z inwersją wypukłą (ang. CITPM) oraz za pomocą zakryć gwiazd przez planetoidy. Uzyskane kształty 3D, osie obrotu i średnice są zgodne w granicach 5%, potwierdzając wiarygodność metody CITPM dla danych wysokiej jakości. Wyznaczone bezwładności cieplne (od kilku do >200 J m^{-2} $s^{-½}$ K^{-1}) ukazują zróżnicowane powierzchnie. Autor opracował dane fotometryczne dla 16 wolno rotujących planetoid, co pomogło rozwiązać niejednoznaczności biegunów. Szczegółowo

	scharakteryzowano planetkę (269) Justitia, ograniczając jej rozmiar do 55–60 km i wyznaczając jej własności cieplne; wyniki wsparły kampanię zakryciową i misję MBR Explorer. Stworzone przez autora narzędzia STEROID i occultationFit, usprawniły analizy. Praca dostarcza precyzyjnych charakterystyk planetoid, potwierdza wiarygodność metody CITPM i wspomaga badania gęstości i planowanie misji kosmicznej.
Streszczenie pracy w jęz. angielskim (max 1400 znaków)	Asteroids are key tracers of Solar System history, yet many have poorly known physical properties. Accurate sizes are crucial for bulk density and internal structure, but estimates often differ by over 30%, causing major uncertainties. This thesis tackles these issues by combining photometry, thermophysical modelling, and stellar occultations within two long-term international campaigns. Fifteen main-belt asteroids were analysed using the Convex Inversion Thermophysical Model (CITPM) and multichord stellar occultations. Reconstructed 3D shapes, spin axes, and diameters agree within 5%, validating the CITPM for high-quality data. Derived thermal inertias (few to >200 J m^{-2} $s^{-½}$ K^{-1}) show diverse surface properties. The author also processed photometric data for 16 slow rotators, which helped to solve previous size inconsistencies and mirror-pole ambiguities. A detailed study of (269) Justitia constrained its size to 55–60 km and provided first thermal properties for the first time, aiding an occultation campaign and informing the Emirates MBR Explorer mission. Two open-source Python tools created by an author, STEROID and occultationFit, ensured reproducible analyses. This work provides precise characterisations, confirms CITPM reliability, and offers insights for density studies and space mission planning.
liczba stron	56 stron wstępu do pracy + zbiór 4 publikacji